Novel Sensor for the In Situ Measurement of Uranium Fluxes
Project Number: DE-FG02-08ER64585
Kirk Hatfield (PI), University of Florida
kirk.hatfield@essie.ufl.edu; tel 352 392-9537; Fax 352 392-3394

Executive Summary:

The goal of this project was to develop a sensor that incorporates the field-tested concepts of the passive flux meter to provide direct in situ measures of flux for uranium and groundwater in porous media. Measurable contaminant fluxes [J] are essentially the product of concentration [C] and groundwater flux or specific discharge [q]. The sensor measures [J] and [q] by changes in contaminant and tracer amounts respectively on a sorbent. By using measurement rather than inference from static parameters, the sensor can directly advance conceptual and computational models for field scale simulations. The sensor was deployed in conjunction with DOE in obtaining field-scale quantification of subsurface processes affecting uranium transport (e.g., advection) and transformation (e.g., uranium attenuation) at the Rifle IFRC Site in Rifle, Colorado. Project results have expanded our current understanding of how field-scale spatial variations in fluxes of uranium, groundwater and salient electron donor/acceptors are coupled to spatial variations in measured microbial biomass/community composition, effective field-scale uranium mass balances, attenuation, and stability. The coupling between uranium, various nutrients and micro flora can be used to estimate field-scale rates of uranium attenuation and field-scale transitions in microbial communities. This research focuses on uranium (VI), but the sensor principles and design are applicable to field-scale fate and transport of other radionuclides. Laboratory studies focused on sorbent selection and calibration, along with sensor development and validation under controlled conditions. Field studies were conducted at the Rifle IFRC Site in Rifle, Colorado. These studies were closely coordinated with existing SBR (formerly ERSP) projects to complement data collection. Small field tests were conducted during the first two years that focused on evaluating field-scale deployment procedures and validating sensor performance under controlled field conditions. In the third and fourth year a suite of larger field studies were conducted. For these studies, the uranium flux sensor was used with uranium speciation measurements and molecular-biological tools to characterize microbial community and active biomass at synonymous wells distributed in a large grid. These field efforts quantified spatial changes in uranium flux and field-scale rates of uranium attenuation (ambient and stimulated), uranium stability, and quantitatively assessed how fluxes and effective reaction rates were coupled to spatial variations in microbial community and active biomass. Analyses of data from these field experiments were used to generate estimates of Monod kinetic parameters that are 'effective' in nature and optimal for modeling uranium fate and transport at the field-scale.

This project provided the opportunity to develop the first sensor that provides direct measures of both uranium (VI) and groundwater flux. A multidisciplinary team was assembled to include two geochemists, a microbiologist, and two quantitative contaminant hydrologists. Now that the project is complete, the sensor can be deployed at DOE sites to evaluate field-scale uranium attenuation, source behavior, the efficacy of remediation, and off-site risk. Because the sensor requires no power, it can be deployed at remote sites for periods of days to months. The fundamental science derived from this project can be used to advance the development of predictive models for various transport and attenuation processes in aquifers. Proper development of these models is critical for long-term stewardship of contaminated sites in the context of predicting uranium source behavior, remediation performance, and off-site risk.

1.0 Introduction

In recent years the DoE has supported research to understand microbial and geochemical factors controlling uranium fate and transport in the field. This research showed that the addition of acetate (an electron donor) stimulated spatial changes in the subsurface microbial community that in turn reduced soluble U(VI) (UO_2^{2+}) to insoluble U(IV) as the oxide, uraninite (UO_2) (Anderson et al. 2003; and Vrionis et al. 2005). Once the amendment with acetate was terminated, the microbial community again changed in space, but U(IV) remained quite stable (Vrionis et al. 2005). Thus, a bioremediation strategy aimed at UO_2^{2+} reduction would appear to be a promising approach to reducing uranium transport from source areas (Lloyd and Macaskie, 2000). The ultimate goal for DOE is to develop field-scale descriptions of subsurface processes affecting contaminant transport or transformations of uranium. Current DOE supported research at the Rifle IFRC site is focusing on testing hypotheses related to 1) geochemical and microbial controls on stimulated uranium bioreduction, 2) uranium sorption under iron-reducing conditions, 3) uranium stability and removal after biostimulation, and 4) natural rates of uranium bioreduction. Given DOE's ultimate goal, it is necessary to develop appropriate sensors and associated modeling tools to quantify reaction mass balances, uranium stability, and uranium attenuation rates at the field-scale. With these tools and the field-scale assessments they provide, we can expand our understanding of uranium fate and transport across spatial scales and 1) derive or validate methods of upscaling local or pore-scale measures of uranium attenuation rates and mass balances, 2) quantify relationships between spatial changes in uranium and nutrient mass discharges and spatial changes in microbial communities, 3) apply insight gained at the molecular scale to interpret or predict reactions and processes occurring at the field scale, and 4) refine field-scale conceptual and computation models of uranium transport using available data from the local scale.

The current preferred method for estimating field-scale reaction mass balances and contaminant attenuation rates in the subsurface is to measure or estimate contaminant mass fluxes or contaminant mass discharges at multiple well transects. Contaminant mass flux [J] (mass flow per unit area per unit time) is often expressed as the product of the contaminant concentration [C] and groundwater specific discharge [q] or $J = q \cdot C$. Contaminant mass discharge (mass per unit time) is the integrated mass flux over an area or transect. Mass flux and contaminant mass discharge obtained at multiple locations along a flow path are used to quantify spatial changes in geochemistry, field-scale reaction mass balances, and field-scale rates of in situ reactions.

Accuracy varies between techniques used to measure or estimate flux. Most techniques estimate flux from the equation $J = q \cdot C$; where contaminant concentrations are measured and the specific discharge is either measure or estimated [Ballard, 1996, Bockelmann et al. 2003; Borden et al 1997; King et al. 1999; Kao and Wang 2001, and Newell et al. 2004]. Kuebert and Finkel [2006] evaluated eight methods and found that spatially integrated measures from the passive flux meter (PFM) produced the most accurate estimates of contaminant mass discharge with the fewest number of wells in heterogeneous aquifers. The PFM is a sensor developed by Hatfield et al. [2004] which provides direct in situ measures of both contaminant and water fluxes (J and q).

Prior to this project, and to the best of our knowledge, direct measures of radionuclide fluxes have not been conducted in laboratory or in the field by PFM or any other technology. Instead, radionuclide fluxes were typically estimated using observed aqueous contaminant concentrations and measured or calculated groundwater flows. This approach, as suggested above, tends to produce discharge estimation errors in the field because contaminant concentrations and water fluxes used in calculations are rarely sampled and applied over coincident or appropriate time and space scales [Hatfield et al. 2004]. For example depth variations in concentration may have been measured, but not with associated measures of water flux that would then permit a local determination of contaminant flux (the product of concentration and water

flux). A major objective of this project was to demonstrate uranium PFM can be used to quantify uranium stability, mass balances, and attenuation rates at the field-scale.

In order to do this, the initial project objective was to develop a passive flux meter (PFM) for simultaneous and direct *in situ* measurement of both uranium and water fluxes. This was done by adapting field-tested concepts from PFMs designed to measure the fluxes of hydrophobic organics (Hatfield et al 2004; Annable et al. 2005; Campbell et al 2006; and Klammler et al. 2007). Laboratory studies were conducted for sensor development and validation under controlled conditions. Field studies involving the sensors were conducted at the Rifle IFRC site in close coordination with existing DOE projects to complement data collection. The sensors were used to quantify field-scale subsurface processes affecting uranium transport (e.g., measuring advection) and transformation (e.g., uranium attenuation). The uranium PFM and existing molecular biological tools were then used in concert to examine how field-scale rates of measured uranium attenuation are spatially correlated to field-scale transitions in microbial communities. These data can in turn be applied to estimate effective field-scale parameters for microbially-mediated Monod reactions attributed to field-scale uranium attenuation under ambient and stimulated conditions.

The specific research objectives of this project are listed below along with citations for the resulting peer reviewed publications:

1) Conduct a series of laboratory and field tests to select and characterize PFM components (sorbents and resident tracers) and evaluate the overall performance of the multi-layer PFM design (Stucker et al., 2011 and Klammler et al., 2012A).
2) Conduct geochemical modeling to predict sensor performance under a broad range of conditions (Leavitt et al., 2011).
3) Validate the uranium PFM performance under a range of geochemical and microbiological conditions at both the laboratory and field scale (Klammler et al., 2012B; Klammler et al., 2011A; Klammler et al., 2014; and Klammler et al., 2011B).
4) Analyze field results to obtain field-estimates of effective parameters for microbially-mediated Monod reactions attributed to field-scale uranium attenuation under ambient and stimulated conditions (Mohamed and Hatfield, 2010 and Mohamed et al., 2010).

The research results for each objective are summarized in section 2 of this report, and the corresponding peer reviewed publications are provided in the appendix.

2.0 Peer Reviewed Publications
Listed below are the titles and abstracts of nine peer reviewed publications that are direct products of this project. The publications are included in their entirety in the appendix.

Evaluation and application of anion exchange resins to measure groundwater uranium flux at a former uranium mill site. (Stucker et al., 2011) Laboratory tests and a field validation experiment were performed to evaluate anion exchange resins for uranium sorption and desorption in order to develop a uranium passive flux meter (PFM). The mass of uranium sorbed to the resin and corresponding masses of alcohol tracers eluted over the duration of groundwater installation are then used to determine the groundwater and uranium contaminant flux. Laboratory based batch experiments were performed using Purolite A500, Dowex 21K and 21K XLT, Lewatit S6328-A resins and silver impregnated activated carbon to examine uranium sorption and extraction for each material. The Dowex resins had the highest uranium sorption, followed by Lewatit, Purolite and the activated carbon. Recoveries from all ion exchange resins were in the range of 94 to 99% for aqueous uranium in the environmentally relevant concentration range studied (0.01 to 200 ppb). Due to the lower price and well-characterized tracer capacity, Lewatit S6328 A was used for field-testing of PFMs at the DOE UMTRA site in Rifle, CO. The

effect on the flux measurements of extractant (nitric acid)/resin ratio, and uranium loading were investigated. Higher cumulative uranium fluxes (as seen with concentrations > 1 ug U / gram resin) yielded more homogeneous resin samples versus lower cumulative fluxes (<1 ug U / gram resin), which caused the PFM to have areas of localized concentration of uranium. Resin homogenization and larger volume extractions yield reproducible results for all levels of uranium fluxes. Although PFM design can be improved to measure flux and groundwater flow direction, the current methodology can be applied to uranium transport studies.

Water and contaminant flux estimation from multi-layer passive flux meter measurements. (Klammler et al., 2012A) The passive flux meter (PFM) enables measuring cumulative water and contaminant mass fluxes in porous aquifers. It consists of a sorbent material, which is installed in a monitoring well to intercept groundwater flow. Tracer losses and contaminant retention on the sorbent are used to estimate water and contaminant mass fluxes through the device. In the multi-layer PFM different (sorbent) materials are used in an annulus (layer-type) configuration. This allows for retaining leached tracers inside the PFM (no tracer release into aquifer) and facilitates simultaneous deployment of different sorbent types in a single device. In order to estimate undisturbed ambient fluxes in the aquifer, measurements need to be corrected for flow convergence or divergence induced by the well and PFM components. We make use of an analytical solution to the potential flow problem of uniform flow disturbed by a system of concentric rings of contrasting hydraulic conductivities. A flow convergence factor is defined as a function of PFM ring conductivities and radii, where tracer elution and contaminant sorption may occur in arbitrary layers. Results are used for calibration of convergence factors of a multi-layer PFM to laboratory sand box experiments.

Equilibrium modeling of U(VI) speciation in high carbonate groundwaters: Model error and propagation of uncertainty. (Leavitt et al., 2011) The reliability and applicability of geochemical reactive transport models may be limited by determinate (model) errors and random (uncertainty) errors in the equilibrium speciation calculations. Determinate errors in calculated uranium concentrations in high-carbonate groundwaters were investigated using several equilibrium speciation programs and databases. The most significant errors were caused by using databases which were not recently updated. Differing ionic strength equations were not a source of significant errors, but due to the importance of uranyl-carbonate interactions it may be useful to measure dissolved inorganic carbon directly rather than to infer the carbonate concentration from alkalinity titrations.

Uncertainty propagation was examined using first-derivative sensitivity calculations and Monte Carlo simulations. Two types of systems were considered: I. Dissolved U(VI) speciation based on measured analytical constraints and solution phase equilibrium and II. Overall U(VI) speciation which combined the dissolved phase equilibria with previously published adsorption reactions. Dissolved speciation calculations were robust, with minimal amplification of analytical uncertainty. Although calculations using the adsorption model were robust with respect to adsorbed U(VI) concentration prediction, bimodal distributions of dissolved U(VI) concentrations were observed in simulations with background levels of total U(VI) and field estimates of analytical constraints, indicating the model may not be robust with respect to levels of uncertainty comparable to spatial and temporal variability.

Contaminant Discharge and Uncertainty Estimates from Passive Flux Meter Measurements. (Klammler et al., 2012B) A method is presented, which combines (1) a nonparametric method for assigning confidence intervals to mean estimates of independent but skewed data with (2) basic geostatistical principles accounting for data correlation. The former has been proposed by a series of authors and uses a simple cubic transformation of the classic Student t-variable. The latter uses the concepts of dispersion and estimation variance to introduce an effective number of data as a measure of reduction in variance and skewness due to averaging. With the effective number of data an estimation variance, which is conditional to observed data, is defined and its properties compared to other

approaches in literature. The method is discussed with respect to estimating mass discharges at transects from local passive flux meter measurements regarding (1) the benefits of additional sampling in terms of uncertainty reduction and (2) the sensitivity of results to not well defined spatial correlation parameters. Charts are given for this purpose and for a rapid first order determination of the effective number of data independent of transect shape, number of observation wells and spatial correlation parameters.

A Trigonometric Interpolation Approach to Mixed Type Boundary Problems Associated with Permeameter Shape Factors. (Klammler et al., 2011A) Hydraulic conductivity is a fundamental hydrogeological parameter, whose in-situ measurement at a local scale is principally performed through injection tests from screened probes or using impermeable packers in screened wells. The shape factor, F [L], is a proportionality constant required to estimate conductivity from observed flow rate to injection head ratios and it depends on the geometric properties of the flow field. Existing approaches for determination of F are either based on geometric or mathematical simplifications and are limited to particular assumptions about the flow domain's external boundaries. The present work presents a general semi-analytical solution to steady-state axisymmetric flow problems, where external boundaries may be nearby and of arbitrary combinations of impermeable and constant head type. The inner boundary along the probe / well may consist of an arbitrary number of impermeable and constant head intervals resulting in a mixed type boundary value problem, for which a novel and direct solution method based on trigonometric interpolation is presented. The approach is applied to generate practical non-dimensional charts of F for different field and laboratory situations. Results show that F is affected by less than 5 % if a minimum distance of 10 probe / well diameters is kept between the injection screen and a nearby boundary. Similarly, minimum packer lengths of 2 well diameters are required to avoid increasing F by more than 10 %. Furthermore, F is determined for laboratory barrel experiments giving guidelines for achieving equal shape factors as in field situations without nearby boundaries. A fully analytical solution is presented for the theoretical case of infinitely short packers.

Effect of injection screen slot geometry on hydraulic conductivity tests. (Klammler et al., 2014) Hydraulic conductivity and its spatial variability are important hydrogeological parameters and its measurement is typically performed by injection tests at different scales. For injection test interpretation, shape factors are required to account for injection screen geometry. Existing results for such shape factors assume either an ideal screen (i.e., ignoring effects of screen slot geometry) or infinite screen length (i.e., ignoring effects of screen extremes). In the present work we investigate the combined effects of circumferential screen slot geometry and finite screen length on injection shape factors. This is done in terms of a screen entrance resistance by solving a mixed type boundary value problem in an axi-symmetric flow domain using a semi-analytical solution approach. Results are compared to existing analytical solutions for circumferential and longitudinal slots on infinite screens, which are found to be identical. Based on an existing approximation, an expression is developed for a dimensionless screen entrance resistance of infinite screens, which is a function of the relative slot area only. For anisotropic conditions, e.g., when conductivity is smaller in the vertical direction than in the horizontal, screen entrance losses for circumferential slots increase, while they remain unaffected for longitudinal slots.

Approximate Unconditional Up-Scaling of Spatially Correlated Non-Gaussian Variables. (Klammler et al., 2011B) We present a series of simple approximate methods for up-scaling the cumulative distribution function of spatially correlated variables by using an effective number n_e of independent variables. Methods are based on the property of distribution permanence of the gamma and inverse Gaussian distributions under averaging, bootstrap sampling and expansions about the normal and gamma distribution. A stochastic simulation study is used to validate each method and simple parameters are defined to identify respective ranges of applicability. A practical example is presented where core sample rock strength data is up-scaled to shaft size for probabilistic deep foundation design. Supplemental material is available online.

Dimensionless monod parameters to summarize the influence of microbial growth kinetics and inhibition on the attenuation of groundwater contaminants. (Mohamed and Hatfield, 2010) Monod expressions are preferred over zero- and first-order decay expressions in modeling contaminants biotransformation in groundwater because they better represent complex conditions. However, the wide-range of values reported for Monod parameters suggests each case-study is unique. Such uniqueness restricts the usefulness of modeling, complicates an interpretation of natural attenuation and limits the utility of a bioattenuation assessment to a small number of similar cases. In this paper, four Monod-based dimensionless parameters are developed that summarize the effects of microbial growth and inhibition on groundwater contaminants. The four parameters represent the normalized effective microbial growth rate (η), the normalized critical contaminant/substrate concentration (S^*), the critical contaminant/substrate inhibition factor (N), and the bioremediation efficacy (η^*). These parameters enable contaminated site managers to assess natural attenuation or augmented bioremediation at multiple sites and then draw comparisons between disparate remediation activities, sites and target contaminants Simulations results are presented that reveal the sensitivity of these dimensionless parameters to Monod parameters and varying electron donor/acceptor loads. These simulations also show the efficacy of attenuation (η^*) varying over space and time. Results suggest electron donor/acceptor amendments maintained at relative concentrations S^* between 0.5 and 1.5 produce the highest remediation efficiencies. Implementation of the developed parameters in a case study proves their usefulness.

Stochastic evaluation of subsurface contaminant discharge under physical, chemical, and biological heterogeneities. (Mohamed et al., 2010) A finite element 2D Monte Carlo approach is used to evaluate the sensitivity of groundwater contaminant discharges to a Damkohler number and spatial variability in aquifer hydraulic conductivity, initial microbial biomass concentrations, and electron acceptor/donor concentrations. Bioattenuation is most sensitive to spatial variations in incipient biomass and critical electron donors/acceptors for   (i.e., when pore-water residence times are high compared to the time needed for microbial growth or contaminant attenuation). Under these conditions, critical reaction processes can become substrate-limited at multiple locations throughout the aquifer; which in turn increases expected contaminant discharges and their uncertainties at monitored transects. For, contaminant discharge is not sensitive to incipient biomass variations. Physical heterogeneities expedite plume arrival and delay departure at transects and in turn attenuate peak discharges but do not affect cumulative contaminant discharges. Physical heterogeneities do, however, induce transect mass discharge variances that are bimodal functions of time; the first peak being consistently higher. A simple streamtube model is invoked to explain the occurrence of peaks in contaminant discharge variance.

Publications in preparation
In addition to the publications listed above, at least three additional peer reviewed publications are in preparation:

1. Newman, M., J. Cho, H. Klammler, K. Hatfield, M. Annable, A. Peacock, V. Stucker, J. Ranville. 2015. Innovative technologies developed to extend the applicability for passive measurement of aqueous contaminant fluxes at the field-scale. ES&T. (*In Preparation*).
2. Newman, M., H. Klammler, K. Hatfield, J. Cho, M. Annable, A. Peacock, V. Stucker, J. Ranville. 2015. Temporal and spatial characterization of field-scale water and uranium fluxes in a shallow aquifer. Journal of Contaminant Hydrology. (*In Preparation*).
3. Peacock, A., M. Newman, H. Klammler, J. Cho, K. Hatfield, M. Annable, V. Stucker, J. Ranville. Passive methods for quantifying field-scale biomass flux. (*In Preparation*).

4.0 Summary and Conclusions

The overarching goal of the Subsurface Biogeochemical Research (SBR) program is to advance a predictive understanding of the biogeochemical structure and function of subsurface environments in order to enable systems-level environmental prediction and decision support. Part of this goal is to provide the DOE with field-scale descriptions of subsurface processes affecting contaminant transport or transformations. Current DOE supported research at the Rifle IFRC Site in Rifle, Colorado is focused on testing hypotheses related to 1) geochemical and microbial controls on stimulated uranium bioreduction, 2) uranium sorption under iron-reducing conditions, 3) uranium stability and removal after biostimulation, and 4) natural rates of uranium bioreduction. Given the ultimate goal of SBR, it is reasonable to assume sensors, like the uranium PFM, and associated modeling tools, like scalable inverse models, must be developed to quantify reaction mass balances, uranium stability, and uranium attenuation rates at the **field-scale**. With these tools and the field-scale assessments they provide, we can expand our understanding of uranium fate and transport across spatial scales and 1) derive or validate methods of upscaling local or pore-scale measures of uranium attenuation rates and mass balances, 2) quantify relationships between spatial changes in uranium and nutrient mass discharges and spatial changes in microbial communities, 3) apply insight gained at the molecular scale to interpret or predict reactions and processes occurring at the field scale, and 4) refine field-scale conceptual and computation models of uranium transport using available data from the local scale.

From a general contaminant hydrology perspective, PFM measurements of water and contaminant fluxes have significant utility in long-term monitoring, aquifer restoration, and contaminant source remediation. For example, as a tool for long-term monitoring, a transect of flux meters installed immediately downgradient from a groundwater contaminant source can be used to characterize source strength. The spatial distribution of measured fluxes, when integrated over the transect, produce estimates of contaminant mass loadings to groundwater. Because water and contaminant fluxes measured by PFM represent cumulative values acquired over several weeks to several months, reliable time-averaged values can be calculated; making it is possible to calculate reliable monthly and annual contaminant mass loadings to an aquifer. When traditional methods are used, transient contaminant concentrations and groundwater velocities are measured infrequently and at discrete times; as a result, it is not possible to calculate reliable time-averaged fluxes or mass loadings.

Measuring contaminant fluxes over the long-term also has important consequences with respect to natural attenuation. The assimilative capacity of an aquifer can be assessed using the flux meter to quantify the total contaminant flux at two or more sequential transects. This is possible because in the absence of natural biotic or abiotic transformations, the integrated fluxes across each transect will be the same for a stable plume or for transects situated near the source. Unless contaminant fluxes are measured, it is not feasible to quantitatively isolate the attenuation effects of dispersion from degradation. Thus, the uranium PFM can be used to verify the effectiveness of monitored natural attenuation and provide suitable information for assessing environmental risks to downgradient receptors.

The PFM can be an effective tool for monitoring uranium source remediation. Depth variations of both water and uranium fluxes can be measured using a single flux meter; however, a transect of PFM positioned immediately down gradient of a site boundary can isolate the location of large uranium fluxes originating from the site. This type of data can be used to optimize hydraulic management activities and/or source remediation efforts designed to meet 'near source' or down gradient aquifer remediation goals (i.e., plume stabilization or meeting maximum contaminant levels at compliance boundaries). In addition, measured fluxes near the source provide useful information for verifying remedial action performance.

References

Abdelouas, A., Lutze, W. and Nuttall, E. (1998) Chemical reactions of uranium in ground water at a mill tailings site Journal of Contaminant Hydrology 34:343-361.

Anderson, R.T., Vrionis, H.A., Ortiz-Bernad, I., Resch, C.T., Long, P.E., Dayvault, R., Karp, K., Marutzky, S., Metzler, D.R., Peacock, A, White, D.C., Lowe, M., and Lovely, D.R. Stimulating the in situ activity of *Geobactor* species to remove uranium from the groundwater of uranium-contaminated aquifer. Applied and Environmental Microbiology. 2003; 69(10):5884-5891.

Annable, M.D., K. Hatfield, J. Cho, H. Klammler, B. Parker, J. Cherry, and P.S.C. Rao. Field-scale evaluation of the passive flux meter for simultaneous measurement of groundwater and contaminant fluxes. Environmental Science and Technology, 2005, 39 (18), 7194 -7201.

Balkwill, D. L., F. R. Leach, et al. (1988). "Equivalence of microbial biomass measures based on membrane lipid and cell wall components, adenosine triphosphate." Microbial Ecology 16: 73-84.

Ballard, S. The in situ permeable flow sensor: a ground-water flow velocity meter. Ground Water 1996. 34 (2), 231–240

Barton, C.S., Stewart, D.I., Morris, K.S. and Bryant, D.E. (2004) Performance of three resin-based materials for treating uranium-contaminated groundwater within a PRB Journal of Hazardous Materials 116:191-204.

Basu, N., Rao, P.S.C., Poyer, I.C., Annable, M.D., and Hatfield, K. Flux-based assessment at a manufacturing site contaminated with trichloroethylene. J. Contam. Hydrol. 2006; 86 (1-2), 105-127.

Bernhard, G., Geipel, G., Brendler, V. and Nitsche, H. (1998) Uranium speciation in waters of different uranium mining areas Journal of Alloys and Compounds 271-273:201-205.

Baveye, P., and Valocchi, A.J. An evaluation of mathematical models of transport of biologically reacting solutes in saturated soils and aquifers, Water Resour. Res. 1989; 25(6), 1413-1421.

Bedient, P.B., Rifai, H.S., and Newell, C.J. Transport and Remediation, Prentice-Hall, Englewood Cliffs, N. J, 1994.

Bockelmann, A., Ptak, T., Teutsch, G., 2001. An analytical quantification of mass fluxes and natural attenuation rate constants at a former gasworks site. J. Contam. Hydrol. 53, 429– 453.

Bojanowski, R., Radecki, L. and Burns, K 2005 Determination of radium and uranium isotopes in natural waters by sorption on hydrous manganese dioxide followed by alpha-spectrometry J. Radio. Nucl. Chem. 264:437-443.

Borden, R.C., Daniel, R.A., LeBrun IV, L.E., Davis, C.W. Intrinsic biodegradation of MTBE and BTEX in a gasoline-contaminated aquifer. Water Resour. Res. 1997; 33 (5): 1105-1115.

Bryant, D.E., Stewart, D.I., Kee, T.P. and Barton, C.S. (2003) Development of a functionalized polymer-coated silica for the removal of uranium from groundwater Environmental Science and Technology 37: 4011-4016.

Cabaniss, S.E. (1997) Propagation of Uncertainty in Aqueous Equilibrium Calculations: Non-Gaussian Output Distributions Anal. Chem. 69: 3658-3664.

Cabaniss, S.E. (1999) Uncertainty Propagation in Geochemical Calculations: Non-Linearity in Solubility Equilibria Appl. Geochim. 14: 255-262.

Campbell, T. J., K. Hatfield, H. Klammler, M. D. Annable, and P.S.C. Rao. Magnitude and directional measures of water and Cr(VI) fluxes by passive flux meter. Environmental Science and Technology. 2006. 40(20), 6392-6397.

Chanda, M. and Rempel, G.L. (1992a) Removal of uranium from acidic sulfate solution by ion-exchange on poly(4-vinylpyridine) and polybenzamidazole in protonated sulfate form Reactive Polymers 17:159-174.

Chanda, M. and Rempel, G.L. (1992b) Uranium sorption behavior of a macroporous quaternized poly-(4-vinylpyridine) resin in sulfuric acid medium Reactive Polymers 18:141-154.

Chanda, M. and Rempel, G.L. (1995) Polyethyleneimine gel-coat on silica- High uranium capacity and fast kinetics of gel-coated Reactive Polymers 25:25-36.

Chanda, M. and Rempel, G.L. (2003) A superfast sorbent based on textile-grade poly(acrylonitrile) fiber/fabric. Rapid removal of uranium from mildly acidic aqueous solutions of low concentration Industrial and Engineering Chemistry Research 42:5647-5655.

Chandler, D. P., S-M. Li, C.M. Spadoni, G.R. Drake, D. L. Balkwill, J.K. Fredrickson, and F. J. Brockman. 1997. A molecular comparison of culturable aerobic heterotrophic bacteria and 16S rRNA clones derived from a deep subsurface sediment. FEMS Microbiol Ecol, 23, p. 131.

Chapelle, F.H., Bradley, P.M., Lovley, D.r., and Vroblesky, D.A. Measuring rates of biodegradation in a contaminated aquifer using field and laboratory methods. Ground Water. 1996; 34:691-698.

Chin, K.-J., A. Esteve-Nunez, C. Leang, and D.R. Lovley. 2004. Direct Correlation between Rates of Anaerobic Respiration and Levels of mRNA for Key Respiratory Genes in Geobacter sulfurreducens. Appl. Environ. Microbiol., 70(9), 5183-5189. 4.

Cho, J., M.D. Annable, J.W. Jawitz, and K. Hatfield. 2007. Passive fluxmeter measurement of water and nutrient flux in porous media. Journal of Environmental Quality, (In Press).

Chang, Y, Philip E. Long, Roland Geyer, Aaron D. Peacock, Charles T. Resch, Kerry Sublette, Susan Pfiffner, Amanda Smithgall, Robert T. Anderson, Helen A. Vrionis, John R.Stephen, Richard Dayvault, Irene Ortiz-Bernad, Derek R. Lovley, and David C. White. (2005) Microbial Incorporation of 13C-Labeled Acetate at the Field Scale: Detection of Microbes Responsible for Reduction of U(VI) Environ. Sci. Technol.; 39(23) pp 9039 – 9048.

Coates, J.D., V.K. Bhupathiraju, L.A. Achenbach, M.J. McInerney, and D.R. Lovley. 2001. Geobacter hydrogenophilus, Geobacter chapellei and Geobacter grbiciae, three new, strictly anaerobic, dissimilatory Fe(III)-reducers. International Journal of Systematic and Evolutionary Microbiology 51:581-588.

Denison, F.H. and Garnier-LaPlace, J. (2005) The effects of database parameter uncertainty on uranium(VI) equilibrium calculations Geochim. Cosmochim. Acta 69:2183-2191.

Dong, W.M. and Brooks, S.C. (2006) Determination of the formation constants of ternary complexes of uranyl and carbonate with alkaline earth metals (Mg2+, Ca2+, Sr2+, and Ba2+) using anion exchange method Environmental Science and Technology 40:4689-4695.

Dow Chemical, 2007, www.dow.com/liquidseps/prod/pt_u.htm

Dowling, N.J. E., F. Widdel, and D.C. White. 1986. Phospholipid ester-linked fatty acid biomarkers of acetate oxidizing sulfate reducers and other sulfide forming bacteria. J. Gen. Microbiol. 132:1815-1825.

Fox, P.M., Davis, J.A. and Zachara, J.M. (2006) The effect of calcium on aqueous uranium(VI) speciation and adsorption to ferrihydrite and quartz Geochim. Cosmochim. Acta 70:1379-1387.

Francis, A. J., C. J. Dodge, F. L. Lu, G. P. Halada, and C. R. Clayton. XPS and XANES Studies of Uranium Reduction by Clostridium Sp. Environ. Sci. Technol. 1994. 28:636-639.

Fredrickson, J.K., H.M. Kostandarithes, S.W. Li, A.E. Plymale and M.J. Daly. 2000. Reduction of Fe(III), Cr(VI), U(VI), and Tc(VII) by Deinococcus radiodurans R1. Applied and Environmental Microbiology 66:2006-2011

Ganesh, R., K. G. Robinson, L. L. Chu, D. Kucsmas, and G. D. Reed. Reductive precipitation of uranium by Desulfovibrio desulfuricans: Evaluation of cocontaminant effects and selective removal. Wat. Res. 1999. 33:3447-3458.

Geckeis, H., Manh, T.N., Bouby, M. and Kim, J.I. (2003) Aquatic colloids relevant to radionuclide migration: characterization by size fractionation and ICP-mass spectrometric detection Coll. Surf. A-Phys. Engr. Aspects 217:101-108.

Germanicova, M. and Lubal, P. (2006) Spectrophotometric determination of uranium(VI) in the presence of carbonates and oxalates and its application to uranium(VI) speciation analysis Chemicke Listy 100:821-827.

Goudar, C.T. and Strevett, K.A. Estimating in situ Monod biodegradation parameters using a novel explicit solution of a one-dimensional contaminant transport equation. Ground Water. 2000; 38:894-898.

Gu, B.H., Ku, Y.K. and Jardine, P.M. (2004) Sorption and binary exchange of nitrate, sulfate, and uranium on an anion-exchange resin Environmental Science and Technology 38:3184-3188.

Gu, B.H., Ku, Y.K. and Brown, G.M. (2005) Sorption and desorption of perchlorate and U(VI) by strong-base anion-exchange resins Environmental Science and Technology 39: 901-907.

Hatfield, K., M. Annable, J. Cho, P.S.C. Rao, and H. Klammler. A direct passive method for measuring water and contaminant fluxes in porous media. J. Contam. Hydrol. 2004, 75 (3-4): 155-181

Hatfield, K., M.D. Annable, S. Kuhn, P.S.C. Rao, and T. Campbell. 2002. A new method for quantifying contaminant flux at hazardous waste sites. *Groundwater Quality* 2001, IAHS Publication 275, Red Book, Sheffield United Kingdom, pp. 25-32.

Holmes, D.E., K.P. Nevin, R.A. O'Neil, J.E. Ward, L.A. Adams, T.L. Woodard, H.A. Vrionis, and D.R. Lovley. 2005. Potential for Quantifying Expression of the Geobacteraceae Citrate Synthase Gene To Assess the Activity of Geobacteraceae in the Subsurface and on Current-Harvesting Electrodes. Appl. Environ. Microbiol., 71(11), 6870-6877.

Elshahed, M.S., J.M. Senko, T.A. Dewers, J.R. Spear, F.Z. Najar, S.M. Kenton, B.A. Roe and L.R. Krumholz. 2003. Bacterial diversity and sulfur cycling in a mesophilic sulfide-rich spring. Applied Environmental Microbiology, 69(9):5609-5621.

Hubbel, S.P. 2001. The unified neutral theory of biodiversity and biogeography. Princeton University Press, Princeton, NJ.

Istok, J.D., et al. 2004. In situ bioreduction of technetium and uranium in a nitrate-contaminated aquifer. Environmental Science & Technology. 38(2): p. 468-475.

Jackson, B.P., Ranville, J.F., Bertsch, P.M. and Sowder, A.G.(2005) Characterization of colloidal and humic-bound Ni and U in the "dissolved" fraction of contaminated sediment extracts Environmental Science and Technology 39:2478-2485.

Jain, D.K., S. Stroes-Gascoyne, M. Providenti, C. Tanner and I. Cord. 1997. Characterization of Microbial Communities in deep groundwater from granitic rock. Can J. Microbiol, 43, p. 272-283.

Kao, C.M., Wang, Y.S. Field investigation of the natural attenuation and intrinsic biodegradation rates at an underground storage tank site. 2001. Environ. Geol. 40 (4–5), 622– 631.

King, M., Barker, W.G., Devlin, J.F., Butler, B.J. Migration and natural fate of a coal tare creosote plume: 2. Mass balance and biodegradation indicators. J. Contam. Hydrol. 1999. 39, 281– 307.

Klammler, H., M. Newman, E. Szilagyi, J. Padowski, K. Hatfield, J. Jawitz, and M. Annable. 2007. The passive surface water fluxmeter to measure cumulative water and solute fluxes. Environmental Science and Technology, 41 (7), 2485 -2490.

Klammler, H., K. Hatfield, B. Nemer, and S.A. Mathias. 2011A. A Trigonometric Interpolation Approach to Mixed Type Boundary Problems Associated with Permeameter Shape Factors, Water Resour. Res., 47, W03510. http://dx.doi.org/10.1029/2010WR009337.

Klammler, H., Hatfield, K., McVay, M., & Luz, J. A. G. D. 2011B. Approximate up-scaling of geo-spatial variables applied to deep foundation design. Georisk, 5(3-4), 163-172. http://dx.doi.org/10.1080/17499518.2010.546266.

Klammler, H., K. Hatfield, J. Luz, M. Annable, M. Newman, J. Cho, A. Peacock, V. Stucker, J. Ranville and C. Clark. 2012A. Water and contaminant flux estimation from multi-layer passive flux meter measurements, Advances in Fluid Mechanics, WIT Transactions on Engineering Sciences, Vol 74, pp 301-313. https://books.google.com/books?isbn=1845646002.

Klammler H., K. Hatfield, J.A.G. Luz, M.D. Annable, M. Newman, J. Cho, A. Peacock, V. Stucker, J. Ranville, S. Cabaniss, and P. S. Rao. 2012B. Contaminant Discharge and Uncertainty Estimates from Passive Flux Meter Measurements. Water Resources Research, 48, 2. http://dx.doi.org/10.1029/2011WR010535.

Klammler, H., B. Nemer, and K. Hatfield. 2014. Effect of injection screen slot geometry on hydraulic conductivity tests. Journal of Hydrology, 511 (190-198). http://dx.doi.org/10.1016/j.jhydrol.2014.01.038.

Klecka, G.M., Davis, J.W. Gray, D.R. and Madsen, S.S. Natural bioremediation of organic contaminants in groundwater: Cliffs-Dow Superfund Site. Ground Water. 1990; 28:534-543.

Knightes, C.D. and Peters, C.A. Statistical analysis of nonlinear parameter estimation for Monod biodegradation kinetics using bivariate data. Biotechnol. Bioeng. 2000; 69:160-170.

Kuebert, M., Finkel, M. Contaminant mass discharge estimation in groundwater based on multi-level point measurements: A numerical evaluation of expected errors. J. Contam. Hydrol. 2006, 84:55– 80

Leavitt, J.J., K.J. Howe, and S.E. Cabaniss. 2011. Equilibrium modeling of U(VI) speciation in high carbonate groundwaters: Model error and propagation of uncertainty. Applied Geochemistry, 26, 12. http://dx.doi.org/10.1016/j.apgeochem.2011.06.031

Lloyd, J. R., and E. Macaskie. Bioremediation of radionuclide-containing wastewaters, 2000. p. 277-327. In D. R. Lovley (ed.), Environmental Microbe-Metal Interactions. ASM press, Washington, DC.

Lovley, D. R., S. J. Giovannoni, D. C. White, J. E. Champine, E. J. P. Phillips, Y. A. Gorby, and S. Goodwin. Geobacter-Metallireducens Gen-Nov Sp-Nov, a Microorganism Capable of Coupling the Complete Oxidation of Organic-Compounds to the Reduction of Iron and Other Metals. Archiv. Microbiol. 1993a. 159:336-344.

Lovley, D. R., and E. J. P. Phillips. Reduction of Uranium by Desulfovibrio-Desulfuricans. Appl. Environ. Microbiol. 1992. 58:850-856.

Lovley, D. R., E. J. P. Phillips, Y. A. Gorby, and E. R. Landa. 1991. Microbial Reduction of Uranium. Nature 350:413-416

Lovley, D. R., E. E. Roden, E. J. P. Phillips, and J. C. Woodward. Enzymatic Iron and Uranium Reduction by Sulfate-Reducing Bacteria. Marine Geol. 1993b. 113:41-53

MacArthur, R. and W. Wilson. 1967. The Theory of island biogeography. Princeton University Press, Princeton, NJ

MacIntyre, W.G., Boggs, M., Antworth, C.P., and Stauffer, T.B. Degradation kinetics of aromatic organic solutes introduced into a heterogeneous aquifer. 1993; 20:4045-4051.

McAllister, P.M. and Chaing, C.Y. A practical approach to evaluating natural attenuation of contaminants in ground water. Ground Water Monitoring Review. 1994; 14:161-173.

Meinrath, G., Lis, S., Piskula, Z. and Glatty, Z. (2006) An application of the total measurement uncertainty budget concept to the thermodynamic data of uranyl(VI) complexation by sulfate Journal of Chemical Thermodynamics 38:1274-1284.

Miralles-Wilhelem, F. and Gelhar, L.W. Stochastic analysis of sorption macro-kinetics in heterogeneous aquifers. Water Resour. Res. 1996; 32:1541-1549.

Miralles-Wilhelm, F. and Gelhar, L.W. Stochastic analysis of oxygen-limited biodegradation in heterogeneous aquifers with transient microbial dynamics. J. Contam. Hydrol. 2000; 42: 69-97.

Mohamed, M.M.A. and K. Hatfield. Modeling microbial-mediated reduction in batch reactors. Chemosphere, 59(8), 2005; 1207-1217.

Mohamed, M.M.A., K. Hatfield, and I.V. 2007. Perminova. Evaluation of Monod kinetic parameters in the subsurface using moment analysis: theory and numerical testing. Advances in Water Resources. Volume 30, Issue 9, September 2007, Pages 2034-2050.

Mohamed M.M. and K. Hatfield. 2010. Dimensionless monod parameters to summarize the influence of microbial growth kinetics and inhibition on the attenuation of groundwater contaminants, Biodegradation, 22 (877-896). http://dx.doi.org/10.1007/s10532-010-9445-x.

Mohamed M.M., K. Hatfield, A. Hassan, and H. Klammler. 2010. Stochastic evaluation of subsurface contaminant discharge under physical, chemical, and biological heterogeneities, Advances in Water Resources, 33 (7), 801-812. http://dx.doi.org/10.1016/j.advwatres.2010.04.010.

Monod, J. The growth of bacterial cultures. Annu. Rev. Microbiol. 1949; 3, 371-394.

Morgan, E. (1991) Chemometrics: Experimental Design John Wiley and Sons, London, 275 pp.

Newell, C.J., Conner, J.A., Rowen, D.A., 2003. Groundwater Remediation Strategies Tool. Publication Number 4730. API American Petroleum Institute, Houston, TX. 80 pp.

Nitzsche, O., Meinrath, G. and Merkel, B. (2000) Database uncertainty as a limiting factor in reactive transport prognosis Journal of Contaminant Hydrology 44:223-237.
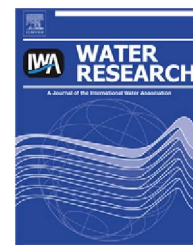
Pawlak, Z. and Rabiega, G. (2002) Comparison of Inductively Coupled Plasma-Mass Spectrometry and Radiochemical Techniques for Total Uranium in Environmental Water Samples, Environ. Sci. Technol., 36, 5395-5398.

Payne, R.B., D.A. Gentry, B.J. Rapp-Giles, L. Casalot, and J.D. Wall. 2002. Uranium reduction by Desulfovibrio desulfuricans strain G20 and a cytochrome c3 mutant. Applied and Environmental Microbiology 68:3129-3132.

Peacock, A.D., Y-J. Chang, J.D. Istok, L. Krumholz, R. Geyer, B. Kinsall, D. Watson, K.L. Sublette, and D.C. White. 2004. Utilization of Microbial Biofilms as Monitors of Bioremediation. Microbial Ecology, Vol. 47, 284-292.

Piatina, T.B. and Hering, J.G. (2000) Direct quantification of metal-organic interactions by size-exclusion chromatography (SEC) and inductively coupled plasma mass spectrometry (ICP-MS) J. Envr. Qual. 29:1839-1845.

Pietzsch, K., and W. Babel. A sulfate-reducing bacterium that can detoxify U(VI) and obtain energy via nitrate reduction. J. Basic Microbiol. 2003. 43:348-361

Schirmer, M., Butler, B.J., Roy, J.W., Frind, E.O., and Barker, J.F. A relative-least-squares technique to determine unique Monod kinetic parameters of BTEX compounds using batch experiments. J. Contam. Hydrol. 1999; 37:69–86.

Schirmer, M., Molson, J.W., Frind, E.O., and Barker, J.F. Biodegradation modeling of a dissolved gasoline plume applying independent laboratory and field parameters. J. Contam. Hydrol. 2000; 46:339-374.

Schumann, D., Andrassy, M., Nitsche, H., Novgorodov, A.F. and Bruchertseifer, H. (1997) Sorption behaviour of uranium on cation and anion exchange resins from HCl/HF-containing aqueous solutions: Model experiments for the determination of chemical properties of element 106 (Seaborgium) Radiochimica Acta 79:217-220.

Serkiz, SM; Allison, JD; Perdue, EM; Allen, HE; Brown, DS 1996 Correcting errors in the thermodynamic database for the equilibrium speciation model MINTEQA2 Water Res. 30:1930-1933

Stewart, D.I., Csovari, M. Barton, C.S., Morris, K and Bryant, D.E. (2006) Performance of a functionalised polymer-coated silica at treating uranium contaminated groundwater from a Hungarian mine site Engineering Geology 85:174-183.

Stucker, V., J. Ranville, M. Newman, A. Peacock, J. Cho, K. Hatfield. 2011. Evaluation and application of anion exchange resins to measure groundwater uranium flux at a former uranium mill site. Water Research, Volume 45, Issue 16. pp. 4866-4876. ISSN 0043-1354. http://dx.doi.org/10.1016/j.watres.2011.06.030.

Tebo, B. M., and A. Y. Obraztsova. Sulfate reducing bacterium grows with Cr(VI), U(VI), Mn(IV) an Fe(III) as electron acceptors. FEMS Microbiol. Letters 1998.162:193-198.

Tillman, D. 1982. Resource competition and community structure. Princeton University Press, Princeton, NJ.

Unsworth, E.R., Jones, P., and Hill, S.J. (2002) The effect of thermodynamic data on computer model predictions of uranium speciation in natural water systems JEM Journal of Environmental Monitoring 4:528-532.

Unsworth, E.R., Jones, P., Cook, J.M. and Hill, S.J. (2005) Uranium speciation in moorland river water samples: A comparison of experimental results and computer model predictions JEM Journal of Environmental Monitoring 7:559-567.

U.S. EPA Method 200.8, Methods for the Determination of the Trace Metals in Waters and Wastewaters. In *Methods for the Determination of Metals in Environmental Samples-Supplement 1*; EPA 600/R-94-111; U.S. Government Publishing Office: Washington, DC, May 1994; available at NIST, PB 94-184942.

Vrionis, Helen A., Robert T. Anderson, Irene Ortiz-Bernad, Kathleen R. O`Neill, Charles, T. Resch, Aaron D. Peacock, Richard Dayvault, David C. White, Philip E. Long, and Derek R. Lovley 2005. Microbiology and Geochemical Heterogeneity in an In Situ Uranium Bioremediation Field Site. Applied and Environmental Microbiology Vol. 71, No. 10 p. 6308-6318.

Wade, R., and T. J. DiChristina. 2000. Isolation of U(VI) reduction-deficient mutants of Shewanella putrefaciens. FEMS Microbiol. Letters 184:143-148.

Weber, CL ; VanBriesen, JM ; Small, MS 2006A stochastic regression approach to analyzing thermodynamic uncertainty in chemical speciation modeling Environmental Science and Technology 40:3872-3878

White, D.C., R.J. Bobbie, J.S. Heron, J.D. King, S.J. Morrison. 1979. Biochemical Measurements of Microbial Mass and Activity from Environmental Samples. In: J.W. Costerton, R.R. Colwell, (eds.), Native Aquatic Bacteria: Enumeration, Activity, and Ecology, ASTM STP 695. American Society for Testing and Materials. Philadelphia, PA, pp. 69-81.

White, DC. and DB Ringelberg. 1995 Utility of signature lipid biomarker analysis in determining in situ viable biomass, community structure, and nutritional/ physiological status of the deep subsurface microbiota. In Amy, PS. and Halderman, DL. (eds) The Microbiology of the Terrestrial Subsurface, CRC Press, Boca Raton, FL

White, D.C., J.O. Stair, and D.B. Ringelberg. 1996. Quantitative comparisons of in situ microbial biodiversity by signature lipid biomarker analysis. J. Indust. Microbiol. 17: 185-196.

White, DC, DB. Ringelberg, and SJ Macnaughton. 1997. Review of PHA and signature lipid biomarker analysis for quantitative assessment of in situ environmental microbial ecology. In 1996 International Symposium on Bacterial Polyhydroxylalkanoates, (G. Eggink, A. Steinbuchel, Y. Poirer, and B Witholt, eds.) NRC Research Press, Ottawa, Canada, pp. 161-170.

Wildung, R.E., Y.A. GOrby, K.M. Krupka, N.J. Hess, S.W. Li, A.E. Plymale, J.P. McKinley, and J.K. Fredrickson. 2000. Effect of electron donor and solution chemistry on products of dissimilatory reduction of technetium by Shewanella putrefaciens. Applied and Environmental Microbiology 66:2451-2460.

Wu, F.C., Evans, D., Dillon, P. ands Schiff, S. (2004) Molecular size distribution characteristics of the metal-DOM complexes in stream waters by high-performance size-exclusion chromatography (HPSEC) and high-resolution inductively coupled plasma mass spectrometry (ICP-MS) Journal of Analytical Atomic Spectrometry 19:979-983.

Appendix of Peer Reviewed Publications

The results for each of the project objectives were published as nine peer reviewed publications as outlined below. The results are provided in their entirety in the following sections.

1. Stucker, V., J. Ranville, M. Newman, A. Peacock, J. Cho, K. Hatfield. 2011. Evaluation and application of anion exchange resins to measure groundwater uranium flux at a former uranium mill site. Water Research, Volume 45, Issue 16. pp. 4866-4876. ISSN 0043-1354. http://dx.doi.org/10.1016/j.watres.2011.06.030.

2. Klammler, H., K. Hatfield, J. Luz, M. Annable, M. Newman, J. Cho, A. Peacock, V. Stucker, J. Ranville and C. Clark. 2012A. Water and contaminant flux estimation from multi-layer passive flux meter measurements, Advances in Fluid Mechanics, WIT Transactions on Engineering Sciences, Vol 74, pp 301-313. https://books.google.com/books?isbn=1845646002

3. Leavitt, J.J., K.J. Howe, and S.E. Cabaniss. 2011. Equilibrium modeling of U(VI) speciation in high carbonate groundwaters: Model error and propagation of uncertainty. Applied Geochemistry, 26, 12. http://dx.doi.org/10.1016/j.apgeochem.2011.06.031

4. Klammler H., K. Hatfield, J.A.G. Luz, M.D. Annable, M. Newman, J. Cho, A. Peacock, V. Stucker, J. Ranville, S. Cabaniss, and P. S. Rao. 2012B. Contaminant Discharge and Uncertainty Estimates from Passive Flux Meter Measurements. Water Resources Research, 48, 2. http://dx.doi.org/10.1029/2011WR010535.

5. Klammler, H., K. Hatfield, B. Nemer, and S.A. Mathias. 2011A. A Trigonometric Interpolation Approach to Mixed Type Boundary Problems Associated with Permeameter Shape Factors, Water Resour. Res., 47, W03510. http://dx.doi.org/10.1029/2010WR009337.

6. Klammler, H., B. Nemer, and K. Hatfield. 2014. Effect of injection screen slot geometry on hydraulic conductivity tests. Journal of Hydrology, 511 (190-198). http://dx.doi.org/10.1016/j.jhydrol.2014.01.038.

7. Klammler, H., Hatfield, K., McVay, M., & Luz, J. A. G. D. 2011B. Approximate up-scaling of geo-spatial variables applied to deep foundation design. Georisk, 5(3-4), 163-172. http://dx.doi.org/10.1080/17499518.2010.546266.

8. Mohamed M.M. and K. Hatfield. 2010. Dimensionless monod parameters to summarize the influence of microbial growth kinetics and inhibition on the attenuation of groundwater contaminants, Biodegradation, 22 (877-896). http://dx.doi.org/10.1007/s10532-010-9445-x.

9. Mohamed M.M., K. Hatfield, A. Hassan, and H. Klammler. 2010. Stochastic evaluation of subsurface contaminant discharge under physical, chemical, and biological heterogeneities, Advances in Water Resources, 33 (7), 801-812. http://dx.doi.org/10.1016/j.advwatres.2010.04.010.

ELSEVIER

WATER RESEARCH

Evaluation and application of anion exchange resins to measure groundwater uranium flux at a former uranium mill site

Valerie Stucker [a], James Ranville [a,*], Mark Newman [b], Aaron Peacock [d], Jaehyun Cho [c], Kirk Hatfield [b]

[a] Department of Chemistry and Geochemistry, Colorado School of Mines, Golden, CO, USA
[b] Department of Civil and Coastal Engineering, University of Florida, Gainesville, FL, USA
[c] Department of Environmental Engineering Sciences, University of Florida, Gainesville, FL, USA
[d] Microbial Insights Inc., Rockford, TN, USA

ARTICLE INFO

ABSTRACT

Laboratory tests and a field validation experiment were performed to evaluate anion exchange resins for uranium sorption and desorption in order to develop a uranium passive flux meter (PFM). The mass of uranium sorbed to the resin and corresponding masses of alcohol tracers eluted over the duration of groundwater installation are then used to determine the groundwater and uranium contaminant fluxes. Laboratory based batch experiments were performed using Purolite A500, Dowex 21K and 21K XLT, Lewatit S6328 A resins and silver impregnated activated carbon to examine uranium sorption and extraction for each material. The Dowex resins had the highest uranium sorption, followed by Lewatit, Purolite and the activated carbon. Recoveries from all ion exchange resins were in the range of 94—99% for aqueous uranium in the environmentally relevant concentration range studied (0.01—200 ppb). Due to the lower price and well-characterized tracer capacity, Lewatit S6328 A was used for field-testing of PFMs at the DOE UMTRA site in Rifle, CO. The effect on the flux measurements of extractant (nitric acid)/resin ratio, and uranium loading were investigated. Higher cumulative uranium fluxes (as seen with concentrations > 1 ug U/gram resin) yielded more homogeneous resin samples versus lower cumulative fluxes (<1 ug U/gram resin), which caused the PFM to have areas of localized concentration of uranium. Resin homogenization and larger volume extractions yield reproducible results for all levels of uranium fluxes. Although PFM design can be improved to measure flux and groundwater flow direction, the current methodology can be applied to uranium transport studies.

1. Introduction

Uranium is a contaminant of concern at many DOE former mining and milling sites. With the passing of the Uranium Mill Tailings Radiation Control Act (UMTRCA) in 1978, tailings were removed to repositories and the surface soil was remediated from 24 inactive uranium mill sites. In Rifle, Colorado, the site of a former uranium and vanadium mill,

the contamination remains in the soils and shallow groundwater due to uranium leached from the tailings prior to removal. Monitored natural attenuation (MNA) was the chosen method for remediating the uranium below ground surface (USEPA, 1999). Surface remediation was completed in 1996, but groundwater treatment is ongoing. Uranium, vanadium, and selenium are the main contaminants of concern at this site (DOE, 2008).

The Rifle, CO site is situated directly adjacent to the Colorado River and has a semi-arid climate, receiving on average 300 mm of precipitation. The first 20–30 feet below ground surface is Colorado River alluvium, which covers the sands, silts and clays of the Wasatch Formation. A more complete description of the Rifle mill site geology and hydrology can be found elsewhere (Yabusaki et al., 2007). By natural flushing, soluble uranium discharges under a natural gradient to the Colorado River where it is further diluted to background levels. Initial groundwater modeling predicted this process to take 100 years to reach background levels (DOE, 2008). Decrease in uranium concentration is, however, occurring slower than anticipated and other remediation strategies are being investigated.

Since 2002, biostimulation experiments have been performed at the site to stimulate microbial reduction of uranium (VI), which is the soluble, mobile form, to immobile uranium (IV) using acetate injections (Anderson et al., 2003; Lovley et al., 1991; Ortiz-Bernad et al., 2004; Yabusaki et al., 2007). To determine the effectiveness of the biostimulation, it is necessary to measure the uranium concentrations upgradient and downgradient of the injection wells. It is also valuable to know the rate of groundwater flow. A rapid flow combined with a high soluble contaminant concentration is of greater concern than a slow moving plume of similar contaminant concentration. To be considered successful, bioremediation usually needs to achieve low soluble contaminant concentrations, however a high concentration may be allowed to remain if little or no flow occurs. Examining the concentration alone may lead to an incomplete understanding of the system. Measuring contaminant flux (J_c), which is the product of the volumetric water flux, or specific discharge (q_0) and the flux-averaged contaminant concentration (c) provides better insight into the outcome of remediation efforts (Hatfield et al., 2004).

There are limitations with the current methods for estimating flux. Concentrations are typically measured independently of the specific discharge, possibly at separate sampling times or location, leading to significant variations and errors in flux calculations. Flux estimates generally rely on modeled flow rates or laborious and intrusive hydrologic tests (tracer injections or pump tests). To acquire more reliable information, the passive flux meter (PFM) was developed to provide simultaneous direct measures of the specific discharge (q_o) and contaminant mass flux (J_c) (Annable et al., 2005; Hatfield et al., 2004). Contaminant measurements made using PFM represent cumulative local fluxes, which can then be used to estimate flux-averaged aqueous concentrations (c), according to Equation (1), for comparison to measured aqueous concentrations.

$$J_c = q_o c \tag{1}$$

PFM schematics and the details of the calculations are provided by Hatfield et al. (2004). The PFMs were initially used to measure the flux of organic contaminants and used silver impregnated (antimicrobial) granulated activated carbon (GAC Ag) as the sorbent material (Annable et al., 2005).

Previously, anion exchange resins such as Dowex 21K and 1-X8, Purolite A500, A600 and A520E, and Lewatit K 6367 have been proven to remove uranium from aqueous solutions (Kolomiets et al., 2005; Phillips et al., 2008) under a large range of pH conditions, from acidic to alkaline, with the most effective sorption observed near neutral pH to alkaline conditions. Chelating resins (Merdivan et al., 2001; Pesavento et al., 2003), such as Chelex 100 and Amberlite XAD-16, and cation exchange resins, such as Dowex-50 (Schumann et al., 1997), have been shown to be most effective at sorbing aqueous uranium in acidic solutions. Due to the near neutral pH at the Rifle site and the expected dominance of anionic uranyl carbonato species, this work focused on anion exchange resins previously shown to be effective.

The goal of the overall project was to develop a PFM to quantify aqueous uranium fluxes at the Rifle site that can be used to evaluate the effectiveness of biostimulation by comparing upgradient and downgradient uranium fluxes. To have an effective PFM, the material must quantitatively sorb all of the uranium passing through it, be capable of releasing the sorbed uranium upon extraction, and predictably retain and release the chosen tracers, preferably without microbial growth occurring on the resin. Because the PFM will be used to evaluate the effectiveness of biostimulation an additional constraint for this application was that elution of resident tracers must not affect results of the other experiments being performed simultaneously at the site. To keep total remediation and monitoring costs at a minimum, resin cost is also a factor for making the final choice. Therefore resins will be evaluated for uranium sorbed and desorbed, tracer capacity and finally, cost. In this specific study uranium speciation and water chemistry conditions (pH, alkalinity, major ions, etc.) were investigated to find the best sorbent material for use in the PFMs at Rifle, CO.

2. Methods

A sample of background Rifle groundwater was analyzed for speciation. Modeling tests were performed to determine the aqueous uranium (VI) speciation using Visual MINTEQ, Version 3.0, over a pH range of 3–10 using the Multi-problem/Sweep function. Only aqueous species were included and sorption and precipitation were ignored. Data on metal and ligand concentrations were obtained from inductively coupled plasma atomic emission spectroscopy (ICP-AES) using a Perkin Elmer 3000 for cation metals, ion chromatography (IC) using a Dionex ICS-90 system for major anions, a Shimadzu TOC analyzer for dissolved organic carbon (DOC) and carbonate was determined by alkalinity titration. The concentrations of these major components in Rifle groundwater can be found in Table 1. These concentration values were used as input for the model and updated constants for the calcium and magnesium species provided by Dong and Brooks (2006) were used to update the database.

Table 1 — Concentrations of components used to model uranium speciation. Only major components affecting uranium species are included.

Component	Concentration
U(VI)	226 ug/L
Ca^{2+}	262 mg/L
Na^+	202 mg/L
Mg^{2+}	128 mg/L
SO_4^{2-}	795 mg/L
CO_3^{2-}	168 mg/L
Cl^-	192 mg/L
NO_3^-	12 mg/L
DOC	4.5 mg/L

2.1. Materials

Numerous sorbents have been developed and used for the removal of uranium from water at near neutral pHs. Organic resins with quaternary amine sites, strong anion-exchange resins, bind uranyl complexes strongly and are available from several manufacturers, for example the Dowex 21K and Purolite A series. (Barton et al., 2004; Chanda and Rempel, 1992a,b; Jelinek and Sorg, 1988; Kolomiets et al., 2004; Vaaramaa et al., 2000) Purolite A500, Dowex 21K and 21K XLT, Lewatit S6328 A and silver impregnated granular activated carbon (GAC Ag) were investigated as possible sorbent materials in the PFMs. The Lewatit resin has been previously used for anion capture in PFMs (Cho et al., 2007). These resins were expected to have good sorption for the uranyl carbonate anion complexes predicted in the Rifle groundwater. Each resin was examined for uranium sorption and desorption and tracer elution properties relative to price. Table 2 shows a comparison of the resin properties and prices at the time of the experiment (fall 2008). Resins were used in the chloride form and rinsed thoroughly five times with deionized water and allowed to air dry. No cleaning procedure was necessary for the GAC Ag.

Adsorption studies were initially done in new, sterile 15 mL polypropylene centrifuge tubes (BD, Franklin Lakes, NJ, PN 352196) using water with added sodium bicarbonate (1 mM) to simulate Rifle alkalinity and pH. Some wall-sorption of uranium was observed using these tubes. After 24 h, polypropylene had sorbed 8% of the uranium present, and 25%

after 72 h. Polystyrene tubes (BD, PN 352095) were then used for comparison. Polystyrene tubes showed less uranium sorption to the walls than did the polypropylene tubes with 17% sorbed after 72 h. Uranium sorption to the tubes increased over time for both materials; however, based on the near complete uranium recovery and mass balance from the resin after material transfer, we concluded that uranium preferentially sorbed to the resin regardless of time or tube material and the tube sorption seen earlier in the blanks was deemed negligible in actual samples. Remaining experiments were done using polystyrene as a precaution to ensure most uranium was sorbing to the resin. Cleaning with nitric acid (3% v/v) was effective in removing all uranium from tubes.

All uranium solutions were made by diluting a 1000 ± 3 ppm U (in 2% nitric acid) ICP standard (High-Purity Standards, Charleston, SC). Dilutions were done using Nano-Pure deionized water for neutral pH, and trace metal grade nitric or hydrochloric acids (Fisher Scientific) for the lower pH standards. Sodium bicarbonate, used to create the groundwater simulant, and the silver nitrate used to impregnate the GAC were ACS grade.

2.2. Adsorption batch studies

Sorbent materials were weighed (100 ± 5 mg) into centrifuge tubes. Uranium standard solutions at concentrations of 5, 10, 50, 100 and 300 ppb were prepared in 1 mM sodium bicarbonate (pH 7.3 ± 0.1) to simulate Rifle groundwater. Uranium concentrations in Rifle groundwater average around 200 ppb. The effects of pH, which will influence the aqueous uranium speciation, were tested by lowering the pH with nitric and hydrochloric acid to pH 3.8. 10 mL of uranium solution were added to each tube containing resin. Each concentration was examined in triplicate at both pHs. The samples were placed on a shaker for 24 h to allow mixing and ion exchange. After the 24-h equilibration period, the resins were allowed to settle and the overlying solutions were decanted into new centrifuge tubes, leaving the resins for the next extraction step. In some cases this procedure was repeated with a 72 h equilibration time to verify that complete ion exchange had been achieved over the shorter time period. Since the PFMs will be in place in the aquifer for weeks at a time, testing the sorption for shorter times was deemed unnecessary based on estimated residence times (of groundwater passing through PFM) that were greater

Table 2 — Comparison of sorbent materials tested using data provided by manufacturer fact sheets. [+]Prices listed are values given for educational groups and may not reflect current industry prices.

Resin	Type	Functional Group	Exchange Capacity (min.eq/L)	Ionic Form (as shipped)	Water Content (%)	Specific Gravity	Price* $/ft³
Purolite A500	Type 1 strong base anion	quaternary amine	1.15	chloride	53—58	1.08	163.00
Dowex 21K 1630	Type 1 strong base anion	quaternary amine	1.2	chloride	50—58	1.06	449.50
Dowex 21K XLT	Type 1 strong base anion	quaternary amine	1.4	chloride	50—60	1.08	384.50
Lewatit S6328 A	Type 1 strong base anion	quaternary amine	1.0	chloride	58—63	1.06	150.00
GAC Ag	activated carbon	carbon	unknown	none	5		266.00

than 24 h. The solutions were analyzed for uranium by inductively coupled plasma-mass spectrometry (ICP-MS).

2.3. Extraction

A 1% nitric acid solution (10 mL) was added to all tubes with resins and shaken overnight. By lowering the pH to less than 1, the uranyl, UO_2^{2+} cation, becomes the dominant form and should be extracted from the anion exchange resin. Furthermore, the high level of nitrate should also cause desorption through competition for anion exchange sites. After 24 h, the acidic solution was decanted, verified to still be acidic (pH <2) by indicator paper, and analyzed by ICP-MS. The same extraction procedure was used for field PFMs, using larger volumes as described later. A uranium mass balance was computed using the values of desorbed uranium and the uranium remaining in solution following the sorption experiments.

2.4. ICP-MS analysis

A Perkin Elmer Elan 6100 ICP-MS was used for all analyses. All samples were acidified with nitric acid prior to analysis and introduced simultaneously into the argon plasma with a 40 ppb In internal standard using a Gilson peristaltic pump. A check standard was used every ten samples to verify instrument performance to be within 10% of the true value. Instrument calibration was done using uranium standards made in 1% nitric acid (Fisher Optima grade). Running conditions complied with manufacturer recommendations and standard quality controls were practiced.

2.5. Resin selection

The ideal resin should have a high uranium sorption capacity that is linear over the concentration range of interest. Linearity allows for predictability in performance and ease in calculations. Linear partition sorption isotherms were developed from the results of each resin batch experiment. The linear partition equation is given as:

$$C_a = K_d C_s \tag{2}$$

where C_a is the concentration of uranium adsorbed to the resin (ug/kg). K_d is the sorption equilibrium coefficient (kg/kg) and C_s is the concentration of uranium remaining in solution (ug/kg).

Sorption (determined from K_d and average percentage sorbed over linear range) and desorption properties (determined by percentage of sorbed uranium extracted with acid), were evaluated. The data was also analyzed using Langmuir and Freundlich isotherms to investigate non-linearity. Fitting the data to the Freundlich isotherm:

$$C_a = KC_s^n \tag{3}$$

provided a better fit than the Langmuir isotherm. If the exponential term, n, is equal to one, this equation reduces to the linear isotherm equation. This linear form was found to be sufficient to describe resin sorption with the exception of the Purolite resin.

Along with the use of ion exchange resin for uranium sorption, a second media consisting of granular activated carbon (GAC) pretreated with a suite of short chain alcohol tracers is used to measure volumetric water flux as presented in Hatfield et al. (2004) and Annable et al., 2005. Additional details of device construction and sampling is provided in Section 3.4 Field Application of this paper.

Flow through experiments were performed in a bench-scale three-dimensional aquifer model using similar methods as presented in Hatfield et al. (2004) and Cho et al., 2007. These tests were used to confirm performance of the resin and estimate the requisite flow convergence terms as presented in Hatfield et al. (2004).

2.6. Field studies

Resins were tested for microbial growth to ensure minimal interference with uranium sorption and desorption. As a precaution for field samples, resins were pretreated with silver nitrate solution to add ionic silver to the resin for anti-bacterial properties. The solutions were then analyzed by ICP-AES for residual silver (the difference assumed to be sorbed to the resin). Silver was added to the resin to be comparable to the silver concentration (~0.03% by weight Ag:resin) on the GAC-Ag used in the initial PFM studies reported by Hatfield et al. (2004).

PFMs were installed in Rifle over a three week period in the summer and the late fall of 2009. The meters were removed from the wells, and a number of vertical segments were separated and homogenized by complete mixing of each sample before being split for uranium, tracer, and microbial analyses. For the data presented in this paper PFM were deployed in 4-inch wells, and each PFM was constructed with six alternating segments of granular activated carbon (GAC) and Lewatit resin (three segments of GAC and three segments of Lewatit). The bottom segment of each PFM was composed of GAC. The PFM were retrieved and sampled with a deployment length of 23 days. Tracer analysis from the GAC segments were used for groundwater flux estimates, and the Lewatit segments were used for uranium flux estimates.

Uranium was extracted from the resins using additions of 10 mL of 1% nitric acid, which were replicated until no additional uranium removal was observed as determined by ICP-MS. Initially, small amounts of resin were used for the extracts to minimize waste produced and mirror the lab experiments. Samples of 100—150 mg and 1—1.5 g of resin were extracted for uranium and concentration values were compared between the different resin sample masses. For the 100 mg resin samples, this took one acid extraction with a second to verify complete uranium removal. Poor reproducibility was observed at lower concentrations (<1 ug U/g resin). Three acid extractions were necessary for the 1 g resin samples, but this larger resin amount had better reproducibility, regardless of uranium concentration or flux. In extractions performed later in the project, 4 g resin samples were extracted in 40 mL of 1% nitric acid, which provided sufficient acid extractant for multiple analyses for uranium and other groundwater anions, while also giving a more representative sample size for improved reproducibility at low

fluxes. The uranium concentration data presented here will be used to calculate the uranium flux through the PFM.

3. Results

3.1. Speciation

Visual MINTEQ computations suggest that over the environmentally relevant pH range (7–8), most of the uranium is present as uranyl carbonato anions or uranyl calcium triscarbonato neutral species (d in Fig. 1). In fact, across the pH range, all of the dominant species are neutral (b,c, and d) as uranyl sulfate, UO_2SO_4, at lower pHs, uranyl carbonate, UO_2CO_3, at the mid range, and uranyl calcium triscarbonato above pH 5.5. The uranyl cation, UO_2^{2+}, becomes more important at the lower pHs (see a in Fig. 1), and this is the basis for removal of uranium from the anion exchange resins using nitric acid. Despite the speciation being predominantly neutral aqueous species, the resins still show strong uranium sorption, demonstrating that anion speciation is not necessarily needed for sorption to an anion exchange resin. More complete geochemical modeling of this system, including sensitivity and error analyses on these samples, can be found in Leavitt et at 2010 (in review).

3.2. Adsorption

All of the sorbent materials tested showed nearly complete uranium adsorption at the near neutral pH in the artificial groundwater sodium bicarbonate solutions. The GAC Ag, which had the lowest sorption at the higher concentrations as seen in Fig. 2, still sorbed an average of 89% of the uranium in solution.

Both of the Dowex resins showed very good linear sorption across the range of concentrations investigated. These resins sorbed an average of 99% of the uranium in solution. The only

difference between the resins is the mesh size, from 16 to 30 for the 21K, and around 30 (but with more uniform size) for the 21K XLT. At the examined range of uranium concentrations, there is no advantage to the smaller resin beads. Lewatit S6328 A also had a linear sorption isotherm, but with a slightly lower sorption percentage, averaging 95% with a K_d of 2000 (kg/kg) for aqueous uranium. These linear sorption isotherms are desirable over the concentration range, so the amount sorbed can easily be used to calculate mass flux.

Purolite A500 shows increased uranium sorption at higher concentrations, a pattern that is different from the other resins. Repeating the procedure for Purolite over 72 h rather than 24 h showed the same trend, with a slight increase in sorption at higher concentrations. While equilibrium had been reached for the other resins after 24 h, the Purolite resin was still sorbing uranium; an average of 94% of the uranium sorbed in 24 h, and 97% had sorbed over 72 h. This same trend was seen in sulfuric acid solutions used by Kolomiets et al. (2005). The other resins tested by this group had reached equilibrium within 25 h, while the Purolite A500 had not (Kolomiets et al., 2005). While the linear isotherm has a good R^2 value (0.91), it was not a linear trend, evidenced by a trend in the residuals, which was not seen with the other resins. Using the Freundlich isotherm equation, this was confirmed with an exponent statistically greater than 1 (1.6 ± 0.1). Currently, we do not have a clear explanation for this phenomenon. One possibility is a surface precipitation process that could be tested using infrared or Raman spectroscopy, but this was not done in this experiment since there were other resins with simpler adsorption trends to use in the PFM.

An overview of the sorption calculations is shown in Table 3. While there could be some improvement in the R squared values and the errors on the slope for our sorption data, the errors were deemed unimportant relative to instrumental errors. With the exception of Purolite A500, each of the other sorbent materials produced Freundlich exponents near one, with only minor statistical differences. The residuals from the
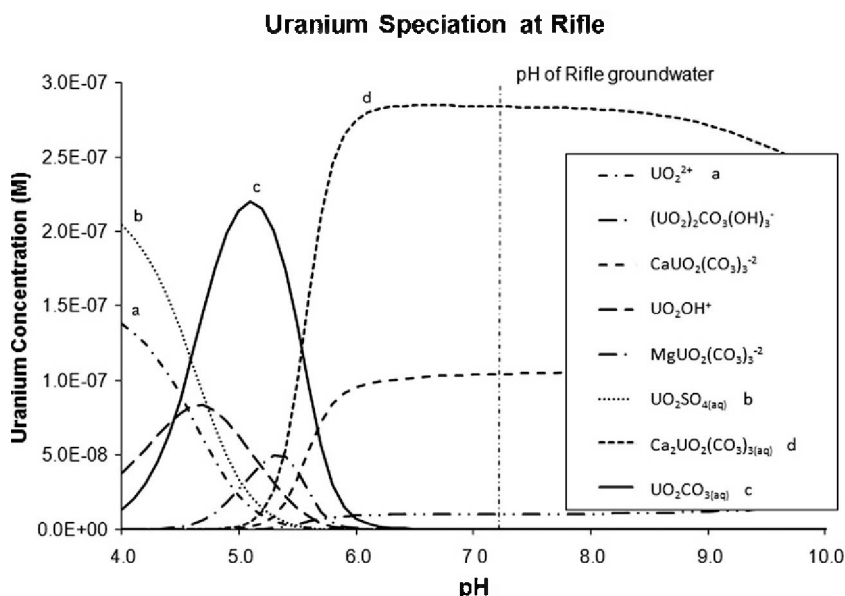

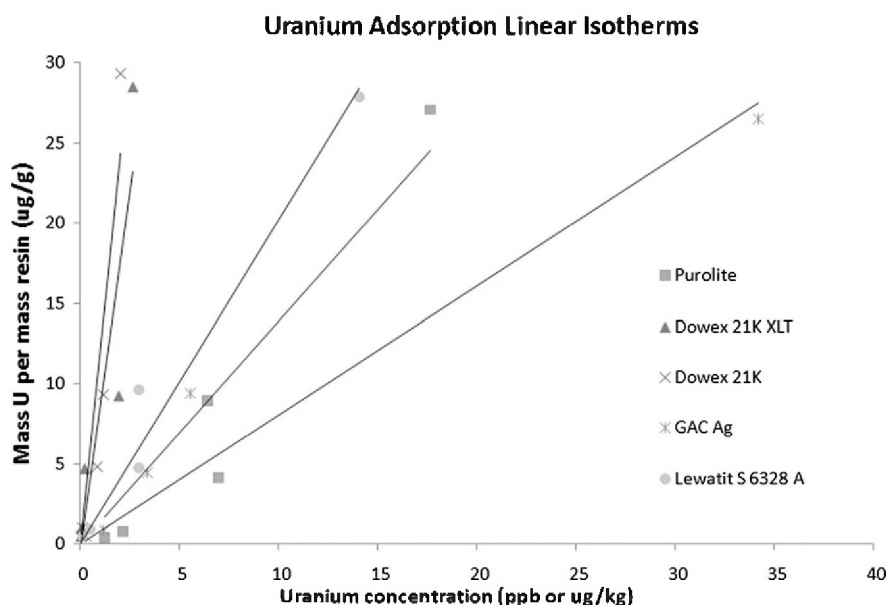Fig. 1 – Rifle speciation modeled using Visual MINTEQ.

Uranium Adsorption Linear Isotherms

Fig. 2 — Sorption isotherms for all materials tested comparing mass uranium sorbed to the resin (μg U/g resin) versus to mass uranium remaining in solution (μg/kg). Each point represents an average of the three replicates with error bars omitted for clarity (values given in text). Lines indicate the linear sorption isotherm from which K_d values were calculated.

linear partition isotherms were also investigated to verify linearity and showed no trend that would indicate a deviation from linearity. Thus, the linear isotherms were presented.

When resins were tested using groundwater collected from the Rifle, CO field site, all of the anion exchange resins performed in a similar manner as in the lab experiments with quantitative sorption at 99% sorbed. This matched the sorption performance seen with Dowex resins in laboratory studies, suggesting improved sorption with all resins in natural waters. Each of the resins maintained the original groundwater pH of 7.2, with only a minor drop to 7.1 for the Dowex resins. The activated carbon did not follow the same pattern of uranium sorption in Rifle groundwater. The pH increased slightly to 7.4. It sorbed around 33% of the calcium in the water, but it removed only 5% of the uranium. This result ruled out the GAC as a sorbent choice for the field PFMs, but it could still be considered in the use of tracers for groundwater flux measurements. This work focused on U(VI) sorption since the solubility of U(IV) is so low and was not expected to influence the results. It has been suggested that

U(IV) complexation to organic ligands can increase solubility, but since the groundwater samples showed complete sorption and we are only interested in total uranium quantification, U(IV) vs U(VI) speciation was not investigated further.

At a lower pH (3.8), uranium cations dominate speciation, and so little uranium adsorption would be expected to sorb to the resins. This was not the case for the Purolite and Lewatit resins when pH was adjusted using nitric acid. With each of the other resins, much lower masses of uranium were sorbed at pH 3.8 than at neutral pH with the same bicarbonate concentrations. Purolite A500 and Lewatit S6328 A both showed the same 94—95% sorption at the lower pH. Gu et al. (2004) had examined Purolite resins and suggested that this phenomenon may be due to the concentration of nitrate on the resin surface allowing for aided uranium adsorption since the resin, has a very high affinity for nitrate anions. All of the resins have quaternary amine groups, but they suggest that the triethylamine groups have a higher affinity for nitrate than the trimethylamine groups present in the Dowex resins. In another experiment pH was lowered using HCl to test if concentrated nitrate aided uranium sorption, and very different results were obtained. As was expected with the acidic pH, there was very little uranium sorption to the resins. As an additional test to confirm this nitrate-aided sorption, we exchanged the chloride ions already present on the resins with nitrate ions by rinsing the resins in excess sodium nitrate before testing the resins for uranium sorption at the lower pH. Uranium sorption was at 12% for Lewatit and 20% for Purolite; these lower sorption results do not suggest a nitrate aided sorption. One possibility is that there might be a uranyl–nitrate complex in solution that is sorbing to the resin rather than the uranyl species sorbing to concentrated nitrates on the resin. More work is necessary to fully understand these results.

Table 3 — Results of resin sorption studies. K_d was determined from the linear slopes, and errors on those slopes are shown along with the R squared value of the linear fit.				
Resin	K_d	Error	R squared	% Sorbed
Purolite A500	1400	160	0.91	94
Dowex 21K 1630	8800	1500	0.82	99
Dowex 21K XLT	12000	1700	0.86	99
Lewatit S6328 A	2000	70	0.97	95
GAC Ag	800	130	0.84	89

A 1% nitric acid solution (pH ~1) was effective at extracting uranium from all resins. Essentially all of the sorbed uranium was desorbed into the acidic solution. This was not the case for the GAC Ag. Repeat acid extractions as well as bicarbonate and carbonate extraction solutions were used, but only a combined, inconsistent 40–70% of the total uranium could be removed from the GAC using the different extraction solutions. This result again confirms the elimination of the GAC Ag as the sorbent of choice for the uranium PFMs since it would be nearly impossible to quantify uranium passing through the meter without a more efficient and reliable extraction method.

3.3. Resin choice

Based on sorption capacity, tracer studies and resin price, Lewatit S6328 A was the chosen resin for the field PFMs. GAC had been eliminated due to poor extraction recovery and lower sorption than the other resins, and Purolite was eliminated due to the unexplained sorption phenomenon at higher concentrations. Table 3 presents a summary of the results from the resin sorption tests. While the Dowex resins exhibited better uranium sorption, the price difference for the 3–4% improvement in sorption, given the lower uranium concentrations at Rifle, was deemed unnecessary for this
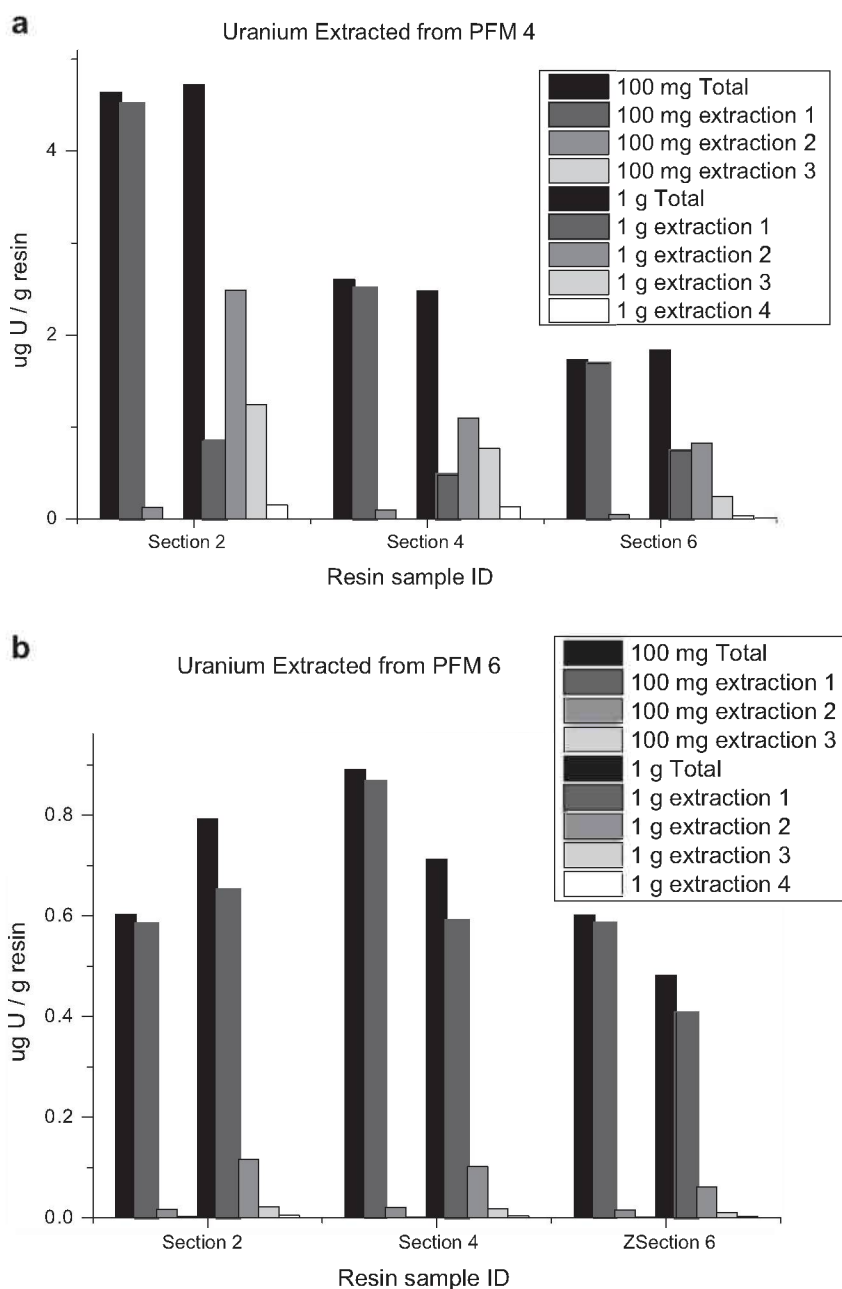

Fig. 3 – a) Uranium extracted from PFM#4 and b) from PFM #6. Since Lewatit was alternated with GAC to obtain tracer information, resin samples were 2, 4 and 6 (top) in the depth sequence. The left-most bar (black) in each series represents the total uranium concentration removed from the resin after all extractions using the two different masses.

experiment, especially given the improved performance in the actual groundwater samples. If it was necessary to get more accurate flux measurements, without having to make a minor correction for incomplete sorption, either Dowex resin would be a better choice. Using this method, the greatest uncertainty a flux measurement lies in the up to 10% error of the ICP-MS, not the slight loss that may be seen by using the Lewatit resin over one of the Dowex resins. Since the resins did not reach a sorption capacity, it would be difficult to use these results to choose the best resin for use in high uranium flux contaminated sites. One consideration for testing samples is that as the U fills the strongest resin binding sites, the apparent partitioning K will change (decrease) and the actual U flux would be underestimated. However, based on the levels of U bound to the resin (Fig. 3), we are in fact well within the experimental range (Fig. 2), so this is not a problem for this work.

3.4. Field application

For the initial field test six PFM were deployed in six 4-inch wells. Each PFM was constructed using a new flux pod design having six alternating segments of granular activated carbon (GAC) and Lewatit resin (three pods or segments of GAC and three pods of Lewatit). The bottom segment of each PFM was GAC. The flux pods are self-contained segments of sorbent that can be stacked on a common center tube. The pods can then be retrieved individually for sampling on site or packaged for shipment to an analytical laboratory for remote sampling and analysis. The objective for using individual segments of sorbent was two-fold: to test the individual capability of the Lewatit resin to capture uranium under field conditions while using the GAC to estimate groundwater flux and to test the new modular flux pod design. This was a necessary step to test the efficiency of the Lewatit as a sorbent under field conditions. However, the alternating segment design does not allow for measurement of water flux and uranium flux at the exact same vertical location. One design modification implemented following this experiment was to develop a three-layer prototype which will allow both groundwater and uranium flux measurements at the same vertical location and mixed media sorbents are now also being tested.

The PFM were retrieved and sampled after a deployment of 23 days (approximately three weeks). Tracer analysis from the GAC segments were used for groundwater flux estimates, and the Lewatit segments were used for uranium flux estimates. For comparison and validation of PFM performance, water samples were collected in each well four days prior to PFM deployment.

Silver additions to the Lewatit resin matched the concentrations on the alternating GAC layers. Solutions decanted after silver addition indicated that the Lewatit resin had in fact been coated to 0.03% silver by weight. This prevented microbial growth on the resin while installed at Rifle. After coating with silver (98% of silver sorbed to the resin), lab experiments were conducted to ensure that the silver was not being released from the resin and uranium sorption remained the same as without added silver. Treating Rifle groundwater with the silver coated resin showed release of silver to be 0.3% of
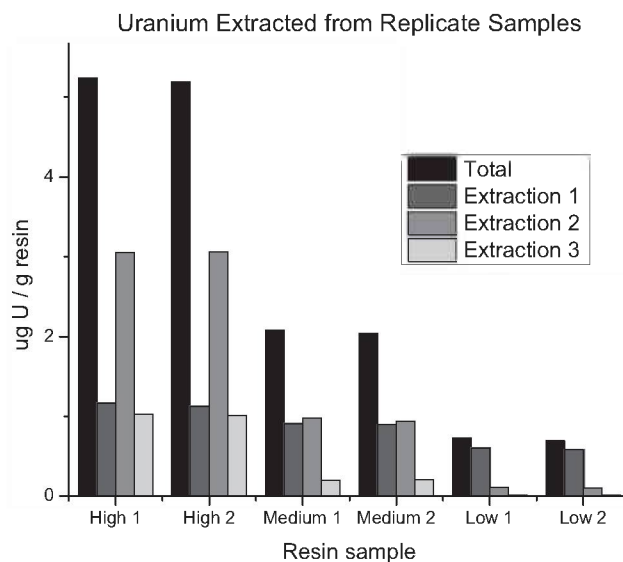

Fig. 4 – The results of using larger amounts of resin (4 g) and acid (40 mL) for extractions. Samples were chosen for this test based on the initial results so that a range of concentrations would be presented. High, medium and low represent the concentration/flux ranges expected from the first set of tests.
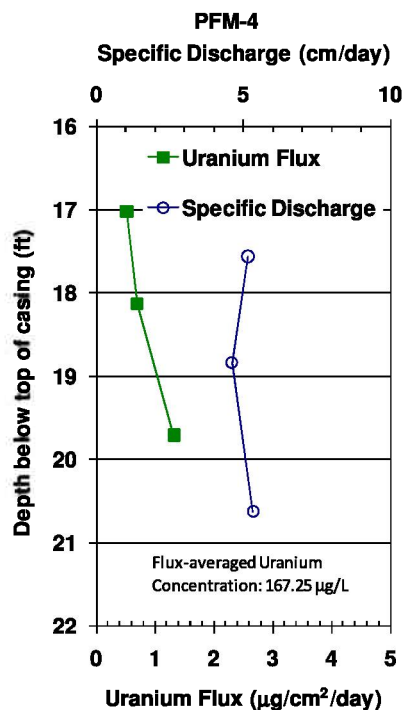

Fig. 5 – Measured fluxes for PFM 4 showing vertical distribution of uranium mass flux and volumetric water flux (specific discharge or Darcy Velocity). The PFM flux-averaged uranium concentration for this well was 167.25 μg/L which compares well with the aqueous uranium concentration (180.95 μg/L) measured in the well.

Table 4 – Summary of uranium mass flux, volumetric water flux (specific discharge or Darcy Velocity), flux-averaged concentration for all PFM segments in all wells, and measured aqueous concentrations for all wells.

| | From Passive Flux Meter (PFM) | | | |
	Uranium Mass Flux ($\mu g/cm^2$ day)	Specific discharge (Darcy Velocity) (cm/day)	Flux averaged uranium concentration ($\mu g/L$)	Measured aqueous uranium concentration ($\mu g/L$)
Minimum	0.13	2.27	57.62	171.00
Maximum	3.57	6.83	615.31	192.30
Standard Deviation	0.84	1.38	140.31	8.84
Mean	0.13	5.00	188.43	180.63

Sample size (n) for each data set: For PFM: $n = 3$ PFM segments (samples) per 6 wells = 18, For aqueous samples = $n = 1$ sample per 6 wells = 6.

the sorbed silver and 99% of aqueous uranium sorbed to the resin, which is unchanged from the sorption to resin with no silver addition, making it suitable for use at the field site. We are unsure of the mechanism by which Ag^+ sorbs to an anion exchange resin, perhaps it is related to the matrix material. A complete understanding of this was not necessary, however, since we were only interested in just adding it for an antimicrobial purpose that would not interfere with uranium sorption.

Uranium was extracted from the resins taken from the Rifle PFMs by the same 1% nitric acid solution used for lab studies. As mentioned before, small quantities of resin were compared to a larger sample to determine homogeneity in sample and method during the first sampling trips. Fig. 3 shows the results of the multiple extractions. If the samples are homogeneous, the final total concentration of uranium extracted from both quantities of resin should be the same. There were some minor discrepancies that can be attributed to either ICP-MS error or sample heterogeneity. PFMs that were exposed to higher water and uranium fluxes were more likely to have a homogeneous composition of uranium on the resin (totals match in Fig. 3a). Lower flows yielded locally concentrated uranium in the PFM on the upgradient side and were more difficult to completely homogenize leading to inconsistent concentration values in samples less than 1 g (see Fig. 3b). Using a large quantity of resin, or the whole sample for the extraction, will improve the accuracy of the uranium masses used for flux calculations. Samples were reanalyzed using the 4 g/40 mL method listed, and replicate samples showed excellent reproducibility with a maximum difference between replicates of 5%, even at the lower concentrations of uranium (Fig. 4). All samples from subsequent trips were analyzed in this manner. Future PFM design may examine water flow direction (which changes with the river water stage) by cross-sectional quartering of samples. This may also be useful for samples with localized concentrated uranium.

3.5. Summary of field results

Observed variations and trends in measured fluxes were consistent amongst wells and similar to the results provided for PFM 4 in Fig. 5, which shows the vertical distribution of uranium mass flux and volumetric water flux (specific discharge). It can be observed that vertical trends in uranium

flux tend to agree with water flux, and the resulting flux-averaged concentration for this well (167.25 $\mu g/L$) compares favorably with the aqueous concentration measured in the well (180.95 $\mu g/L$).

Table 4 provides a summary of uranium mass flux, volumetric water flux (specific discharge), flux-averaged concentration for all PFM segments, and measured aqueous concentrations. The summary provides a comparison of flux-averaged uranium concentrations estimated from all PFM segments across all wells to aqueous uranium concentrations measured in each well. One key point to observe is the similarity of mean concentrations while noting the larger standard deviation for PFM-based flux-averaged estimates. This is because the aqueous concentrations represent the volumetric average within the entire borehole, while the flux-averaged concentrations show much higher resolution with respect to variation with depth (as shown in Fig. 5). The similar mean values for flux-averaged and measured aqueous uranium concentration provides a positive validation for PFM measurement of uranium flux while also providing additional detail with regard to the vertical variation of flux within the well and surrounding formation.

As seen in Fig. 3a, when larger resin samples were extracted for uranium, the second extraction removed the most uranium, whereas the smaller resin amounts demonstrated expected extraction patterns, with the most uranium removed in the first extraction and less in each subsequent extraction. This pattern was seen only in the first sampling trip in samples with high uranium fluxes. This is possibly due to high concentrations of organics binding to the resin and preventing release of uranium in the first extraction. To determine other anions sorbed to the resin and possible desorption interferences, a larger resin sample and volume of acid were used to have sufficient volume for both ICP-MS and ICP-AES analyses. This larger volume also saw better consistency in low flux samples and was used for all future extractions. It was also observed that significant sulfate was removed, with less in each subsequent extraction. Based on the acid strength and nitrate concentration, there were still enough exchangeable nitrate anions to remove all uranium and sulfate together, even with the 2:1 nitrate:sulfate molar charge ratio, supporting the theory that organics are binding and blocking the sites. However, if the binding strength of sulfate to Lewatit resin is much higher than that of nitrate, an excess of 5 times as many exchangeable ions of nitrate to

sulfate may not have been sufficient, also contributing to the pattern of uranium removal.

4. Conclusions

Anion exchange resins provide an effective material for use in a passive flux meter under the water chemistry conditions at the old mill site in Rifle, CO. The Dowex 21K resins had the highest uranium sorption capacity, but are more costly than some of the other resins (i.e. Lewatit) which have sufficient uranium sorption for this purpose and concentration range. Despite geochemical computations indicating mostly neutral uranium species, anion exchange resins were very useful as uranium sorbents. These resins may be good for anionic and neutral species, but more work is needed to understand the sorption mechanisms and speciation covering a larger pH range. Coating the resins with silver nitrate does not affect uranium sorption, and it prevents microbial growth on the resins which could negatively impact the flux measurements and concentrations obtained. PFMs that were placed in high flux areas at the Rifle field site allowed for simple, reliable flux measurements due to homogeneity in the resin samples removed from the PFM; uranium passed through the whole PFM. At sampling locations where uranium fluxes were low the mass of extracted uranium was much more variable from small resin samples and therefore contributed to the error in the flux calculations. When homogenization was incomplete, some of these small resin samples were taken from the upgradient side with more uranium and others were from the downgradient side with little, if any, uranium. The best extraction method found for good reproducibility with sufficient sample size and minimal waste uses 40 mL of a 1% nitric acid solution and 4 g of resin. This finding will be useful in future PFM applications to quantify uranium mass contaminant fluxes in groundwater.

Results from an initial field experiment demonstrated that calculated flux-averaged uranium concentrations compared well with measured aqueous uranium concentrations under field conditions, which provided positive validation for use of ion exchange resins for quantifying uranium flux. Ultimately, these flux measurements will provide insight into the mobility of uranium and effectiveness of current remediation strategies employed at the contaminated former mill site in Rifle, Colorado.

Acknowledgments

REFERENCES

Annable, M.D., Hatfield, K., Cho, J., Klammler, H., Parker, B.L., Cherry, J.A., Rao, P.S.C., 2005. Field-scale evaluation of the passive flux meter for simultaneous measurement of groundwater and contaminant fluxes. Environmental Science and Technology 39, 7194—7201.

Anderson, R.T., Vrionis, H.A., Ortiz-Bernad, I., Resch, C.T., Long, P. E., Dayvault, R., Karp, K., Marutzky, S., Metzler, D.R., Peacock, A., White, D.C., Lowe, M., Lovley, D.R., 2003. Stimulating the in situ activity of Geobacter species to remove uranium from the groundwater of a uranium-contaminated aquifer. Applied Environonmental Microbiology 69, 5884—5891.

Barton, C.S., Stewart, D.I., Morris, K.S., Bryant, D.E., 2004. Performance of three resin-based materials for treating uranium-contaminated groundwater within a PRB. Journal of Hazardous Materials 116, 191—204.

Chanda, M., Rempel, G.L., 1992a. Removal of uranium from acidic sulfate-solution by ion-exchange on poly(4-vinylpyridine) and polybenzimidazole in protonated sulfate form. Reactive Polymers 17, 159—174.

Chanda, M., Rempel, G.L., 1992b. Uranium sorption behavior of a macroporous, quaternized poly(4-vinylpyridine) resin in sulfuric-acid medium. Reactive Polymers 18, 141—154.

Cho, J.Y., Annable, M.D., Jawitz, J.W., Hatfield, K., 2007. Passive flux meter measurement of water and nutrient flux in saturated porous media: bench-scale laboratory tests. Journal of Environmental Quality 36, 1266—1272.

DOE, 2008. Rifle, Colorado, Processing Sites and Disposal Site. http://www.lm.doe.gov/Rifle/Disposal/Documents.aspx (accessed 28.07.08).

Dong, W.M., Brooks, S.C., 2006. Determination of the formation constants of ternary complexes of uranyl and carbonate with alkaline earth metals (Mg^{2+}, Ca^{2+}, Sr^{2+}, and Ba^{2+}) using anion exchange method. Environmental Science and Technology 40, 4689—4695.

Gu, B.H., Ku, Y.K., Jardine, P.M., 2004. Sorption and binary exchange of nitrate, sulfate, and uranium on an anion-exchange resin. Environmental Science and Technology 38, 3184—3188.

Hatfield, K., Annable, M., Cho, J., Rao, P.S.C., Klammler, H., 2004. A direct passive method for measuring water and contaminant fluxes in porous media. Journal of Contaminant Hydrology 75, 155—181.

Jelinek, R.T., Sorg, T.J., 1988. Operating a small full-scale ion-exchange system for uranium removal. Journal American Water Works Association 80, 79—83.

Kolomiets, D.N., Konopleva, L.V., Sheremet'ev, M.V., Golubeva, T. E., Shatalov, V.V., 2004. Improvement of the sorption technology for extracting uranium from solutions and pulps. Atomic Energy 97, 463—467.

Kolomiets, D.N., Troshkina, I.D., Sheremet'ev, M.F., Konopleva, L.V., 2005. Sorption of uranium from sulfuric acid leaching solutions by strongly basic anion exchangers. Russian Journal of Applied Chemistry 78, 722—726.

Lovley, D.R., Phillips, E.J.P., Gorby, Y.A., Landa, E.R., 1991. Microbial reduction of uranium. Nature 350, 413—416.

Merdivan, M., Duz, M.Z., Hamamci, C., 2001. Sorption behaviour of uranium(VI) with N, N-dibutyl-N'-benzoylthiourea impregnated in Amberlite XAD-16. Talanta 55, 639—645.

Ortiz-Bernad, I., Anderson, R.T., Vrionis, H.A., Lovley, D.R., 2004. Vanadium respiration by Geobacter metalireducens: novel strategy for in situ removal of vanadium from groundwater. Applied Environmental Microbiology 70, 3091—3095.

Pesavento, M., Biesuz, R., Alberti, G., Sturini, M., 2003. Characterization of the sorption of uranium(VI) on different complexing resins. Analytical and Bioanalytical Chemistry 376, 1023–1029.

Phillips, D.H., Gu, B., Watson, D.B., Parmele, C.S., 2008. Uranium removal from contaminated groundwater by synthetic resins. Water Research 42, 260–268.

Schumann, D., Andrassy, M., Nitsche, H., Novgorodov, A.F., Bruchertseifer, H., 1997. Sorption behaviour of uranium on cation and anion exchange resins from HCl/HF-containing aqueous solutions: model experiments for the determination of chemical properties of element 106 (Seaborgium). Radiochimica Acta 79, 217–220.

USEPA, 1999. In: Use of Monitored Natural Attenuation at Superfund, RCRA Corrective Action, and Underground Storage Tank Sites. OSWER.

Vaaramaa, K., Lehto, J., Jaakkola, T., 2000. Removal of U-234, U-238, Ra-226, Po-210 and Pb-210 from drinking water by ion exchange. Radiochimica Acta 88, 361–367.

Yabusaki, S.B., Fang, Y., Long, P.E., Resch, C.T., Peacock, A.D., Komlos, J., Jaffe, P.R., Morrison, S.J., Dayvault, R.D., White, D.C., Anderson, R.T., 2007. Uranium removal from groundwater via in situ biostimulation: field-scale modeling of transport and biological processes. Journal of Contaminant Hydrology 93, 216–235.

Water and contaminant flux estimation from multi-layer passive flux meter measurements

H. Klammler[1,2,3], K. Hatfield[2,3], J. Luz[1], M. Annable[3,4], M. Newman[2,3], J. Cho[3,4], A. Peacock[5], V. Stucker[6], J. Ranville[6] & C. Clark II[7]

[1]Dept. of Env. Sc. and Sust. Dev., Fed. Univ. of Bahia, Brazil.
[2]Dept. of Civil and Coastal Eng., Univ. of Florida, USA.
[3]Inter-Disc. Prog. in Hydrologic Sc., Univ. of Florida, USA.
[4]Dept. of Env. Eng. Sc., Univ. of Florida, USA.
[5]Microbial Insights, Inc., Rockford, USA.
[6]Dept. of Chem. and Geochem., Colorado School of Mines, USA.
[7]Dept. of Civil and Env. Eng., Florida A&M University.

Abstract

The passive flux meter (PFM) enables measuring cumulative water and contaminant mass fluxes in porous aquifers. It consists of a sorbent material, which is installed in a monitoring well to intercept groundwater flow. Tracer losses and contaminant retention on the sorbent are used to estimate water and contaminant mass fluxes through the device. In the multi-layer PFM different (sorbent) materials are used in an annulus (layer-type) configuration. This allows for retaining leached tracers inside the PFM (no tracer release into aquifer) and facilitates simultaneous deployment of different sorbent types in a single device. In order to estimate undisturbed ambient fluxes in the aquifer, measurements need to be corrected for flow convergence or divergence induced by the well and PFM components. We make use of an analytical solution to the potential flow problem of uniform flow disturbed by a system of concentric rings of contrasting hydraulic conductivities. A flow convergence factor is defined as a function of PFM ring conductivities and radii, where tracer elution and contaminant sorption may occur in arbitrary layers. Results are used for calibration of convergence factors of a multi-layer PFM to laboratory sand box experiments.

Keywords: aquifer, groundwater, plume, flow convergence, sand box.

1 Introduction

Groundwater contamination is recognized as a dangerous threat to ecosystems and human drinking water supplies. Besides contaminant concentrations (mass per volume), contaminant mass fluxes (mass per cross sectional area per time) have been used more recently as relevant measures for contaminant source identification, risk assessment, decision making and remediation performance control (ITRC [1]). Currently, three fundamental approaches are available for measuring contaminant fluxes: (1) Multi-level sampling (MLS; Einarson and Mackay [2]), which is based on separate measurements of contaminant concentrations and water fluxes for subsequent multiplication to obtain contaminant fluxes. (2) Integral pump tests (IPT; Bockelmann et al. [3]), which extract contaminated groundwater from the aquifer through pumping from a well and monitor contaminant concentrations at the well head over time. (3) Passive flux meter measurements (PFM; Hatfield et al. [4], Annable et al. [5]) based on the installation of sorbent materials in observation wells, where the sorbents initially contain known amounts of resident tracers. From detected tracer losses from a sorbent and contaminant masses sorbed onto a sorbent through laboratory analyses, cumulative (i.e., time integrated or averaged over the period of installation) water and contaminant fluxes may be obtained simultaneously as depth profiles along the well.

PFMs have typically been deployed in observation wells as self-contained units consisting of a single sorbent material, which acts as both a leaching tracer reservoir and a contaminant trap. As a consequence, it has to be assured that (1) the sorption properties of the sorbent material are appropriate for both tracer(s) and target contaminants, and (2) that the chemical properties of the tracer(s) are such that tracer release (even though minimal) into the aquifer does not cause legal or environmental problems. In an effort to circumvent these two issues (e.g., for measuring water and contaminant fluxes at Rifle, CO, USA) a multi-layer PFM has been developed and tested, which consists of multiple concentric rings (layers) of different materials (which may be sorbents or not).

Figure 1 compares the two different PFM configurations, where figure 1a shows a single sorbent installed inside a well screen, while figure 1b illustrates the annular composition of a multi-layer PFM installed in a screened well. From the periphery towards the center k_i [L/T] and r_i [L] denote the hydraulic conductivities and outer radii of the different rings. k_0 corresponds to the aquifer, k_1 is the well screen, k_2 an outer sorbent layer for contaminant sorption (e.g., Lewatit resin for uranium), k_3 an intermediate sorbent layer (e.g., granular activated carbon (GAC) for alcoholic tracers) to retain tracers eluded from an inner sorbent layer of k_5 (e.g., also consisting of GAC for alcoholic tracers). Between the two GAC layers, there is a thin perforated stainless steel pipe of conductivity k_4, which serves to separate the inner GAC from the outer one for installation and laboratory analysis. The center circle of radius r_6 is an impermeable pipe for physical stabilization and water evacuation during PFM installation and removal. Table 1 summarizes the properties of the multi-layer PFM configuration used in laboratory sand box

experiments for determination of k_1 and k_4 and subsequent deployment for measuring water and uranium fluxes at the uranium field site in Rifle.
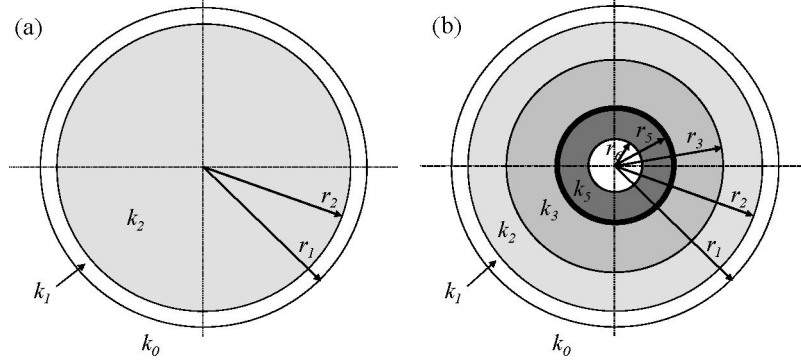

Figure 1: Horizontal cross sections of well screens and (a) a PFM consisting of a single sorbent and (b) a multi-layer PFM as used in laboratory testing. Bold black circle is of outer radius r_4 and conductivity k_4.

Table 1: Summary of multi-layer PFM properties as depicted in figure 1b with k_1 and k_4 to be determined from laboratory box experiments.

Ring n°. i [-]	Conductivity k_i [m/day]	Outer radius r_i [cm]	Material / purpose
0	33	infinite	Aquifer (sand)
1	k_1	5.7	Well screen (slotted PVC pipe)
2	250	5.1	Lewatit resin for uranium sorption
3	350	3.8	GAC for tracer retention
4	k_4	2	Perforated pipe for separation
5	350	1.9	GAC for tracer elution
6	0	0.8	Impermeable center pipe

Similar to the simple PFM, the multi-layer PFM provides data in terms of tracer losses from sorbent ring 5 and contaminant masses retained from sorbent ring 2. Following the method of Hatfield et al. [4] the apparent flux $q_{PFM,i}$ [L/T] through the i-th ring of a PFM may be found as

$$q_{PFM,i} = \frac{(1 - m_{ri})(r_i^2 - r_{i+1}^2)\pi \theta_i R_i}{2 r_i t} \tag{1}$$

where m_{ri} [-] is the relative mass of a tracer remaining (with respect to the initial mass of that tracer) after time of exposure t [T] in the i-th ring of relative water

content θ_i [-] and retardation factor R_i [-]. The attribute "apparent" indicates that flow is generally not uniform inside a multi-layer PFM and $q_{PFM,i}$ is to be understood as a discharge per unit transect area of the i-th ring perpendicular to incident flow direction. In analogy, an apparent contaminant mass flux $J_{PFM,i}$ [M/(TL^2)] trough the i-th ring may be obtained from

$$J_{PFM,i} = \frac{M_{si}}{2r_i bt} \tag{2}$$

where M_{si} [M] is the mass of contaminant sorbed in the i-th layer over a PFM interval of length b [L]. Eqn (1) is valid as long as none of the stream tubes through the i-th layer are completely cleared (empty) of tracer, while eqn (2) is valid as long as none of the contaminant previously sorbed onto the i-th layer is again released from it. As a consequence, within their ranges of validity eqns (1) and (2) do not depend on the properties (e.g., non-uniformity) of the flow field in the respective rings. Note that for $r_{i+1} = 0$ (i.e., the i-th layer is the center circle) eqn (1) reduces to eqn (18) of Hatfield et al. [4], whose coefficient of 1.67 appears as $\pi/2 \approx 1.57$ here. This is a consequence of the range of validity stipulated (an analogous observation applies to eqn (2)).

However, due to the more complex configuration of the multi-layer PFM and flow refraction between layers of different conductivities, an assessment of undisturbed ambient water and contaminant fluxes in the aquifer is not straight-forward. Klammler et al. [6] present an analytical solution to the potential flow problem through the multi-layer PFM and they develop flow convergence factors for estimation of undisturbed (uniform) ambient fluxes. These factors, however, are with respect to the inner-most ring (center circle) only and are not applicable to other rings. The present work generalizes the convergence factors of Klammler et al. [6] to arbitrary layers in a multi-layered PFM configuration and uses the result for calibration of unknown parameters (well screen and perforated pipe conductivities k_1 and k_4) through a laboratory sand box experiment, such that they may be applied to the multi-layer PFM deployment at Rifle for measuring water and uranium fluxes.

2 General flow field solution

The solution of Klammler et al. [6] is based on potential flow through porous media (Strack [7]). It makes use of a flow field analogy between uniform flow disturbed by a cylindrical inhomogeneity in hydraulic conductivity and uniform flow disturbed by an impermeable or infinitely permeable cylinder. Its application is best illustrated by a numerical example, for which we use the flow domain of figure 1b (table 1) with values of $k_1 = 2.3$ m/d and $k_4 = 3.2$ m/d. This leads to the flow field (stream lines) of figure 2 with the stream function Ψ_i [L^3/T] in the i-th ring given by

$$\Psi_i = q_i rb\left(1 - \frac{a_i^2}{r^2}\right)\sin\gamma \tag{3}$$

where r [L] and γ [-] are the radial and angular coordinates, respectively, b [L] is the thickness of the flow domain (length of PFM interval in eqn (2)) and the parameters a_i [L] and q_i [L/T] are given in table 2 and obtained as follows: Starting with an initial value of $a_6 = 0$ in table 2, the columns of k_{ia} [L/T] and a_i are populated from bottom up by alternately applying eqns (4) and (5). Subsequently, the column of q_i is populated from top down by consecutive use of eqn (6). Most parameters in table 2 are auxiliary variables without direct physical equivalences (some of them complex / imaginary). Exceptions are q_0 (undisturbed flux in the aquifer; assumed uniform), k_{6a} (equal to conductivity k_6 of inner ring), k_{0a} (equal to aquifer conductivity k_0) and q_6 (specific discharge in inner ring). Since $k_6 = 0$, it is further seen that a_5 is equal to the center pipe radius r_6. Following this example, the step-wise solution scheme of eqns (3) through (6) is generally applicable to an arbitrary number of layers.

$$k_{ia} = k_i \frac{1 - \left(\dfrac{a_i}{r_i}\right)^2}{1 + \left(\dfrac{a_i}{r_i}\right)^2} \tag{4}$$

$$a_{i-1} = r_i \sqrt{\frac{1 - \dfrac{k_{ia}}{k_{i-1}}}{1 + \dfrac{k_{ia}}{k_{i-1}}}} \tag{5}$$

$$q_i = q_{i-1} \frac{1 + \dfrac{k_i}{k_{ia}}}{1 + \dfrac{k_{i-1}}{k_{ia}}} \tag{6}$$

3 Flow convergence factors for arbitrary layers

Using the solution of Ψ_i from eqn (3) for an arbitrary number of layers, the apparent flux $q_{PFM,i}$ [L/T] through the i-th ring of eqn (1) may be found. It is equal to the difference of the stream function between the lateral-most points (e.g., for $i = 2$ points A and B in figure 2) of the ring divided by the cross sectional area perpendicular to flow.
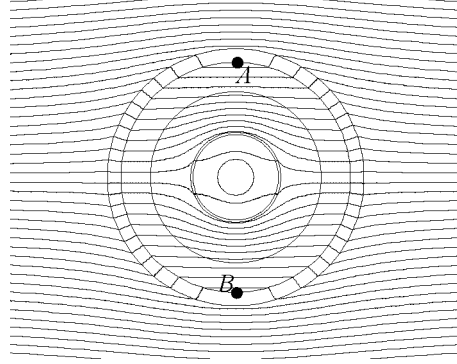
Figure 2: Flow field solution depicted as stream lines (lines of constant Ψ_i) for flow domain of figure 1b (table 1).

Table 2: Summary of flow field parameters and convergence factors for multi-layer PFM of figure 1b for $k_1 = 2.3$ m/d and $k_4 = 3.2$ m/d. $j = \sqrt{-1}$ is the imaginary unit.

Ring n°. i [-]	a_i [cm]	k_{ia} [m/day]	q_i/q_0 [-]	α_i [-]
0	2.94	33	$q_0/q_0 = 1$	1
1	5.05j	19.12	0.41	0.73
2	0.79	238.38	0.83	0.81
3	1.73	229.46	1.01	0.80
4	1.88j	49.78	0.13	0.25
5	0.80	244.59	0.32	0.26
6	$a_6 = 0$	0	0	0

$$q_{PFM,i} = \frac{\Psi_i(r_i,\frac{\pi}{2}) - \Psi_i(r_i,-\frac{\pi}{2})}{2r_i b} = \frac{\Psi_i(r_i,\frac{\pi}{2})}{r_i b} = q_i\left(1 - \frac{a_i^2}{r_i^2}\right) \qquad (7)$$

In the undisturbed aquifer the flow is assumed to be of uniform flux q_0, such that a flow convergence (or divergence) factor α_i [-] for the i-th ring may be defined by

$$\alpha_i = \frac{q_{PFM,i}}{q_0} = \frac{q_i}{q_0}\left(1 - \frac{a_i^2}{r_i^2}\right) \qquad (8)$$

In other words, the flow convergence factor expresses how much flow crosses the i-th ring of a multi-layer PFM with respect to the ambient flow through a ring of the same size, if the aquifer was not disturbed by the well and PFM components. A value of α_i larger than one may be viewed as a situation of flow convergence, while a value smaller than one reflects a condition of flow divergence. For a single layer PFM, flow convergence occurs when the PFM sorbent is more permeable than the aquifer and flow divergence occurs when the contrary is true. For multi-layer PFMs, however, $\alpha_i \geq 1$ and $\alpha_i \leq 1$ may occur simultaneously in different layers of a single device depending on the sequence of k_i. Returning to the example of figure 1b and using values of r_i from table 1 with values of q_i/q_0 and a_i from table 2, the values of α_i as given in the last column of table 2 are directly obtained from eqn (8) (note hereby that some values of a_i are imaginary).

The flow convergence factor α_i from eqn (8) is a generalization over that of Klammler et al. [6], because it is applicable to any layer. If i is equal to the total number of layers present, such that α_i applies to the center circle of the flow domain as shown in figure 1, for example, then eqn (8) becomes equal to α_i from Klammler et al. [6]. Moreover, for $i = 1$, 2 and 3 (and an arbitrary total number of layers), eqns (3), (12) and (13) of Klammler et al. [6] may be written in a generalized form by using k_{1a}, k_{2a} and k_{3a} from eqn (4) instead of k_1, k_2, and k_3 resulting in

$$\alpha_1 = \frac{2}{1 + \dfrac{k_0}{k_{1a}}} \tag{9}$$

$$\alpha_2 = \frac{4}{\left(1 + \dfrac{k_0}{k_1}\right)\left(1 + \dfrac{k_1}{k_{2a}}\right) + \left(1 - \dfrac{k_0}{k_1}\right)\left(1 - \dfrac{k_1}{k_{2a}}\right)\left(\dfrac{r_2}{r_1}\right)^2} \tag{10}$$

$$\alpha_3 = \frac{8}{\left(1 + \frac{k_0}{k_1}\right)\left(1 + \frac{k_1}{k_2}\right)\left(1 + \frac{k_2}{k_{3a}}\right) + \left(1 - \frac{k_0}{k_1}\right)\left(1 - \frac{k_1}{k_2}\right)\left(1 + \frac{k_2}{k_{3a}}\right)\left(\frac{r_2}{r_1}\right)^2 + \left(1 + \frac{k_0}{k_1}\right)\left(1 - \frac{k_1}{k_2}\right)\left(1 - \frac{k_2}{k_{3a}}\right)\left(\frac{r_3}{r_2}\right)^2 + \left(1 - \frac{k_0}{k_1}\right)\left(1 + \frac{k_1}{k_2}\right)\left(1 - \frac{k_2}{k_{3a}}\right)\left(\frac{r_3}{r_1}\right)^2} \tag{11}$$

For $i = 4$, the result of Appendix B in Klammler et al. [6] is incomplete and after substituting k_4 by k_{4a} it should be

$$\alpha_4 = \frac{16}{A + B + C + D + E + F + G + H} \tag{12}$$

with

$$A = \left(1 + \frac{k_0}{k_1}\right) \cdot \left(1 + \frac{k_1}{k_2}\right) \cdot \left(1 + \frac{k_2}{k_3}\right) \cdot \left(1 + \frac{k_3}{k_{4a}}\right)$$

$$B = \left(1 - \frac{k_0}{k_1}\right) \cdot \left(1 - \frac{k_1}{k_2}\right) \cdot \left(1 + \frac{k_2}{k_3}\right) \cdot \left(1 + \frac{k_3}{k_{4a}}\right) \cdot \left(\frac{r_2}{r_1}\right)^2$$

$$C = \left(1 + \frac{k_0}{k_1}\right) \cdot \left(1 - \frac{k_1}{k_2}\right) \cdot \left(1 - \frac{k_2}{k_3}\right) \cdot \left(1 + \frac{k_3}{k_{4a}}\right) \cdot \left(\frac{r_3}{r_2}\right)^2$$

$$D = \left(1 - \frac{k_0}{k_1}\right) \cdot \left(1 + \frac{k_1}{k_2}\right) \cdot \left(1 - \frac{k_2}{k_3}\right) \cdot \left(1 + \frac{k_3}{k_{4a}}\right) \cdot \left(\frac{r_3}{r_1}\right)^2$$

$$E = \left(1 + \frac{k_0}{k_1}\right) \cdot \left(1 + \frac{k_1}{k_2}\right) \cdot \left(1 - \frac{k_2}{k_3}\right) \cdot \left(1 - \frac{k_3}{k_{4a}}\right) \cdot \left(\frac{r_4}{r_3}\right)^2$$

$$F = \left(1 + \frac{k_0}{k_1}\right) \cdot \left(1 - \frac{k_1}{k_2}\right) \cdot \left(1 + \frac{k_2}{k_3}\right) \cdot \left(1 - \frac{k_3}{k_{4a}}\right) \cdot \left(\frac{r_4}{r_2}\right)^2$$

$$G = \left(1 - \frac{k_0}{k_1}\right) \cdot \left(1 + \frac{k_1}{k_2}\right) \cdot \left(1 + \frac{k_2}{k_3}\right) \cdot \left(1 - \frac{k_3}{k_{4a}}\right) \cdot \left(\frac{r_4}{r_1}\right)^2$$

$$H = \left(1 - \frac{k_0}{k_1}\right) \cdot \left(1 - \frac{k_1}{k_2}\right) \cdot \left(1 - \frac{k_2}{k_3}\right) \cdot \left(1 - \frac{k_3}{k_{4a}}\right) \cdot \left(\frac{r_2 r_4}{r_1 r_3}\right)^2 \tag{13}$$

Note that eqns (9) through (13) are equivalent formulations to the step-wise procedure of eqns (4) through (6). While closed form expressions of α_i for $i > 4$ may be derived, they become increasingly lengthy and computational implementation of eqns (4) through (6) (e.g., in a spreadsheet) may be more convenient.

Not immediately obvious from eqns (9) through (13) and more easily verifiable using eqns (5), (6) and (8) is that the ratio α_i/α_{i-1} is only a function of k_m and r_m, where $m \geq i - 1$. More intuitively, this means that flow refraction between two adjacent layers does not depend on the radii and conductivities of any outside layers or the aquifer. This may be convenient for comparing flux estimates from different layers independent of the perhaps uncertain aquifer conductivity k_0 and will be explored for estimating k_1 and k_4 below. However, it also precludes the possibility of estimating an unknown k_0 from two flux estimates in different layers (as may be attempted in analogy to the method presented in Klammler et al. [6]).

Assuming that contaminant transport is dominated by advection (i.e., contaminant particles travel along the same stream tubes as water particles and effects of diffusion and dispersion are neglected), $q_{PFM,i}$ and q_0 in the first equality of eqn (8) may be substituted by $J_{PFM,i}$ from eqn (2) and the undisturbed ambient contaminant mass flux J_0 [M/(L²T)], respectively. It is recalled that m_{ri} for estimation of $q_{PFM,i}$ and M_{si} for estimation of $J_{PFM,i}$ do not have to stem from the same PFM layer (i.e., index i in eqns (1) and (2) generally takes different values).

However, if m_{ri} and M_{si} are obtained from the same layer, then the same flow convergence factor α_i applies.

4 Laboratory experiments and calibration

For application of the multi-layer PFM configuration of figure 1b at the uranium site in Rifle and determination of unknown conductivities k_1 and k_4, laboratory sand box experiments are performed. Box size is 39 x 30.5 x 17.9 cm (length L x width W x height H) and table 1 contains the sand conductivity as well as well screen and PFM parameters. "Ambient" water fluxes q_0 and uranium fluxes J_0 through the box are obtained from

$$q_0 = \frac{Q_0}{WH} \tag{14}$$

$$J_0 = q_0 C_u \tag{15}$$

where Q_0 [L^3/T] is the independently measured water discharge through the box and C_u [M/L^3] is the uranium concentration in the influent water. Eleven tests of different durations were run for water flux obtaining estimates $q_{PFM,5}$ from eqn (1) for comparison to q_0 of eqn (14). In five of these tests uranium was added at $C_u \approx$ 200 µg/l for comparison of $J_{PFM,2}$ from eqn (2) with J_0 of eqn (15).

Table 3: Summary of results from sand box experiments.

t [days]	q_0 [cm/day]	$q_{PFM,5}$ [cm/day]	α_5 [-]	J_0 [µg/(cm^{2}day)]	$J_{PFM,2}$ [µg/(cm^{2}day)]	α_2 [-]
3.00	15.95	4.12	0.26			
2.87	16.85	4.03	0.24			
2.92	16.85	3.44	0.20		N/A	
2.99	18.48	4.13	0.22			
4.24	17.03	3.84	0.23			
4.05	19.44	4.09	0.21			
5.92	7.87	2.40	0.30	1.68	1.86	1.11
3.94	11.52	3.64	0.32	2.38	1.80	0.76
1.95	25.02	6.17	0.25	5.05	2.16	0.43
1.51	31.78	7.93	0.25	6.15	2.96	0.48
12.00	3.87	1.68	0.43	0.80	1.05	1.30
		Average α_5 =	0.26		Average α_2 =	0.81

Table 3 summarizes the results of the sand box experiments and indicates average values of $\alpha_2 = J_{PFM,2}/J_0 = 0.81$ and $\alpha_5 = q_{PFM,5}/q_0 = 0.26$. At this point we

return to table 2 and revert the previous assumption that the conductivities k_1 and k_4 of the well screen and the perforated pipe are known. Instead, the experimental values of α_2 and α_5 are used to determine effective values of k_1 and k_4 to be used in the interpretation of field deployments. For this purpose, advantage is taken of the previous conclusion that the ratio $\alpha_5/\alpha_2 = 0.32$ is not affected by k_1. Thus, k_4 may be directly found, which is most conveniently achieved by systematically varying k_4 for an arbitrary value of k_1 and observing the results in terms of α_5/α_2. Figure 3 shows the outcome of this process and leads to two possible values of k_4 = 3.2 and 18851 m/day. For each of the values found for k_4, the same process is repeated with k_1 to reach the required value of $\alpha_2 = 0.81$ (or equally $\alpha_5 = 0.26$). This is illustrated in figure 4 and shows that again two values of k_1 may be combined with each value of k_4, thus resulting in the four solutions given in the first two rows of table 4.

For each of the four solutions pairs, a flow convergence factor α_q for water flux and a flow convergence factor α_J for uranium may be computed for the deployment conditions at the Rifle site. These conditions are identical to those of figure 1b, except for the presence of a filter pack of radius 10.2 cm and conductivity 160 m/day around the well screen and inside an aquifer of conductivity of approximately 2.5 m/d. Considering these modifications, results for α_q and α_J from application of eqns 4, 5, 6 and 8 are given in the last two rows of table 4. It may be seen that $\alpha_q/\alpha_J = \alpha_5/\alpha_2 = 0.32$ remains constant and, more interestingly, that the solutions are pair wise identical (up to chart reading and rounding errors). It appears that this is not a coincidence as the same behaviour may be observed for other hypothetical values of aquifer and filter pack conductivities and radii. From the remaining two solution, $\alpha_q = 0.20$ and $\alpha_J = 0.61$ are proposed for use at the Rifle site, since they are associated with a low value of $k_1 = 2.3$ (and either value of k_4). This choice is justified by two related arguments: (1) From an independent borehole dilution test (no PFM installed) in the sand box a value of $k_1 = 87$ m/day is estimated. This may be regarded as an upper bound for k_1 as flow in the vicinity of an open borehole is radial. Flow components in the tangential direction through the well screen are hindered by the fact that screen slots are not continuous along the circumference of a PVC screen. (2) As illustrated by the flow field in figure 2, low k_1 and k_4 cause flow in the respective rings to be essentially radial, which is in agreement with the geometric properties of the screen slots and the pipe perforations acting as water conduits. Large values of k_1 and k_4, in turn, would lead to a certain degree of flow short circuiting along these rings, which is considered less plausible, particularly since the sorbents are granular and tend to settle into the well and close possible voids along the pipe or screen surfaces.

5 Summary

Based on an existing solution to the potential flow problem of uniform flow disturbed by an arbitrary number of concentric rings of contrasting conductivities, flow convergence (or divergence) factors are developed for interpretation of multi-layer PFM measurements. Flow convergence factors convert water and

contaminant fluxes measured in an arbitrary layer of the PFM into estimates of respective undisturbed ambient fluxes (i.e., unaffected by the presence of well and PFM). Using the results in combination with laboratory sand box experiments, effective conductivities of a well screen and another separation screen between layers are determined. With these conductivities, flow convergence factors for measuring water and uranium fluxes at a site in Rifle, CO, USA, are proposed.
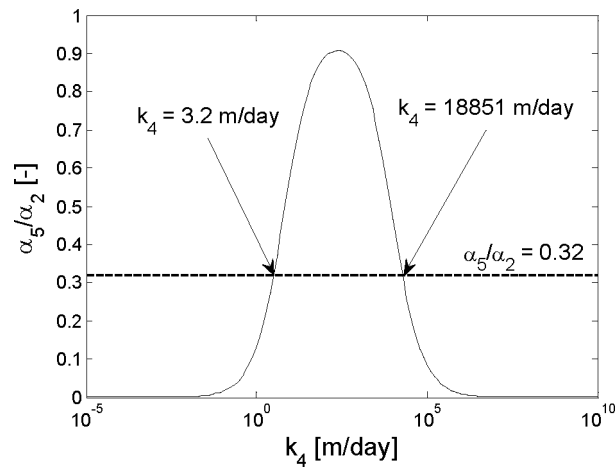

Figure 3: α_5/α_2 as a function of k_4 for arbitrary k_1 to achieve target value $\alpha_5/\alpha_2 = 0.32$.
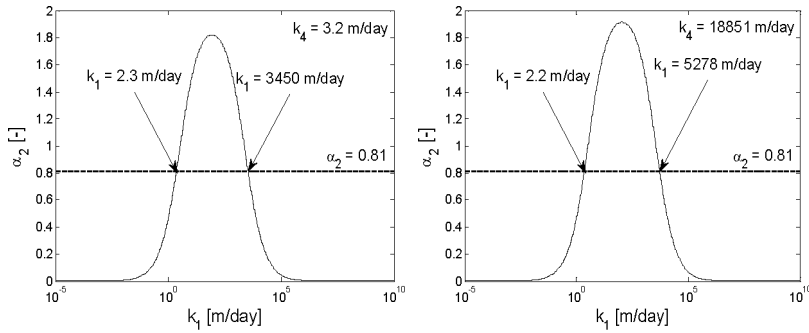
Figure 4: α_2 as a function of k_1 for $k_4 = 3.2$ and 18851 m/day to achieve target value $\alpha_2 = 0.81$.

Table 4: Possible combinations of k_1 and k_4 in m/day to achieve $\alpha_2 = 0.81$ and $\alpha_5 = 0.26$ from box experiments and resulting α_q and α_J for the Rifle deployment.

k_1	2.3	3450	2.2	5278
k_4	3.2		18851	
α_q	0.20	0.36	0.20	0.37
α_J	0.61	1.13	0.61	1.16

Acknowledgements

References

[1] ITRC, *Use and Measurement of Mass Flux and Mass Discharge. MASSFLUX-1.* Interstate Technology & Regulatory Council: Washington, D.C., 2010.

[2] Einarson, M.D., Mackay, D.M., Predicting impacts of groundwater contamination. *Environmental Science and Technology*, **35(3)**, pp. 66A-73A, 2001.

[3] Bockelmann, A., Zamfirescu, D., Ptak, T., Grathwohl, P. & Teutsch, G., Quantification of mass fluxes and natural attenuation rates at an industrial site with a limited monitoring network: a case study. *Journal of Contaminant Hydrology*, **60(1-2)**, pp. 97-121, 2003.

[4] Hatfield, K., Annable, M., Cho, J., Rao, P.S.C. & Klammler, H., A direct passive method for measuring water and contaminant fluxes in porous media. *Journal of Contaminant Hydrology*, **75(3-4)**, pp. 155-181, 2004.

[5] Annable, M., Hatfield, K., Cho, J., Klammler, H., Parker, B., Cherry, J. & Rao, P.S.C., Field-scale evaluation of the passive flux meter for simultaneous measurement of groundwater and contaminant fluxes. *Environmental Science and Technology*, **39(18)**, pp. 7194-7201, 2005.

[6] Klammler, H., Hatfield, K., Annable, M., Agyei, E., Parker, B., Cherry, J. & Rao, P.S.C., General analytical treatment of the flow field relevant to the interpretation of passive flux meter measurements. *Water Resources Research*, **43(4)**, W04407, 2007.

[7] Strack, O.D.L., *Groundwater Mechanics*, Prentice Hall: Englewood Cliffs, N.J., 1989.

Equilibrium modeling of U(VI) speciation in high carbonate groundwaters: Model error and propagation of uncertainty

Janet J. Leavitt [a], Kerry J. Howe [a], Stephen E. Cabaniss [b,*]

[a] Department of Civil Engineering, University of New Mexico, MSC01 1070, Albuquerque, NM 87131-0001, USA
[b] Department of Chemistry and Chemical Biology, University of New Mexico, MSC03 2060, Albuquerque, NM 87131-0001, USA

ABSTRACT

Remediation of U-contaminated sites relies upon thermodynamic speciation calculations to predict U(VI) movement in the subsurface. However, reliability and applicability of geochemical speciation and reactive transport models may be limited by determinate (model) errors and random (uncertainty) errors in the equilibrium speciation calculations. This study examines propagated uncertainty in two types of subsurface calculations: I. Dissolved U(VI) speciation based on measured analytical constraints and solution phase equilibria and II. Overall U(VI) speciation which combined the dissolved phase equilibria with previously published adsorption reactions. Three levels of uncertainty, instrumental uncertainty, temporal variation and spatial variation across a site, were investigated using first-derivative sensitivity calculations and Monte Carlo simulations. Dissolved speciation calculations were robust, with minimal amplification of uncertainty and normal output distributions. The most critical analytical constraints in the dissolved system are pH, DIC, total U and total Ca, with some effect from dissolved SO_4^{2-}. When considering adsorption equilibria, calculations were robust with respect to adsorbed U(VI) concentration prediction, but bimodal distributions of dissolved U(VI) concentrations were observed in simulations with background levels of total U(VI) and higher (spatial and temporal variability) estimates of input uncertainty. Consequently, sorption model predictions of dissolved U(VI) may not be robust with respect these higher levels of uncertainty.

© 2011 Elsevier Ltd. All rights reserved.

1. Introduction

Contamination resulting from U mining and milling is an issue of concern due to the radioactivity, toxicity and solubility of U. Uranium(VI) minerals are soluble in circumneutral groundwaters at micromolar levels, well in excess of recommended levels for potential drinking water (USEPA, 2000; WHO, 2003). The mobility of U(VI) in groundwater can be influenced by speciation since UO_2^{2+} exhibits cation adsorption behavior with subsurface minerals, resulting in decreased mobility (Davis et al., 2002). In the presence of high carbonate concentrations, the major species shifts to uranyl-carbonates resulting in decreased adsorption to the minerals and allowing U(VI) to remain mobile (Davis and Curtis, 2003, Barnett et al., 2000). In the presence of high carbonate and alkaline earth metals such as Ca, the major species shifts to Ca-triscarbonato-uranyl species which further decrease U adsorption (Bernhard et al., 1996, 1998, 2001; Dong and Brooks, 2006). Therefore, determining the speciation of U at given conditions is crucial to the reliability of predicting its fate and transport in natural waters.

The measurement of U speciation in the subsurface environment is prohibitively difficult and expensive, and speciation calculations are often employed to estimate *in situ* speciation (Abdelouas et al., 1998; Davis and Curtis, 2003; Fox et al., 2006; Yabusaki et al., 2007; Fang et al., 2009). These calculations, performed by various speciation codes, rely upon a database of reactions and reaction energies (thermodynamic constraints) and a set of measured or postulated concentrations (analytical constraints).

The algorithms used by the speciation codes should provide sufficiently exact and consistent answers; however, the reliability of the predicted concentrations is subject to potential problems related to the user-defined thermodynamic and analytical constraints. Principal problems may include:

(i) important reactions omitted from or incorrectly defined in the database (Serkiz et al., 1996; Bernhard et al., 1996, 1998; Unsworth et al., 2002),
(ii) choice of approximations used to represent complex phenomena, e.g., ionic strength correction or adsorption model (Davis and Curtis, 2003; Weber et al., 2006),
(iii) uncertainty in thermodynamic constraints (equilibrium constants) (Criscenti et al., 1996; Cabaniss 1997, 1999; Nitzsche et al., 2000; Denison and Garnier-LaPlace, 2005; Weber et al., 2006),

* Corresponding author.
  E-mail address: cabaniss@unm.edu (S.E. Cabaniss).

(iv) uncertainty in analytical constraints, e.g., measurement error or representing 'groundwater concentration' as an average over several wells or sampling depths (Criscenti et al., 1996; Cabaniss 1997, 1999).

Errors associated with (i) and (ii) will here be termed determinate error, while those associated with (iii) and (iv) will be referred to as indeterminate error or uncertainty.

Quantifying the reliability of model predictions is not routine (Criscenti et al., 1996; Denison and Garnier-LaPlace, 2005; Weber et al., 2006; Meinrath et al. 2006). Provided that determinate errors are adequately addressed, first-derivative sensitivity analyses and Monte Carlo simulations can suggest bounds of reliability or uncertainty for calculated speciation results of a defined system. First-derivative sensitivity analyses can be used to identify critical input parameters by evaluating the effect of each input constraint (thermodynamic or analytical) on calculated equilibrium concentrations. Monte Carlo simulations can estimate the effects of thermodynamic and analytical uncertainties of known distribution on calculated equilibrium concentrations (Criscenti et al., 1996; Cabaniss, 1997, 1999; Nitzsche et al., 2000; Denison and Garnier-LaPlace, 2005; Weber et al., 2006). For the Monte Carlo simulations, the equilibrium system is solved for P trials in which different values of input constraints are selected randomly from the uncertainty distributions of those constraints. The resulting distribution of calculated concentrations as P approaches infinity represents the predicted uncertainty in that concentration. If the resulting distribution is approximately Gaussian (normal), a mean and standard deviation can be specified. Sometimes non-Gaussian distributions, such as a bimodal distribution may occur and as a result a mean and standard deviation cannot be adequately determined (Cabaniss, 1999; Denison and Garnier-LaPlace, 2005).

This article describes an investigation of the impact of thermodynamic and analytical uncertainty on the speciation of U(VI) in high-carbonate groundwaters. First-derivative sensitivity analyses and Monte Carlo simulations were performed to determine the uncertainty in U(VI) speciation resulting from typical levels of analytical uncertainty, spatial variability and temporal variability.

2. Computational data and methods

2.1. Site

The specific site of interest is the Uranium Mill Tailing Remedial Action (UMTRA) Old Rifle Site in Rifle, Colorado, USA. This site

Table 1
Input parameters used to define the Old Rifle site for thermodynamic equilibrium calculations (Ranville and Stucker, pers. comm.).

| Old Rifle groundwater sample | | | | | |
Component	Mean (M)	Standard deviation (Log M)	Component	Mean (M)	Standard deviation (Log M)
Ca^{2+}	6.54E−03	0.007	Cl^-	5.42E−03	0.004
Na^+	8.79E−03	0.007	NO_3^-	1.94E−04	0.013
Mg^{2+}	5.27E−03	0.007	UO_2^{2+}	8.37E−07	0.007
SO_4^{2-}	8.26E−03	0.007	K^+	3.07E−04	0.007
CO_3^{2-}	8.85E−03	0.043	Sr^{2+}	3.42E−05	0.007
Temperature (°C)	25	–	pH	7.18	0.02

covers approximately 9 ha and consists of an alluvial floodplain 6–7.5 m deep directly above an impermeable boundary. It is surrounded to the north, west and east by the Wasatch Formation and bounded by the Colorado River to the south (Fig. 1). Aqueous U(VI) concentrations at this site, considering spatial and temporal variability, range between 0.32 μM and 1.48 μM (Yabusaki et al., 2007; DOE, 2009) with dissolved inorganic carbonate (DIC) levels in the average range of 7.8–8.6 mM. Solution chemistry at this site is believed to be typical of high-DIC groundwaters at other contaminated sites (Davis and Curtis, 2003).

2.2. Equilibrium systems

Two equilibrium systems are considered here, both using groundwater measurements from the Old Rifle Site (Table 1, V. Stucker and J. Ranville, pers. comm.). Each system requires a set of analytical constraints (total concentration and pH) and a set of thermodynamic constraints (equilibrium reactions with formation constants, K).

System I represents only dissolved species, and uses the analytical constraints in Table 1. Total concentrations, not free ion concentrations are given for all values except pH; thus, total dissolved U(VI) = U(VI)$_{diss}$ = 0.837 μM. Thermodynamic constants for dissolved U species are given in Table 2. Additional data were taken from the National Institute of Standard and Technology (NIST) Reference database 46 ver. 8.0 (NIST, 2004) and the Visual MINTEQ ver. 2.53 database (Gustafsson, 2009). Equilibrium constants for the Ca(II)-triscarbonato-uranyl species, $Ca_2UO_2(CO_3)_3^0$ and $CaUO_2(CO_3)_3^{2-}$, were taken from recent work by Dong and Brooks (2006). As noted by those authors, the previous equilibrium
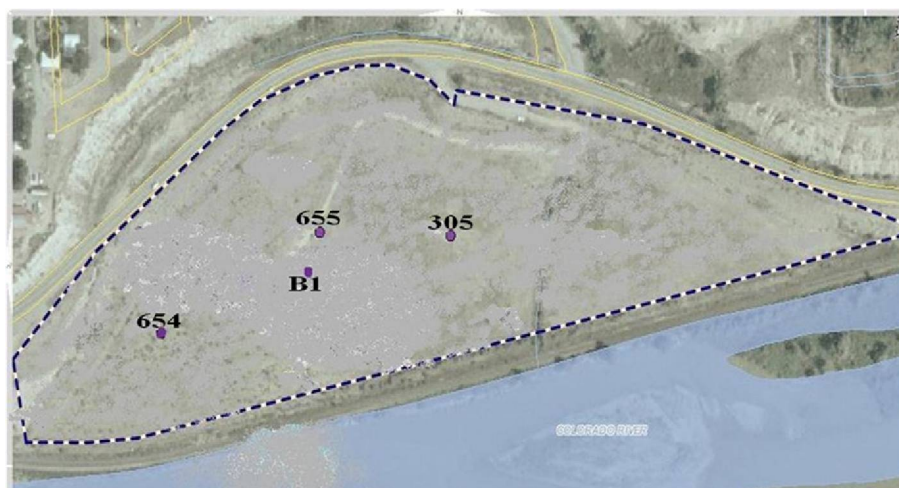

Fig. 1. Old Rifle Area. Wells pictured are data sources for Monte Carlo analysis.

Table 2
Thermodynamic constraints used in Titrator uncertainty calculations. Formation constants written using H^+, UO_2^{2+}, Ca^{2+}, Mg^{2+}, Sr^{2+}, Na^+, K^+, CO_3^{2-}, SO_4^{2-}, NO_3^-, Cl^- and H_2O as components.

Species name	Log K	Uncertainty (±)	Source
$(UO_2)_2(OH)_2^{2+}$	−5.620	0.040	Guillaumont et al. (2003)
$(UO_2)_2CO_3(OH)_3^-$	−0.858	0.851	Guillaumont et al. (2003)
$(UO_2)_2OH^{3+}$	−2.700	1.000	Guillaumont et al. (2003)
$(UO_2)_3(CO_3)_6^{6-}$	54.000	1.000	Guillaumont et al. (2003)
$(UO_2)_3(OH)_4^{2+}$	−11.900	0.300	Guillaumont et al. (2003)
$(UO_2)_3(OH)_5^+$	−15.550	0.120	Guillaumont et al. (2003)
$(UO_2)_3(OH)_7^-$	−32.200	0.800	Guillaumont et al. (2003)
$(UO_2)_4(OH)_7^+$	−21.900	1.000	Guillaumont et al. (2003)
$Ca(NO_3)_{(aq)}$	−4.500	0.100	Gustafsson (2009)
$Ca_2UO_2(CO_3)_{3\,(aq)}$	30.700	0.050	Dong and Brooks (2006)
$CaCl^+$	0.400	0.000	NIST (2004)
$CaCO_{3\,(aq)}$	3.220	0.070	NIST (2004)
$CaHCO_3^+$	11.529	0.100	NIST (2004)
$CaNO_3^+$	0.500	0.200	NIST (2004)
$CaOH^+$	−12.700	0.100	NIST (2004)
$CaSO_{4\,(aq)}$	2.360	0.070	NIST (2004)
$CaUO_2(CO_3)_3^{2-}$	27.180	0.060	Dong and Brooks (2006)
$H_2CO_3^{*}{}_{(aq)}$	16.681	0.006	NIST (2004)
HCO_3^-	10.329	0.009	NIST (2004)
HSO_4^-	1.990	0.010	NIST (2004)
$KCl_{(aq)}$	−0.300	0.100	NIST (2004)
$KNO_{3\,(aq)}$	−0.190	0.080	NIST (2004)
$KOH_{(aq)}$	−13.757	0.100	NIST, 2004
KSO_4^-	0.850	0.010	NIST (2004)
$Mg_2CO_3^{2+}$	3.590	0.100	NIST (2004)
$MgCl^+$	0.600	0.100	NIST (2004)
$MgCO_{3\,(aq)}$	2.920	0.070	NIST (2004)
$MgHCO_3^+$	11.339	0.060	NIST (2004)
$MgOH^+$	−11.417	0.030	NIST (2004)
$MgSO_{4\,(aq)}$	2.260	0.070	NIST (2004)
$NaCl_{(aq)}$	−0.300	0.000	NIST (2004)
$NaCO_3^-$	1.270	0.100	NIST (2004)
$NaHCO_{3\,(aq)}$	10.029	0.010	NIST (2004)
$NaNO_{3\,(aq)}$	−0.550	0.000	NIST (2004)
$NaOH_{(aq)}$	−13.897	0.030	NIST (2004)
$NaSO_4^-$	0.790	0.090	NIST (2004)
OH^-	−13.997	0.003	NIST (2004)
$SrCl^+$	0.220	0.050	NIST (2004)
$SrCO_{3\,(aq)}$	2.810	0.000	NIST (2004)
$SrHCO_3^+$	11.539	0.030	NIST (2004)
$SrNO_3^+$	0.600	0.200	NIST (2004)
$SrOH^+$	−13.177	0.100	NIST (2004)
$SrSO_{4\,(aq)}$	2.300	0.100	NIST (2004)
$UO_2(CO_3)_2^{2-}$	16.610	0.090	Guillaumont et al. (2003)
$UO2(CO3)_3^{4-}$	21.840	0.040	Guillaumont et al. (2003)
$UO_2(OH)_{2\,(aq)}$	−12.150	0.070	Guillaumont et al. (2003)
$UO_2(OH)_3^-$	−20.250	0.420	Guillaumont et al. (2003)
$UO_2(OH)_4^{2-}$	−32.400	0.680	Guillaumont et al. (2003)
$UO_2(SO_4)_2^{2-}$	4.140	0.070	Guillaumont et al. (2003)
UO_2Cl^+	0.170	0.020	Guillaumont et al. (2003)
$UO_2Cl_{2\,(aq)}$	−1.100	0.400	Guillaumont et al. (2003)
$UO_2CO_{3\,(aq)}$	9.940	0.030	Guillaumont et al. (2003)
$UO_2NO_3^+$	0.300	0.150	Guillaumont et al. (2003)
UO_2OH^+	−5.250	0.240	Guillaumont et al. (2003)
$UO_2SO_{4\,(aq)}$	3.150	0.020	Guillaumont et al. (2003)
$UO_2(SO_4)_3^{4-}$	3.020	0.38	Guillaumont et al. (2003)
$SrUO_2(CO_3)_3^{2-}$	26.860	0.040	Dong and Brooks (2006)
$MgUO_2(CO_3)_3^{2-}$	26.110	0.040	Dong and Brooks (2006)
$Mg_2UO_2(CO_3)_{3\,(aq)}$	28.360	0.200	Dong and Brooks (2006)

value obtained for the neutral species by Bernhard et al. (2001) and Kalmykov and Choppin (2000) appear mutually consistent. The value obtained for the latter Ca(II)-triscarbonato-uranyl species is higher than that obtained by Kalmykov and Choppin (2000) and stated to be more reliable due to the obtained formation constants indicating the binding of Ca^{2+} to $UO_2(CO_3)_3^{4-}$ is larger than that of Ca^{2+} to $CaUO_2(CO_3)_3^{2-}$ which is in agreement with the predicted orientation in stepwise formation constants.

System II represents both dissolved and adsorbed U(VI) species. Adsorption of U(VI) to sediment surfaces was modeled using the 'composite sediment' model of Curtis, Davis and co-workers (Davis and Curtis, 2003; Kohler et al., 2004) as implemented by Fang et al. (2009). Briefly, adsorption of U(VI) over a restricted range of pH (near pH 7) and ionic strength is represented by a set of three surface sites of varying concentrations and formation constants. WOH, SOH and SSOH are the weak, strong and strongest sites, occurring in a ratio of 10,000:10:1 in the sediment, as given in Table 3. Calculations based on this model are consistent with observed overall sorption constants for the Old Rifle Site (Fang et al., 2009). The labile U(VI) concentration U(VI)$_{lab}$, the amount of U desorbable from soil, was estimated to be 7.81 µM by assuming 5.25 nmol U(VI) g^{-1} of <2 mm sediment taken from the contaminated area within the site (Kohler et al. 2004; S. Yabusaki, pers. comm.). It was assumed that the <2 mm sediment was 20% of the total sediment and that this fraction was the only sediment that contained labile U(VI). For System II, U(VI)$_{Tot}$ = U(VI)$_{lab}$ + U(VI)$_{diss}$.

2.3. Uncertainty calculations

Equilibrium calculations, including derivatives and Monte Carlo simulations, used Titrator version 3.0 (Cabaniss, 1997, 2009). DIC was specified as total carbonate, not alkalinity, and ionic strength corrections used the Guntelberg approximation (Stumm and Morgan, 1996).

First derivatives of each calculated concentration with respect to each constraint were calculated numerically using log concentrations and uncertainties,

$$\frac{d\log C}{dX} = \frac{\log C_{X-\Delta x} - \log C_X + \Delta x}{2\Delta X}$$

where C is the molar concentration of a species, X is the log of a constraint (analytical or thermodynamic) and $2\Delta x$ is the small interval over which the derivative is calculated (Cabaniss, 1997). Here, $\Delta x = 0.01$ log units.

For Monte Carlo simulations, each constraint was assigned a standard deviation in log molar units, $S_{\log M}$. This is related to the relative standard deviation in measured concentration (RSD$_M$) by the approximate 'rule of thumb' RSD$_M$ = 2.303 $S_{\log M}$ (Harris, 2007). Thus, a standard deviation in log concentration $S_{\log M}$ = 0.007 corresponds to a relative error of 0.016, or 1.6% in molar concentration. The assumption of log normal analytical uncertainty thus corresponds to a constant relative error, which corresponds reasonably well to observation.

The Monte Carlo simulations used three different levels of uncertainty in the analytical constraints (Table 4). Based on the derivative calculations, total Ca(II), U(VI), DIC, and SO_4^{2-} and pH were selected as 'critical parameters' for which a standard deviation was

Table 3
Parameters used to determine adsorption site concentration and equilibrium calculations. All adsorption reactions were taken from Fang et al. (2009) and assigned a standard deviation of 0.1 for uncertainty analysis.

Particle density (kg/L)	2.75	Very strong binding sites (%)	0.01
Porosity	0.23	Strong binding sites (%)	0.1
Particle fraction < 2 mm	0.27	Weak binding sites (%)	99.89
Concentration of adsorption sites (µmol/g < 2 mm)		16.34	
Adsorption species		Equilibrium data (log K)	
$SSOUO_2^+$		12.28	
$SOUO_2^+$		6.950	
$WOUO_2^+$		2.740	
SSOUOOH		0.033	
SOUOOH		−2.120	
WOUOOH		−5.010	

Table 4
Critical input concentrations as defined by first-derivative analyses used in Monte Carlo simulations. All other inputs parameters are standard as listed in Table 1 (data from DOE (2009)).

Critical parameter	Analytical uncertainty		Temporal uncertainty		Spatial uncertainty	
	Mean (M)	Standard deviation (log M)	Mean (M)	Standard deviation (log M)	Mean (M)	Standard deviation (log M)
Ca^{3+}	6.54E−03	0.007	4.94E−03	0.096	4.74E−03	0.096
SO_4^{2-}	8.26E−03	0.007	8.25E−03	0.017	6.32E−03	0.161
CO_3^{2-}	8.85E−03	0.043	8.37E−03	0.083	7.82E−03	0.113
UO_2^{2+}	8.37E−07	0.007	5.96E−07	0.078	4.04E−07	0.326
pH	7.18	0.020	7.04	0.120	7.13	0.160

calculated at each level; standard deviations for other parameters remained constant. Instrumental uncertainty represents laboratory measurement uncertainty, and is thus the minimum achievable level; the instrumental uncertainties in Table 4 are based on water quality data taken from Well B1 in 2009 (Stucker and Ranville, pers comm.). Temporal uncertainty represents seasonal variability at a single well, and can be thought of as the uncertainty from using a few samples per year to represent annual concentrations. The average concentrations and temporal standard deviations were calculated using 10 years of data (1998–2008, taken from DOE, 2009) from Well 655. Spatial uncertainty represents variability due to the location of wells within the subsurface U plume, ignoring background areas, and can be thought of as the uncertainty due to sampling a large plume in only a few sites. The average concentrations and spatial standard deviations were calculated from wells 305, 655 and 654 data obtained in 2007 (DOE, 2009).

For the Monte Carlo simulations which include adsorption reactions, concentrations for $U(VI)_{Tot}$ are equal to $U(VI)_{lab}$ = 7.81 μM (from above) plus the soluble concentrations for each uncertainty level listed in Table 4. Uncertainties in the total U were assumed to be the same as in System I. Because the site concentrations are fixed by the model (for a given sediment composition and porosity), they were assumed to have zero uncertainty in the Monte Carlo simulations.

Standard deviations in the log formation constants are taken from the same source as the constants (Guillaumont et al., 2003; NIST, 2004) when available. When standard deviations were unavailable, including the log Ks of adsorption in Table 3, a value of 0.1 log units was assumed. This value is at the lower end of the range for metal–ligand formation constants, slightly larger than most well-studied systems (e.g., NIST, 2004) but smaller than the values estimated for more complex constants and less well-studied systems (Turner and Sassman, 1996).

Monte Carlo simulations were performed for six scenarios based on instrumental, temporal and spatial uncertainty, each with and without adsorption reactions. All simulations were performed with P = 10,000 trials because the resulting distributions are not significantly different with more trials (Cabaniss, 1997). All scenarios incorporate the given thermodynamic (log K) parameters and uncertainties listed in Table 2 and the critical parameter concentrations with uncertainties listed in Table 4.

3. Results

3.1. Speciation

In both System I and System II, dissolved U(VI) speciation is dominated by Ca-triscarbonato-uranyl species. The highest concentration species is $Ca_2(CO_3)_3UO_2^0$, ~80% of dissolved U(VI), while $Ca(CO_3)_3UO_2^{2-}$ accounts for most of the remaining 20% of the U(VI). Uranyl ion is only ~$10^{-15.4}$ M, not a significant fraction of the total U but is a key modeling parameter since U sorption,

precipitation and complexation constants are typically expressed in terms of this concentration.

In System II, most of the total U(VI) is adsorbed, but the fraction dissolved depends strongly on the total U(VI). At low total U(VI) (<3 μM), dissolved U accounts for less than 1% and as little 0.01% of the total (Fig. 2), while at total U(VI) above 4 μM the fraction dissolved is >10%. This dramatic change in the partitioning of U between sorbed and dissolved species is due to the 'titration' of strong adsorption sites (SSOH) with UO_2^{2+}, and has a significant effect on uncertainty propagation as shown below.

3.2. Uncertainty in System I

The two dominant Ca-triscarbonato-uranyl species were less sensitive (lower derivative values) to changes in input constraints than the free uranyl ion concentration, as expected from their much greater stability. Analytical input constraints with the largest effect on calculated U(VI) speciation are the system pH, DIC, and concentrations of total Ca(II), U(VI) and (to a lesser extent) SO_4^{2-} (Fig. 3). The first four of these all have a direct role in the formation of the ternary Ca-uranyl-triscarbonato species, while SO_4^{2-} affects the speciation less directly by complexing Ca(II). Based on this analysis, these five constraints were selected as critical parameters for the Monte Carlo simulations.

Distributions of calculated species concentrations for 10,000 Monte Carlo trials at all uncertainty levels are monomodal and approximately symmetrical, consistent with a Gaussian distribution of propagated uncertainty (Fig. 4). For each level of uncertainty, calculated standard deviations for the dominant species concentrations ($Ca_2UO_2(CO_3)_3^0$ and $CaUO_2(CO_3)_3^{2-}$ in Table 5) are similar to the input uncertainty for total U(VI) (from Table 4), indicating minimal amplification of uncertainty in the calculation. However, the standard deviation of the free uranyl ion concentration
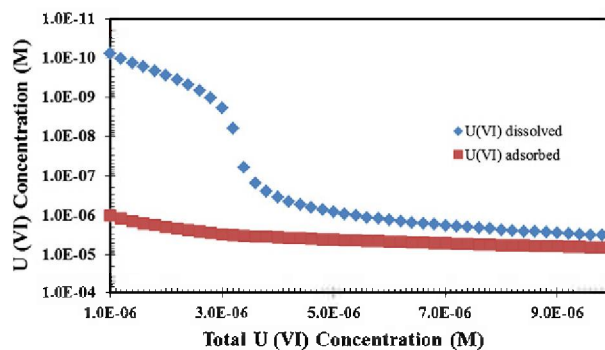

Fig. 2. Log concentrations of calculated adsorbed and dissolved U(VI) as a function of total U(VI) in the system. Note that although the concentration of adsorbed U is a smooth function of total U(VI), the concentration of dissolved U is not, showing a steep 'endpoint' corresponding to the concentration of the strongest adsorption sites (~3.3 μM).
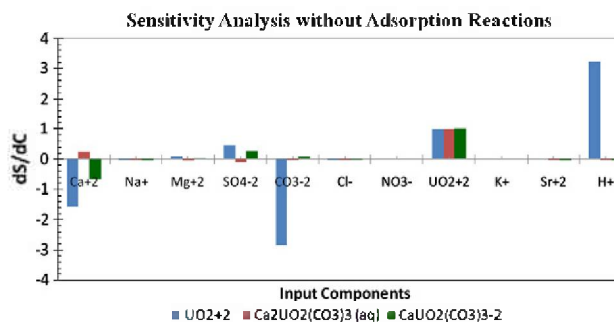
Fig. 3. Sensitivity (first derivative) analysis for effects of uncertainty on three key U(VI) species concentrations for 11 analytical constraints in a dissolved-only system. Note the major roles played by total Ca(II), total U(VI), DIC and pH.

$[UO_2^{2+}]$ is much higher. Extending the range of the total U(VI) to higher and lower values (0.1–2.0 μM total U(VI)) gives the same critical species, the same monomodal distributions and the same elevated amplification of uncertainty for uranyl ion concentration.

If the chief purpose of the calculation is to predict principal species concentrations, this system is robust. However, since the uranyl ion concentration is used in the calculation of adsorption and precipitation, the substantial amplification of uncertainty (the output uncertainty in log $[UO_2^{2+}]$ is more than double the log $U(VI)_{Tot}$ input uncertainty) may be problematic.

3.3. Uncertainty in System II

First derivative calculations using 8.65 μM total U(VI) are somewhat similar to System I with the addition of significant sensitivity to strong (SOH) and very strong (SSOH) surface site concentrations. The pH, DIC and total concentrations of Ca and U(VI) have the largest effects, although the magnitude of these derivatives is smaller than in System I (compare Figs. 3 and 5). One notable difference is the sensitivity of the Ca-triscarbonato-uranyl species concentrations to DIC and pH, which is much greater than in System I. The SOH and SSOH concentrations also have important effects, although the system is not very sensitive to WOH concentration.

Monte Carlo simulations of System II with 8.65 μM total U(VI) show Gaussian distributions of calculated concentrations at the
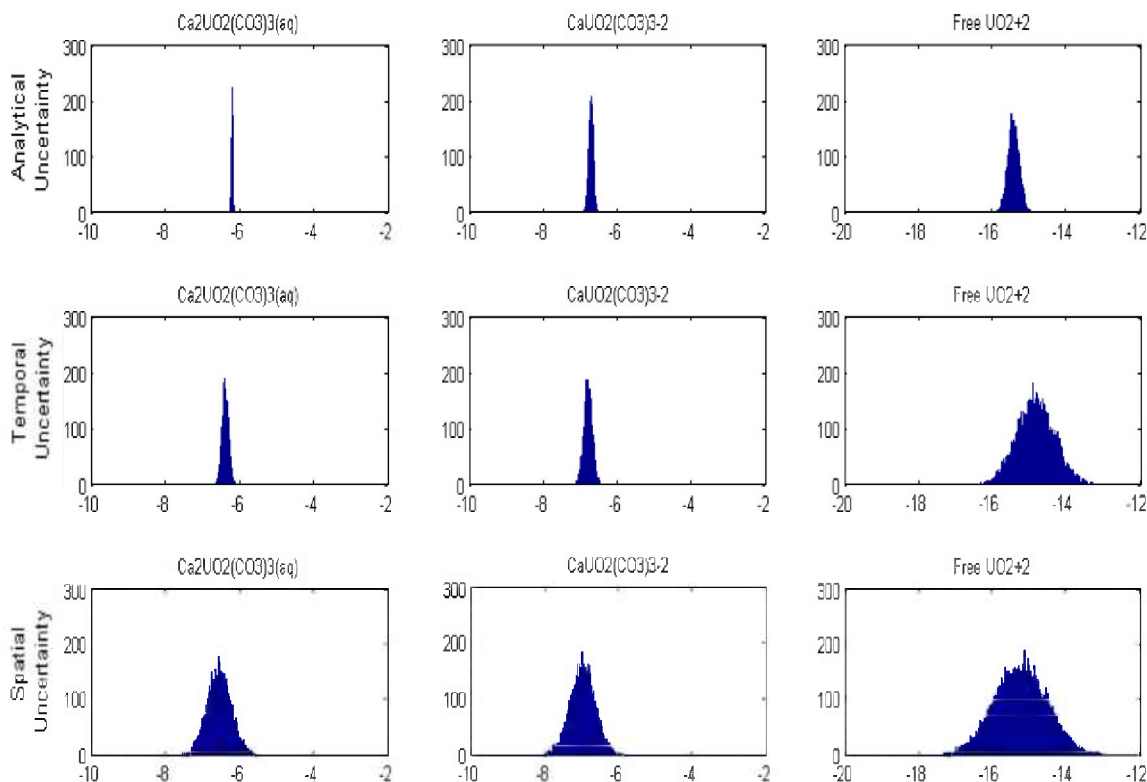

Fig. 4. Monte Carlo simulations of System I (dissolved-only), showing frequency of result versus log concentration. Top row is lowest uncertainty (analytical), bottom row is highest uncertainty (spatial). Plots normalized for consistent heights, not areas.

Table 5
Summary statistics of distributions in Fig. 4 (System I).

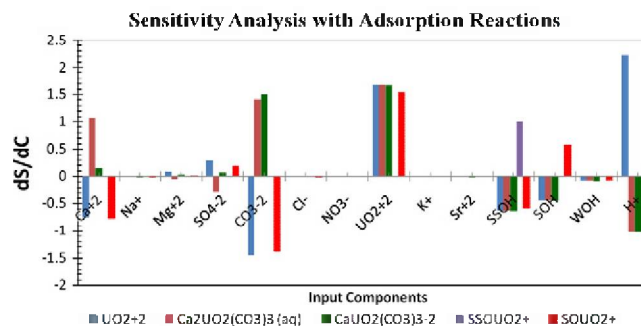| Species	Analytical uncertainty		Temporal uncertainty		Spatial uncertainty	
Error without adsorption reactions						
	Mean (log M)	Standard deviation (log M)	Mean (log M)	Standard deviation (log M)	Mean (log M)	Standard deviation (log M)
UO_2^{2+}	−15.4	0.152	−14.9	0.501	−15.3	0.723
$Ca_2UO_2(CO_3)_3$ (aq)	−6.20	0.020	−6.39	0.088	−6.55	0.328
$CaUO_2(CO_3)_3^{2-}$	−6.73	0.061	−6.80	0.113	−6.98	0.338

Fig. 5. Sensitivity (first derivative) analysis for effects of uncertainty on U(VI) species concentrations for 14 analytical constraints in dissolved-solid partitioning system. Note the major roles played by total Ca(II), total U(VI), DIC and pH and the relatively modest effect of total surface sites (SSOH and SOH) under these conditions of high total U(VI).

standard deviation in log concentration of calculated U(VI) species is 4 times the log standard deviation in U(VI)$_{Tot}$ (Table 6).

Unlike the System I simulations, varying total U(VI) concentration in calculations with adsorption has a pronounced effect on both the shape of the output distributions and the uncertainty amplification. At lower U(VI)$_{Tot}$ concentrations, output distributions of U(VI) are highly non-Gaussian and uncertainty amplification is larger. As an example, Fig. 7 presents distributions from System II simulations with U(VI)$_{Tot}$ = 3.50 μM, corresponding to an uncontaminated portion of the Old Rifle site. Output distributions are bi-modal for all but the lowest (instrumental) uncertainty levels in Table 4, and the uncertainties are significantly amplified for all dominant species except SSOUO$_2^+$ and for aquo UO$_2^{2+}$ (Table 7). Under these conditions of lower U(VI)$_{Tot}$ and higher uncertainty in analytical constraints, the equilibrium calculation cannot be considered robust.

The source of the asymmetrical, bimodal distributions and the concomitant amplification of uncertainty is the relationship between the total U(VI) concentration and the abundance of the strongest binding sites. Although the surface complexation model represents adsorbed U in a smooth fashion, the total dissolved U (sum of all dissolved species concentrations) has a steep slope near
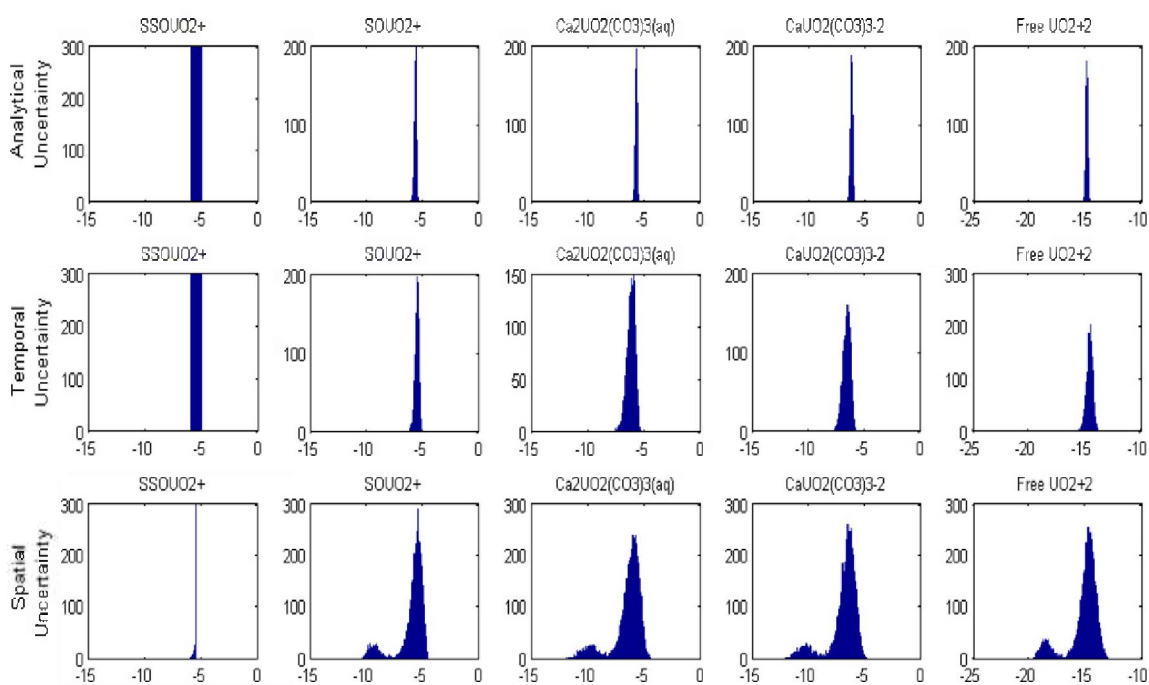
lower levels of uncertainty (analytical uncertainty and temporal variation). However, at the highest level of uncertainty represented by spatial conditions specified in Table 4, asymmetric bimodal distributions are apparent (Fig. 6). With high uncertainty inputs, the

Fig. 6. Monte Carlo simulations of System II (dissolved and adsorbed) with 8.65 μM total U(VI) showing frequency of result versus log concentration. Top row is lowest uncertainty (analytical), bottom row is highest uncertainty (spatial). Note the asymmetrical distributions at the highest uncertainty level and the consistency of the SSOUO$_2^+$ species. Plots normalized for consistent heights, not areas.

Table 6
Summary statistics of distributions in Fig. 6 (System II, 8.65 μM total U(VI)).

| Adsorption reaction statistics					
Species	Analytical uncertainty		Temporal uncertainty		Spatial uncertainty	
	Mean (log M)	Standard deviation (log M)	Mean (log M)	Standard deviation (log M)	Mean (log M)	Standard deviation (log M)
UO$_2^{2+}$	−14.9	0.091	−14.6	0.268	−15.2	1.33
Ca$_2$UO$_2$(CO$_3$)$_3$ (aq)	−5.72	0.085	−6.18	0.346	−6.52	1.35
CaUO$_2$(CO$_3$)$_3^{2-}$	−6.23	0.098	−6.59	0.325	−6.94	1.35
SSOUO$_2^+$	−5.48	0.000	−5.48	0.000	−5.50	0.066
SOUO$_2^+$	−5.68	0.091	−5.52	0.171	−6.01	1.26
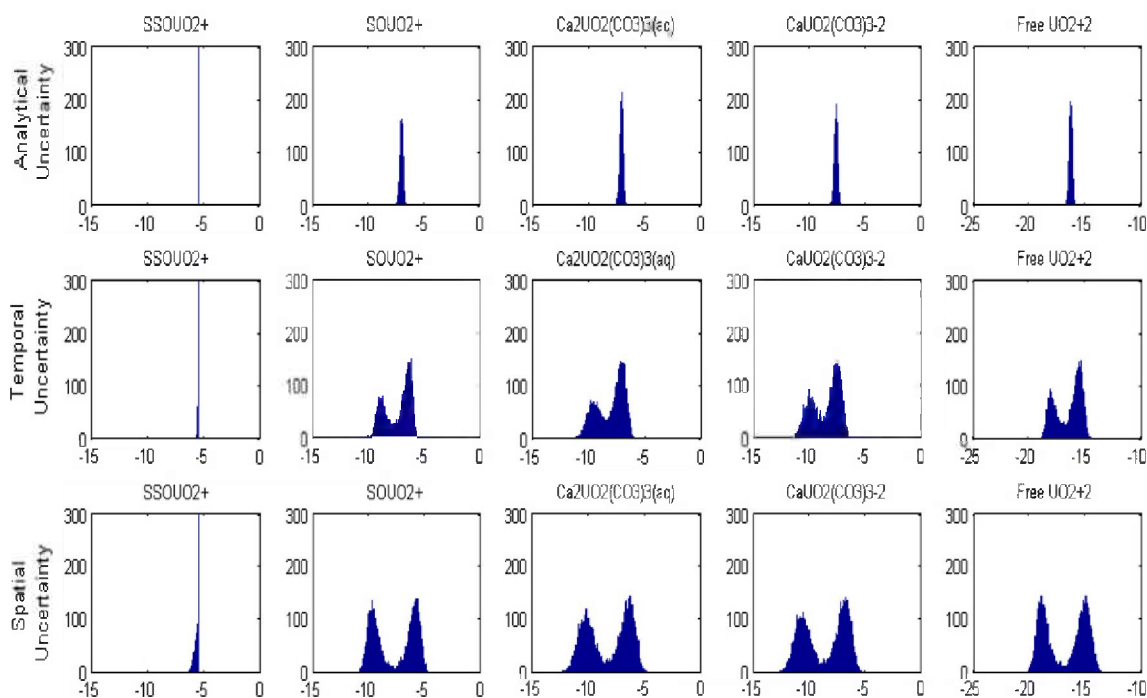
Fig. 7. Monte Carlo simulations of System II (dissolved and adsorbed) with 3.50 μM total U(VI) showing frequency of result versus log concentration. Top row is lowest uncertainty (analytical), bottom row is highest uncertainty (spatial). Note the pronounced bimodal distributions at the higher uncertainty levels. Plots normalized for consistent heights, not areas.

Table 7
Summary statistics of distributions in Fig. 7 (System II, 3.50 μM total U(VI)).

Species	Analytical uncertainty		Temporal uncertainty		Spatial uncertainty	
	Mean (log M)	Standard deviation (log M)	Mean (log M)	Standard deviation (log M)	Mean (log M)	Standard deviation (log M)
UO_2^{2+}	−16.4	0.134	−16.5	1.16	−16.9	1.89
$Ca_2UO_2(CO_3)_3$ (aq)	−7.12	0.138	−8.07	1.20	−8.23	1.92
$CaUO_2(CO_3)_3^{2-}$	−7.64	0.146	−8.48	1.20	−8.66	1.92
$SSOUO_2^+$	−5.49	0.000	−5.50	0.04	−5.60	0.18
$SOUO_2^+$	−7.05	0.136	−7.38	1.15	−7.67	1.86

3.3 μM total U(VI) concentration, corresponding to the concentration of the strongest binding sites (Fig. 2).

4. Conclusions and recommendations

Uncertainty propagation is straightforward in calculations of dissolved speciation only, but more problematic when adsorption is considered. In the former case, and at low levels of uncertainty and high total U(VI), calculated species concentrations have Gaussian output distributions and modest uncertainty amplification. In systems including adsorption reactions with higher levels of uncertainty and/or lower total U(VI), distributions of calculated concentrations are often bimodal and amplification of uncertainty is significant. These behaviors are related to a steep slope or 'endpoint' behavior in dissolved U(VI) due to the filling of all the strong adsorption sites. Since the bimodal distributions represent system instability with respect to uncertain inputs, the adsorption model may be unreliable when used under these conditions. Users should avoid predicting solid-dissolved partitioning of U(VI) based upon this sorption model at lower total U concentrations (<4 μM) and levels of uncertainty corresponding to spatial and temporal variability of the system. On the other hand, predictions of U(VI) speciation in the contaminant 'plume' appear to be robust, as are dissolved-phase calculations at all U levels.

References

Abdelouas, A., Lutze, W., Nuttall, E., 1998. Chemical reactions of uranium in ground water at a mill tailings site. J. Contam. Hydrol. 34, 343–361.
Barnett, M.O., Jardine, P.M., Brooks, S.C., Selim, H.M., 2000. Adsorption and transport of uranium(VI) in subsurface media. Soil Sci. Soc. Am. J. 64, 908–917.
Bernhard, G., Geipel, G., Brendler, V., Nitsche, H., 1996. Speciation of uranium in seepage waters of a mine tailing pile studied by time-resolved laser-induced fluorescence spectroscopy (TRLFS). Radiochim. Acta 74, 87–91.
Bernhard, G., Geipel, G., Brendler, V., Nitsche, H., 1998. Uranium speciation in waters of different uranium mining areas. J. Alloys Compd. 271, 201–205.

Bernhard, G., Geipel, G., Reich, T., Brendler, V., Amayri, S., Nitsche, H., 2001. Uranyl(VI) carbonate complex formation: validation of the $Ca_2UO_2(CO_3)_3$ (aq.) species. Radiochim. Acta 89, 511–518.

Cabaniss, S.E., 1997. Propagation of uncertainty in aqueous equilibrium calculations: non-Gaussian output distributions. Anal. Chem. 69, 3658–3664.

Cabaniss, S.E., 1999. Uncertainty propagation in geochemical calculations: non-linearity in solubility equilibria. Appl. Geochem. 14, 255–262.

Cabaniss, S.E., 2009. Titrator-Delphi. <code.google.com/p/titrator-delphi> (accessed November 2009).

Criscenti, L.J., Laniak, G.F., Erickson, R.L., 1996. Propagation of uncertainty through geochemical code calculations. Geochim. Cosmochim. Acta 69, 3551–3568.

Davis, J.A., Curtis, G.P., 2003. Application of Surface Complexation Modeling to Describe Uranium (VI) Adsorption and Retardation at the Uranium Mill Tailings Site at Naturita, Colorado. NUREG/CR-6820.

Davis, J.A., Payne, T.E., Waite, T.D., 2002. Geochemisty of soil radionuclides. Soil Sci. Soc. Am., Madison, WI, 61–86.

Denison, F.H., Garnier-LaPlace, J., 2005. The effects of database parameter uncertainty on uranium(VI) equilibrium calculations. Geochim. Cosmochim. Acta 69, 2183–2191.

DOE (Department of Energy), 2009. Geospatial Environmental Mapping System: Rifle Old, CO, Processing Site. gems.lm.doe.gov/imf/imf.jsp?site=rifleoldprocessing&title=Rifle Old, CO, Processing Site (accessed April 2009).

Dong, W.M., Brooks, S.C., 2006. Determination of the formation constants of ternary complexes of uranyl and carbonate with alkaline earth metals (Mg^{2+}, Ca^{2+}, Sr^{2+}, and Ba^{2+}) using anion exchange method. Environ. Sci. Technol. 40, 4689–4695.

Fang, Y.L., Yabusaki, S.B., Morrison, S.J., Amonette, J.P., Long, P.E., 2009. Multicomponent reactive transport modeling of uranium bioremediation field experiments. Geochim. Cosmochim. Acta 73, 6029–6051.

Fox, P.M., Davis, J.A., Zachara, J.M., 2006. The effect of calcium on aqueous uranium(VI) speciation and adsorption to ferrihydrite and quartz. Geochim. Cosmochim. Acta 70, 1379–1387.

Guillaumont, R., Fanghanel, T., Neck, V., Fuger, J., Palmer, D.A., Grenthe, I., Rand, M.H., 2003. Chemical thermodynamics 5, Update on the Chemical Thermodynamics of Uranium, Neptunium, Plutonium, Americium and Technetium. Elsevier, Amsterdam.

Gustafsson, J.P., 2009. Visual MINTEQ. <www.lwr.kth.se/English/OurSoftware/vminteq/index.html> (accessed June 2009).

Harris, D.C., 2007. Quantitative Chemical Analysis, seventh ed. WH Freeman, New York.

Kalmykov, S.N., Choppin, G.R., 2000. Mixed $Ca^{2+}/UO_2^{2+}/CO_3^{2-}$ complex formation at different ionic strengths. Radiochim. Acta 88, 603–606.

Kohler, M., Curtis, G.P., Meece, D.E., Davis, J.A., 2004. Methods for estimating adsorbed uranium(VI) and distribution coefficients of contaminated sediments. Environ. Sci. Technol. 38, 240–247.

Meinrath, G., Lis, S., Piskula, Z., Glatty, Z., 2006. An application of the total measurement uncertainty budget concept to the thermodynamic data of uranyl(VI) complexation by sulfate. J. Chem. Thermodyn. 38, 1274–1284.

NIST, 2004. Critically Selected Stability Constant of Metal Complex Database, ver. 8.0. US Department of Commerce, Gaithersburg, MD.

Nitzsche, O., Meinrath, G., Merkel, B., 2000. Database uncertainty as a limiting factor in reactive transport prognosis. J. Contam. Hydrol. 44, 223–237.

Serkiz, S.M., Allison, J.D., Perdue, E.M., Allen, H.E., Brown, D.S., 1996. Correcting errors in the thermodynamic database for the equilibrium speciation model MINTEQA2. Water Res. 30, 1930–1933.

Stumm, W., Morgan, J.J., 1996. Aquatic Chemistry, third ed. John Wiley and Sons, Inc., New York, NY.

Turner, D.R., Sassman, S.A., 1996. Approaches to sorption modeling for high-level waste performance assessment. J. Contam. Hydrol. 21, 311–332.

Unsworth, E.R., Jones, P., Hill, S.J., 2002. The effect of thermodynamic data on computer model predictions of uranium speciation in natural water systems. J. Environ. Monitor. 4, 528–532.

USEPA, 2000. National primary drinking water regulations. Radionuclides final rule. <http://www.federalregister.gov/articles/2000/12/07/00-30421/national-primary-drinking-water-regulations-radionuclides-final-rule>.

Weber, C.L., Vanbriesen, J.M., Small, M.S., 2006. A stochastic regression approach to analyzing thermodynamic uncertainty in chemical speciation modeling. Environ. Sci. Technol. 40, 3872–3878.

WHO, 2003. Uranium in Drinking-Water. Background Document for Preparation of WHO Guidelines for Drinking-Water Quality. World Health Organization, Geneva (WHO/SDE/WSH/03.04/118).

Yabusaki, S.B., Fang, Y., Long, P.E., Resch, C.T., Peacock, A.D., Komlos, J., Jaffe, P.R., Morrison, S.J., Dayvault, R.D., White, D.C., Anderson, R.T., 2007. Uranium removal from groundwater via in situ biostimulation: field-scale modeling of transport and biological processes. J. Contam. Hydrol. 93, 216–235.

Contaminant discharge and uncertainty estimates from passive flux meter measurements

Harald Klammler,[1,2,3] Kirk Hatfield,[2,3] Joana Angélica Guimarães da Luz,[1]
Michael D. Annable,[3,4] Mark Newman,[2,3] Jaehyun Cho,[3,4] Aaron Peacock,[5]
Valerie Stucker,[6] James Ranville,[6] Steven A. Cabaniss,[7] and P. S. C. Rao[8]

[1] The passive flux meter (PFM) measures local cumulative water and contaminant fluxes at an observation well. Conditional stochastic simulation accounting for both spatial correlation and data skewness is introduced to interpret passive flux meter observations in terms of probability distributions of discharges across control planes (transects) of wells. An estimator of the effective number of independent data is defined and applied in the development of two significantly simpler approximate methods for estimating discharge distributions. One method uses a transformation of the t statistic to account for data skewness and the other method is closely related to the classic bootstrap. The approaches are demonstrated with passive flux meter data from two field sites (a trichloroethylene [TCE] plume at Ft. Lewis, WA, and a uranium plume at Rifle, CO). All methods require that the flux heterogeneity is sufficiently represented by the data and maximum differences in discharge quantile estimates between methods are ~7%.

1. Introduction

[2] Subsurface contaminants are a well-known threat to groundwater at source locations and as contaminant plumes that may emerge. Identification, monitoring, risk assessment (including transport modeling), and the design of remediation strategies are fundamental engineering tasks related to this problem. Over the past decades these tasks and have received significant research efforts from the theoretical to the field level [*U.S. Environmental Protection Agency (EPA)*, 1998, 2004; *Einarson and Mackay*, 2001; *Rao et al.*, 2002; *Stroo et al.*, 2003]. Historically, estimates of contaminant source mass remaining and/or contaminant concentration in a plume have been used to characterize contaminated sites. However, more recently, contaminant mass discharge from a source zone at a given control plane (transect) has been recognized as more useful, since it

directly quantifies the contaminant mass released from a source per unit time, which may impact a potential receptor [*Einarson and Mackay*, 2001; *Interstate Technology and Regulatory Council (ITRC)*, 2010].

[3] Current field measurements supporting estimation of contaminant mass discharge employ one of three basic approaches: integral pump tests (IPT) [*Teutsch et al.*, 2000; *Bockelmann et al.*, 2001, 2003], multilevel sampling (MLS) [*Borden et al.*, 1997; *Einarson and Mackay*, 2001], and passive flux meter measurements (PFM) [*Hatfield et al.*, 2004; *Annable et al.*, 2005]. IPT uses inverse modeling on monitored contaminant concentrations at one or more pumping wells. This approach has the advantage of interrogating a large and continuous portion of the aquifer; however, it requires prior knowledge (or separate measurement/assumption) of certain aquifer properties. In addition, significant alterations of groundwater flow and contaminant transport regimes are induced, such that contaminated groundwater is often extracted for surface disposal. MLS uses separate measurements of local contaminant concentrations, hydraulic conductivities, and the hydraulic gradient at a control plane. Estimates of contaminant mass discharges require spatial interpolation of concentrations and conductivities as well as assumptions about the hydraulic gradient for the calculation and summation of local mass fluxes. While these are potential sources of uncertainty, less hydrogeological knowledge or assumptions are required than for IPT and the natural flow field remains practically undisturbed. The PFM provide direct measurements of local cumulative (i.e., time integrated or averaged) contaminant mass fluxes as depth profiles along monitoring wells, without necessarily requiring hydraulic conductivity and gradient data. Besides inherent measurement errors in

---
[1]Department of Environmental Sciences and Sustainable Development, Federal University of Bahia, Barreiras, Bahia, Brazil.

[2]Department of Civil and Coastal Engineering, University of Florida, Gainesville, Florida, USA.

[3]Inter-Disciplinary Program in Hydrologic Sciences, University of Florida, Gainesville, Florida, USA.

[4]Department of Environmental Engineering Sciences, University of Florida, Gainesville, Florida, USA.

[5]Microbial Insights, Inc., Rockford, Tennessee, USA.

[6]Department of Chemistry and Geochemistry, Colorado School of Mines, Golden, Colorado, USA.

[7]Department of Chemistry and Chemical Biology, University of New Mexico, Albuquerque, New Mexico, USA.

[8]Department of Civil Engineering, Purdue University, West Lafayette, Indiana, USA.

local fluxes, spatial interpolation of fluxes over unsampled portions of a transect is the main source of uncertainty in PFM-based mass discharges estimates.

[4] None of the above approaches are capable of delivering error-free estimates of mass discharges. As a result, *Jarsjö et al.* [2005] perform uncertainty analysis for an IPT, while *Li et al.* [2007], *Schwede and Cirpka* [2010], *Troldborg et al.* [2010], and *Cai et al.* [2011] use geostatistical conditional stochastic simulation approaches for quantification of uncertainty in mass discharge estimates from MLS measurements. To reduce estimation uncertainty, *Li and Abriola* [2009] present a multistage and multicriteria strategy for multilevel sampling. Comparative theoretical and field studies of different methods are available by *Kübert and Finkel* [2006], *Herold et al.* [2008], *Goltz et al.* [2009], and *Belland-Pelletier et al.* [2011]. Taken together, these studies recommend pump test methods in highly heterogeneous settings where "point" sample methods suffer from large interpolation uncertainties, and identify PFM measurements as less error prone than MLS methods. The latter is related to the fact that PFMs directly measure local mass fluxes along continuous vertical sampling lines rather than concentrations (to be multiplied by collocated and simultaneously measured or estimated water fluxes) at a finite number of MLS points.

[5] The objective of the present study is to investigate methods for estimating probability distributions of water and contaminant mass discharges from PFM measurements. If the empirical distribution of the sampled PFM fluxes is representative of the transect (i.e., if it accurately indicates the frequency of occurrence of each sampled and unsampled flux value in the transect), then the arithmetic sample mean gives an unbiased estimate of the spatial mean of all fluxes in the transect. In the presence of irregular sampling patterns, this representativeness can be achieved by application of a declustering technique [*Goovaerts*, 1997], which assigns smaller weights to more closely spaced data ("clusters") and larger weights to more largely spaced data; hence, the name "declustering." Classical and bootstrap statistics provide tools for quantifying uncertainty about mean estimates of sample data; however, the inherent assumption of independent and identically distributed (i.i.d.) data is commonly violated by the presence of spatial correlation [*Journel*, 1994] between observed fluxes.

[6] In contrast, the principles of kriging are founded on correlated random variables. However, the definition of probability distributions for estimation errors requires either the assumption of mulitvariate Gaussianity [*Goovaerts*, 1997] or data transformations, e.g., indicator kriging or as in the work of *Kitanidis and Shen* [1996]. The typically large ranges of variability (e.g., coefficients of variation near or above one) of contaminant mass fluxes, in combination with the physical requirement of non-negativity, lead to strong deviations from Gaussianity characterized by positive skewnesses. Data transformations required to obtain Gaussian distributions are necessarily nonlinear leading to biased estimates of mean transect fluxes when back-transformed after averaging. Methods to determine probability distributions of mean transect fluxes in the presence of irregular sampling patterns, spatial correlation, and non-Gaussianity are limited. Geostatistics offers the conditional

stochastic simulation approaches cited above as well as a method using resampling from conditional stochastic simulation [*Journel*, 1994]. Moreover, *Zhu and Morgan* [2004] and *Chen and Shao* [1999] apply the block bootstrap method for inference of distributions of spatial means in the case of data correlation. However, no explicit guidelines for the choice of bootstrap block size and shape in dependence of sample number, pattern (especially irregular and sparse patterns), and correlation structure are presently available, neither may the actual shape and size of the transect be accounted for.

[7] Here we present and demonstrate a conditional stochastic simulation approach and two simpler approximate methods for determining probability distributions of contaminant mass discharges from PFM field data. Section 2 focuses on stochastic simulation: section 2.1 uses the unconditional stochastic simulation paradigm to introduce the concepts of randomization and ordinary block kriging as well as fundamental assumptions and the required variables. This includes the derivation of a so-called "weighted data dispersion variance." Section 2.2 is a step-by-step outline of the conditional simulation approach taken in the case studies and emphasizes guidelines for reliable variogram inference as well as for the validation of results. A parameter termed "missing variance" $\Delta\sigma^2$ [-] is proposed to quantify the representativeness of PFM flux data with respect to local flux heterogeneity over a transect. Section 3 is dedicated to the introduction and discussion of an "effective number of independent data" n_e [-], which forms the basis for the development of the two approximate methods in section 4. These approximate methods avoid performing stochastic simulation and may represent more practical tools for field engineers. Field data from a TCE plume at Ft. Lewis, WA, and from a uranium plume at Rifle, CO, are used in section 5 for demonstration and a discussion of the results including a validation of the approximate methods against conditional stochastic simulation. Also, an example of how to quantify expected benefits in terms of uncertainty reduction due to additional PFM sampling is presented. Finally, section 6 contains an evaluation of the assumptions initially taken based on the case study results.

2. Stochastic Simulation Approach

2.1. Fundamental Concepts, Assumptions, and Variables

[8] Without actually generating any realizations, we use the unconditional stochastic simulation (Monte Carlo) paradigm in section 2.1 to review the concepts of randomization and ordinary block kriging as well as to define the fundamental assumptions and variables required. An example of a geometrical setup of the problem at hand is illustrated in Figure 1. The goal is to estimate the probability distribution of mass discharge Q [M/T] across a rectangular transect T containing n [-] local ("quasi-point") PFM measurements $q_{i\mathrm{PFM}}$ ($i = 1, 2, \ldots, n$) [M/(L^{2}T)] of mass fluxes along observations wells. Hereby, it is assumed that $q_{i\mathrm{PFM}}$ are error-free. Unconditional stochastic simulation can deliver realizations $q(\boldsymbol{u})$ of a random function (or stochastic process) representing possible spatial distributions of local fluxes q at locations described by coordinate vector $\boldsymbol{u}$ inside a transect. The unconditional realizations are
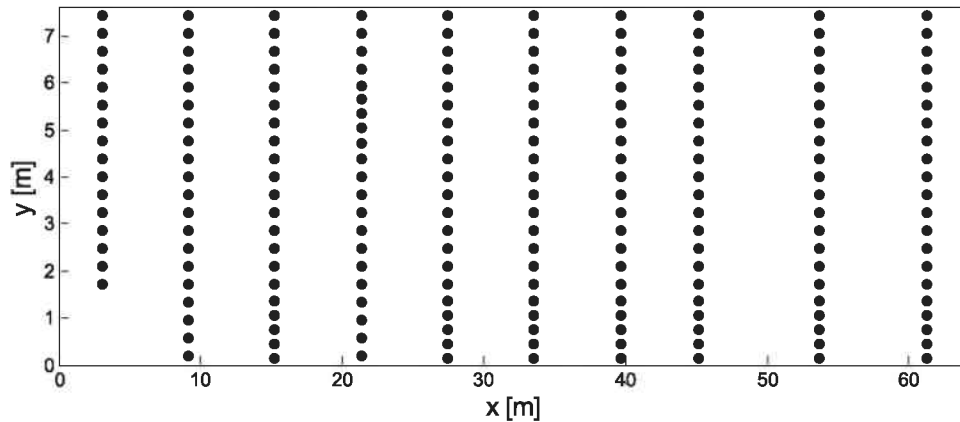
Figure 1. PFM sampling locations over transect at Ft. Lewis, WA.

interpreted as (partially) unknown scenarios of the real world with an equal likelihood of occurrence, where one single realization is assumed to perfectly match the real-world situation. The problem is that this single realization may not be identified and the outcomes of different realizations are used to make probabilistic statements about the unknown real-world situation. The constraints typically imposed in unconditional stochastic simulation are those of a given point or univariate distribution pdf(q) and a particular spatial correlation structure (variogram $\gamma[h]$ or covariance function $C[h]$, where h is a spatial separation vector). Up to second order, pdf(q) is defined by its mean μ_0 and variance $\sigma_0^2 = C(0)$, where the random function q is called second order stationary, if μ_0 and $C(h)$ are location independent. Not considered in the present work are deterministic trend functions that may be combined with random function $q(u)$; nor do we consider uncertainties in the type and parameters of $C(h)$. For the remainder of section 2.1 $C(h)$ does not have to be specified, while it is inferred from sample data $q_{i\text{PFM}}$ for each practical example presented below. In cases where the spatial variance in q increases continuously with the size of the domain investigated, such that process variance σ_0^2 and, hence, covariance function $C(h)$ are not defined, the variogram $\gamma(h)$ and the intrinsic hypothesis (i.e., stationarity of the increments [*Journel and Huijbregts*, 1978]) may still be used in what follows.

[9] Each unconditional realization may be fictitiously sampled for fluxes q_i [M/(L^{2}T)] at the n locations of actual PFM field measurements $q_{i\text{PFM}}$ and a discharge may be estimated. Similarly, a respective true discharge Q across the transect may be computed for each unconditional realization resulting in a specific estimation error (i.e., estimated minus true value) per realization. Over many unconditional realizations the estimation errors form a distribution, which may be used as a performance (uncertainty) metric of the discharge estimate adopted. In what follows, rather than working with discharge Q over transect T of known size A [L^2], the mean transect flux $q_T = Q/A$ [M/(L^{2}T)] over T will be used as the magnitude to be estimated. Thus, for each unconditional realization, a value of q_T may be computed by

$$q_T = \frac{1}{A} \int_T q(u)du, \tag{1}$$

which follows a probability distribution of variance $\sigma_{q_T}^2$ given by [*Journel and Huijbregts*, 1978]

$$\sigma_{q_T}^2 = \frac{1}{A^2} \int_T \int_T C(u - v)du\,dv, \tag{2}$$

where v is a coordinate vector analogous to u. Note that equation (2) is nothing but the average value of $C(h)$ over all possible pairs of locations within T. In the same way as for q_T, the fictitiously sampled fluxes q_i of each unconditional realization are used to compute estimates $\bar{q}$ of q_T through the linear operator

$$\bar{q} = \sum_{i=1}^{n} \lambda_i q_i, \tag{3}$$

where in the present work λ_i are taken to be the ordinary block kriging weights [*Journel and Huijbregts*, 1978; *Goovaerts*, 1997; *Kitanidis*, 1997]. Moreover, the ensemble variance $\sigma_{\bar{q}}^2$ of $\bar{q}$ is known to be

$$\sigma_{\bar{q}}^2 = \sum_{i=1}^{n} \sum_{j=1}^{n} \lambda_i \lambda_j C(u_i - u_j), \tag{4}$$

which, in analogy to equation (2), is nothing but the weighted average of $C(h)$ over all possible pairs of sampling locations u_i and u_j. Finally, the covariance $\sigma_{\bar{q}q_T}^2$ between q_T and $\bar{q}$ results as

$$\sigma_{\bar{q}q_T}^2 = \frac{1}{A} \sum_{i=1}^{n} \lambda_i \int_T C(u_i - v)dv, \tag{5}$$

which represents the weighted average of $C(h)$ over all possible combinations of one sampling location u_i and a location v in T. With this, over many unconditional realizations, the random estimation error $e = \bar{q} - q_T$ possesses an ensemble mean value of zero (unbiasedness) and an ensemble variance σ_e^2 of

$$\sigma_e^2 = \sigma_{\bar{q}}^2 + \sigma_{q_T}^2 - 2\sigma_{\bar{q}q_T}^2, \tag{6}$$

which is obtained as the variance of the difference of two correlated random variables q_T and $\bar{q}$. Using ordinary block

kriging weights in equation (3) assures that σ_e^2 is a minimum under the constraint that $\sum_{i=1}^{n} \lambda_i = 1$. The denomination "ordinary kriging" (versus "simple kriging," for example) refers to the fact that $\sum_{i=1}^{n} \lambda_i = 1$ is used to impose unbiasedness, such that the mean μ_0 of pdf(q) of the stochastic process does not appear in the estimator (equation (3)). In turn, "block kriging" (versus "point kriging," for example) indicates that the estimated variable q_T is defined as a spatial average over a domain T ("block" in traditional mining language) rather than at a single point.

[10] In addition to evaluating the estimator in equation (3) for each unconditional realization, one may also compute a respective spatial variance s^2 of the weighted histogram of the (fictitiously) measured local fluxes q_i in each realization. Hereby, λ_i are to be interpreted as declustering weights [*Journel and Huijbregts*, 1978; *Goovaerts*, 1997] used to estimate the frequency or probability of occurrence of each value q_i over the transect (rather than over the sampling locations), such that

$$s^2 = \sum_{i=1}^{n} \lambda_i (q_i - \bar{q})^2. \qquad (7)$$

[11] The mean of s^2 over many unconditional realizations is called the "weighted data dispersion variance" $\sigma_{D\lambda}^2$ equal to

$$\sigma_{D\lambda}^2 = \sigma_0^2 - \sigma_{\bar{q}}^2, \qquad (8)$$

as derived in the appendix and with $\sigma_{\bar{q}}^2$ from equation (4). For generating unconditional realizations it is important that $\sigma_{D\lambda}^2$ be close to σ_0^2, such that the variability of the underlying process is well represented by the data. In the same way, an unweighted dispersion variance of local fluxes over the transect may be defined as [*Journel and Huijbregts*, 1978]

$$\sigma_{DT}^2 = \sigma_0^2 - \sigma_{q_T}^2, \qquad (9)$$

with $\sigma_{q_T}^2$ from equation (2). Thus, σ_{DT}^2 is the mean variance of local fluxes (i.e., dispersion) inside transect T taken over many unconditional realizations. Note that the difference between equations (2) and (9) is that $\sigma_{q_T}^2$ is the ensemble (i.e., over many realizations) variance of a spatial mean, while σ_{DT}^2 is the ensemble mean of a spatial variance; the sum of both is equal to σ_0^2. Analogous observations apply to $\sigma_{\bar{q}}^2$ and $\sigma_{D\lambda}^2$. Equations (6), (8), and (9) exist under the intrinsic hypothesis and respective expressions in terms of the variogram are obtained by simply substituting $-\gamma(\boldsymbol{h})$ for $C(\boldsymbol{h})$ and, consequently, zero for σ_0^2 [*Journel and Huijbregts*, 1978].

2.2. Conditional Simulation for Discharge Estimation

[12] As mentioned in the introduction (section 1), different conditional simulation approaches have recently been applied for contaminant discharge estimation. Conditional simulation differs from unconditional simulation in that all conditional realizations honor (reproduce) the measured data values at their locations. Moreover, for the conditional simulation near PFM sampling locations it is sufficient that $\sigma_{D\lambda}^2$ is close to σ_{DT}^2 (equations (8) and (9)). This is a less restrictive condition than for unconditional simulation, since $\sigma_{DT}^2 < \sigma_0^2$ (spatial data dispersion grows with domain size), and a dimensionless parameter $\Delta\sigma^2$ termed "missing variance" is defined here as

$$\Delta\sigma^2 = \frac{\sigma_{DT}^2 - \sigma_{D\lambda}^2}{\sigma_{DT}^2}. \qquad (10)$$

[13] This magnitude quantifies the relative portion of variability contained in the domain of interest T, which is not actually described by the available data after declustering. A graphical illustration of all steps involved in the conditional simulation approach is given in Figure 2 with further descriptions given here:

2.2.1. Variogram Analysis of Raw Data q_{iPFM} (Step A)

[14] Figure 1 shows an example of a rectangular transect with monitoring wells and PFM flux measurement intervals (typically $\sim$30 cm in length), indicated by dots at the center of each interval. For each dot, spatial coordinates and an observed value of q_{iPFM} are available for the generation of an experimental variogram and structural analysis [*Journel and Huijbregts*, 1978] to obtain a first estimate of the spatial covariance function $C(\boldsymbol{h})$. The experimental variogram points for shorter lag distances $|\boldsymbol{h}|$ are typically better defined (based on more data pairs) and contain more important information for spatial interpolation (simulation). As a consequence, a good variogram fit near the origin is considered more valuable than at larger lag distances [*Kitanidis*, 1997].

2.2.2. Data Declustering Using Ordinary Block Kriging Weights (Step B)

[15] In the present work, the transect is identical to the simulation domain and it is roughly defined as extending one half-well separation distance beyond the lateral-most wells in the horizontal direction and from the bottom of the bottom-most to the top of the top-most PFM sampling interval. To achieve a representative flux distribution over the transect from irregularly spaced data, declustering is required. In the present work, the ordinary block kriging weights λ_i from equation (3) are used for this purpose [*Journel and Huijbregts*, 1978] as they accommodate the spatial arrangement of the sampling locations, the spatial correlation structure, as well as the position and size of the transect. The declustered data histogram is denoted by pdf$_\lambda(q_{iPFM})$ to indicate that the declustered frequency of occurrence of local flux q_{iPFM} is equal to λ_i rather than $1/n$.

2.2.3. Conversion to Gaussianity Through Normal Score Transformation (Step C)

[16] Because of typically skewed data distributions, this step is required in order to take advantage of the properties of Gaussianity and to allow for using a relatively simple algorithm for the generation of Gaussian realizations. Theoretically, Gaussianity has to be achieved for the joint distribution of the random function at all locations (multi-Gaussianity), however, as a consequence of generally
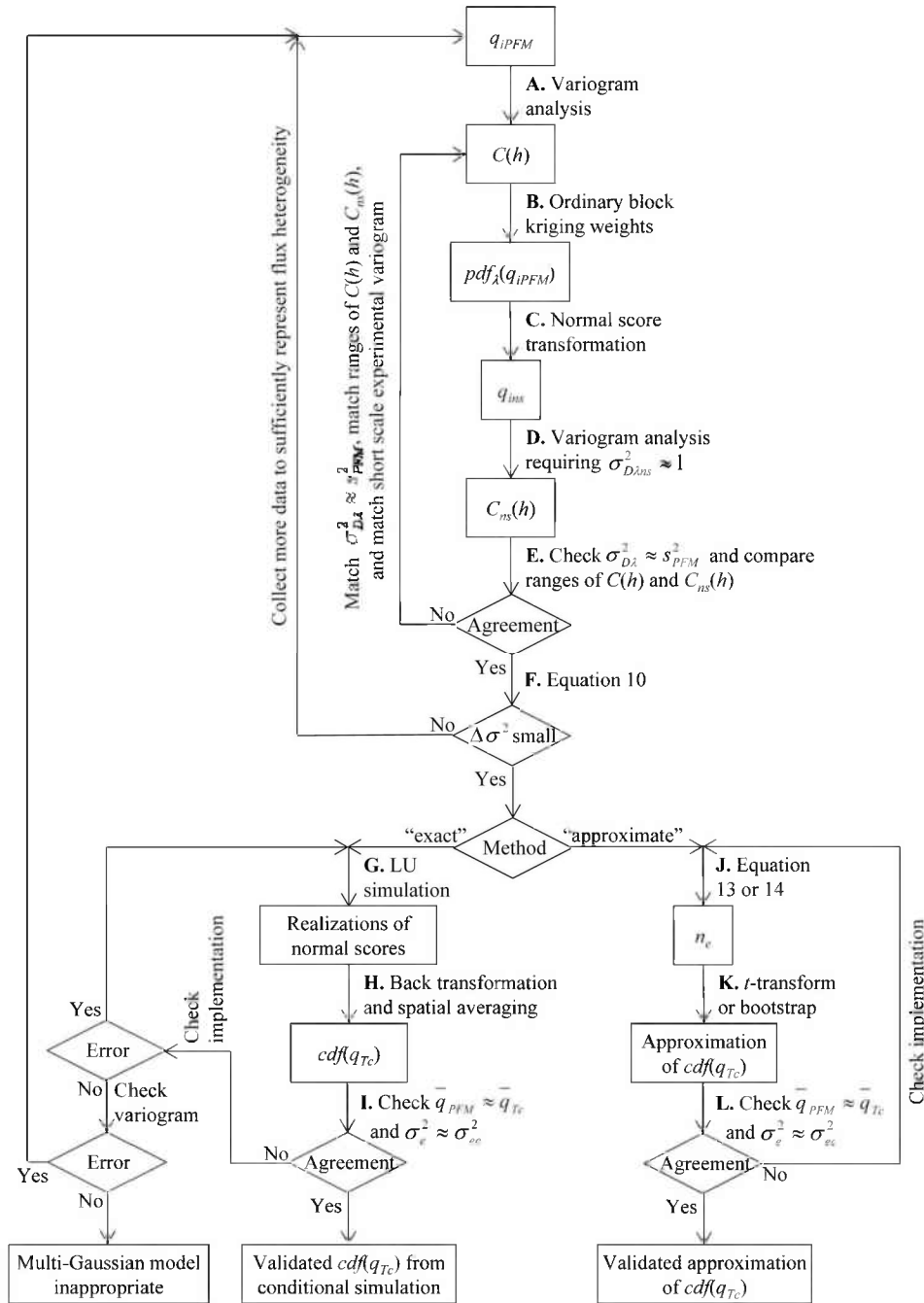
Figure 2. Flowchart for conditional simulation approach (section 2.2) and approximate methods (section 4).

limited amounts of data for verification, we limit our attention to univariate Gaussianity (i.e., the transformation of $pdf_\lambda[q_{iPFM}]$ to a normal distribution). The present work uses normal score transformation [*Goovaerts*, 1997], which is a numerical technique using a piecewise linear transformation function to achieve Gaussianity. In other words, the declustered data histogram is converted to a standard normally distributed histogram (zero mean and unit variance) by simply mapping respective quantiles onto each other. This is, if all measured fluxes q_{iPFM} are arranged in ascending order, then flux q_{jPFM} corresponds to a weighted cumulative distribution

function value $\mathrm{cdf}_\lambda(q_{jPFM}) \approx \frac{\lambda_j}{2} + \sum_{i=1}^{j-1} \lambda_i$ [*Goovaerts*, 1997], and the respective quantile of the normal distribution yields the normal score transform q_{ins} of q_{iPFM}. Thus, a correspondence table between q_{iPFM} and q_{ins} is constructed.

2.2.4. Variogram Analysis of Normal Score Data q_{ins} (Step D)

[17] In the same way as under step A, variogram analysis is performed on q_{ins} to fit a respective covariance function $C_{ns}(h)$. Because step C converts the declustered data into

a standard normal distribution of unit variance, $C_{ns}(h)$ is fitted, such that the declustered normal score dispersion variance $\sigma^2_{D\lambda ns}$, obtained from equations (4) and (8) with $C_{ns}(h)$ instead of $C(h)$, is ~ 1. This helps in assuring that $C_{ns}(h)$ is compatible with the conditioning data and that the simulated normal scores over the transect are close to standard normally distributed. The latter is required, such that pdf$_\lambda(q_{iPFM})$, which was particularly determined for the transect, is reproduced by the conditional simulation output after back-transformation in step H.

2.2.5. Joint Variogram Analysis of Raw Data and Normal Scores With Adjustment of $C(h)$ to Meet Weighted Data Dispersion Variance (Step E)

[18] Distributions of contaminant fluxes are typically positively skewed with many small data values and few very large ones. It is well known (and because of the squaring of flux differences involved) that the experimental variogram of the raw data is quite sensitive to large values, which may complicate a reliable fitting of $C(h)$ through step A. More robust measures of dispersion (avoiding squaring) or variogram analysis on transformed data (avoiding large values, but preserving ranks) do not affect the spatial correlation features along the lag distance axis [*Deutsch and Journel*, 1992], and may thus be used to assist with inferring spatial correlation lengths. This also applies to normal score data [*Chiles and Delfiner*, 1999] as obtained from step C and as such, we perform a joint modeling of $C(h)$ and $C_{ns}(h)$ to assure that they have the same correlation lengths. Moreover, given the declustered PFM flux histogram pdf$_\lambda(q_{iPFM})$, its variance s^2_{PFM} is obtained by equations (3) and (7) with q_{iPFM} instead of q_i, and s^2_{PFM} is used as an estimator of its ensemble mean $\sigma^2_{D\lambda}$ [*Journel and Huijgrebts*, 1978] to further improve the fit of $C(h)$. In other words, $C(h)$ is modified (e.g., through adjusting horizontal and vertical variogram sills), such that $\sigma^2_{D\lambda}$ from equation (8) is approximately equal to s^2_{PFM}. A convenient property of this approach is that a scaling of the variance axis of $C(h)$ does not affect λ_i and, consequently, s^2_{PFM} at all. Because of the normal score transformation, $C_{ns}(h)$ is also relatively robust with respect to changes in λ_i through range adjustments and a single manual iteration for fitting of $C(h)$ is performed in this work. Overall, as apparent from Figure 2, $C(h)$ is determined based on three sources of information: the experimental variogram of raw data q_{iPFM} for variogram fitting near the origin, the weighted data dispersion variance $\sigma^2_{D\lambda}$ estimated by s^2_{PFM} to adjust scaling on the variance axis, and the correlation length(s) of the normal score variogram to adjust scaling along the distance axis.

2.2.6. Check for Representative Flux Sampling (Step F)

[19] The "missing variance" $\Delta\sigma^2$ from equation (10) can be computed prior to any conditional simulation and elevated values may indicate that local flux heterogeneity pdf(q) over the transect is not sufficiently represented by the data collected. If this is the case, it may still be reasonable to quantify discharge and uncertainty in terms of an error variance σ^2_e without, however, being able to make reliable statements about the exact distribution of the estimation error (by any method considered herein). To overcome this limitation, additional PFM measurements or alternative approaches including complementary data, such

as contaminant concentrations, hydraulic head, and/or conductivities [*Schwede and Cirpka*, 2010; *Troldborg et al.*, 2010] may be required. While further investigation is needed to see whether a maximum admissible value for $\Delta\sigma^2$ may be defined, the case studies in section 5 indicate that $\Delta\sigma^2$ smaller than $\sim 5\%$ leads to satisfactory results for discharge distributions.

2.2.7. Conditional Simulation Using q_{ins} and $C_{ns}(h)$ (Step G)

[20] LU decomposition (lower-upper triangle or also known as Cholesky decomposition) [*Goovaerts*, 1997] is chosen as a fast algorithm for multi-Gaussian conditional simulation of up to several thousand grid points. It possesses the advantage that all data and grid locations are considered simultaneously as a whole, rather than as little portions inside local neighborhoods. This avoids approximation errors, which may deteriorate the simulation performance in terms of histogram or variogram reproduction.

2.2.8. Back-Transformation and Spatial Averaging (Step H)

[21] The resulting conditional realizations of normal scores are back-transformed into fluxes by the inverse of the transformation in step C, which is quantile matching (with linear interpolation) in the inverse direction. At the tails, i.e., outside of the range of q_{iPFM} measured, extrapolation models have to be chosen ("distributional extrapolation"). It was found, however, that with sufficiently dense PFM sampling, enough data is available, such that this choice does not influence results (i.e., the missing variance $\Delta\sigma^2$ and consequent probability of simulating local flux values outside the range of measured fluxes are sufficiently small). Hence, the lower tail is linearly extrapolated to zero, which is generally equal to the minimum data value if transects span entire plumes, while the upper tail is limited to the maximum data value. Given the conditionally simulated fluxes at all grid points, spatial averaging is performed on each realization to obtain conditionally simulated values of transect average fluxes $q_{Tc}^{(j)}$ (by using a discrete form of equation (1)). The additional subscript "c" indicates that q_T is conditioned to measured fluxes and the index "j" denotes the number of the realization that q_{Tc} corresponds to. Knowing that a total number N (i.e., $j = 1$, 2, ..., N) of conditional realizations are generated, a discrete approximation of the conditional cumulative distribution function cdf(q_{Tc}) may be obtained. The latter is regarded as the probability distribution of the unknown transect average flux q_T in the field [*Goovaerts*, 1997]. The ensemble mean $\bar{q}_{Tc}$ of cdf(q_{Tc}) approximated by

$$\bar{q}_{Tc} = \frac{1}{N}\sum_{j=1}^{N} q_{Tc}^{(j)}, \tag{11}$$

is used as a conditional simulation based estimate of the true q_T, while the respective estimation error variance is given by

$$\sigma^2_{ec} = \frac{1}{N}\sum_{j=1}^{N}\left(q_{Tc}^{(j)} - \bar{q}_{Tc}\right)^2. \tag{12}$$

[22] In the present work, $N = 1000$ conditional realizations are used, which results in insignificant uncertainty

(because of a finite number of realizations) in equations (11) and (12) as well as in cdf(q_{Tc}) over the principal range of interest (i.e., approximately between 0.01 and 0.99 quantiles). Once cdf(q_{Tc}) is known, a multiplication of quantiles by transect area A produces the cdf of transect discharge Q as cdf(Q) = cdf(Aq_{Tc}).

2.2.9. Validation of Results (Step I)

[23] As a consequence of good histogram reproduction, $\bar{q}_{Tc}$ from equation (11) should be in good agreement with the mean of pdf$_\lambda$(q_{iPFM}). By step B, the mean of pdf$_\lambda$(q_{iPFM}) is again equal to the ordinary block kriging estimate $\bar{q}_{PFM}$ obtained from equation (3) with actual sample values of q_{iPFM}. Furthermore, Gaussian conditional simulation algorithms are based on the properties of simple kriging [*Goovaerts*, 1997]. It is known that these properties are well approximated by those of ordinary kriging, if a sufficient amount of data is available within the domain of interest (i.e., small $\Delta\sigma^2$ [*Emery*, 2007]). Thus, the error variance σ_{ec}^2 from equation (12) should be in good agreement with σ_e^2 from equation (6). Note that both variances are independent of higher order moments (e.g., distribution skewness of pdf[q_{iPFM}]) and that issues related to conditional bias (i.e., overestimation of variance in areas of low variability and underestimation of variance in areas of high variability) do not arise in the present situation. This is because estimation is over the whole transect encompassing all data and both high and low variability zones. Thus, as indicated by Figure 2, the output of the conditional simulation method may be validated to some degree by verifying $\bar{q}_{PFM} \approx \bar{q}_{Tc}$ and $\sigma_e^2 \approx \sigma_{ec}^2$. Significant discrepancies may indicate errors in the implementation of the conditional simulation routine or the possibility of improvements in variogram fits (within the requirements of steps A, D, and E). If none of the above is the case, then a conditional simulation approach based on transformation of a multi-Gaussian field may be inadequate for the data at hand.

3. Effective Number of Independent Data n_e

3.1. Purpose, Definition, and Basic Properties

[24] The implementation of the conditional simulation approach of step G may not be a straightforward task for practitioners. In an effort to offer simpler alternatives, which closely approximate well-calibrated conditional simulation results (i.e., successfully validated in step I), an effective number of independent data n_e is defined and proposed for use with two estimation methods from classic independent and identically distributed (i.i.d.) statistics. The parameter n_e contains information about the transect and sampling geometries as well as of the spatial correlation structure. Similar to *Kitanidis* [1997, p. 157], *Deutsch* [2004], or *Klammler et al.* [2011] it is defined by

$$n_e = \frac{\sigma_{D\lambda}^2}{\sigma_e^2},\tag{13}$$

where σ_e^2 is the ordinary block kriging variance of equation (6) and $\sigma_{D\lambda}^2$ is the weighted data dispersion variance of equation (8). In analogy to classical statistics of uncorrelated data, n_e acts as a proportionality factor between the variance of observed data ($\sigma_{D\lambda}^2$ or its estimator s_{PFM}^2, see the appendix) and the variance of a mean estimate (σ_e^2).

This means that the ratio in equation (13) between the spatial variance of the n correlated flux data and the ensemble variance of the error of the transect mean estimate is equal to the ratio of the variance of n_e hypothetical data values (which are statistically independent) and the variance of their mean estimate (compare "standard error equation" from i.i.d. statistics). Thus, in terms of the error variance of a mean estimate, n correlated data achieve the same variance reduction as n_e uncorrelated data. It may be observed that the effective number of independent data n_e is unaffected by the scaling of $C(h)$ along the variance axis, since both $\sigma_{D\lambda}^2$ and σ_e^2 are scaled by the same factor. Furthermore, in the same way as $\sigma_{D\lambda}^2$ and σ_e^2, n_e exists under the intrinsic hypothesis and can range from zero to infinity. That is, $n_e = 0$ is obtained for a single-point sample leading to the trivial case of $\sigma_{D\lambda}^2 = 0$, while $n_e \to \infty$ is obtained when the entire transect is sampled. The latter corresponds to complete sampling of a finite population in classical statistics, where uncertainty is totally removed. Intuitively speaking, in the range $n_e < n$, redundancy between nearby sampling locations prevails, while for $n_e > n$ the favorable effect of correlation between sampled and unsampled locations is predominant, which decreases the interpolation uncertainty between monitoring wells.

3.2. Properties of n_e Related to PFM Discharge Estimation

[25] From above, it may be understood that n_e acts as a kind of effective parameter quantifying the efficiency of a sampling pattern in terms of variance reduction between data dispersion (observed flux heterogeneity) and estimation error of the spatial mean. In order to analyze some general aspects related to n_e and PFM discharge estimation, section 3.2 assumes regularly spaced monitoring wells along a rectangular transect with a constant number of 10 vertical PFM sampling intervals. Evaluating equations (2), (4), and (5) for the computation of n_e generally requires numerical methods [*Journel and Huijbregts*, 1978] and direct statements about the quantitative behavior of n_e for practical purposes are difficult to make. For this reason, Figure 3 (bold continuous lines) shows a normalized representation of the order of magnitude of n_e as a function of the number of PFM wells n_w [-], horizontal and vertical correlations lengths a_h and a_v [L], as well as transect width X [L] (x direction) and depth Y [L] (y direction). The spherical covariance model [*Goovaerts*, 1997] is used for $C(h)$ and integration is performed on discretized transects of 10×200 (depth per width) rectangular cells. This implies that each PFM well corresponds to a grid column and the sampling over depth is exhaustive as it is typical for PFM measurements (every cell in a PFM grid column is considered "sampled" corresponding to a PFM sampling interval). Each chart in Figure 3 corresponds to a particular value of $a_vX/(a_hY)$ representing the aspect ratio of the transect after scaling to isotropic correlation length. In Figure 3f $a_v = \infty$, which reduces the problem to one-dimension in the x direction and, hence, a_h/X is used for the abscissa as opposed to a_v/Y in Figures 3a–3e. For $a_h = \infty$, in contrast, the problem is reduced to the y direction, which is entirely sampled, thus leading to $\sigma_e^2 = 0$ and $n_e = \infty$ (no uncertainty left). Both cases correspond to zonal anisotropies [*Goovaerts*, 1997] and may be relevant for PFM applications. The former
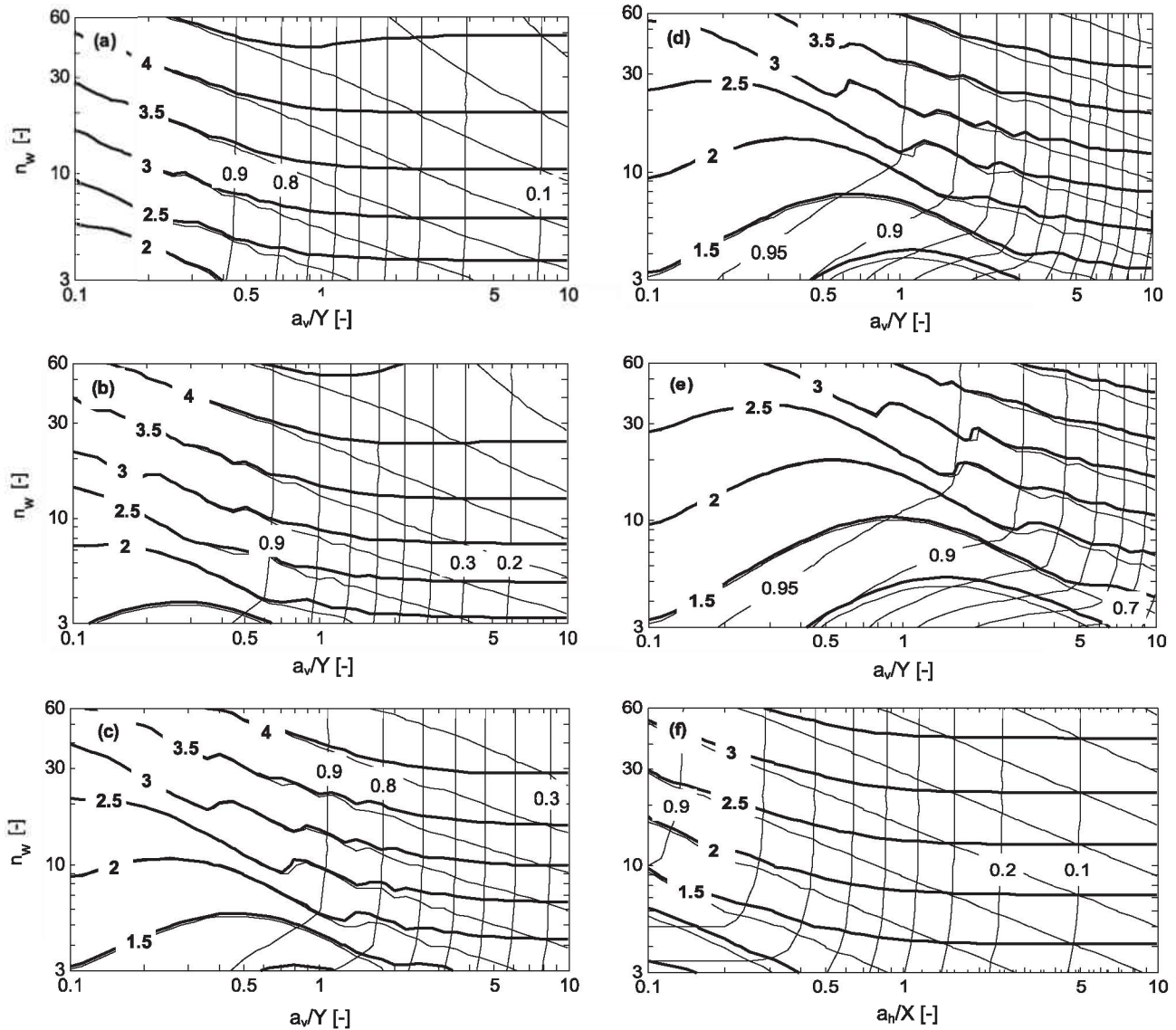
Figure 3. Contour lines of $\sigma_{D\lambda}^2/\sigma_0^2$ (dashed lines), $-\log_{10}\sigma_e^2/\sigma_0^2$ (thin continuous lines), and $\log_{10}n_e$ (bold continuous lines) for PFM transects of $a_vX/(a_hY) = \{1, 2, 5, 10, 20, \infty\}$ in (a)–(f), respectively. PFM wells are assumed to be regularly spaced ($\lambda_i = 1/n$) and possess 10 vertical sampling intervals. Spherical model for $C(\mathbf{h})$.

($a_v = \infty$) is known as a random areal trend and can reflect the fact that certain wells are located in high- and others in low-flux zones (e.g., plume core versus periphery). The latter ($a_h = \infty$) typically reflects random stratigraphic layering. Apparent irregularities of contour lines for σ_e^2/σ_0^2 and n_e over certain ranges in Figure 3 are caused by a type of periodicity appearing when a_h reaches multiples of the PFM well-separation distance. Without disturbing the general tendency of n_e, the strongest effect occurs at $a_h = X/n_w$. The periodicity is found to be an artifact of the spherical covariance model adopted and it is not observed with the smoother exponential covariance function. For either model of $C(\mathbf{h})$, the contour lines of n_e share similar characteristics and become horizontal as $a_h > X$ and $a_v > Y$, i.e., when $C(\mathbf{h})$ becomes linear over the extent of the transect. In such

a case (e.g., Rifle case study in section 5.2), n_e becomes independent of the individual values of a_h and a_v reducing to a function of the anisotropy ratio a_h/a_v only.

[26] The structure of $C(\mathbf{h})$ may be nested, which means it consists of a number m [-] of substructures $C_j(\mathbf{h})$ of different geometric or zonal anisotropies such that $C(\mathbf{h}) = \sum_{j=1}^{m} C_j(\mathbf{h})$. According to the principle of factorial kriging [*Goovaerts*, 1997], the substructures may be regarded as related to mutually independent stochastic subprocesses, which add up to the composite process corresponding to $C(\mathbf{h})$. As a consequence, dispersion and estimation variances of the subprocesses ($\sigma_{D\lambda j}^2$ and σ_{ej}^2, respectively) also add up to the respective variances of the

composite process, and n_e from equation (13) can be expressed more generally as

$$n_e = \frac{\sum_{j=1}^{m} \sigma_{D\lambda j}^2}{\sum_{j=1}^{m} \sigma_{ej}^2} = \frac{\sum_{j=1}^{m} \sigma_{ej}^2 n_{ej}}{\sum_{j=1}^{m} \sigma_{ej}^2}. \qquad (14)$$

[27] Note that the same declustering weights obtained for the compound covariance function $C(\mathbf{h})$ under step B in section 2.2 are used for all variogram components in equation (14). If data are approximately regularly spaced, the contour lines of $\sigma_{D\lambda}^2/\sigma_0^2$ (dashed) and σ_e^2/σ_0^2 (thin continuous) in Figure 3 may be applied to individual substructures of a nested $C(\mathbf{h})$ to approximate n_e through equation (14). For each substructure, σ_0^2 in Figure 3 has to be taken as the variance of that substructure only. The last expression in equation (14) shows that the compound n_e may also be represented as a weighted sum of all substrutures' n_{ej}, where weighting is proportional to the relative contribution σ_{ej}^2/σ_e^2 of each structure to the total estimation error σ_e^2.

[28] Figures 3 provides a means to evaluate the sensitivity of n_e with respect to the (somewhat subjective) choice of variogram ranges and the number of PFM wells installed over a transect. The latter is of interest for the evaluation of the benefit of additional sampling in terms of uncertainty reduction in discharge estimates. Under the hypothesis that $C(\mathbf{h})$ is not significantly different after additional sampling, Figure 3 shows, for example, that over most of the range represented (especially for $a_v/Y > 0.5$), doubling the number n_w of PFM wells approximately increases n_e by a factor of $10^{0.5} \approx 3$. For shorter correlation lengths (e.g., approaching a nugget variogram and data independence), $n_e \approx n$ is known from section 3.1 and a proportional increase in n_w leads to the

same proportional increase in n and, hence, n_e. Thus, it may be stated that doubling the number n_w of wells results in an overproportional increase in the effective number of independent data n_e by a factor between ~2 and 3. By virtue of the final expression in equation (14), this remains valid also for nested variogram structures. However, by inspection of equation (15) or Figure 4 in section 4.1, for example, it is seen that the width of confidence intervals is (inversely) proportional to $\sqrt{n_e}$. This means that doubling n_w may be expected to decrease the width of confidence intervals about a discharge estimate underproportionally by a factor between $\sim\sqrt{2} \approx 1.4$ and $\sqrt{3} \approx 1.7$. This is in agreement with *Kübert and Finkel* [2006], who numerically simulate contaminant transport and PFM measurements in heterogeneous aquifers and who observe that the reduction in estimation uncertainty due to increasing n_w decreases as n_w grows.

[29] Further inspection of Figure 3 shows that the relative data dispersion variance $\sigma_{D\lambda}^2/\sigma_0^2$ increases with n_w until PFM well separation becomes smaller than a_h. At this point the observed data represent practically all of the variability σ_{DT}^2/σ_0^2 contained in the transect and data dispersion cannot increase any more with n_w. Based on results of the case studies below, it may be tentatively stipulated, for example, that distributional extrapolation is acceptable as long as the declustered (weighted) data dispersion variance accounts for at least 95% of the transect dispersion variance (i.e., $\Delta\sigma^2 < 0.05$). Lines for $\Delta\sigma^2 = 0.05$ in Figure 3 are not shown for clearness of the plots, but they are found to be close to the contour lines of $n_e = 30$, such that the approximate condition $n_e \geq 30$ may be given to contain distributional extrapolation within 5%. For a transect of given parameters X/Y, n_w, and a_h, reducing a_v decreases $a_v X/(a_h Y)$ and results in an increase in n_e, which may be attributed to less correlation (less data redundancy) in the vertically aligned data. In contrast, a decrease in a_h increases $a_v X/$
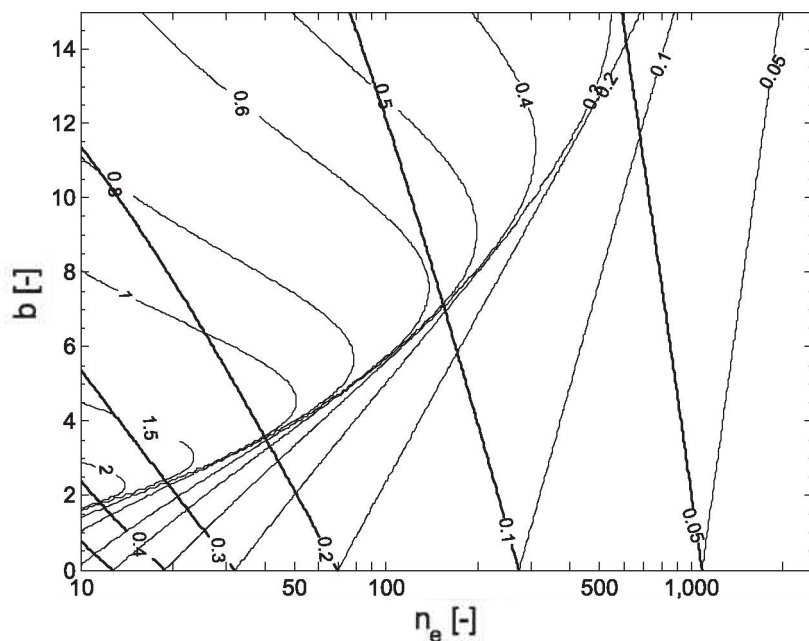

Figure 4. Contour lines of $t'_{n_e-1,1-0.05}/\sqrt{n_e}$ (thick lines) and $-t'_{n_e-1,1-0.95}/\sqrt{n_e}$ (thin lines) as functions of an effective number of independent data n_e (equation (13) or (14)) and declustered data coefficient of skewness b (equation (18)) for use in equation (15).

$(a_h Y)$ and decreases n_e, which reflects the reduced correlation between sampled and unsampled (to be interpolated) locations. In other words, short-vertical and large-horizontal correlation scales, as typical for hydrogeological field situations, tend to increase n_e. This acts favorably on the uncertainty of discharge estimates, when sampling in the vertical direction is dense and indicates, in agreement with *Kübert and Finkel* [2006], a significant potential for the PFM method to deliver reliable discharge estimates.

4. Approximate Methods Using n_e

[30] Section 4 presents two relatively simple methods from classical i.i.d. statistics, which both make use of n_e to approximate conditional simulation results. One applies a transformation of the t statistic, which is capable of accounting for distribution skewness and the other method uses the classic bootstrap on the full $\mathrm{pdf}_\lambda(q_{i\mathrm{PFM}})$. Steps J and K in Figure 2 illustrate how n_e and the approximate methods are implemented in the present work and how they circumvent the need for conditional simulation to arrive at an approximation of $\mathrm{cdf}(q_{Tc})$. The idea of the approximate methods is based on the fact that the averaging of n_e independent data following a distribution $\mathrm{pdf}_\lambda(q_{i\mathrm{PFM}})$ leads to the same mean estimate and error variance as averaging over the spatially correlated random function through the conditional simulation approach. This means that the first- and second-order statistics of spatial averaging are exactly honored by using n_e, while the influence of spatial correlation on higher-order moments is approximately incorporated through n_e and its effect due to the central limit theorem. Similar to step I above, step L in Figure 2 validates results up to second order, but may only indicate errors in the implementation of the approximate methods.

4.1. Transformation of the t Statistic

[31] *Willink* [2005], *Zhou and Dinh* [2005], as well as *Yanagihara and Yuan* [2005] independently present identical methods for improved determination of nonparametric confidence intervals for mean estimates of a wide range of skewed i.i.d. samples. The method is based on a transformation of the common Student's t statistic leading to a parameter denoted as t_2, T_1, and $\tilde{t}$ by the above authors, respectively. For the present purpose, we propose the use of this method in combination with $\mathrm{pdf}_\lambda(q_{i\mathrm{PFM}})$ and n_e instead of $\mathrm{pdf}(q_{i\mathrm{PFM}})$ and n as in the i.i.d. case. With this, the quantile q_α of the distribution of the spatial mean estimate, which is not exceeded by a probability α, is approximated by

$$q_\alpha = \overline{q}_{\mathrm{PFM}} - \frac{t'_{n_e-1,1-\alpha} s_{\mathrm{PFM}}}{\sqrt{n_e}}, \qquad (15)$$

where s_{PFM} is the declustered data standard deviation obtained as the square root of equation (7) by using $q_{i\mathrm{PFM}}$ instead of q_i and $\overline{q}_{\mathrm{PFM}}$ instead of $\overline{q}$. Thus, a two-sided $1-2\alpha$ confidence interval about the mean estimate $\overline{q}_{\mathrm{PFM}}$ from equation (3) results as $[q_\alpha, q_{1-\alpha}]$, where $t'_{ne-1,1-\alpha}$ in equation (15) is a cubic function of the classic Student's t variable $t_{ne-1,1-\alpha}$ for n_e-1 degrees of freedom [*Willink*, 2005],

$$t'_{n_e-1,1-\alpha} = \frac{\sqrt[3]{1 + 6a(t_{n_e-1,1-\alpha} - a)} - 1}{2a}. \qquad (16)$$

[32] This transformation is graphically represented in Figure 4 and incorporates distribution asymmetry in the parameter a in terms of the declustered sample coefficient of skewness b,

$$a = \frac{b}{6\sqrt{n_e}}, \qquad (17)$$

$$b = \frac{\sum_{i=1}^{n} \lambda_i (q_{i\mathrm{PFM}} - \overline{q}_{\mathrm{PFM}})^3}{s_{\mathrm{PFM}}^3}. \qquad (18)$$

[33] Equation (17) reflects the consequence of the central limit theorem that both variance and skewness of the distribution of the mean estimate decrease with n_e. For symmetric distributions ($b = 0$) or large n_e, a becomes small and equation (16) reduces to $t'_{ne-1,1-\alpha} = t_{ne-1,1-\alpha}$. Otherwise, for positive skewness ($b > 0$), equation (16) results in asymmetric confidence intervals, which reflect a larger probability of underestimation and which work toward the requirement of non-negativity (confidence intervals shifted to right). For two-sided confidence intervals of $1-2\alpha \leq 0.99$ and i.i.d. samples, *Willink* [2005] concludes that equation (16) is appropriate for $n_e \geq 30$.

4.2. Bootstrap

[34] The bootstrap [*Efron and Tibshirani*, 1998] is a method based on distribution resampling, which is applicable to a diverse range of statistical problems. In its simplest form it consists of randomly drawing (with replacement) n values from an i.i.d. sample to compute a desired sample statistics (e.g., mean). Repeated performance of this process populates a distribution, from which a mean estimate and uncertainty intervals can be inferred. From a geostatistical standpoint, bootstrapping may be considered as a degenerate form of unconditional stochastic simulation over n locations, which are spatially uncorrelated. Similar to *Klammler et al.* [2011], in the present work, we propose and demonstrate the use of the bootstrap by resampling n_e times with equal likelihood from the declustered data distribution $\mathrm{pdf}_\lambda(q_{i\mathrm{PFM}})$. For computational convenience, it is noted that this is equivalent to resampling n_e times from the unweighted (i.e., raw) sample distribution $\mathrm{pdf}(q_{i\mathrm{PFM}})$, where each datum is drawn with probability λ_i.

5. Application to Estimate Discharges From PFM Field Measurements

5.1. Estimating TCE Discharge at Ft. Lewis, WA, Military Base

5.1.1. Ten Well Scenario

[35] At Ft. Lewis, WA, Military Base extensive use of TCE as a degreasing substance led to the emergence of numerous TCE plumes in the groundwater. For one of the plumes investigated, transect limits (width $X = 64.3$ m, depth $Y = 7.6$ m, area $A = XY = 490$ m^2), PFM well locations, and segmentation are illustrated in Figure 1. Approximately uniform well spacing of 6 m results in $n_w = 10$ wells with ~ 21 PFM sampling intervals per well of 35 cm in length leading to a total of $n = 204$ local flux measurements. The experimental variogram points for the horizontal

and vertical directions are depicted in Figures 5a and 5b for the normal scores and the raw data, respectively. Performing steps A through E of the proposed method (see section 2.2 and Figure 2), the sum of two spherical models is chosen to represent $C_{ns}(\boldsymbol{h})$ and the following parameters are fitted: $\sigma_{0ns1}^2 = 0.4$, $a_{h1} = 25$ m, $a_{v1} = 3$ m, and $\sigma_{0ns2}^2 = 0.85$, $a_{h2} = 25$ m, $a_{v2} = \infty$. The same correlation ranges are adopted for $C(\boldsymbol{h})$ and the respective sills are fitted as $\sigma_{01}^2 = 4.5$ g^2/(m^4 d^2) and $\sigma_{02}^2 = 9$ g^2/(m^4 d^2). Both $\sigma_{D\lambda ns}^2 \approx 1$ and $\sigma_{D\lambda}^2 \approx s_{PFM}^2$, as indicated by the horizontal lines in Figures 5a and 5b, are satisfied to approximately $\pm 1\%$ and the fit to the experimental variogram points, especially for short lag distances, appears to be quite good. At larger lag distances the fit becomes worse; however, the variogram sills do represent the correct average degree of variability. Using $C(\boldsymbol{h})$ from Figure 5b and λ_i from ordinary block kriging, equations (3), (7), and (18) (with q_{PFM} instead of q_i) give an estimated mean TCE flux over the transect of $\bar{q}_{PFM} = 1.53$ g/(m^2 d), a declustered data dispersion variance $s_{PFM}^2 = 10.7$ g^2/(m^4 d^2), and a coefficient of skewness $b = 3.10$. The respective declustered histogram is depicted in Figure 5c with a "missing variance" $\Delta\sigma^2$ from step F amounting to $\sim 3\%$.

[36] The variogram analysis indicates both larger statistical continuity as well as a higher degree of variability in the horizontal direction. The former may be attributed to horizontally more continuous hydrogeological conditions of aquifer and source zone, while the latter reflects variability in local fluxes between plume center and lateral periphery.

Applying Figure 3 to the first variogram structure with $a_v X/(a_h Y) = 1.0$, $n_w = 10$ and $a_{v1}/Y = 0.4$ gives $\sigma_{D\lambda 1}^2/\sigma_{01}^2 = 0.91$ and $\sigma_{e1}^2/\sigma_{01}^2 = 10^{-3.2}$ (Figure 3a). For the second structure with $a_{h2}/X = 0.4$ and $n_w = 10$, respective variances $\sigma_{D\lambda 2}^2/\sigma_{02}^2 = 0.72$ and $\sigma_{e2}^2/\sigma_{02}^2 = 10^{-2.2}$ are obtained (Figure 3f). From this $n_e \approx 177$ is determined from equation (14), which is close to $n_e = 169$ from direct application of equation (13) with λ_i from ordinary block kriging. Besides rounding errors (e.g., chart readings are only to the first decimal of the exponents), the difference is due to the assumption of equal well and sample spacing in Figure 3. The assumption of 10 vertical PFM intervals per well in Figure 3 can be shown to be of minor significance, because for the range depicted ($a_v/Y \geq 0.1$) additional samples are increasingly redundant (correlated to previous samples). Finally, validation by step I (see Figure 2) indicates acceptable properties of the conditional simulation output: The discrepancies between $\bar{q}_{PFM}$ and $\bar{q}_{Tc}$ and between σ_e^2 and σ_{ec}^2 amount to $\sim 4\%$ each. Figure 6a is a representation of the spatial distribution of the ensemble means of local fluxes (20 vertical $\times$ 160 horizontal grid elements) from 1000 conditional realizations and illustrates an estimated position and shape of the plume core. Figure 6b contains the estimated cumulative distribution functions (cdf's) of TCE discharge $Q = A q_{Tc}$ illustrating good agreement between conditional simulation and the approximation methods. Means and standard deviations of all methods are listed in the top part of Table 1 for comparison to "target values" from block kriging. Table 1 further lists the 5%
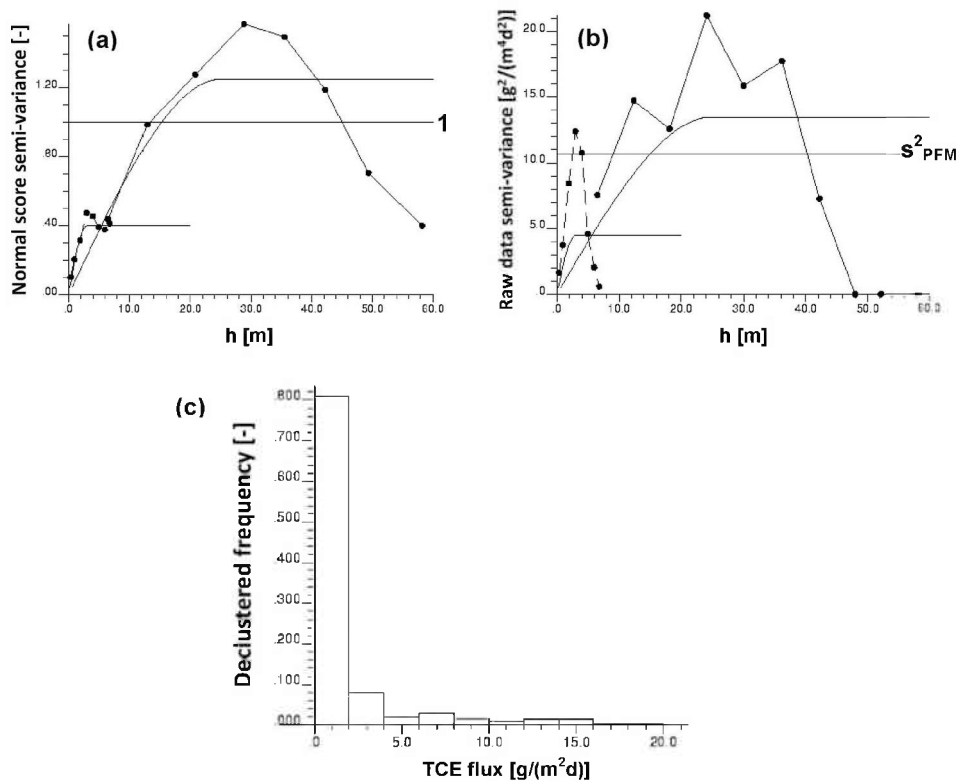

Figure 5. Horizontal (continuous lines) and vertical (dashed lines) experimental variograms of (a) normal scores and (b) raw data with spherical model fits for TCE fluxes from 10 wells at Ft. Lewis, WA. (c) Declustered data histogram.
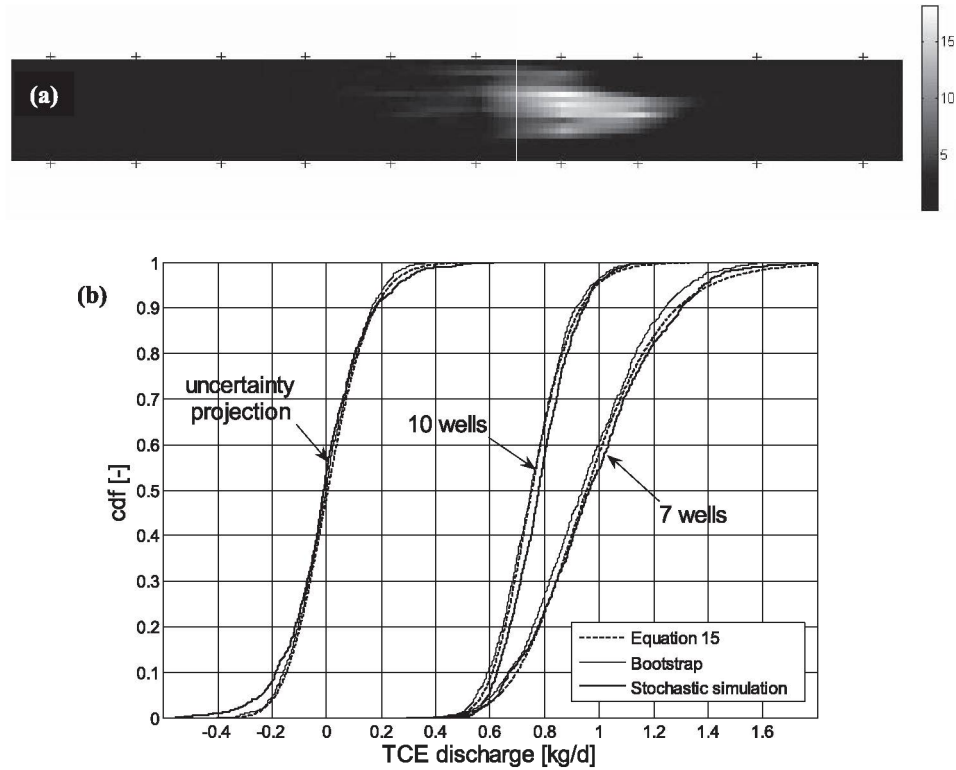
Figure 6. (a) Distribution of ensemble means of local fluxes in $g/(m^2\ d)$ from all conditional realizations. Crosses indicate PFM well locations according to Figure 1. (b) Cumulative distribution functions of TCE discharge. Graphs denoted by "7 wells" and "10 wells" compare results from conditional simulation, equation (15), and bootstrap for the respective number of observation wells indicated. Graphs called "uncertainty projection" compare unconditional simulation, equation (15), and bootstrap for predicting variance reduction due to additional sampling. One thousand realizations were used for all stochastic simulations and bootstrap.

and 95% quantiles of estimated discharge distributions showing maximum discrepancies of ~7% between conditional simulation and the approximation methods.

5.1.2. Seven Well Scenario

[37] Although the above confidence intervals are slightly asymmetric about the respective means, the large value of n_e causes the discharge distributions to be quite close to normal (indicated by a small value of $a = 0.04$ in equation (16)). In general, however, discharge distributions may strongly deviate from normality, and to demonstrate the performance of the proposed approximate methods under such scenarios the above analysis is repeated after excluding the local flux data from three wells (third, fifth, and ninth well from left to right in Figure 1) resulting in $n = 141$ data points. Following again the method of section 2.2 (see Figure 2), for variogram model fitting it is found that all parameters may be maintained, except for $\sigma_{01}^2 = 10.0\ g^2/(m^4\ d^2)$, which is illustrated by Figure 7. This results in a mean, variance, and coefficient of skewness of the declustered data

Table 1. Comparison of n_e, $\Delta\sigma^2$, and Selected Statistics of Estimated Discharges From All Methods and Sites Investigated[a]

Site	Discharge Parameter	Block Kriging	Conditional Simulation	t Transformation	Bootstrap
Ft. Lewis (10 wells) $n_e = 169$ $\Delta\sigma^2 = 3\%$	Mean	750	777	765	746
	Standard deviation	124	121	130	117
	5% quantile	–	595	570	550
	95% quantile	–	985	992	975
Ft. Lewis (7 wells) $n_e = 77$ $\Delta\sigma^2 = 4\%$	Mean	946	973	977	948
	Standard deviation	221	230	241	217
	5% quantile	–	630	632	610
	95% quantile	–	1385	1408	1335
Rifle $n_e = 250$ $\Delta\sigma^2 = 1\%$	Mean	19.0	18.8	19.1	19.1
	Standard deviation	1.33	1.38	1.41	1.41
	5% quantile	–	16.5	16.8	16.7
	95% quantile	–	21.0	21.5	21.5

[a]Parameters of TCE discharge at Ft. Lewis are in $g\ d^{-1}$ and parameters of uranium discharge at Rifle are in $mg\ d^{-1}$.
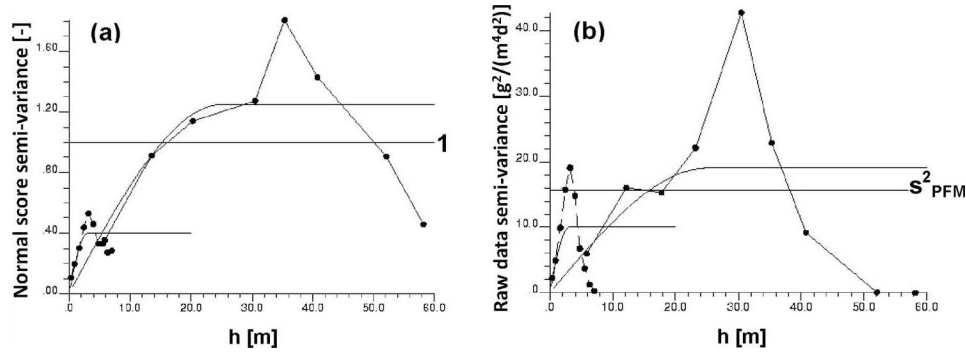
Figure 7. Analogous to Figures 5a and 5b, but for data from seven wells only.

histogram of $\overline{q}_{PFM} = 1.93$ g/(m^2 d), $s_{PFM}^2 = 15.6$ g^2/(m^4 d^2), $b = 2.51$, and a significantly reduced value of $n_e = 77$ from equation (13). Although well spacing is even less uniform in this case than in the 10 well scenario above, application of Figure 3 with $n_w = 7$ to both variogram structures of Figure 7b and using equation (14) leads to an excellent approximation of $n_e \approx 80$ (this calculation is analogous to the procedure for the 10 wells above and not shown here). Step F results in a "missing variance" $\Delta\sigma^2$ of $\sim$4% and validation step I provides relative differences between $\overline{q}_{PFM}$ and $\overline{q}_{Tc}$ and between σ_e^2 and σ_{ec}^2 of $\sim$4% and 7%, respectively. The probability distributions of TCE discharge for this scenario are superimposed in Figure 6b and are seen to be in comparably good agreement similar to the 10 well scenario considered previously. The center part of Table 1 further confirms a good matching of the "target values" from block kriging. However, the degree of skewness of the discharge distributions is more pronounced than in the 10 well scenario. This is reflected by the right shift (with respect to mean) of the 5% and 95% quantiles as well as a slight increase in parameter a to 0.05. It is noted that declustered sample means (946 versus 750 g d^{-1}) and TCE discharge estimates from the seven and 10 well scenarios are significantly different. However, the confidence interval between the 5% and 95% quantiles of the seven well scenario almost fully contains the corresponding interval of the 10 well scenario.

5.1.3. Uncertainty Projection

[38] Finally, the above methods for uncertainty quantification may also be adopted to assess the benefits of obtaining additional PFM measurements in terms of uncertainty reduction on the discharge estimate. This is termed "uncertainty projection" and is demonstrated by maintaining the scenario from above, where data is available from seven observation wells, and where it is intended to perform complementary measurements at three additional wells, such that the sampling pattern of Figure 1 is again complete. The principle is most easily illustrated by inspection of equation (15) revealing that any measure of dispersion or uncertainty (e.g., confidence interval width on both sides of the mean estimate or variance of discharge cdf) around a mean estimate $\overline{q}_{PFM}$ is purely determined by the last term of equation (15). Assuming that additional sampling may change $\overline{q}_{PFM}$, but does not significantly alter declustered data variance, skewness, and spatial correlation structure, the last term in equation (15) becomes a pure function of n_e

and may be determined for future sampling events knowing only the locations (and not actual values) of additional observations. In the present case, the projected value of n_e becomes 238 (from equation (13) with sampling locations and variogram from Figures 1 and 7b, respectively). Results correspond to the dashed line in the group of graphs denoted by "uncertainty projection" in Figure 6b. Since this cdf is independent of $\overline{q}_{PFM}$, it is arbitrarily shifted to $\overline{q}_{PFM} = 0$.

[39] In similar ways the bootstrap and stochastic simulation methods may be used for the same purpose. For the bootstrap approximation, n_e is simply increased to the projected value after additional sampling, and the declustered sample distribution, from which it is drawn, may be arbitrarily shifted (here to $\overline{q}_{PFM} = 0$). The result is shown by the thin continuous line in the group "uncertainty projection" of Figure 6b. With the stochastic simulation approach conditional realizations cannot be generated as long as the additional data values are unknown. However, following section 2.1, unconditional realizations may be generated and fictitiously sampled at the existing and additional sample locations to obtain respective values of $\overline{q}$ and q_T for each realization (equations (1) and (3)). From this, a distribution of the estimation errors $e = \overline{q} - q_T$ may be built, which corresponds to the augmented sampling network. The respective result is also superimposed in Figure 6b (the bold continuous line in the group "uncertainty projection") and shows good agreement with the t transformation and bootstrap methods as well as with the shape of the actual discharge distributions for the 10 well scenario.

5.2. Estimating Uranium Discharge at La Quinta Gallery, Rifle, CO

[40] At the La Quinta Gallery site in Rifle, CO, a former uranium mill resulted in the persistence of a groundwater uranium plume on the northern border of the Colorado River. Measurements of local uranium fluxes in a transect of $X = 3$ m and $Y = 3.5$ m are available from three wells ($n = 29$; $A = 10.5$ m^2) as depicted in Figure 8a. By the same procedure as above (Figure 2), declustering weights are found by ordinary block kriging resulting in the histogram of Figure 8b with $\overline{q}_{PFM} = 1.81$ mg/(m^2 d), $s_{PFM}^2 = 4.4$ mg^2/(m^4 d^2), and $b = 1.53$. A conditional stochastic simulation (1000 realizations; 31 horizontal $\times$ 36 vertical grid elements) is used to obtain the spatial distribution of ensemble means of local fluxes in Figure 8c as well as the probabilistic uranium
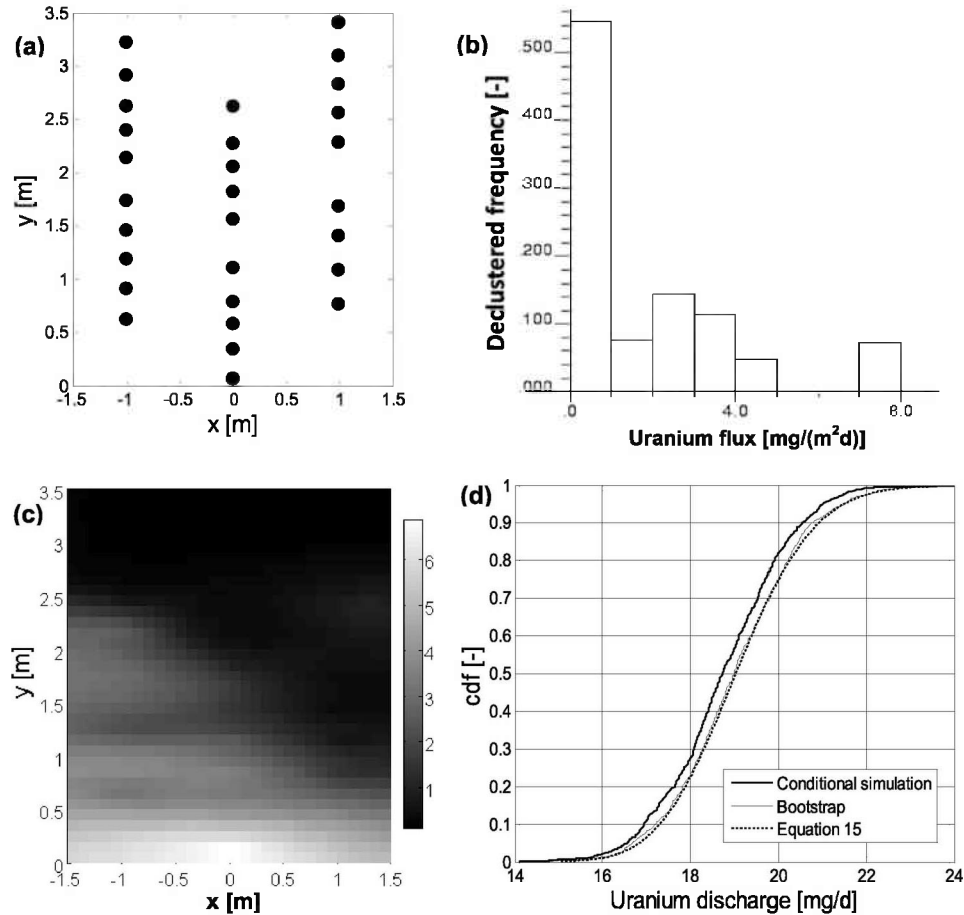
Figure 8. (a) PFM sampling locations over transect at Rifle, CO., with (b) declustered data histogram. (c) Distribution of ensemble means of local fluxes in mg/(m²d) from 1000 conditional realizations. (d) Uranium discharge distributions from the methods discussed.

discharge distribution of Figure 8d (thick continuous line). Simulation output is validated by step I, which results in relative differences between $\bar{q}_{\mathrm{PFM}}$ and $\bar{q}_{Tc}$ and between σ_e^2 and σ_{ec}^2 of ~1% and 8%, respectively; the "missing variance" $\Delta\sigma^2$ is ~1%. Figure 8d also contains cdf's from the two approximate methods and agreement in terms of quantile differences is seen to be within ~3%. Selected statistics of the discharge distributions are again summarized in Table 1 (bottom part).

[41] The experimental normal score and raw data variograms (connected dots) with linear variogram model fits (simple lines) used in the analysis are depicted in Figures 9a and 9b, respectively. The slopes adopted are 0.2 and 0.8 m⁻¹ for normal scores and 1 and 3.2 mg²/(m⁵ d²) for raw data (horizontal and vertical, respectively) resulting in $n_e = 250$ from equation (13). In order to be able to apply Figure 3 for obtaining an approximate value of n_e, it is assumed that a_h/X and a_v/Y are much larger than one, such that the shape of the spherical variogram inside the transect is basically linear. Because the slopes are known and proportional to the reciprocals of the respective ranges, it is found that $a_v/a_h = 1/3.2$, leading to $a_vX/(a_hY) = 0.27$, which is beyond the range of charts in Figure 3. However, Figure 3a for $a_vX/(a_hY) = 1$ with $a_v/Y \gg 1$ may be used to arrive at a lower bound of n_e as ~200. Because of the small

amount of data available, fewer data pairs exist within the lag classes and experimental variogram values are less reliable (especially in the horizontal direction). For a reasonable histogram reproduction of the conditional simulation method it is again observed that $\sigma_{D\lambda ns}^2 \approx 1$ (horizontal line in Figure 9a; step D in Figure 2) is an important criterion. While the latter is achieved to ±1%, $\sigma_{D\lambda}^2/s_{\mathrm{PFM}}^2 \approx 0.9$ (step E in Figure 2) is used as a compromise in the raw data variogram fit of Figure 9b to avoid larger discrepancies between experimental and theoretical variograms. The problem in this case seems to be related to the particular sampling configuration of Figure 8a, where the center well is shifted downward such that the largest data values at its bottom and the smallest data values at the top of the lateral wells (compare Figure 8c, which honors data values) receive the largest declustering weights. Thus, the declustering process does not affect the data mean very much, but does significantly inflate s_{PFM}^2 to almost 50% above its raw value before declustering. The experimental variogram, in contrast, is computed in the classic way from unweighted data and does not account for this fact. Hence, variogram fits slightly above the experimental variogram points are justified in agreement with the requirements of steps D and E in Figure 2. The linearity of the variograms is a consequence of the smooth trend apparent in Figure 8c. The
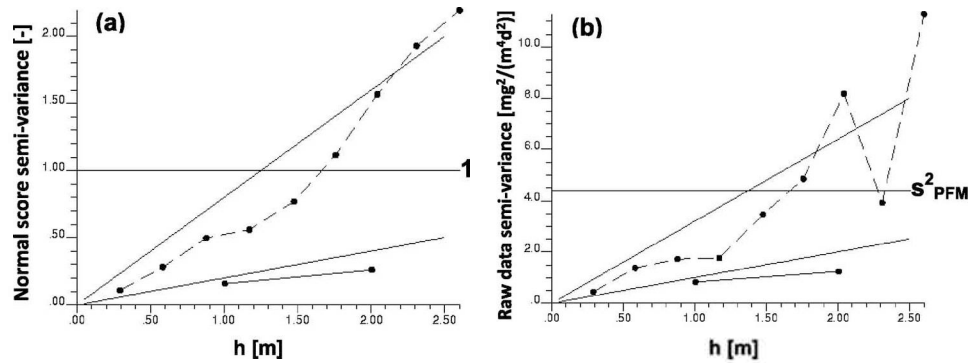
Figure 9. Horizontal (continuous lines) and vertical (dashed lines) experimental variograms of (a) normal scores and (b) raw data with linear model fits for uranium fluxes at Rifle, CO.

point variance (sill) σ_0^2 remains unknown, such that equations (6), (8), and (9) have to be evaluated in terms of the variogram $\gamma(h)$ rather than $C(h)$ (compare to the remark at the end of section 2.1). Further evident from Figure 8c is that the transect does not contain the entire plume such that results in terms of uranium discharge are limited to the transect studied, rather than the whole plume.

6. Evaluation of Assumptions and Further Observations

6.1. Modeling of a Spatial Trend

[42] The approach presented here is generally valid under the intrinsic hypothesis and no spatial trends are explicitly modeled. This may be contrary to the intuition that expected fluxes are higher near the plume core than at its periphery, for example. However, the fact that stochastic simulation is used with sufficient PFM data, such that all locations in a transect are effectively conditioned (correlated) to observed data, results in the automatic modeling of a spatial trend function. This means that the conditional simulation output is not stationary [*Chiles and Delfiner*, 1999] as is nicely reflected by Figures 6a and 8c showing the spatial distribution of ensemble means of local fluxes. An analogous argument applies to the stationarity of flux variance. Thus, the present work takes advantage of sufficient available data to implicitly account for spatial trends, which avoids the need for explicit trend modeling with respective uncertainties involved. This is further supported by a closely related discussion of trend modeling related to kriging by *Journel and Rossi* [1989]. However, if not all transect locations were correlated to one or more data locations, then a relatively small value of $\Delta\sigma^2$ (e.g., $< 5\%$) would still be sufficient to perform the conditional simulation approach. The latter assures that data is representative of the flux distribution over the transect, which is what ultimately matters for discharge estimation (rather than the exact location and shape of the plume within the transect).

6.2. Uncertainties in Choice of Variogram Model and Parameters

[43] The present work does not account for uncertainties in the choice of variogram models and their parameters. If these uncertainties can be reliably quantified, then a Bayesian approach similar to that of *Troldborg et al.* [2010] may

be combined with the present one. However, the discussion related to Figure 3 gives an idea about how sensitive n_e, the fundamental parameter influencing discharge uncertainty, is with respect to changes (or uncertainties) in variogram ranges. Moreover, theoretical variogram models are not simply fitted to experimental variogram points. Rather, joint analysis of normal score and raw data variograms contributes to a reliable choice of variogram ranges and honoring data dispersion variances assists in fitting variogram sills or slopes (steps D and E in Figure 2). Eventually, if conditional simulation is performed, successful validation of the output (step I in Figure 2) may confer additional confidence to variogram models and parameters used. It is further noted in this context that the choice of variogram models used (e.g., spherical in Ft. Lewis case study versus a possible exponential fit) is rather arbitrary and not expected to significantly influence results. The reason for this is that what matters most for the present problem are integral properties of the variogram over the extent of the transect (compare equations (2), (4), and (5)), rather than its exact shape. Meeting these integral properties is assured by matching the dispersion variances in steps D and E. An extreme example is the linear variogram of the Rifle case study, which may be modeled by any variogram type that is linear near the origin and with appropriate and large enough sills and ranges (beyond the transect scale). As a further consequence of this, the present work also neglects the circumstance [*Chiles and Delfiner*, 1999] that the raw data and normal score variograms $C(h)$ and $C_{ns}(h)$ should be related depending on the properties of the normal score transform applied (i.e., they would generally not be of the same type as assumed here).

6.3. Uncertainty in Local PFM Measurements

[44] Measured contaminant fluxes by the PFM method are associated with a random measurement error (e.g., related to sampling and/or analysis), which is assumed negligible in this study. Because of its causes, measurement uncertainty is typically considered spatially uncorrelated and manifests as a nugget variance component in the data variogram [*Kitanidis*, 1997]. It may be accounted for in the conditional simulation approach by conditioning to uncertain data [*Troldborg et al.*, 2010] as well as in the ordinary block kriging system [*Kitanidis*, 1997]. For the case studies presented, especially from the more reliable vertical variograms

(Figures 5, 7, and 9), no significant nugget variance is apparent. This demonstrates the fact that flux measurements predominantly reflect spatial variability, which is over several orders of magnitude, rather than measurement errors within a certain percentage range. In addition to this and in agreement with a conclusion by *Cai et al.* [2011], measurement errors also undergo a process of averaging such that neglecting them is justified.

6.4. Additional Information

[45] The present work assumes that the only data available are local PFM flux measurements inside a transect of interest. In principal, the conditional simulation approach using PFM measurements may be generalized to accommodate additional types of "indirect" information (e.g., hydraulic conductivity, head and/or concentration measurements, contaminant source properties, etc.) as demonstrated by *Schwede and Cirpka* [2010] or *Troldborg et al.* [2010]. However, along the lines of section 6.1, we argue that if $\Delta\sigma^2$ is sufficiently small, i.e., if the plume is effectively sampled by the "direct" PFM flux measurements (in the sense that they are part of the discharge to be estimated), then the expected benefit of including additional "indirect" information is not very significant. This may especially be the case if rather complex nonlinear stochastic simulation and conditioning methods have to be adopted. A closely related advantage of working with flux data only is the complete linearity of the problem, which allows for using straightforward ordinary block kriging to define an effective number of independent data for use in combination with one of the simple approximation methods presented. Overall, it may be observed at this point that the methods presented herein are generally applicable to any linearly averaging quantity measured inside a domain of interest. This includes the estimation of water discharges from local water flux measurements (e.g., through PFM) as well as the estimation of mean contaminant concentration over a transect from MLS measurements (e.g., for alternative discharge estimation).

7. Summary and Conclusions

[46] The problem of determining probability distributions or confidence intervals for mean estimates of correlated skewed data is known in many fields of science and engineering. In the present work, estimation and uncertainty quantification of contaminant mass discharges in the groundwater from local contaminant flux data (based on passive flux meter, "PFM," measurements) over a transect are discussed and demonstrated. Conditional stochastic simulation appears to represent the state-of-the-art method for this purpose. It requires a representative flux histogram over the transect, which is found through data declustering using ordinary block kriging weights (which account for spatial correlations as well as transect limits). In order to achieve reliable histogram reproduction over many realizations, the importance of considering data dispersion variances in the process of variogram-model fitting is highlighted. The declustered data histogram is assumed to correctly reflect the frequency of occurrence of local fluxes over the transect. As a consequence, its mean represents an unbiased estimate of the mean flux over the transect and should be honored by any discharge estimation method. Based on the

stochastic simulation paradigm, an effective number of independent data n_e is further introduced as an expected factor of variance reduction between the declustered data variance and the ordinary block kriging variance. As such, n_e should also be closely honored by conditional simulation results. Based on n_e we further develop two simple "approximate" methods for estimating discharge and uncertainty. One uses a transformation of the t statistic to account for skewness, while the other is closely related to the classic bootstrap method and uses the full declustered data histogram. Moreover, by means of n_e it is shown that one of the advantages of PFM measurements is the complete sampling of fluxes in the vertical direction, which is exactly the direction of typically larger spatial variability (shorter correlation lengths). This leads to less redundancy between data values and a higher degree of representativeness of flux variability in the plume.

[47] All three methods presented explore two fundamental properties of the problem: (1) linearity, i.e., the integral of local fluxes over the transect gives discharge, and (2) the data sufficiently well represents local flux variability over the transect. As a consequence of (1), the approaches are equally appropriate for estimating water discharges from PFM water flux measurements or for estimating average concentrations over an MLS transect with respective uncertainties. In order to evaluate (2), the "missing variance" $\Delta\sigma^2$ is introduced and found to be smaller than 5% in the case studies presented. Large values of $\Delta\sigma^2$ indicate that (2) may not be satisfied (whether an approximate limiting value exists and how large it is, is still an open question). In such a case, quantification of an estimation error variance may still be reliable, while the confidence in discharge quantile estimates becomes questionable. In order to overcome the latter, additional PFM sampling or application of more comprehensive (possibly nonlinear) approaches including complementary site data [*Schwede and Cirpka*, 2010; *Troldborg et al.*, 2010] may be required. Whenever linearity and data requirements are satisfied, the two approximate methods may be of significant practical value for estimating the probability distributions of discharges as they circumvent the need for implementing the much more complex tool of conditional stochastic simulation (compare Figure 2), and do not require the assumption of multi-Gaussianity of normal scores. Although not utilized in the present work, the latter also alleviates the need for normal score transformation, provided that other robust measures of spatial variability (e.g., variogram of logarithms of fluxes) are used for joint fitting of variogram ranges. Conditional simulation, in contrast, may be useful for additional validation of adopted variogram models (step I in Figure 2), and in addition to discharge distributions, it delivers spatial information about plume shape and location.

[48] All of the methods discussed are demonstrated for two different field sites with PFM data from TCE (Ft. Lewis, WA) and uranium (Rifle, CO) plumes. Besides the different types of contaminants, the two selected sites vary in transect size, number of observation wells, and spatial correlation structure. The latter may be the case because of different geological (aquifer heterogeneity) and contaminant source conditions as well as the scale of the study (entire plume versus a portion thereof). Results are based on 1000 conditional realizations and represented in the

form of spatial distributions of ensemble means of local fluxes as well as discharge probability distributions (cdf's). For both sites, quantile estimates of discharge from the different methods are seen to agree within ~7%. As an additional hypothetical scenario, some observation wells at Ft. Lewis were ignored to illustrate the effect that having fewer data available will increase estimation uncertainty as well as the skewness of the estimation error distribution. The same hypothetical scenario is also used to successfully predict uncertainty reduction due to additional sampling by the three methods investigated.

Appendix A: Weighted Data Dispersion Variance

[49] The weighted data dispersion variance $\sigma_{D\lambda}^2$ is the ensemble mean (expectation) of the spatial variance s^2 of the weighted (declustered) data histogram over many unconditional realizations, which are fictitiously sampled for fluxes q_i at the actual measurement locations. Substituting equation (3) into (7) and taking the square leads to

$$s^2 = \sum_{i=1}^{n} \lambda_i \left(q_i - \sum_{j=1}^{n} \lambda_j q_j \right)^2$$
$$= \sum_{i=1}^{n} \lambda_i \left[q_i^2 - 2q_i \sum_{j=1}^{n} \lambda_j q_j + \left(\sum_{j=1}^{n} \lambda_j q_j \right)^2 \right]. \tag{A1}$$

[50] Multiplying λ_i into the brackets and splitting up the summation gives

$$s^2 = \sum_{i=1}^{n} \lambda_i q_i^2 - 2\sum_{i=1}^{n} \lambda_i q_i \sum_{j=1}^{n} \lambda_j q_i + \sum_{k=1}^{n} \lambda_k \left(\sum_{j=1}^{n} \lambda_j q_j \right)^2. \tag{A2}$$

[51] Knowing that $\left(\sum_{j=1}^{n} \lambda_j q_j \right)^2 = \sum_{i=1}^{n} \lambda_i q_i \sum_{j=1}^{n} \lambda_j q_j = \sum_{\substack{i=1\\j=1}}^{n} \lambda_i \lambda_j q_i q_j$ further yields

$$s^2 = \sum_{i=1}^{n} \lambda_i q_i^2 - \left(2 - \sum_{k=1}^{n} \lambda_k \right) \sum_{i=1}^{n} \sum_{j=1}^{n} \lambda_i \lambda_j q_i q_j. \tag{A3}$$

[52] Taking the expectation $E[]$ and with $\sum_{k=1}^{n} \lambda_k = 1$ as imposed with equation (3) leads to

$$\sigma_{D\lambda}^2 = E[s^2] = \sum_{i=1}^{n} \lambda_i E[q_i^2] - \sum_{i=1}^{n} \sum_{j=1}^{n} \lambda_i \lambda_j E[q_i q_j], \tag{A4}$$

where the weighting constants are written outside the expectation operator. Using $E[q_i^2] = \sigma_0^2 + \mu_0^2$ and $E[q_i q_j] = C(\mathbf{u}_i - \mathbf{u}_j) + \mu_0^2$ (based on stationarity of process mean μ_0 and variance σ_0^2) with $\sum_{i=1}^{n} \sum_{j=1}^{n} \lambda_i \lambda_j = 1$ finally results in

$$\sigma_{D\lambda}^2 = \sigma_0^2 - \sum_{i=1}^{n} \sum_{j=1}^{n} \lambda_i \lambda_j C(\mathbf{u}_i - \mathbf{u}_j), \tag{A5}$$

where the last term is equal to $\sigma_{\bar{q}}^2$ from equation (4).

List of Variables

Dimensionless

n number of local flux data collected

n_e effective number of independent data; numerical index "j," if present, denotes different variogram components

n_w number of wells in transect

m number of nested variogram components

N number of realizations in conditional stochastic simulation

i,j,k index variables

λ_i data declustering weights; ordinary block kriging weights for estimating q_T

t Student's t variable

t' cubic transformations of t accounting for distribution skewness

b weighted data coefficient of skewness; coefficient of skewness of PFM measured flux histogram after declustering

a auxiliary variable

T transect (spatial averaging domain for which discharge is sought)

$\Delta\sigma^2$ "missing variance"; portion of flux variability σ_{DT}^2 over transect not represented by declustered data variance $\sigma_{D\lambda}^2$

Lengths and Areas

x,y horizontal and vertical coordinates

$\mathbf{u}_{(i,j)},\mathbf{v}$ spatial coordinate vectors of components x and y

$\mathbf{h}$ spatial separation vector between two locations

a_h,a_v horizontal and vertical correlation lengths of $q()$; numerical index "j," if present, denotes different variogram components

X,Y transect length and depth

A transect area

Fluxes and Discharges

q spatially random function representing local fluxes within transect

μ_0 expectation (ensemble mean) of q; mean of pdf(q)

$q_{i\text{PFM}}$ measured local fluxes from PFM field deployment

q_{ins} measured local fluxes from PFM field deployment after normal score transformation

$\bar{q}_{\text{PFM}}$ Weighted mean of $q_{i\text{PFM}}$; ordinary block kriging estimate of q_T from field data; mean of declustered PFM data histogram; obtained from equation (3) by using $q_{i\text{PFM}}$ instead of q_i

q_i fictitiously sampled fluxes from unconditional realizations at actual PFM measurement locations

$\bar{q}$ weighted mean of q_i; ordinary block kriging estimate of q_T for each unconditional realization

q_T spatial mean of local fluxes over transect for each unconditional realization

q_{Tc} spatial mean of local fluxes over transect for each conditional realization

e estimation error (difference between estimate $\bar{q}$ and true value q_T for each unconditional realization)

$\bar{q}_{Tc}$ mean of q_{Tc} obtained from averaging over many conditional realizations

q_α — α-quantile of q_{Tc} (q_{Tc} which is not exceeded with probability α)

Q — discharge across transect

Flux and Normal Score Variances

$C()$ — spatial covariance function of q; numerical index "j," if present, denotes different variogram components

$C_{ns}()$ — spatial covariance function of normal scores (i.e., of local fluxes after transformation to standard normal distribution)

$\gamma()$ — (semi) variogram of q

σ_0^2 — variance of q; variogram sill if existing; numerical index "j," if present, denotes different variogram components

σ_{0ns}^2 — same as σ_0^2, but for normal scores of fluxes

$\sigma_{\bar{q}}^2$ — variance of $\bar{q}$; ensemble variance of the declustered data mean; corresponds to calculating $\bar{q}$ from equation (3) for each realization using unconditionally simulated data at the sampling locations and then taking the variance over many realizations

$\sigma_{q_T}^2$ — variance of q_T; ensemble variance of the transect mean of q; corresponds to calculating q_T from equation (1) for each unconditional realization and then taking the variance over many realizations

$\sigma_{\bar{q}q_T}^2$ — covariance between $\bar{q}$ and q_T; corresponds to calculating $\bar{q}$ and q_T from equations (1) and (3) for each unconditional realization and then taking the covariance between them over many realizations

σ_e^2 — variance of estimation error; corresponds to calculating $e = \bar{q} - q_T$ for each unconditional realization and then taking the variance over many realizations; numerical index "j," if present, denotes different variogram components

σ_{DT}^2 — dispersion variance of q over transect; ensemble mean of the spatial variance of local fluxes in the transect; corresponds to taking the variance of all q inside T for each unconditional realization and then averaging the variances over many realizations

$\sigma_{D\lambda}^2$ — declustered data dispersion variance; ensemble mean of the spatial variance of the declustered data; corresponds to taking the variance of the declustered data, which are unconditionally simulated at the sampling locations, for each realization and then averaging the variances over many realizations; numerical index "j," if present, denotes different variogram components

$\sigma_{D\lambda ns}^2$ — same as $\sigma_{D\lambda}^2$, but for normal scores of fluxes

σ_{ec}^2 — variance of q_{Tc} from conditional realizations

s^2 — weighted variance of q_i; declustered data variance for each unconditional realization

s_{PFM}^2 — weighted variance of q_{iPFM}; variance of the PFM measured flux histogram after declustering; obtained from equation (7) by using q_{iPFM} instead of q_i and $\bar{q}_{PFM}$ instead of $\bar{q}$

References

Annable, M. D., K. Hatfield, J. Cho, H. Klammler, B. Parker, J. Cherry, and P. S. C. Rao (2005), Field-scale evaluation of the passive flux meter for simultaneous measurement of groundwater and contaminant fluxes, *Environ. Sci. Technol.*, 39(18), 7194–7201.

Beland-Pelletier, C., M. Fraser, J. Barker, and T. Ptak (2011), Estimating contaminant mass discharge: A field comparison of the multilevel point measurement and the integral pumping investigation approaches and their uncertainties, *J. Contam. Hydrol.*, 122(1–4), 63–75.

Bockelmann, A., T. Ptak, and G. Teutsch (2001), An analytical quantification of mass fluxes and natural attenuation rate constants at a former gasworks site, *J. Contam. Hydrol.*, 53(3–4), 429–453.

Bockelmann, A., D. Zamfirescu, T. Ptak, P. Grathwohl, and G. Teutsch (2003), Quantification of mass fluxes and natural attenuation rates at an industrial site with a limited monitoring network: Aa case study, *J. Contam. Hydrol.*, 60(1–2), 97–121.

Borden, R. C., R. A. Daniel, L. E. LeBrun, and C. W. Davis (1997), Intrinsic biodegradation of MTBE and BTEX in a gasoline-contaminated aquifer, *Water Resour. Res.*, 33(5), 1105–1115.

Cai, Z., R. D. Wilson, M. A. Cardiff, and P. K. Kitanidis (2011), Increasing confidence in mass discharge estimates using geostatistical methods, *Ground Water*, 49(2), 197–208.

Chen, L., and J. Shao (1999), Bootstrap minimum cost estimation of the average chemical concentration in contaminated soils, *Environmetrics*, 10(2), 153–161.

Chiles J. P., and P. Delfiner (1999), *Geostatistics—Modeling Spatial Uncertainty*, 720 pp., Wiley-Interscience, N.Y.

Deutsch, C. V. (2004), "A statistical resampling program for correlated data: spatial_bootstrap," Center for Computational Geostatistics Annual Report 6, Univ. of Alberta, Edmonton, available at http://www.uofaweb.ualberta.ca/ccg//pdfs/2004%20401-Spatial_Bootstrap.pdf.

Deutsch, C. V., and A. G. Journel (1992), *GSLIB—Geostatistical Software Library and User's Guide*, 340 pp., Oxford Univ. Press, N.Y.

Efron, B., and R. J. Tibshirani (1998), *An Introduction to the Bootstrap*, 456 pp., CRC Press, N.Y.

Einarson, M. D., and D. M. Mackay (2001), Predicting impacts of groundwater contamination, *Environ. Sci. Technol.*, 35(3), 66A–73A.

Emery, X. (2007), Conditioning simulations of Gaussian random fields by ordinary kriging, *Math. Geol.*, 39(6), 607–623.

Goltz, M. N., M. E. Close, H. Yoon, J. Huang, M. J. Flintoft, S. Kim, and C. Enfield (2009), Validation of two innovative methods to measure contaminant mass flux in groundwater, *J. Contam. Hydrol.*, 106(1–2), 51–61.

Goovaerts, P. (1997), *Geostatistics for Natural Resources Evaluation*, 496 pp., Oxford Univ. Press, N.Y.

Hatfield, K., M. D. Annable, J. Cho, P. S. C. Rao, and H. Klammler (2004), A direct method for measuring water and contaminant fluxes in porous media, *J. Contam. Hydrol.*, 75(3–4), 155–181.

Herold, M., T. Ptak, and P. Grathwohl (2008), A comparison of mass flow rate estimates based on point scale and integral measurements, *Grundwasser*, 13(4), 231–250 (in German).

Interstate Technology and Regulatory Council (ITRC) (2010), Use and Measurement of Mass Flux and Mass Discharge, MASSFLUX-1, 154 pp., Integrated DNAPL Site Strategy Team, Washington, D.C., available at http://www.itrcweb.org.

Jarsjö, J., M. Bayer-Raich, and T. Ptak (2005), Monitoring groundwater contamination and delineating source zones at industrial sites: Uncertainty analyses using integral pumping tests, *J. Contam. Hydrol.*, 79(3–4), 107–134.

Journel, A. G. (1994), Resampling from stochastic simulations, *Environ. Ecol. Stat.*, 1(1), 63–91.

Journel, A., and C. J. Huijbregts (1978), *Mining Geostatistics*, 660 pp., Academic, London, U.K.

Journel, A. G., and M. E. Rossi (1989), When do we need a trend model in kriging?, *Math. Geol.*, 21(7), 715–739.

Kitanidis, P. K. (1997), *Introduction to Geostatistics: Applications to Hydrogeology*, 272 pp., Cambridge Univ. Press, Cambridge, U.K.

Kitanidis, P. K., and K. F. Shen (1996), Geostatistical interpolation of chemical concentration, *Adv. Water Resour.*, 19(6), 369–378.

Klammler, H., K. Hatfield, M. McVay, and J. Luz (2011), Approximate upscaling of geo-spatial variables applied to deep foundation design, in *Georisk: Assessment and Management of Risk for Engineered Systems and Geohazards*, vol. 5, pp. 163–172, Taylor and Francis, Oxon, U.K. doi:10.1080/17499518.2010.546266.

Kübert, M., and M. Finkel (2006), Contaminant mass discharge estimation in groundwater based on multi-level measurements: A numerical evaluation of expected errors, *J. Contam. Hydrol.*, 84(1–2), 55–80.

Li, K. B., and L. M. Abriola (2009), A multistage multicriteria spatial sampling strategy for estimating contaminant mass discharge and its uncertainty, *Water Resour. Res.*, *45*, W06407, doi:10.1029/2008WR 007362.

Li, K. B., P. Goovaerts, and L. M. Abriola (2007), A geostatistical approach for quantification of contaminant mass discharge uncertainty using multilevel sampler measurements, *Water Resour. Res.*, *43*, W06436, doi:10.1029/ 2006WR005427.

Rao, P. S. C., J. W. Jawitz, C. G. Enfield, R. W. Falta Jr., M. D. Annable, and A. L. Wood (2002), Technology integration for contaminant site remediation: Cleanup goals and performance criteria, in *Groundwater Quality: Natural and Enhanced Restoration of Groundwater Pollution*, edited by S. F. Thornton and S. E. Oswald, pp. 571–578, IAHS Publication 275, Oxfordshire, U.K.

Schwede, R. L., and O. A. Cirpka (2010), Stochastic evaluation of mass discharge from pointlike concentration measurements, *J. Contam. Hydrol.*, *111*(1–4), 36–47.

Stroo, H. F., M. Unger, C. H. Ward, M. C. Kavanaugh, C. Vogel, A. Leeson, J. A. Marqusee, and B. P. Smith (2003), Remediating chlorinated solvent source zones, *Environ. Sci. Technol.*, *37*(11), 224A–230A.

Teutsch, G., T. Ptak, R. Schwarz, and T. Holder (2000), Ein neues integrales Verfahren zur Quantifizierung der Grundwasserimmission: I. Beschreibung der Grundlagen, *Grundwasser 4*(5), 170–175 (in German).

Troldborg, M., W. Nowak, N. Tuxen, P. L. Bjerg, R. Helmig, and P. J. Binning (2010), Uncertainty evaluation of mass discharge estimates from a contaminated site using a fully Bayesian framework, *Water Resour. Res.*, *46*, W12552, doi:10.1029/2010WR009227.

U.S. Environmental Protection Agency (EPA) (1998), Technical protocol for evaluating natural attenuation of chlorinated solvents in groundwater, Cincinnati, Ohio, available at http://www.epa.gov/superfund/health/con-media/gwdocs/protocol.htm.

U.S. Environmental Protection Agency (EPA) (2004), The DNAPL remediation challenge: Is there a case for source depletion?, 88 pp., Cincinnati, Ohio.

Willink, R. (2005), A confidence interval and test for the mean of an asymmetric distribution, *Comm. Stat.Theory Methods*, *34*(4), 753–766.

Yanagihara, H., and K. H. Yuan (2005), Four improved statistics for contrasting means by correcting skewness and kurtosis, *British J. Math. Statist. Psychol.*, *58*(2), 209–237.

Zhou, X. H., and P. Dinh (2005), Nonparametric confidence intervals for the one- and two-sample problems, *Biostatistics*, *6*(2), 187–200.

Zhu, J., and G. D. Morgan (2004), A nonparametric procedure for analyzing repeated measures of spatially correlated data, *Environ. Ecol. Stat.*, *11*(4), 431–443.

M. D. Annable and J. Cho, Department of Environmental Engineering Sciences, University of Florida, 217 Black Hall, Gainesville, FL 32611-6450, USA.

S. A. Cabaniss, Department of Chemistry and Chemical Biology, University of New Mexico, MSC03 2060, Albuquerque, NM 87131, USA.

J. A. Guimarães da Luz and H. Klammler, Department of Environmental Sciences and Sustainable Development, Federal University of Bahia, Rua José Seabra, Barreiras, Bahia, 47805-100 Brazil. (haki@gmx.at)

K. Hatfield and M. Newman, Department of Civil and Coastal Engineering, University of Florida, 365 Weil Hall, Gainesville, FL 32611-6450, USA.

A. Peacock, Microbial Insights, Inc., 2340 Stock Creek Boulevard, Rockford, TN 37853-3044, USA.

J. Ranville and V. Stucker, Department of Chemistry and Geochemistry, Colorado School of Mines, 1500 Illinois Street, Golden, CO 80401, USA.

P. S. C. Rao, Department of Civil Engineering, Purdue University, 550 Stadium Mall Drive, West Lafayette, IN 47907-2045, USA.

A trigonometric interpolation approach to mixed-type boundary problems associated with permeameter shape factors

Harald Klammler,[1,2,3] Kirk Hatfield,[1,2] Bassel Nemer,[1,2] and Simon A. Mathias[4]

[1] Hydraulic conductivity is a fundamental hydrogeological parameter, whose in situ measurement at a local scale is principally performed through injection tests from screened probes or using impermeable packers in screened wells. The shape factor F [L] is a proportionality constant required to estimate conductivity from observed flow rate to injection head ratios, and it depends on the geometric properties of the flow field. Existing approaches for determination of F are either based on geometric or mathematical simplifications and are limited to particular assumptions about the flow domain's external boundaries. The present work presents a general semianalytical solution to steady state axisymmetric flow problems, where external boundaries may be nearby and of arbitrary combinations of impermeable and constant head type. The inner boundary along the probe or well may consist of an arbitrary number of impermeable and constant head intervals resulting in a mixed-type boundary value problem, for which a novel and direct solution method based on trigonometric interpolation is presented. The approach is applied to generate practical nondimensional charts of F for different field and laboratory situations. Results show that F is affected by less than 5% if a minimum distance of 10 probe or well diameters is kept between the injection screen and a nearby boundary. Similarly, minimum packer lengths of two well diameters are required to avoid increasing F by more than 10%. Furthermore, F is determined for laboratory barrel experiments giving guidelines for achieving equal shape factors as in field situations without nearby boundaries. F for the theoretical case of infinitely short packers is shown to be infinitely large.

1. Introduction

[2] Hydraulic conductivity K [L/T] with its horizontal and vertical variability is a parameter of paramount importance for the modeling and management of a large number of natural and engineered processes, including infiltration, irrigation, drainage, groundwater extraction and injection, soil compaction, landfill impermeabilization, and contaminant transport [*Sedighi et al.*, 2006; *Sudicky*, 1986; *Hvorslev*, 1951]. Under saturated conditions, i.e., below the water table of an aquifer, classically, pump or slug tests with their well-known individual advantages and drawbacks are performed for investigations of K at different scales [*Weight and Sonderegger*, 2001]. Accordingly, these tests may be performed on an entire well or on various portions of a well screen by use of single- or double-packer systems [*Butler*

[1]Department of Civil and Coastal Engineering, University of Florida, Gainesville, Florida, USA.
[2]Interdisciplinary Program in Hydrologic Sciences, University of Florida, Gainesville, Florida, USA.
[3]Department of Environmental Sciences and Sustainable Development, Federal University of Bahia, Barreiras, Brazil.
[4]Department of Earth Sciences, Durham University, Durham, UK.

et al., 2009; *Price and Williams*, 1993]. Different types of small-diameter (i.e., lower centimeter range) drive point (also called push-in or direct-push) probes have also been proposed for quick and flexible investigation of K in unconsolidated media at highly local (i.e., <1 m^3) scales. Because of the small spatial scale the associated flow systems reach steady state rapidly and do not require a permanent installation of an injection well or piezometers around it. Using such push-in probes with short injection screen intervals near the probe tips, *Hinsby et al.* [1992] demonstrate a "mini slug test" method, while *Butler et al.* [2007] and *Dietrich et al.* [2008] apply a "direct-push permeameter" and a "direct-push injection logger," respectively. The difference between the latter two direct-push methods is that the injection logger uses the variability in recorded ratios of injection pressures and flow rates as a function of depth to estimate variability in local K without, however, assigning absolute K values. The "push-in permeameter" uses two additional head observations along the probe to also quantify absolute values of K. Whenever the goal is to estimate such absolute values of K, a so-called shape factor (often denoted by F [L]) is required, which serves as the proportionality constant between ratios of observed injection flow rates Q [L^3/T] to injection heads ϕ_0 [L] and K. Thus, knowing F and observing Q/ϕ_0, K can be estimated from

$$K = \frac{Q}{\phi_0 F} \qquad (1)$$

[3] More precisely, ϕ_0 hereby is the excess hydraulic head at the screen because of pumping with respect to ambient (no pumping) conditions, and as used in the sequel, it is assumed to be constant both in time (steady state) as well as over the injection screen surface.

[4] Many variants of in situ measurement methods for K have been developed, and a correspondingly large number of theoretical models have been invoked for test interpretation, i.e., determination of F. However, a common feature of virtually all methods is that an axially (or rotationally) symmetric potential flow field is generated through injection or extraction of water from some cylindrical well or probe surface, which may or may not include the tip of a well or probe. An important and complicated issue is the presence of mixed-type boundary conditions, which arises because of the simultaneous presence of both no-flow and constant head segments along the inner boundary associated with the well or probe surface.

[5] Early models which persist until the present day apply geometric approximations of the cylindrical (constant head) injection surface by spheroids [*Mathias and Butler*, 2006; *Hvorslev*, 1951]. Other approximations use distributed point sources along a line [*Zlotnik and Ledder*, 1996] or over a cylindrical surface [*Peursem et al.*, 1999]. More recently, computationally intensive finite difference or finite element methods have been used to better reproduce geometric and hydraulic boundary conditions at the injection screen [*Liu et al.*, 2008; *Ratnam et al.*, 2001]. Another approach that has proved popular involves conversion of the mixed-type boundary problem along the well or probe into a single-type boundary problem by either assuming approximate flux distributions along constant head boundary segments [*Chang and Chen*, 2002, 2003; *Rehbinder*, 2005; *Perina and Lee*, 2006; *Mathias and Butler*, 2007] or assuming approximate head distributions along no flow boundary segments [*Rehbinder*, 1996]. While the analytical approaches of *Rehbinder* [1996, 2005] use predefined continuous functions for these approximations, *Chang and Chen* [2002, 2003], *Perina and Lee* [2006], and *Mathias and Butler* [2007] use adjustable functions by making them piecewise constant in a semianalytical approach.

[6] In what follows we take advantage of a general solution given by *Zaslavsky and Kirkham* [1964] to derive different forms of steady state solutions to the axisymmetric flow problem for all possible combinations of constant head and impermeable top, bottom, and lateral boundaries at arbitrary distances. We further present a novel, direct, and simple semianalytical method related to trigonometric interpolation to directly deal with the mixed boundary value problem along the injection well or probe (i.e., without requiring conversion into a single-type boundary value problem as done in previous work) and use the observed convergence behavior to extrapolate toward exact solutions. Results are applied to investigate effects of nearby boundaries on injection test results and to provide practical charts of shape factors F for different scenarios. Validation is achieved by comparison with equivalent results previously obtained by *Mathias and Butler* [2007] for sufficiently distant boundaries such that they can be ignored. A clarification is also made concerning the divergent series

contained within *Mathias and Butler*'s [2007] previous analytical solution for infinitesimally short packers.

[7] Although injection tests from push-in probes or packered-off screen intervals may be limited to local scales not containing any external boundaries, situations may arise where proximity to a confining layer, a surface water body, or the water table has to be accounted for [*Lui et al.*, 2008]. In particular, injection near constant head boundaries may be strongly distorted because of flow short-circuiting between the screen and the boundary. Similarly, laboratory testing in sand barrels is a routine procedure for injection test calibration, and the effects of nearby impermeable barrel walls deserve particular investigation.

2. General Solution of the Flow Problem

[8] An example of an axisymmetric flow domain is given in Figure 1, where r [L] and z [L] are the radial and vertical coordinates, respectively, being delimited by $a < r < b$ [L] and $0 < z < d$ [L]. To represent the radius of the probe or well, a is used, which is assumed to span the entire distance d between top and bottom boundaries, while b is the radial distance to a lateral boundary. Moreover, h_1 through h_4 [L] delimit different boundary type segments along the well or probe. The governing Laplace equation for steady state flow and isotropic hydraulic conductivity in axisymmetric cylindrical coordinates is

$$\frac{\partial^2 \phi}{\partial r^2} + \frac{1}{r}\frac{\partial \phi}{\partial r} + \frac{\partial^2 \phi}{\partial z^2} = 0, \qquad (2)$$
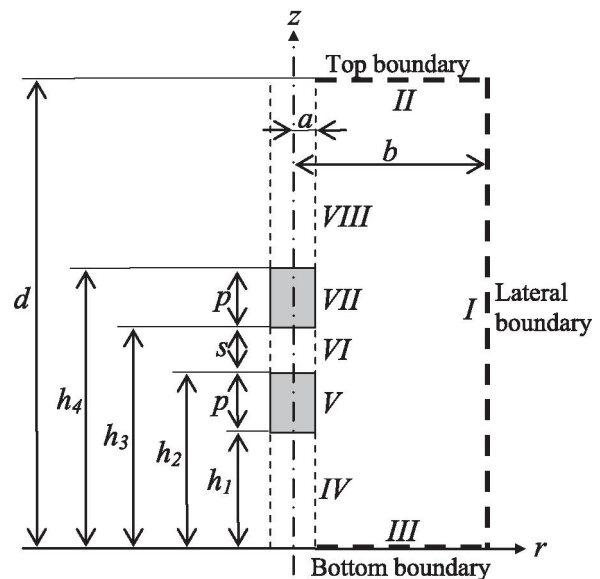

Figure 1. Example of axisymmetric flow domain with double-packer injection from a fully screened well and nearby boundaries. I, constant head or impermeable lateral boundary; II, constant head or impermeable top; III, constant head or impermeable bottom; IV and VIII, constant head open well screen intervals; V and VII, impermeable packers; VI, constant head injection screen interval. The flow domain is delimited by two coaxial cylinders between $0 < z < d$ and $a < r < b$. For injection from a push-in probe, boundaries IV and VIII are impermeable as well (i.e., $h_1 = 0$ and $h_4 = d$).

where $\phi = \phi(r, z)$ [L] is the hydraulic head distribution in the flow domain. A general solution of equation (2) is given by *Zaslavsky and Kirkham* [1964] as

$$
\begin{aligned}
\phi(r,z) = {} & [c_1 \sin(m_1 z) + c_2 \cos(m_1 z)][c_3 I_0(m_1 r) + c_4 K_0(m_1 r)] \\
& + [c_5 \sinh(m_2 z) + c_6 \cosh(m_2 z)][c_7 J_0(m_2 r) + c_8 Y_0(m_2 r)] \\
& + c_9 z \ln(r/m_3) + c_{10} \ln(r/m_3) + c_{11} z + c_{12},
\end{aligned}
\tag{3}
$$

where c_i for $i = 1, 2, \ldots, 12$ and m_i for $i = 1, 2, 3$ are arbitrary real constants (m_i being positive) and I_0, K_0, J_0, and Y_0 are Bessel functions of order zero [*Dwight*, 1947]. By superimposing solutions of equation (3) with different sets of constants, specific boundary conditions, including arrangements of mixed-type boundary conditions (this becomes clearer in the subsequent discussion), can be met. This will first be done for external boundaries I, II, and III shown in Figure 1 and subsequently for internal boundary segments IV–VIII along the well or probe.

2.1.   External Boundaries

[9]   While the types of internal boundary conditions along the probe are defined by the injection test setup, the types of external boundaries may be different combinations of constant head and impermeable. Both top and bottom boundaries may be considered impermeable, for example, if an injection test is performed in a (thin) stratum between two confining layers. In the case of permeability injection testing of a sealing layer under a landfill, for example, both top and bottom boundaries may be well approximated by two constant head boundaries. A mix of constant head top and impermeable bottom boundary may well represent conditions in a (shallow) unconfined aquifer or beneath surface water bodies. If the distance between injection screen and one or both of top and bottom boundaries is sufficiently small, an impact of the nearby boundary (boundaries) onto the outcome of the injection test may be expected and accounted for by a respective adjustment in the shape factor F. Similarly, modeling an impermeable lateral boundary is of interest for laboratory barrel tests, where either top, bottom, or both boundaries are constant head, while the lateral barrel wall is impermeable. Thus, the external boundary conditions in Figure 1 may be represented as follows: I, constant head (I$_c$) or impermeable (I$_i$) lateral boundary; II, constant head (II$_c$) or impermeable (II$_i$) top boundary; III, constant head (III$_c$) or impermeable (III$_i$) bottom boundary. Mathematically, this can be expressed as

$$
\text{I}_c \quad \phi = 0 \quad \text{at} \quad r = b \quad \text{for} \quad 0 \leq z \leq d,
\tag{4a}
$$

$$
\text{I}_i \quad \frac{\partial \phi}{\partial r} = 0 \quad \text{at} \quad r = b \quad \text{for} \quad 0 \leq z \leq d,
\tag{4b}
$$

$$
\text{II}_c \quad \phi = 0 \quad \text{at} \quad z = d \quad \text{for} \quad a \leq r \leq b,
\tag{5a}
$$

$$
\text{II}_i \quad \frac{\partial \phi}{\partial z} = 0 \quad \text{at} \quad z = d \quad \text{for} \quad a \leq r \leq b,
\tag{5b}
$$

$$
\text{III}_c \quad \phi = 0 \quad \text{at} \quad z = 0 \quad \text{for} \quad a \leq r \leq b,
\tag{6a}
$$

$$
\text{III}_i \quad \frac{\partial \phi}{\partial z} = 0 \quad \text{at} \quad z = 0 \quad \text{for} \quad a \leq r \leq b.
\tag{6b}
$$

[10]   Using extensions of *Kirkham* [1959] and *Boast and Kirkham* [1971], solutions in terms of the hydraulic head ϕ, which honor equations (4), (5) and (6) under all possible scenarios of boundary type combinations, may be based on the following considerations and written as follows.

[11]   1. Considering constant head top and bottom boundaries, i.e., $\phi(z = 0) = \phi(z = d) = 0$ for all $a \leq r \leq b$, of all the terms in z in equation (3), these conditions can be met by $\sin(m_1 z)$ with $m_1 = n\pi/d$ as well as n and N being arbitrary positive integers, such that after superposition

$$
\phi(r,z) = \sum_{n=1}^{N} B_n f_0(m_1 r) \sin(m_1 z), \quad m_1 = n\pi/d.
\tag{7}
$$

[12] B_n are a new set of constants encompassing c_1, c_3, and c_4, and $f_0(m_1 r)$ is a function to be defined involving terms of equation (3) containing $K_0(m_1 r)$ and $I_0(m_1 r)$.

[13]   2. Considering impermeable top and bottom boundaries, i.e., $\partial \phi/\partial z = 0$ at $z = 0$ and $z = d$ for all $a \leq r \leq b$, of the terms in z in equation (3), these conditions can be met by $\cos(m_1 z)$ with $m_1 = n\pi/d$ as well as by $\ln(r/m_3)$ with arbitrary m_3 and by the final (arbitrary) constant, which may be incorporated into m_3. Superposition of these solutions gives

$$
\phi(r,z) = B_0 \frac{\ln(b/r)}{\ln(b/a)} + \sum_{n=1}^{N} B_n f_0(m_1 r) \cos(m_1 z), \quad m_1 = n\pi/d.
\tag{8}
$$

[14] B_n and f_0 are analogous to equation (7), and B_0 is an additional constant; $c_{12} = 0$ and $m_3 = b$ are chosen such that the leading term on the right-hand side becomes zero for $r = b$, as required for a constant zero head boundary at radial distance b. The constant term $\ln(b/a)$ in the denominator is added to simplify expressions in the sequel by taking the ratio to 1 for $r = a$ and allowing for a particular interpretation of B_0.

[15]   3. Considering impermeable top and constant head bottom boundary, i.e., $\phi(z = 0) = 0$ and $\partial \phi/\partial z = 0$ at $z = d$ for all $a \leq r \leq b$, of the terms in z in equation (3), the first (constant head) condition may be met by $\sin(m_1 z)$, $\sinh(m_2 z)$, $z\ln(r/m_3)$, and z, where m_1, m_2, and m_3 may be arbitrary. Among these solutions, however, the second (no flow) condition may only be satisfied by $\sin(m_1 z)$ with $m_1 = (2n - 1)\pi/(2d)$ such that superposition leads to

$$
\phi(r,z) = \sum_{n=1}^{N} B_n f_0(m_1 r) \sin(m_1 z), \quad m_1 = (2n - 1)\pi/(2d).
\tag{9}
$$

[16]   It is observed that equations (7), (8), and (9) meet boundary conditions II and III independent of the choice of the coefficients B_0 and B_n and the function f_0. This allows using f_0 to independently satisfy the type of lateral boundary condition I in equations (7), (8), and (9). From equation (3) and its terms in z retained in equations (7), (8), and (9), it is evident that f_0 has to consist of linear combinations of $K_0(m_1 r)$ and $I_0(m_1 r)$ as follows.

[17] 1. For constant head lateral boundary, i.e., $\phi = 0$ at $r = b$ for all $0 \leq z \leq d$, this can be achieved by imposing $c_3 I_0(m_1 b) + c_4 K_0(m_1 b) = 0$ in equation (3) and results in

$$f_{0c}(m_1 r) = \frac{\frac{K_0(m_1 r)}{K_0(m_1 b)} - \frac{I_0(m_1 r)}{I_0(m_1 b)}}{\frac{K_0(m_1 a)}{K_0(m_1 b)} - \frac{I_0(m_1 a)}{I_0(m_1 b)}} \approx \frac{K_0(m_1 r)}{K_0(m_1 a)}, \qquad (10)$$

where additional constants are included to make $f_{0c} = 1$ at $r = a$ for later convenience. For later convenience and knowing that $dK_0(r)/dr = -K_1(r)$ and $dI_0(r)/dr = I_1(r)$, we also introduce

$$f_{1c}(m_1 r) = -\frac{1}{m_1}\frac{df_{0c}}{dr} = \frac{\frac{K_1(m_1 r)}{K_0(m_1 b)} + \frac{I_1(m_1 r)}{I_0(m_1 b)}}{\frac{K_0(m_1 a)}{K_0(m_1 b)} - \frac{I_0(m_1 a)}{I_0(m_1 b)}} \approx \frac{K_1(m_1 r)}{K_0(m_1 a)}. \qquad (11)$$

[18] 2. For impermeable lateral boundary, i.e., $\partial\phi/\partial r = 0$ at $r = b$ for all $0 \leq z \leq d$, this condition may be achieved by assuring $f_{1i} = -(1/m_1)df_{0i}/dr = 0$ for $r = b$ in equations (7) and (9). Since f_{0i} has to be a linear combination of I_0 and K_0 and because of the respective derivatives given above, f_{1i} has to be a linear combination of I_1 and K_1, such that imposing $c_3 I_1(m_1 b) + c_4 K_1(m_1 b) = 0$ leads to

$$f_{1i}(m_1 r) = -\frac{1}{m_1}\frac{df_{0i}}{dr} = \frac{\frac{K_1(m_1 r)}{K_1(m_1 b)} - \frac{I_1(m_1 r)}{I_1(m_1 b)}}{\frac{K_1(m_1 a)}{K_1(m_1 b)} - \frac{I_1(m_1 a)}{I_1(m_1 b)}} \approx \frac{K_1(m_1 r)}{K_1(m_1 a)}, \qquad (12)$$

where additional constants are used to make $f_{1i} = 1$ for $r = a$. From this, f_{0i} may be obtained by integration as

$$f_{0i}(m_1 r) = \frac{\frac{K_0(m_1 r)}{K_1(m_1 b)} + \frac{I_0(m_1 r)}{I_1(m_1 b)}}{\frac{K_1(m_1 a)}{K_1(m_1 b)} - \frac{I_1(m_1 a)}{I_1(m_1 b)}} \approx \frac{K_0(m_1 r)}{K_1(m_1 a)}. \qquad (13)$$

[19] In the case of equation (8), where top and bottom are already impermeable, an impermeable lateral boundary only makes physical sense if the same flow injected is again extracted by the well or probe (e.g., vertical recirculation well [*Zlotnik and Ledder*, 1996; *Peursem et al.*, 1999]). If this is the case, then it can be shown that $B_0 = 0$, and hence, $\partial\phi/\partial r = 0$ for $r = b$ is again met. The approximations given with equations (10)–(13) are for large values of b/a and become exact for $b \to \infty$, i.e., laterally unbounded flow domains (both $K_0(m_1 b)$ and $K_1(m_1 b)$ approach zero in this case, while both $I_0(m_1 b)$ and $I_1(m_1 b)$ approach infinity).

2.2. Trigonometric Interpolation Approach to the Mixed-Type Internal Boundaries

[20] In equations (7), (8), and (9), the values of the coefficients B_0 and B_n do not affect compliance with the external boundary conditions I, II, and III such that these coefficients can be used to independently meet the internal (mixed) boundary conditions along the device (i.e., for $r = a$). According to Figure 1, for a double-packer test these boundaries are constant head open screen interval at bottom (IV), impermeable bottom packer (V), constant head injection screen interval (VI), impermeable top packer (VII), and

constant head open screen interval at top (VIII). Mathematically, this may be written as

$$\text{IV} \quad \phi = \phi_{\text{IV}} \quad \text{at} \quad r = a \quad \text{for} \quad 0 \leq z \leq h_1, \qquad (14)$$

$$\text{V} \quad \frac{\partial\phi}{\partial r} = 0 \quad \text{at} \quad r = a \quad \text{for} \quad h_1 \leq z \leq h_2, \qquad (15)$$

$$\text{VI} \quad \phi = \phi_0 \quad \text{at} \quad r = a \quad \text{for} \quad h_2 \leq z \leq h_3, \qquad (16)$$

$$\text{VII} \quad \frac{\partial\phi}{\partial r} = 0 \quad \text{at} \quad r = a \quad \text{for} \quad h_3 \leq z \leq h_4, \qquad (17)$$

$$\text{VIII} \quad \phi = \phi_{\text{VIII}} \quad \text{at} \quad r = a \quad \text{for} \quad h_4 \leq z \leq d, \qquad (18)$$

where ϕ_{IV} and ϕ_{VIII} [L] are the constant hydraulic heads in the bottom and top open screen intervals, respectively. In order to determine B_0 and B_n, the respective "raw" solution of $\phi(r, z)$ for a given set of external boundary conditions from equations (7), (8), or (9) is substituted into equations (14)–(18). Considering, for example, the case of impermeable top and bottom boundaries in combination with a constant head lateral boundary, equation (8) (with $f_0 = f_{0c}$ and f_{1c} from equations (10) and (11)) is used to obtain the following system of equations to impose the internal boundary conditions.

$$\phi(a,z) = B_0 + \sum_{n=1}^{N} B_n \cos(m_1 z) = \phi_{\text{IV}}, \quad 0 \leq z \leq h_1, \qquad (19)$$

$$-\frac{\partial\phi}{\partial r}\bigg|_{r=a} = \frac{B_0}{a\ln(b/a)} + \sum_{n=1}^{N} B_n \frac{n\pi}{d} f_{1c}(m_1 a)\cos(m_1 z) = 0,$$
$$h_1 \leq z \leq h_2, \qquad (20)$$

$$\phi(a,z) = B_0 + \sum_{n=1}^{N} B_n \cos(m_1 z) = \phi_0, \quad h_2 \leq z \leq h_3, \qquad (21)$$

$$-\frac{\partial\phi}{\partial r}\bigg|_{r=a} = \frac{B_0}{a\ln(b/a)} + \sum_{n=1}^{N} B_n \frac{n\pi}{d} f_{1c}(m_1 a)\cos(m_1 z) = 0,$$
$$h_3 \leq z \leq h_4, \qquad (22)$$

$$\phi(a,z) = B_0 + \sum_{n=1}^{N} B_n \cos(m_1 z) = \phi_{\text{VIII}}, \quad h_4 \leq z \leq d. \qquad (23)$$

[21] To achieve an exact solution, N must be set to infinity, for which equations (7), (8), and (9) become Fourier series. Although *Sneddon* [1966] discusses solutions to similar systems of equations, analytical solutions for the mixed-type boundary value problems are generally intractable.

[22] However, by limiting N to finite values (i.e., truncating the trigonometric series) and discretizing the device length $0 \leq z \leq d$ into a number N_B (dimensionless) of equidistant intervals delimited by z_{i-} and z_{i+} with $i = 1, 2, \ldots, N_B$, such that $z_{1-} = 0$, $z_{NB+} = d$, $z_{i+} = z_{(i+1)-}$, $z_{i+} - z_{i-} = d/N_B$, and $z_i = (z_{i+} + z_{i-})/2$, equations (19)–(23) may be

rewritten in a discretized form by simply substituting z_i for z everywhere. With this, equations (19)–(23) constitute a linear system of N_B equations in $N + 1$ unknown coefficients. This system may be regarded in a curve-fitting context, where it is the goal to determine the unknown coefficients of equation (8) (for finite N) to best approximate the right-hand sides of equations (19)–(23) containing punctual information about ϕ and $\partial\phi/\partial r$. For $N_B > N + 1$, this may be done in a linear regression (i.e., least squares) sense, while for $N_B = N + 1$, curve fitting becomes exact and thus transitions into the field of trigonometric interpolation. For $N_B < N + 1$, the system is underdetermined. In the present

$$\frac{Q_{\mathrm{VIII}}}{2\pi aK} = -\int_{h_4}^{d} \left.\frac{\partial\phi}{\partial r}\right|_{r=a} \mathrm{d}z = \frac{B_0(d - h_4)}{a\ln\frac{b}{a}}$$
$$-\sum_{n=1}^{N} B_n f_{1c}(m_1 a)\sin(m_1 h_4) = 0. \tag{25}$$

[24] The result is an extended system of $N_B + 2$ linear equations in $N_B + 2$ unknowns, for which many standard methods are available for the solution. For example, equations (19)–(25) may be converted from summation into matrix form $[\mathbf{A}] \times [\mathbf{B}] = [\mathbf{C}]$, giving

$$\begin{bmatrix}
1 & \cos(\pi z_1/d) & \cos(2\pi z_1/d) & \cdots & \cos(N z_1/d) & -1 & 0 \\
\vdots & \vdots & \vdots & & \vdots & \vdots & \vdots \\
1 & \cos(\pi z_{N_{\mathrm{IV}}}/d) & \cos(2\pi z_{N_{\mathrm{IV}}}/d) & \cdots & \cos(N z_{N_{\mathrm{IV}}}/d) & -1 & 0 \\
\frac{1}{a\ln(b/a)} & \frac{\pi}{d}f_{1c}(\frac{\pi a}{d})\cos(\frac{\pi z_{N_{\mathrm{IV}}+1}}{d}) & \frac{2\pi}{d}f_{1c}(\frac{2\pi a}{d})\cos(\frac{2\pi z_{N_{\mathrm{IV}}+1}}{d}) & \cdots & \frac{N\pi}{d}f_{1c}(\frac{N\pi a}{d})\cos(\frac{N\pi z_{N_{\mathrm{IV}}+1}}{d}) & 0 & 0 \\
\vdots & \vdots & \vdots & & \vdots & \vdots & \vdots \\
\frac{1}{a\ln(b/a)} & \frac{\pi}{d}f_{1c}(\frac{\pi a}{d})\cos(\frac{\pi z_{N_{\mathrm{V}}}}{d}) & \frac{2\pi}{d}f_{1c}(\frac{2\pi a}{d})\cos(\frac{2\pi z_{N_{\mathrm{V}}}}{d}) & \cdots & \frac{N\pi}{d}f_{1c}(\frac{N\pi a}{d})\cos(\frac{N\pi z_{N_{\mathrm{V}}}}{d}) & 0 & 0 \\
1 & \cos(\pi z_{N_{\mathrm{V}}+1}/d) & \cos(2\pi z_{N_{\mathrm{V}}+1}/d) & \cdots & \cos(N\pi z_{N_{\mathrm{V}}+1}/d) & 0 & 0 \\
\vdots & \vdots & \vdots & & \vdots & \vdots & \vdots \\
1 & \cos(\pi z_{N_{\mathrm{VI}}}/d) & \cos(2\pi z_{N_{\mathrm{VI}}}/d) & \cdots & \cos(N\pi z_{N_{\mathrm{VI}}}/d) & 0 & 0 \\
\frac{1}{a\ln(b/a)} & \frac{\pi}{d}f_{1c}(\frac{\pi a}{d})\cos(\frac{\pi z_{N_{\mathrm{VI}}+1}}{d}) & \frac{2\pi}{d}f_{1c}(\frac{2\pi a}{d})\cos(\frac{2\pi z_{N_{\mathrm{VI}}+1}}{d}) & \cdots & \frac{N\pi}{d}f_{1c}(\frac{N\pi a}{d})\cos(\frac{N\pi z_{N_{\mathrm{VI}}+1}}{d}) & 0 & 0 \\
\vdots & \vdots & \vdots & & \vdots & \vdots & \vdots \\
\frac{1}{a\ln(b/a)} & \frac{\pi}{d}f_{1c}(\frac{\pi a}{d})\cos(\frac{\pi z_{N_{\mathrm{VII}}}}{d}) & \frac{2\pi}{d}f_{1c}(\frac{2\pi a}{d})\cos(\frac{2\pi z_{N_{\mathrm{VII}}}}{d}) & \cdots & \frac{N\pi}{d}f_{1c}(\frac{N\pi a}{d})\cos(\frac{N\pi z_{N_{\mathrm{VII}}}}{d}) & 0 & 0 \\
1 & \cos(\pi z_{N_{\mathrm{VII}}+1}/d) & \cos(2\pi z_{N_{\mathrm{VII}}+1}/d) & \cdots & \cos(N\pi z_{N_{\mathrm{VII}}+1}/d) & 0 & -1 \\
\vdots & \vdots & \vdots & & \vdots & \vdots & \vdots \\
1 & \cos(\pi z_N/d) & \cos(2\pi z_N/d) & \cdots & \cos(N\pi z_N/d) & 0 & -1 \\
\frac{h_1}{a\ln(b/a)} & f_{1c}(\frac{\pi a}{d})\sin(\frac{\pi h_1}{d}) & f_{1c}(\frac{2\pi a}{d})\sin(\frac{2\pi h_1}{d}) & \cdots & f_{1c}(\frac{N\pi a}{d})\sin(\frac{N\pi h_1}{d}) & 0 & 0 \\
\frac{d-h_4}{a\ln(b/a)} & -f_{1c}(\frac{\pi a}{d})\sin(\frac{\pi h_4}{d}) & -f_{1c}(\frac{2\pi a}{d})\sin(\frac{2\pi h_4}{d}) & \cdots & -f_{1c}(\frac{N\pi a}{d})\sin(\frac{N\pi h_4}{d}) & 0 & 0
\end{bmatrix} \times \begin{bmatrix} B_0 \\ B_1 \\ \vdots \\ B_N \\ \phi_{\mathrm{IV}} \\ \phi_{\mathrm{VIII}} \end{bmatrix} = \begin{bmatrix} 0 \\ \vdots \\ 0 \\ \vdots \\ \phi_0 \\ \vdots \\ \phi_0 \\ 0 \\ \vdots \\ 0 \end{bmatrix}, \tag{26}$$

work, N_B is set equal to the number of unknown coefficients, i.e., $N + 1$ or N, depending on whether B_0 is present or not. Note that the discretized well flux approach presented previously by *Mathias and Butler* [2007] represents a special case of the more general approach presented above.

[23] Before solving the resulting system it is noted that ϕ_{IV} and/or ϕ_{VIII} in equations (19)–(23) are only known if the top and bottom open screen intervals are connected to constant head top and/or bottom boundaries. For impermeable top and bottom boundaries, ϕ_{IV} and ϕ_{VIII} are initially unknown, but instead, two additional equations can be formulated imposing zero total (i.e., integrated over z) inflows or outflows Q_{IV} and Q_{VIII} $[L^3/T]$ from the open screen intervals below and above the packers, respectively:

$$\frac{Q_{\mathrm{IV}}}{2\pi aK} = -\int_{0}^{h_1} \left.\frac{\partial\phi}{\partial r}\right|_{r=a} \mathrm{d}z = \frac{B_0 h_1}{a\ln\frac{b}{a}} + \sum_{n=1}^{N} B_n f_{1c}(m_1 a)\sin(m_1 h_1) = 0, \tag{24}$$

such that matrix division immediately results in the required vector $[\mathbf{B}] = [\mathbf{A}]^{-1}[\mathbf{C}]$ of unknown coefficients B_0 and B_n from equation (8) as well as ϕ_{IV} and ϕ_{VIII}. Note that the index "N_x" with z in equation (26) stands for the number of discretization points z_i between $z = 0$ and the top of the boundary segment denoted by "x" in Figure 1 (e.g., $z_{N_{\mathrm{IV}}}$ is the last discretization point at the top of boundary segment IV, and $z_{N_{\mathrm{IV}}+1}$ is the first one in boundary segment V; also $N_{\mathrm{VIII}} = N$). Appendix A gives further details about the convergence behavior for increasing N and shows that resulting flow field parameters, including F, may be hyperbolically extrapolated to the exact solutions corresponding to $N \to \infty$. Thus, the problem is solved in a novel and direct way without the need for previous conversion of the mixed-type into a single-type boundary value problem.

[25] For the simpler configuration of injection from a push-in probe (i.e., in the absence of open screen intervals above and below the packers), equations (19), (23), (24), and (25) become irrelevant. The system reduces to equations

(20), (21), and (22) with $h_1 = 0$ and $h_4 = d$, which further corresponds to a respective reduction of equation (26). In the opposite case of infinitesimally short packers such that $h_1 = h_2$ and $h_3 = h_4$, all boundary segments along the probe are of the constant head type, and the problem reduces to a single-type boundary value problem. Under this scenario (and known ϕ_{IV} and ϕ_{VIII}) the present trigonometric interpolation approach becomes identical to performing the discrete Fourier (in particular sine or cosine) transform on $\phi(a, z_i)$. The discrete Fourier transform is again known to become identical to the (classic) Fourier decomposition of a continuous periodic function if $N_B \rightarrow \infty$. The latter is performed in Appendix B to obtain a fully analytical solution and discussion of the infinitesimally short packer problem.

2.3. Shape Factor F

[26] Integrating local radial fluxes $q_{pr} = -\partial\phi/\partial r$ leaving the probe (i.e., for $r = a$), the injection flow rate Q $[L^3/T]$ may be written as

$$Q = -2\pi a K \phi_0 \int_{h_2}^{h_3} \left.\frac{\partial\phi_u}{\partial r}\right|_{r=a} dz, \tag{27}$$

where $\phi_u = \phi(r, z)/\phi_0$ (dimensionless). By substituting equation (27) into equation (1) a general expression of F is obtained.

$$F = -2\pi a \int_{h_2}^{h_3} \left.\frac{\partial\phi_u}{\partial r}\right|_{r=a} dz. \tag{28}$$

[27] In the simpler case of injection through a single screen from a push-in probe (or packers extending to top and bottom boundaries) and in the case of using shorter packers between impermeable top and bottom boundaries the integration limits in equation (28) may be set from zero to d, for which the following simplified expressions are found.

[28] Constant head top and bottom boundaries

$$F = 4\pi a \sum_{n=1}^{N} B_{nu} f_1(m_1 a), \quad m_1 = (2n - 1)\pi/d, \tag{29}$$

[29] Impermeable top and bottom boundaries

$$F = \frac{2\pi d}{\ln\frac{b}{a}} B_{0u}, \tag{30}$$

[30] Impermeable top and constant head bottom boundary

$$F = 2\pi a \sum_{n=1}^{N} B_{nu} f_1(m_1 a), \quad m_1 = (2n - 1)\pi/(2d), \tag{31}$$

where $B_{0u} = B_0/\phi_0$ and $B_{nu} = B_n/\phi_0$, i.e., dimensionless coefficients for unit injection head. As above, f_1 in equations (29) and (31) is chosen from equations (11) and (12) to honor a constant head or impermeable lateral boundary, respectively. Interesting to note is that equation (30) only depends on B_{0u}, which by inspecting equation (8) with

$r = a$ in a Fourier series context, is seen to represent the mean head along the device (for unit ϕ_0). In other words, B_0 is the head required at a fully screened probe to inject an equal flow rate Q as from a partially screened probe using an injection head ϕ_0. Also, for a fully screened probe, B_n for $n > 0$ in equation (8) become zero, and the solution correctly collapses to radial flow toward a fully penetrating well in a confined aquifer with a constant head outer boundary. Equation (30) further reflects that b/a needs to be finite in order to achieve flow (i.e., $F > 0$) for a finite injection head if both top and bottom boundaries are impermeable.

3. Results and Validation

[31] For the example configuration of equations (19)–(25) (and $N_B = 1280$), Figure 2 depicts resulting dimensionless head ϕ_p/a and dimensionless radial flux q_{pr}/K distributions along a fully screened well with injection between two packers. Solid lines correspond to the case of both top and bottom boundaries impermeable, while dashed lines are for constant head top and bottom boundaries; the lateral boundary is constant head in both cases. Compliance with prescribed constant head and no flow boundary conditions over their respective intervals may be easily verified in both cases along with the fact that ϕ_p is constant but larger than zero in the open screen intervals beyond the packers if the adjacent boundaries are impermeable. Furthermore, Figure 2b suggests (in agreement with Figure A1) that local fluxes at the transitions between constant head and impermeable boundary segments along the probe or well become locally very large or infinite. Finally, it may be correctly observed that flow along the open screen intervals is negative (i.e., inward) if top and bottom boundaries are constant head (dashed line), while the direction of flow along the open screen intervals is inward and then outward for impermeable top and bottom boundaries (solid line) to meet the condition of zero total inflow and outflow over those segments as imposed by equations (24) and (25). Figure 3 further illustrates and validates solutions by showing contour plots of $\phi(r, z)$ for different internal and external boundary conditions. Figures 3a and 3b correspond to the solid and dashed lines of Figure 2, respectively. Compliance with external boundary conditions is verified by observing constant head lines approaching impermeable boundaries perpendicularly and by constant head lines becoming parallel to constant head boundaries in their vicinity. Figures 3c and 3d represent two cases of injection from a probe (i.e., packers extend to top and bottom boundaries) where the lateral boundaries are impermeable (e.g., as in laboratory barrel experiments). In Figure 3c both top and bottom are constant head, while in Figure 3d, only the top is constant head and the bottom impermeable.

3.1. Injection From a Probe (Field Conditions)

[32] As shown in Figure A1 of Appendix A, the convergence behavior of F with increasing N is of the same hyperbolic type as with other flow field parameters and may, hence, be conveniently extrapolated to exact solutions for $N \rightarrow \infty$. For an error margin of 1% in extrapolated F values, Figure 4 summarizes the resulting shape factors from equations (29), (30), and (31) for injection from a probe with $h_1 = 0$ and $h_4 = d$ in Figure 1 as a function of s/a
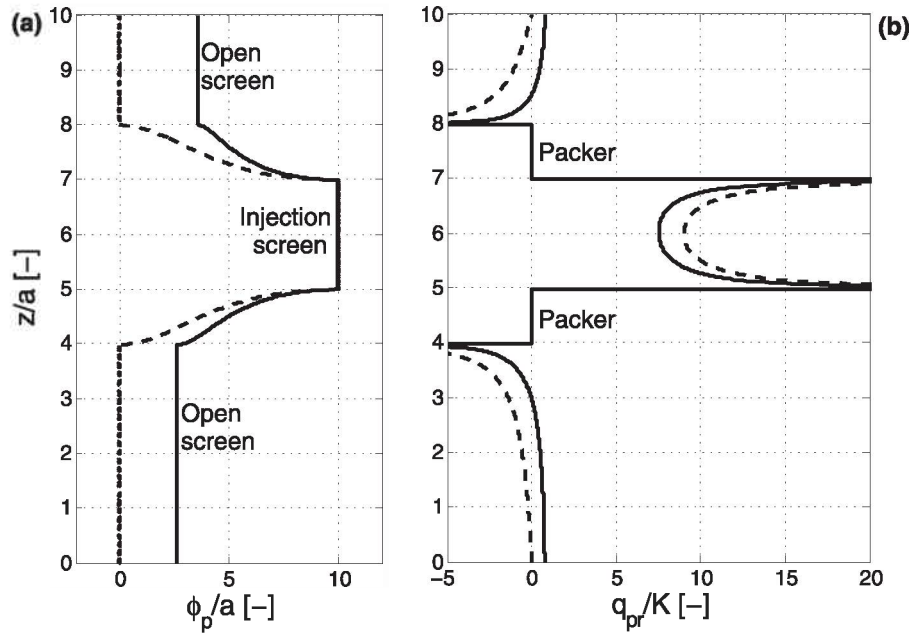
Figure 2. (a) Hydraulic head ϕ_p / a and (b) radial flux q_{pr}/K distributions along fully screened well for injection between two packers. Solid lines are for the example configuration of Appendix A where top and bottom boundaries are impermeable. Dashed lines are for the same configuration but with constant head top and bottom boundaries.

(where $s = h_3 - h_2$ [L] is the length of the injection screen vertically centered between boundaries), d/s, and different top and bottom boundary types (thick solid line, constant head top and bottom; thin solid line, impermeable top and bottom; dashed line, constant head top and impermeable bottom or vice versa). Typical for field conditions, the constant head lateral boundary is located at $b/a = 1000$, which is large enough to not affect the outcome if at least one of top and bottom boundaries is constant head. In case both top and bottom boundaries are impermeable, as stated above, a finite value of b/a is required for $F > 0$. As to be expected, for a given geometric configuration, i.e., s/a and d/s, F/a is always largest if both top and bottom are constant head and smallest if both are impermeable. For increasing values of d/s, however, it is seen that the types of top and bottom boundaries have a decreasing effect on F/a, i.e., the three curves for a given value of s/a converge to a shape factor, whose value increases with s/a and which corresponds to an infinite flow domain, where the types and distances of top and bottom boundaries do not matter anymore. On the other hand, for small values of d/s approaching 1 such that top and bottom boundaries approach the injection screen extremes, F/a approaches infinity if at least one of the boundaries is constant head (flow short-circuiting; see Appendix B). If both boundaries are impermeable, then F approaches a minimum equal to $2\pi d / \ln(b / a)$, which corresponds to the case of a fully penetrating well in a confined aquifer.

[33] While Figure 4 is limited to injection screens vertically centered between top and bottom boundaries, Figure 5 displays F/a for different values of screen length s/a and distance h_1/s to a single nearby boundary. In Figure 5, $d/s = 50$ is set to be large enough for the distant boundary to not have a significant impact on results (compare Figure 4), and the lateral boundary is located at infinity. Thick lines correspond to the injection screen approaching a constant head boundary, while thin lines are for nearby impermeable boundaries. It is seen that for large values of h_1/s, values of F/a agree with those from Figure 4 for large values of d/s; as h_1 decreases, the screen approaches one of the boundaries. As to be expected, if the approached boundary is constant head, the thick lines indicate that F/a increases (up to a theoretically infinite value for $h_1 = 0$; see Appendix B), and if the boundary is impermeable, then F/a decreases to a minimum value. In general, it may be observed from Figure 5 that the proximity of the injection screen to an impermeable or constant head boundary does not significantly affect F by more than an absolute value of $\pm a$ as long as $h_1/s > 5$. By multiplying the abscissa by s/a of each line, F/a is obtained as a function of h_1/a. The double arrows in Figure 5 are located at $h_1/a = 20$, which appears to be the limit, below which the relative impact on F because of a nearby boundary exceeds approximately 5%. As conductivity measurements may vary over several orders of magnitude, the latter interpretation in terms of h_1/a seems to be more useful in practice.

[34] For the absence of any nearby boundaries, Figure 6 gives a graphical validation of the present approach against previous ones defined by *Hvorslev* [1951] (spheroidal approximation),

$$F = \frac{2\pi s}{\ln\left[\frac{s}{2a} + \sqrt{1 + \left(\frac{s}{2a}\right)^2}\right]} = \frac{2\pi s}{a \sinh\left(\frac{s}{sa}\right)}, \tag{32}$$

by the American Society for Testing and Materials (ASTM) [*Chapuis and Chenaf*, 2003] (equal surface area spherical approximation),

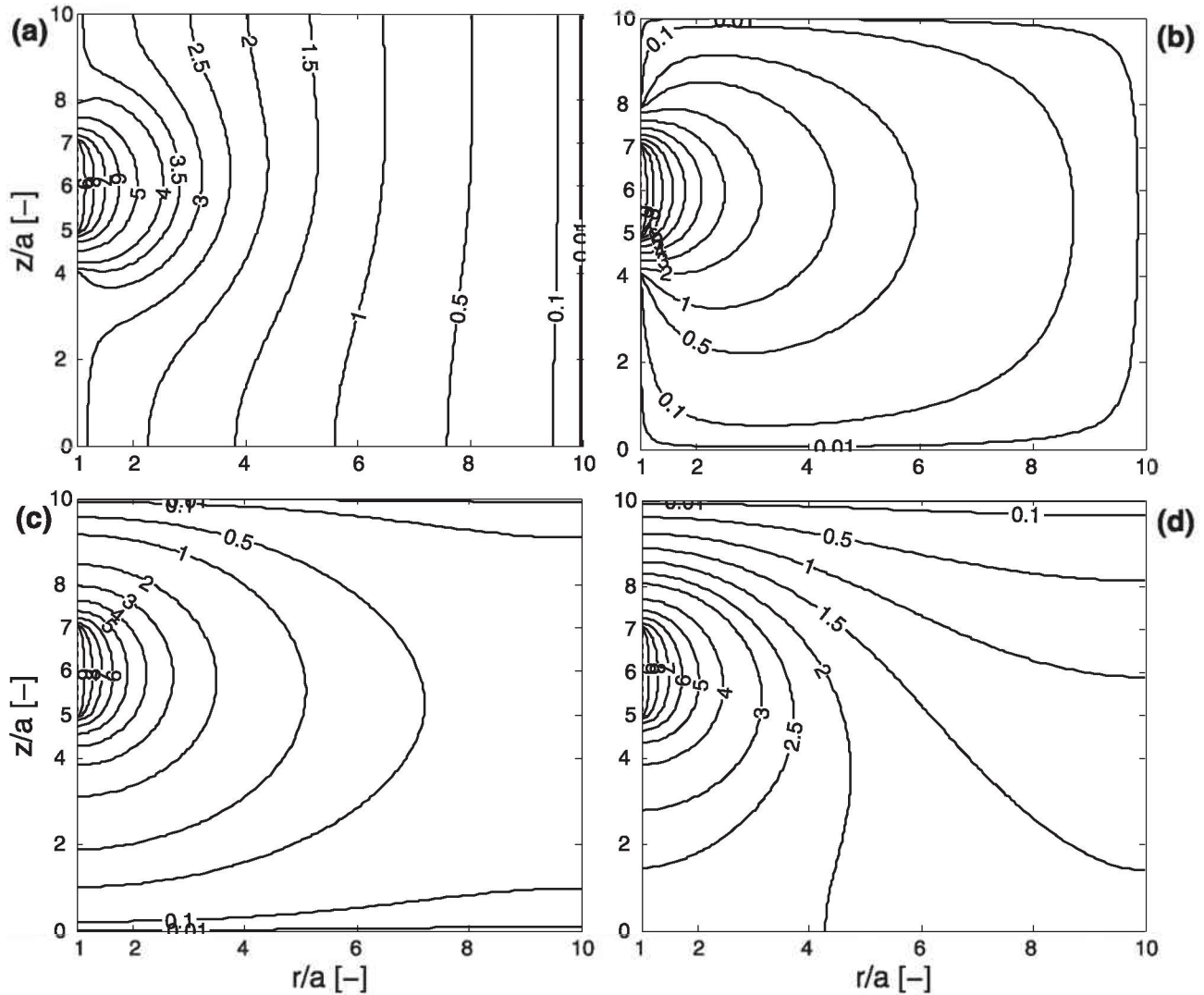$$F = 2\pi\sqrt{2sa} \approx 8.9\sqrt{sa}, \tag{33}$$

Figure 3. Solutions of $\phi(r, z)$ for $\phi_0/a = b/a = d/a = 10$ and (a) injection between double packers with impermeable top and bottom and constant head lateral boundaries, (b) injection between double packers with constant head top, bottom, and lateral boundaries, (c) injection from probe with constant head top and bottom and impermeable lateral boundaries, and (d) injection from probe with constant head top and impermeable bottom and lateral boundaries.

and by *Ratnam et al.* [2001] (finite element plus curve fitting),

$$F = 0.5691s + 7.4144\sqrt{sa}. \qquad (34)$$

[35] For *Mathias and Butler*'s [2007] full semianalytical approach as well as *Rehbinder*'s [2005] long packer approximation, no simple expressions are available. Figure 6 illustrates that the ASTM formula is in good agreement down to $s/a \approx 1$, while Hvorslev's formula begins to significantly overestimate F/a below $s/a \approx 2$. The latter is a known shortcoming and is discussed by *Mathias and Butler* [2006], who offer an improvement for Hvorslev's formula for $s/a < 2$. Equation (33) is based on a spherical equal surface approximation of the screen and, hence, becomes increasingly inaccurate as s/a grows. While equations (32) and (33) are based on geometrical simplifications, the other approximations try to honor the exact geometry of the boundaries and rely on more complex mathematical approximations. The

agreement of the results of *Ratnam et al.* [2001] and *Rehbinder* [2005] (thin black line) with the present results is seen to be good over the entire range depicted. Excellent agreement (with, in fact, indistinguishable lines in Figure 6; thick black line) is achieved with the results of *Mathias and Butler* [2007]. Yet another independent validation of the present method may be obtained by comparison with results from a large numerical model for a direct-push permeameter of *Liu et al.* [2008], who report hydraulic heads at two locations along a probe for injection from a short screen. Agreement is good (within 5% of injection head) when assuming impermeable top and bottom boundaries and even better (within 0.5% of injection head) when assuming constant head top and bottom.

3.2. Injection From a Probe (Laboratory Conditions)

[36] Calibration of injection probes under field conditions is problematic, as true values of hydraulic conductivity are
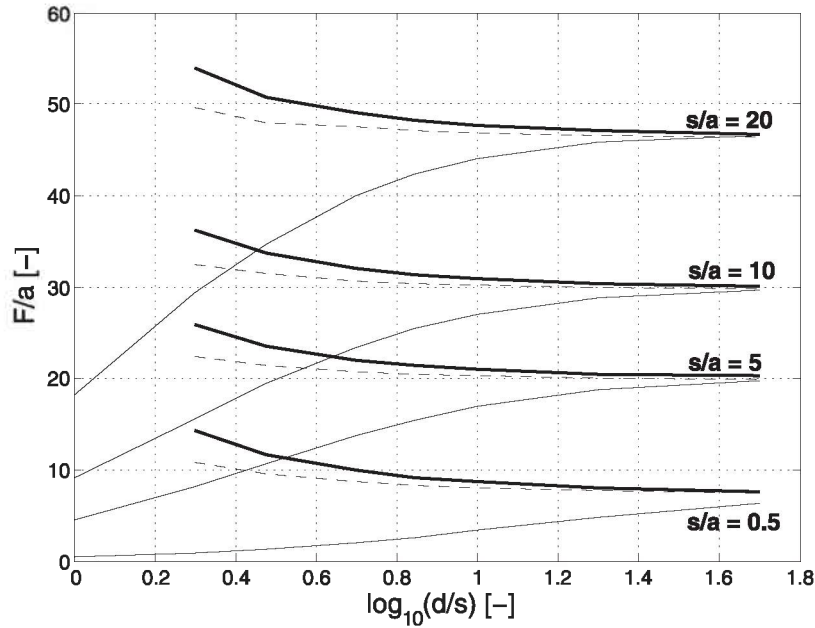
Figure 4. F/a for injection from vertically centered single-screen probe (no open screen intervals except for injection screen) as a function of s/a and $\log_{10}(d/s)$ and for different top and bottom boundary conditions (constant head lateral boundary at $b/a = 1000$). Thick solid line, constant head top and bottom; thin solid line, impermeable top and bottom; dashed line, constant head top and impermeable bottom (or vice versa).
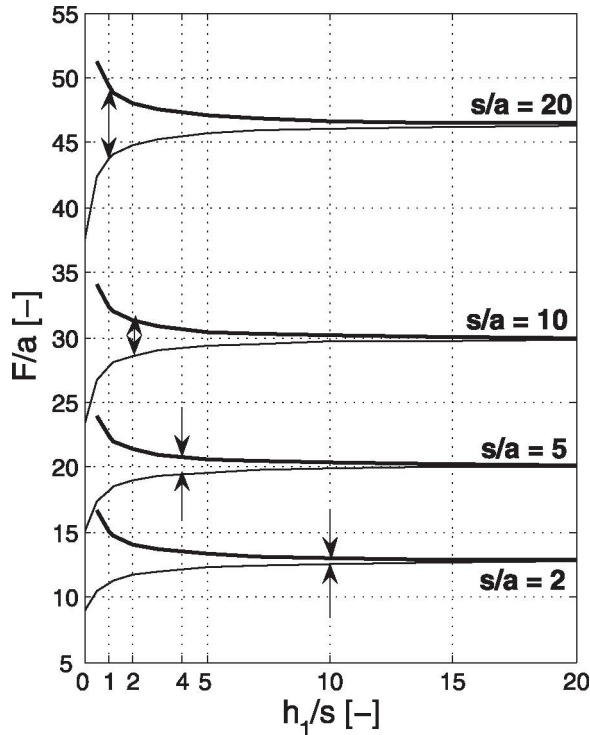

Figure 5. F/a for injection from noncentered single-screen probe (no open screen intervals except for injection screen) as a function of s/a and distance to boundary h_1/s ($d/s = 50$ and lateral boundary at infinity). Thick solid line, approaching constant head boundary; thin solid line, approaching impermeable boundary. Double arrows indicate locations of $h_1/a = 20$.

generally not available. Laboratory barrel experiments are convenient because the entire barrel packed with test material above a bottom gravel pack may be used as a column in a constant or falling head conductivity experiment for obtaining independent and relatively reliable measurements of K. Figure 7 depicts F/a for different screen and barrel geometries (s/a, d/a, and b/a) as well as boundary conditions at the barrel bottom (gravel pack or not). The top boundary is always constant head (i.e., water level above test material), while the barrel wall represents an impermeable boundary. The thick black line is the same as in Figure 6 and corresponds to a field situation where external boundaries do not have a significant impact. For the remaining lines, two lines with a particular color and pattern are given to correspond to the same boundary and barrel geometries (see legend). The top line of each pair of lines corresponds to a constant head bottom boundary, while the bottom one corresponds to an impermeable bottom. Obviously, the particular barrel geometry and type of bottom boundary condition significantly affect F, and hence, they need to be accounted for explicitly in the test interpretation. However, it is interesting to note that barrels of $d/b = 1$ with impermeable bottoms (bottom blue lines) as well as barrels of $d/b = 2$ with constant head bottoms (top green lines) lead to shape factors very close to field conditions in the absence of nearby boundaries (black line). For $b/a > 25$ this holds with high accuracy for $s/a < 10$ and up to an approximate error of 10% for $s/a < 20$. Thus, designing a barrel test of known K_{lab} such that its shape factor is equal to F under field conditions allows for an extremely simple injection test interpretation as $K_{field} = K_{lab} Q_{field} \phi_{0lab} / (Q_{lab} \phi_{0field})$. This avoids dealing with probe specific shape factors in laboratory and field practice.
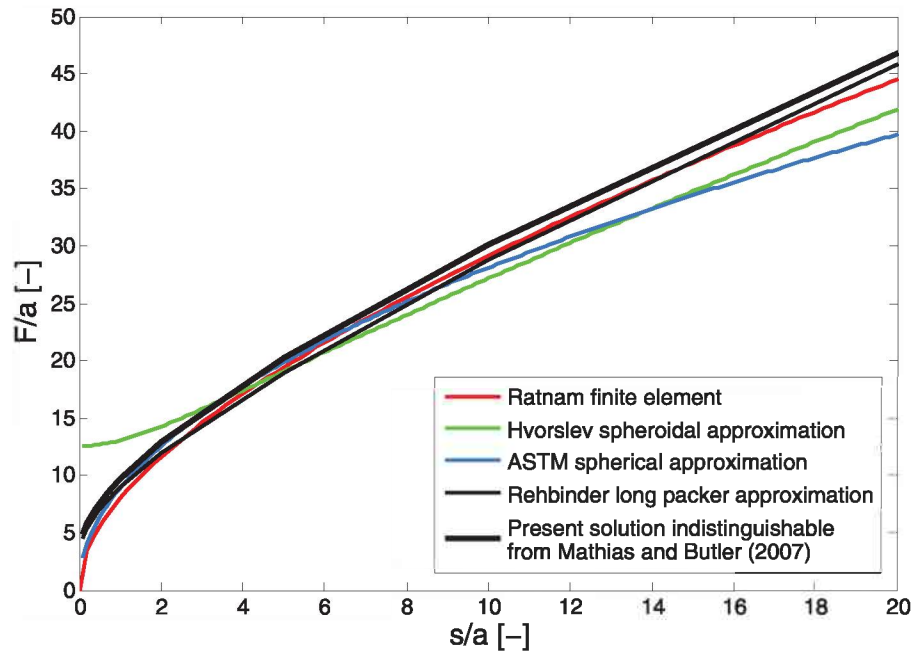
Figure 6. F/a from different approaches for injection from probe and different injection screen geometries. All boundaries are constant head and distant with $d/s = 50$ and $b/a >> 1$.

3.3. Injection Using Single or Double Packers

[37] The solid lines in Figure 8 summarize shape factors F/a from the present solutions for cases of injection from a screen interval of length s delimited by two impermeable packers of finite (and equal) length p with open screen intervals above and below the packers. While F/a is a function of b/a even if $b/a >> 1$ when both top and bottom boundaries are impermeable, Figure 8 considers all boundaries constant head with $b/a >> 1$ and $d/s = 50$, i.e., far away from the screen. Shorter packers (smaller p/s), as expected, increase F/a in an approximately constant manner, which indicates that changes in packer length only affect the flow fields in the vicinity of the screen ends, thus being essentially independent of s/a unless s/a is very small. It is interesting to note for practice that above $p/s \approx 1$, F is only slightly affected by the finite length of the packers; especially for $s/a > 5$, the difference in F to longer packers is consistently smaller than approximately a. By multiplying the values of p/s in Figure 8 with s/a from the abscissa, lines of F/a over s/a for constant values of p/a are obtained. The circles and squares represent points on such lines for $p/a = 1$ and 4, respectively. Similar to Figure 5, it may be observed that the influence of packer length on F may be more conveniently expressed in relative terms using p/a instead of the perhaps more intuitive first choice p/s. In particular, it can be inferred from the circles and squares in Figure 8 that $p/a = 1$ and 4, for example, correspond to increases in F by approximately 20% and 10%, respectively, with respect to $p >> a$. The influence of nearby top or bottom boundaries on double-packer injection tests depends on a series of parameters (s/a, p/a, h_1/a, and type of boundary approached) and is best evaluated individually for a given test configuration (i.e., s/a and/or p/a). For injection between a packer and an impermeable

bottom layer (single packer test), F/a may also be found from Figure 8 by entering the chart with $p/(2s)$ instead of p/s and $2s/a$ instead of s/a and then halving the respective outcome for F/a. This is a consequence of the fact that the flow field for a single-packer injection test corresponds exactly to one half of the flow field of a double-packer injection test.

[38] Figure 8 is also valuable for the situation of injection from a probe if p is taken to represent the impermeable probe tip length under the injection screen. For this case, a lower bound for F/a is found by assuming that the inner boundaries above and below these fictitious packers are impermeable, while an upper bound for F/a is found by assuming that the inner boundaries above and below the fictitious packers are constant head, i.e., infinitely conductive. In reality, the inner boundary above the top packer is impermeable (probe casing), and below the bottom packer (i.e., below the probe tip) is the transition to a cylinder of some finite conductivity. From this, it may be concluded that errors in F because of the conceptual assumption of a long probe tip beneath the injection screen become less than a for $p/s \geq 1$ (given $s/a \geq 5$) or less than 10% for $p/a \geq 4$.

[39] The scenario of double-packer injection with distant boundaries is also considered by *Mathias and Butler* [2007] and by *Rehbinder* [1996] for a short-packer approach, and their results are used for additional validation of the present results in Figure 8. While Rehbinder's short-packer solution (shown as dashed lines for $p/s = 0.05$ and 1) presents moderate agreement, the results of *Mathias and Butler* [2007] are again indistinguishable from the present ones. However, as shown in Appendix B, *Mathias and Butler*'s [2007] result for infinitesimally short packers contains an unsatisfactorily divergent infinite series. The 10,000 terms
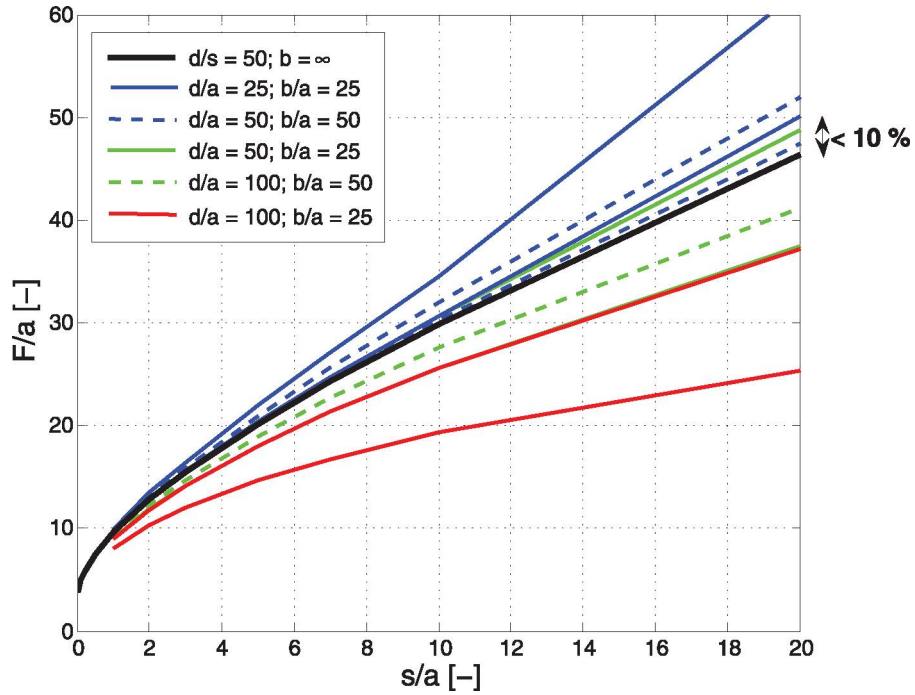
Figure 7. F/a for injection in laboratory barrel setups of different geometries s/a, d/a, and b/a as well as different bottom boundary types. Top and lateral boundaries are always constant head and impermeable, respectively. For each line pattern and color, there are two lines; the top line is for constant head bottom boundary (e.g., gravel pack hydraulically connected to constant head upper boundary), and the bottom line is for impermeable bottom boundary (no gravel pack). The bottom dashed blue and top dashed green lines are practically indistinguishable, which is also true for the bottom solid green and top solid red lines.
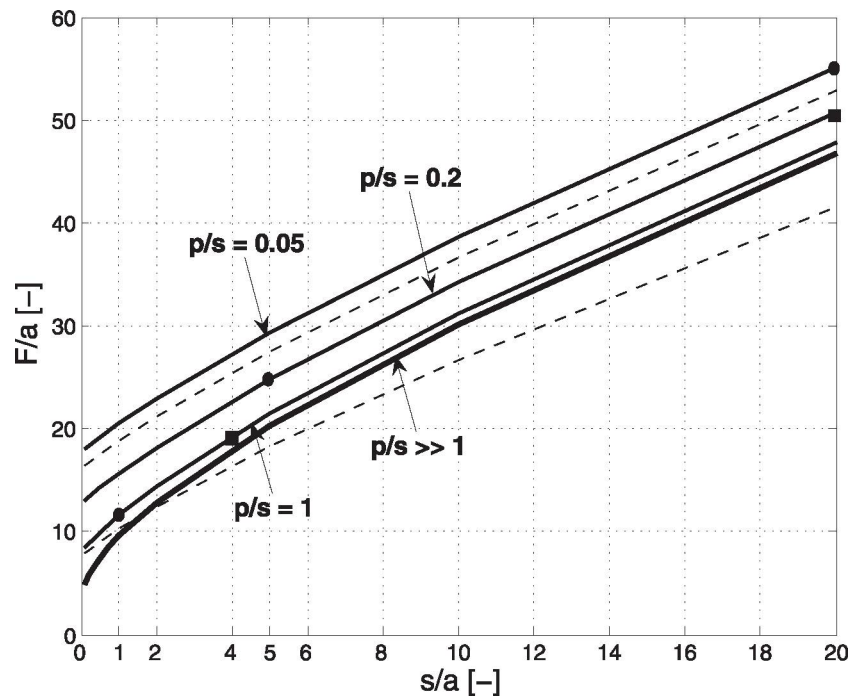

Figure 8. F/a for different injection screen (s/a) and packer (p/s) geometries from the present approach with all boundaries constant head and distant at $d/s = 50$ and $b/a \gg 1$ (solid lines; indistinguishable from the full solution of *Mathias and Butler* [2007]). Dashed lines are *Rehbinder*'s [1996] short-packer approximation for $p/s = 0.05$ and 1. Circles indicate locations of $p/a = 1$, and squares indicate $p/a = 4$.

used to approximate the infinite series in their equations (21) and (31) are insufficient to achieve convergence for very small values of p/s. However, the regression relationship given in their equation (40) accurately approximates the case when $p/s = 0.005$ and should be assumed for $p/s = 0.005$ (as opposed to $p/s = 0$, which is what is currently stated in their paper). Fortunately, this does not impair the validity and relevance of *Mathias and Butler*'s [2007] results for all practical purposes.

3.4. Anisotropic Conductivity

[40] In practice it is common to encounter situations where hydraulic conductivity in the horizontal direction K_r $[L/T]$ is significantly different (e.g., several orders of magnitude larger) than its vertical counterpart K_z $[L/T]$. Given the respective anisotropy ratio $\rho^2 = K_z/K_r$ (dimensionless), a scaling of the horizontal coordinate to $r' = r\rho$ while maintaining $z' = z$ allows for treating the resulting flow domain as isotropic with conductivity K_r (such that continuity of flows after scaling is assured [*Hvorslev*, 1951]). Thus, the present approach remains generally valid if hydraulic conductivity is axially anisotropic with the principal anisotropy axes being horizontal and vertical. In particular, results for F/a reported above remain directly applicable if $a' = a\rho$ is used instead of a such that equation (1) estimates K_r to subsequently obtain $K_z = \rho^2 K_r$. However, ρ is generally not known before hand and needs to be assumed or measured independently.

4. Summary

[41] Subsurface hydraulic conductivity K is a fundamental hydrogeological parameter whose in situ measurement is generally performed through injection tests from screened probes or well screen intervals delimited by impermeable packers. While K is directly proportional to an observed ratio of injection flow rate Q to injection head ϕ_0, it is also proportional to the shape factor F, which is determined by the geometry of the injection flow field and, hence, the geometry of the injection device (internal boundary conditions) as well as the flow domain (external boundary conditions). For the purpose of evaluating F over a wide range of scenarios, the present work presents general solutions to the axisymmetric steady state flow problem for arbitrary combinations of external boundary types and distances. The internal boundary may consist of an arbitrary number of impermeable and constant head intervals. The resulting mixed-type boundary value problem is solved directly in a novel and relatively simple way using a trigonometric interpolation approach. This avoids previous conversion into a single boundary type problem as required with recent alternative approaches and allows for a simple (hyperbolic) extrapolation from approximate to exact results. Through an adequate scaling of the radial coordinate the approach becomes generally valid for flow domains with anisotropic conductivity, where K is different between the vertical and horizontal directions.

[42] A series of dimensionless charts is given to allow for a quick determination of F for different injection screen geometries s/a under a range of scenarios: (1) injection from a probe (or using long double packers) centered between different combinations of impermeable and constant head top and bottom boundaries at different distances,

(2) injection from a probe (or using long double packers) near a single impermeable or constant head boundary, (3) injection in laboratory barrel experiments with all boundaries nearby, the lateral being impermeable, and (4) injection between double packers of different lengths and distant external boundaries. Interesting findings include F being affected by less than 5% if a minimum distance of approximately 10 times the probe diameter is maintained to an impermeable or constant head horizontal boundary (Figure 5). Similarly, using a minimum packer length of twice the well diameter does not affect F by more than 10% compared to longer packers; the latter also applies to the length of impermeable tips of push-in probes below the screen. For injection tests in sand barrels (e.g., for probe calibration) it is found that shape factors within 10% of those of field situations (in the absence of nearby boundaries) may be created by using $d/b = 1$ for impermeable barrel bottoms and $d/b = 2$ if a gravel pack at the barrel bottom is deployed to establish a constant head boundary (with water freely draining out of barrel).

[43] Comparison and validation of results is performed against a number of existing approximate, semianalytical, and numerical approaches available for scenarios where the influence of external boundaries is negligible. Notably, respective shape factors of the present approach are identical to those obtained by the method of *Mathias and Butler* [2007]. However, for extreme cases of very short packers, *Mathias and Butler*'s [2007] solution was found to be incomplete. We present a respective correction in the form of a fully analytical solution for the limit of infinitesimally short packers (see Appendix B).

Appendix A: Convergence Behavior

[44] For the wide range of boundary configurations investigated, it was observed that the B_n coefficients always converge to zero as n increases and that particular flow field parameters (e.g., F or local heads and fluxes) converge hyperbolically toward a stable value for $N_B \to \infty$ (such hyperbolic convergence is also observed by *Boast and Kirkham* [1971]). Figure A1 represents examples of the latter for arbitrarily chosen $b/a = d/a = \phi_0/a = 10$, $h_1/a = 4$, $h_2/a = 5$, $h_3/a = 7$, and $h_4/a = 8$, i.e., for injection from a screen of length $2a$ delimited by two packers of length a, which are asymmetrically located in a stratum between two confining layers. Depicted as functions of $1/N_B$ are the relative heads ϕ/a (dashed lines) and relative fluxes q/K (dot-dashed lines) for $z/a = 4.5$, 6, and 8 (indicated in the indices), i.e., for the center of the bottom packer, the center of injection interval, and the top extreme of top packer, respectively. N_B is increased from an initial value of 10 through consecutive multiplication by 2 until 1280 (circles). It is observed that all ϕ/a and q/K approach a relatively straight line toward the left when plotted over $1/N_B$. This allows for simple linear extrapolation of two consecutive data points onto $1/N_B = 0$, i.e., the exact solutions for $N_B \to \infty$, and a sufficiently large value of N_B is reached when two consecutive extrapolated values are within a prescribed margin. An exception to this is q_8/K, which provides some evidence that flow is singular (infinite flux) at the transitions between impermeable and constant head boundaries along the well or probe. As infinite fluxes
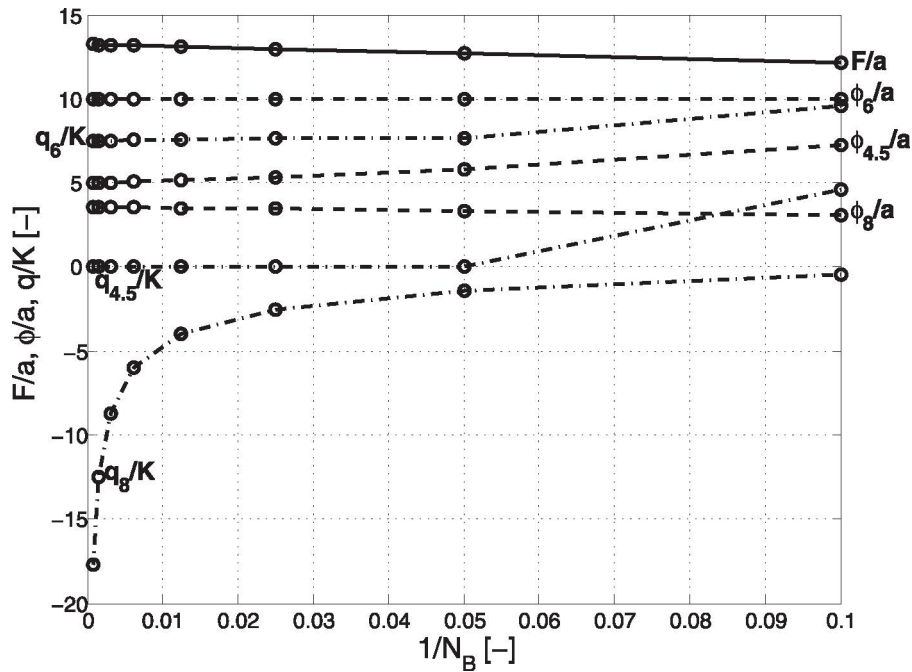
Figure A1. Hyperbolic convergence of F/a, ϕ/a, and q/K with N_B for injection using double packers between two confining layers, where indices indicate locations $z/a = 4.5$, 6, and 8 along the well. Here $b/a = d/a = \phi_0/a = 10$, $h_1/a = 4$, $h_2/a = 5$, $h_3/a = 7$, and $h_4/a = 8$.

are physically impossible, the governing equation (equation (3)) of the present approach appears to be invalid near the extremes of well casings and packers. However, F converges to a finite value, indicating that injection flow does remain finite (integrable). Successful validation of F against independent (e.g., numerical) methods, which do not produce these flow singularities, demonstrates that equation (3) is, indeed, physically valid everywhere else (i.e., at all non-singular locations) in the flow domain. Although not a necessary requirement, maximum convergence with N_B is achieved if the screen and packer limits coincide with discretization interval limits and if average values over discretization intervals are used for any location inside a respective interval. An attempt to lower required N_B by enlarging interval spacing distant from the screen and packers (as done by *Mathias and Butler* [2007]) leads into the context of trigonometric interpolation for unevenly spaced data and was not further pursued as computational time was found not to act as a limiting factor.

Appendix B: Analytical Solution for Infinitesimally Short Packers

[45] If $h_1 = h_2$ and $h_3 = h_4$ in Figure 1, the impermeable packers become infinitesimally short, and the internal boundary conditions are all of the constant head type, which is a significant simplification with respect to the general mixed boundary problem. A fully analytical solution is found for this case and provides some interesting theoretical insight on whether total injection flow becomes infinite or not, a topic which *Rehbinder* [1996] and *Mathias and Butler* [2007] are in disagreement about. For the sake of concurrence with these previous studies, consider constant head top, bottom, and lateral boundaries, such that equa-

tions (7) and (10) apply. Equation (10) is identical to 1 for $r = a$ (i.e., along the well surface), and if $N \to \infty$, the coefficients B_n in equation (7) become the coefficients of a sine-Fourier series of the known head distribution along the well ($\phi(a, z) = 0$ for $0 \leq z \leq h_2$ and $h_3 \leq z \leq d$; $\phi(a, z) = \phi_0$ for $h_2 \leq z \leq h_3$), which may be found as

$$B_n = \frac{2\phi_0}{n\pi}[\cos(m_1 h_2) - \cos(m_1 h_3)], \quad m_1 = n\pi/d, \quad (B1)$$

such that the analytical solution of the problem is complete. By using equation (28) a general expression of F is obtained as

$$F = 4a \sum_{n=1}^{\infty} \frac{f_{1c}(m_1 a)}{n}[\cos(m_1 h_2) - \cos(m_1 h_3)]^2. \quad (B2)$$

[46] From equation (11) it may be seen that $f_{1c}(m_1 a)$ converges to 1 as n increases and the squared term in brackets is always positive. This and the fact that $\sum_{n=1}^{\infty} \frac{1}{n} \to \infty$ is sufficient to prove that equation (B2) does not converge; that is, F and, hence, Q are infinitely large in the case of infinitesimally short packers (the only exception to this is the case of $h_2 = h_3$, i.e., when the injection screen interval itself becomes infinitesimally short). Clearly, infinitesimally short packers and infinite injection flows are beyond physical reality; however, the result bears some significance in that practitioners are warned from arbitrarily minimizing packer sizes as, depending on particular site conditions, the governing equation (3) based on Darcy flow may not hold over significant portions of the flow domain near the short packers. These conclusions are also applicable to injection screens immediately next to a top or bottom constant head

boundary where the geometric distance (flow paths) between source (screen) and sink (boundary) is even shorter. Note, however, that flow singularities discussed in Appendix A do not share the property of causing F and Q to be infinite.

[47] In contrast, if both top and bottom boundaries are impermeable, equation (30) dictates that F has to be finite at steady state even for infinitesimally short packers since B_{0u} was found to be the (naturally finite) mean head along the well. Also, the same flow entering the open screen intervals needs to leave them again and reenter the aquifer flow field until meeting the lateral constant head boundary. Using a similar procedure as in equations (B1) and (B2) for constant head top and bottom boundaries, it may be shown that the head difference between the injection screen and the open screen intervals above and below the infinitesimally short packers becomes infinitesimally small, such that the whole well behaves as if injection was uniformly applied along all of it (no packers present). For a given set of parameters a, b, and d the shape factor F is then a maximum, independent of s.

References

Boast, C. W., and D. Kirkham (1971), Auger hole seepage theory, *Soil Sci. Soc. Am. Proc.*, *35* (3), 365–373.

Butler, A. P., S. A. Mathias, A. J. Gallagher, D. W. Peach, and A. T. Williams (2009), Analysis of flow processes in fractured chalk under pumped and ambient conditions, *Hydrogeol. J.*, *17*, 1849–1858, doi:10.1007/s10040-009-0477-4.

Butler, J. J., P. Dietrich, V. Wittig, and T. Christy (2007), Characterizing hydraulic conductivity with the direct-push permeameter, *Ground Water*, *45*, 409–419, doi:10.1111/j.1745-6584.2007.00300.x.

Chang, C. C., and C. S. Chen (2002), An integral transform approach for a mixed boundary problem involving a flowing partially penetrating well with infinitesimal well skin, *Water Resour. Res.*, *38*(6), 1071, doi:10.1029/2001WR001091.

Chang, C. C., and C. S. Chen (2003), A flowing partially penetrating well in a finite-thickness aquifer: A mixed-type initial boundary value problem, *J. Hydrol.*, *271*, 101–118, doi:10.1016/S0022-1694(02)00323-2.

Chapuis, R. P., and D. Chenaf (2003), Variable-head field permeability tests in driven flush-joint casings: Physical and numerical modeling, *Geotech. Testing J.*, *26*(3), 1–12.

Dietrich, P., J. J. Butler, and K. Faiß (2008), A rapid method for hydraulic profiling in unconsolidated formations, *Ground Water*, *46*, 323–328, doi:10.1111/j.1745-6584.2007.00377.x.

Dwight, H. B. (1947), *Tables of Integrals and Other Mathematical Data*, Macmillan, New York.

Hinsby, K., P. L. Bjerg, L. J. Andersen, B. Skov, and E. V. Clausen (1992), A mini slug test method for determination of a local hydraulic conductivity of an unconfined sandy aquifer, *J. Hydrol.*, *136*, 87–106.

Hvorslev, M. J. (1951), Time lag and soil permeability in groundwater observations, *Bull. U.S. Army Corps of Eng. Waterw. Exp. Stn.*, *36*.

Kirkham, D. (1959), Exact theory of flow into a partially penetrating well, *J. Geophys. Res.*, *64*(9), 1317–1327.

Liu, G., G. C. Bohling, and J. J. Butler (2008), Simulation assessment of the direct-push permeameter for characterizing vertical variations in hydraulic conductivity, *Water Resour. Res.*, *44*, W02432, doi:10.1029/2007WR006078.

Mathias, S. A., and A. P. Butler (2006), An improvement on Hvorslev's shape factors, *Geotechnique*, *56*(10), 705–706, doi:10.1680/geot.2006.56.10.705.

Mathias, S. A., and A. P. Butler (2007), Shape factors for constant-head double-packer permeameters, *Water Resour. Res.*, *43*, W06430, doi:10.1029/2006WR005279.

Perina, T., and T. C. Lee (2006), General well function for pumping from a confined, leaky or unconfined aquifer, *J. Hydrol.*, *317*, 239–260, doi:10.1016/j.jhydrol.2005.05.020.

Peursem, D. V., V. Zlotnik, and G. Ledder (1999), Groundwater flow near vertical recirculatory wells: Effect of skin on flow geometry and travel times with implications for aquifer remediation, *J. Hydrol.*, *222*, 109–122.

Price, M., and A. T. Williams (1993), A pumped double-packer system for use in aquifer evaluation and groundwater sampling, *Proc. ICE*, *2*, *101*, 85–92.

Ratnam, S., K. Soga, and R. W. Whittle (2001), Revisiting Hvorslev's intake factors using the finite element method, *Geotechnique*, *51*(7), 641–645.

Rehbinder, G. (1996), The double packer permeameter with narrow packers: Analytical solution for non-steady flow, *Appl. Sci. Res.*, *56*(4), 255–279.

Rehbinder, G. (2005), Relation between non-steady supply pressure and flux for a double packer permeameter: An approximate analytical solution, *Flow Turbul. Combust.*, *74*, 1–20, doi:10.1007/s10494-005-2757-y.

Sedighi, A., H. Klammler, C. Brown, and K. Hatfield (2006), A semi-analytical model for predicting water quality from aquifer storage and recovery system, *J. Hydrol.*, *329*, 403–412, doi:10.1016/j.jhydrol.2006.02.035.

Sneddon, I. N. (1966), *Mixed Boundary Value Problems in Potential Theory*, North-Holland, Amsterdam.

Sudicky, E. A. (1986), A natural gradient experiment on solute transport in a sand aquifer: Spatial variability of hydraulic conductivity and its role in the dispersion process, *Water Resour. Res.*, *22*(13), 2069–2092.

Weight, W. D., and J. L. Sonderegger (2001), *Manual of Applied Field Hydrogeology*, McGraw-Hill, New York.

Zaslavsky, D., and D. Kirkham (1964), The streamline function for axially symmetric groundwater movement, *Soil Sci. Soc. Am. Proc.*, *28*, 156–160.

Zlotnik, V., and G. Ledder (1996), Theory of dipole flow in uniform anisotropic aquifers, *Water Resour. Res.*, *32*(4), 1119–1128.
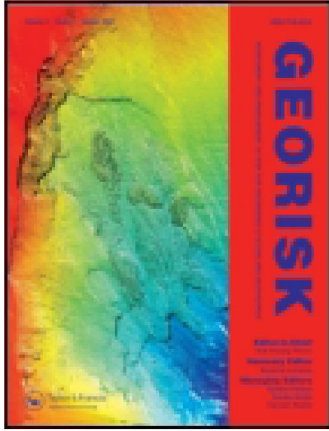
K. Hatfield, H. Klammler, and B. Nemer, Department of Civil and Coastal Engineering, University of Florida, 365 Weil Hall, PO Box 116580, Gainesville, FL 32611, USA. (haki@gmx.at)

S. A. Mathias, Department of Earth Sciences, Durham University, Durham DH1 3HP, UK.

Approximate up-scaling of geo-spatial variables applied to deep foundation design

Harald Klammler [a] [b] [c] , Kirk Hatfield [a] [b] , Michael McVay [a] & Joana Angélica Guimarães da Luz [c]

[a] Department of Civil and Coastal Engineering , University of Florida , Gainesville, FL, 32611-6450, USA

[b] Inter-Disciplinary Program in Hydrologic Sciences , University of Florida , Gainesville, FL, 32611-6450, USA

[c] Department of Environmental Sciences and Sustainable Development , Federal University of Bahia , Barreiras, Bahia, 47805-100, Brazil
Published online: 15 Feb 2011.

PLEASE SCROLL DOWN FOR ARTICLE

Taylor & Francis
Taylor & Francis Group

Approximate up-scaling of geo-spatial variables applied to deep foundation design

Harald Klammler[a,b,c]*, Kirk Hatfield[a,b], Michael McVay[a] and Joana Angélica Guimarães da Luz[c]

[a]Department of Civil and Coastal Engineering, University of Florida, Gainesville, FL 32611-6450, USA; [b]Inter-Disciplinary Program in Hydrologic Sciences, University of Florida, Gainesville, FL 32611-6450, USA; [c]Department of Environmental Sciences and Sustainable Development, Federal University of Bahia, Barreiras, Bahia 47805-100, Brazil

We present a series of simple approximate methods for up-scaling the cumulative distribution function of spatially correlated variables by using an effective number n_e of independent variables. Methods are based on the property of distribution permanence of the gamma and inverse Gaussian distributions under averaging, bootstrap sampling and expansions about the normal and gamma distributions. A stochastic simulation study is used to validate each method, and simple parameters are defined to identify respective ranges of applicability. A practical example is presented where core sample rock strength data are up-scaled to shaft size for probabilistic (risk-based) deep foundation design. Supplemental material is available online.

Keywords: probability of failure; reliability; change of support; geostatistics; Edgeworth; gamma expansion; bootstrap; inverse Gaussian

1. Introduction

Spatial scale is one of the most fundamental parameters in science and engineering. However, data are typically not defined on the same scale of support as required for subsequent processing and decision-making, which raises the question about the effect of changing scales. This is known as the 'change of support' problem, and for the particular case of changing support from small to large, as the 'up-scaling' problem. The topic has received considerable attention in the (geo-) statistical literature (Chilés and Delfiner 1999, Gotway and Young 2002) relating to many fields of application including mining/petroleum engineering, hydrology, agriculture, etc. A classic example is the use of core sample data (1 cm scale) in the determination of total recoverable ore tonnage in a reserve by estimating the cumulative ore content of mining blocks (10 m scale) above a certain cut-off level. Many times core sample data also need to be used as input to numerical models of a desired domain size and limited number of discrete cells (possibly at a 1–100 m scale).

The present work is motivated by a practical problem in geotechnical engineering – in particular, reliability- (or risk-) based deep foundation design (e.g. for bridges; Phoon *et al.* 2003, AASHTO 2004), where it is the goal to assure compliance with a target (maximum permissible) probability of failure p_f of a foundation in order to limit the level of risk of potential damages (e.g. collapse or excessive settlement). For this purpose, both design load Q and foundation resistance R are generally regarded as random variables such that the design goal may be expressed mathematically as

$$P[R < Q] \leq p_f, \qquad (1)$$

where P[ ] denotes the probability (risk) of the event in brackets (load exceeding resistance) to occur. Evaluation of Equation (1) requires knowledge of the exact probability density functions (pdfs) and/or cumulative distribution functions (cdfs) of R and Q. Limiting attention to the resistance side, the sources of uncertainty affecting cdf(R) may be categorised into three principal classes: (1) spatial variability of ground properties, (2) measurement errors and (3) uncertainty in data transformation (Phoon and Kulhawy 1999a, 1999b). A method to estimate a lump value of all uncertainty types is based on past experience and the compilation and analysis of comprehensive load test databases, which allow for assessment of prediction error distributions (and possibly model calibration) for different combinations of site conditions, prediction and construction methods (Zhang *et al.* 2001, 2008, Haldar and Babu 2008). However, inherent shortcomings with this method are that it does not offer an explicit possibility to account for site-specific data and that the characteristics of a site/job have to be matched with a sufficient number of corresponding observations from the past. As an alternative, general approaches have been proposed that evaluate the contributing

*Corresponding author. Email: haki@gmx.at

sources of uncertainty separately and then combine them according to appropriate physical and statistical laws (Phoon and Kulhawy 1999a, 1999b, Foye *et al.* 2006). Approaches that explicitly account for spatial variability are not very abundant and consider shallow foundations in two (Paice *et al.* 1996, Fenton and Griffiths 2002, 2003, Popescu *et al.* 2005, Babu *et al.* 2006) and three (Fenton and Griffiths 2005) dimensions. Fenton *et al.* (2005, 2008) relate their previous results to Load and Resistance Factor Design (LRFD) and investigate effects of data in the vicinity of a shallow foundation to reduce resistance uncertainty. Furthermore, Fenton and Griffiths (2007) present a preliminary finite element study for a single-object deep foundation subject to vertically variable ground properties.

The present work develops methods for investigating the effects of spatial variability on cdf(R), where R is considered as the total ultimate (i.e. deformation independent) axial resistance of a drilled shaft due to side friction and neglecting end bearing (which is common practice with design in Florida limestone, for example; FDOT 2006). Thus, as illustrated in Figure 1, R is known to be equal to the integral of local ground (i.e. rock or soil) strength (or unit side friction) q over the lateral shaft surface area A_s (typically a cylinder; Klammler *et al.* 2010):

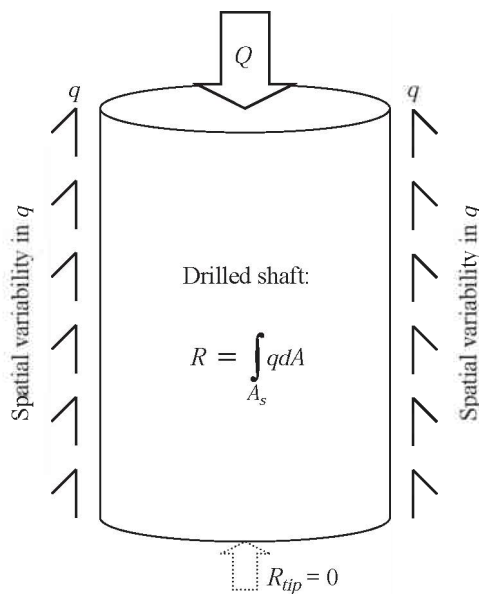$$R = \int_{A_s} q \, dA. \tag{2}$$

Figure 1. Schematic of ultimate (and, hence, deformation independent) axial shaft resistance R due to side friction only. Tip resistance R_{tip} is neglected according to design practice in Florida limestone (FDOT 2006).

However, in early design stages, exact shaft locations are unknown (i.e. in some sense random) and local ground strength data are available, for example, based on core sample analysis from a number of (somehow also randomly located) borings on a site. The resulting problem of Equation (2) is to up-scale the observed cdf(q) at (quasi-) point support to cdf(R) at a support equal to the lateral shaft surface for subsequent use in Equation (1). Note that the problem as stated does focus on transitions in spatial scale; however, support sizes of both q and, consequently, R are considered larger than the representative elementary volume (REV) of what may be considered local strength or unit side friction in rock/soil (e.g. measured with samples obtained from drilling cores). The term 'quasi-point support' for the scale of q will be merely used to designate a scale much smaller than the scale of spatial variability of q (i.e. the separation distance beyond which local values of q become uncorrelated).

Klammler *et al.* (2010) studied the problem of Equation (2) with log-normal up-scaling (Isaaks and Srivastava 1989) using the well-known approximation that the sums (or averages) of log-normal variables are again log-normal. However, this approach is limited to log-normal distributions of q, which may be prohibitive in practice. Approximate analytical models for up-scaling of spatially correlated variables of arbitrary distributions include affine and indirect log-normal corrections (Isaaks and Srivastava 1989) and are recommended for use only when reduction in variance is below 30%, since they do not honor the Central Limit Theorem (Deutsch 2002). More sophisticated approaches, including disjunctive kriging, the discrete Gaussian and mosaic methods, are described in Cressie (1993) and Chilés and Delfiner (1999), while stochastic simulation (Deutsch 2002) is a numerical alternative based on random field generation. However, application of the latter methods is limited in geotechnical design practice due to their elevated complexity, and critical underlying assumptions may not always be based on sufficient data. For a more detailed overview of up-scaling techniques see Gotway and Young (2002).

From this, we detect a lack of spatial up-scaling methods which are both appropriate for any degree of variance reduction (i.e. spatial averaging) and which are simple enough for practical implementation by engineers with limited (geo-) statistical background. By using the concept of effective numbers of independent variables the present paper develops a series of simple approximate methods, which combine the variance reduction principle due to spatial averaging from geostatistics with distributional properties from classical statistics. Averaging (or

summing) of independent variables is a thoroughly studied field (Petrov 1975), and the concept of effective numbers of independent data has been explored previously in many different ways (Bayley and Hammersley 1946, Kitanidis 1997, Deutsch 2004, Pardo-Iguzquiza and Dowd 2004). Two parametric (gamma and inverse Gaussian) and three non-parametric (bootstrap-based and expansions about the normal and gamma distributions) methods are developed in the present work and validated against results from stochastic simulations. The existing method of parametric log-normal up-scaling is also included in the validation study to obtain a comparative evaluation of its performance under different conditions and to study its range of applicability. Limiting assumptions in the present and previous approaches are stationarity of the underlying random process and that the variogram is sufficient to describe spatial variability (Deutsch 2002).

2. Variance reduction and effective number of independent variables

In concordance with the problem of shaft resistance posed in Equation (2), we focus on arithmetic averaging of spatially correlated random functions (regionalised variables; Journel and Huijbregts 1978), which can be expressed in a general form by

$$Z_v(u) = \frac{1}{v} \int_v Z_0(x)dx, \qquad (3)$$

where x is a coordinate vector and $Z_0(x)$ a regionalised variable defined on point support and described by a cumulative distribution function (cdf) with expectation μ_0 and variance σ_0^2 as well as a variogram or, equivalently, a spatial covariance function $C(h)$, with h being a spatial separation vector between two locations x and x'. $Z_v(u)$ is the corresponding effective (i.e. arithmetically averaged) parameter for support size $v = \int_v dx$ centred on coordinate vector u.

Note that v can be a joint or disjoint domain in one, two, or three (or more) dimensions. Equation (2) is a particular case of Equation (3) for $Z_0 = q$, $v = A_s$ and $Z_v = R/A_s$, the latter being equivalent to mean unit side friction over the lateral shaft surface. As such, the present work considers cdf and $C(h)$ of $Z_0(x)$ as reliably known, while the location u of v is random (i.e. unknown or distant from available data). Hence, there is no conditioning to data (unconditional up-scaling) and $Z_0(x)$ can be abbreviated to Z_0 as well as $Z_v(u)$ to Z_v, whose cdf of expectation μ_v and variance σ_v^2 is sought.

It is well known (Deutsch 2002) from the Central Limit Theorem that up-scaling of linearly averaging

variables entails constant expectation ($\mu_v = \mu_0$), while variance, skewness and higher-order cumulants decrease. The simplest case is that of Gaussian random fields where up-scaled distributions are again Gaussian; however, distributions are not generally preserved between scales. The reduced variance σ_v^2 is found from (Deutsch 2002)

$$\sigma_v^2 = \frac{1}{v^2} \int_v \int_v C(x - x')dxdx'. \qquad (4)$$

Equation (4) only depends on $C(h)$ and v and is valid independent of the underlying distribution type. If Equation (4) is applied to a finite number n of uncorrelated random variables it reduces to $\sigma_v^2 = \sigma_0^2/n$, which is the relationship for the variance of a mean estimate in classical statistics requiring the assumption of 'i.i.d.' (independent and identically distributed) variables. By following a concept briefly introduced in the opposite context of estimating a process mean from limited data by Kitanidis (1997) or Deutsch (2004), an effective number of independent variables n_e can be defined as

$$n_e = \frac{\sigma_0^2}{\sigma_v^2}, \qquad (5)$$

which expresses the number of independent random variables that are subject to the same amount of variance reduction when averaged as spatial averaging of a regionalised variable Z_0 with covariance structure $C(h)$ over a domain v.

3. Parametric methods

Data distributions encountered in science and engineering are mostly non-negative and positively skewed with a rather long tail to the right. The log-normal is a two-parameter distribution that has been widely applied to fit these observations before and after up-scaling (direct log-normal up-scaling; Isaaks and Srivastava 1989, Vargaz-Guzmán 2005). However, it is well known that averages of even independent log-normal variables are not exactly log-normally distributed (Santos Filho *et al.* 2005). In contrast, other non-negative and positively skewed two-parameter distributions like the gamma and inverse Gaussian appear to be more appropriate for this type of 'direct' up-scaling than the log-normal distribution, as they possess the property of strict distributional permanence under arithmetic averaging of independent variables (Krishnamoorthy 2006). For example, the average of two or more independent and identically distributed gamma variables is again gamma distributed, however with different parameters. This preservation of distribution type with

up-scaling does not strictly hold for spatially correlated variables, but, motivated by the widely used approximate direct log-normal up-scaling, the present work proposes approximate direct gamma and inverse Gaussian up-scaling. With this, in analogy to the classic direct log-normal (*LN*) up-scaling, given that Z_0 may be assumed to be either gamma (*GA*) or inverse Gaussian (*IG*), the up-scaled cdf is approximated by the same distribution type. This significantly widens the range of applicability of the simplest 'direct' (i.e. using approximate distribution permanence) up-scaling techniques, which honor the Central Limit Theorem for large degrees of variance reduction (such as *LN*, *GA* and *IG* also approach normality as the variance decreases).

For convenience, expressions for pdfs and cdfs of these distributions are given in the online supplemental material. Table 1 summarises the meanings of the two parameters (p_1, p_2) for each distribution (including *LN*) and the relationships to distribution expectation μ and coefficient of variation $CV = \sigma/\mu$ (in order to remain close to common geotechnical practice we prefer the use of CV to σ or σ^2). Direct up-scaling is simply performed by applying $\mu = \mu_v = \mu_0$ and $CV = \sigma_v/\mu_v$ [using Equation (4)] in columns 2 and 3 to estimate distributional parameters p_1 and p_2 such that the cdf and pdf of Z_v are fully defined. Distributional fits/tests can be performed to evaluate which (if any) distribution type best fits Z_0. However, the last column of Table 1 provides simple expressions of the coefficient of skewness *sk* of each distribution in terms of *CV*. The three distributions may be ordered according to increasing *sk* for a given *CV*, thus suggesting the ratio *sk/CV* as an efficient field parameter to discern (up to third order) which distribution may be most adequate for given data. *sk/CV* ≈ 2 suggests a gamma fit, *sk/CV* ≈ 3 an inverse Gaussian and *sk/CV* $\approx 3 + CV^2 > 3$ a log-normal fit.

Table 1. Parameters of *GA*, *IG* and *LN* distributions (Krishnamoorthy 2006).

	p_1	p_2	*sk*
Gamma	μCV^2 (scale)	$\dfrac{1}{CV^2}$ (shape)	$2CV$
Inverse Gaussian	μ (mean)	$\dfrac{\mu}{CV^2}$ (shape)	$3CV$
Log-normal	$\ln \dfrac{\mu}{\sqrt{1 + CV^2}}$ (log-mean)	$\sqrt{\ln(1 + CV^2)}$ (log-std. dev.)	$3CV + CV^3$

4. Non-parametric methods

4.1. Bootstrap

Stochastic simulation is a non-parametric method using the cdf and the variogram of Z_0 to generate realisations of random fields, which are averaged over *v* to obtain a discrete cdf of Z_v in a Monte Carlo sense. However, as initially mentioned, the fact that random field realisations have to be drawn from a population of given cdf and variogram involves a significant degree of computational complexity and software operational skills for (geo-) statistically untrained engineers (the risk of blindly trusting computer outputs is not acceptable). The first non-parametric method proposed here avoids the generation of random field realisations by making use of the effective number of independent variables n_e defined in Equation (5). That is, $C(h)$ is known such that σ_v can be determined from Equation (4) followed by n_e from Equation (5). Instead of arithmetic averaging over *v* in each of *N* random field realisations, arithmetic averaging over n_e independent samples randomly drawn from the cdf of Z_0 is performed *N* times to arrive at a discrete approximation for the cdf of Z_v. If *N* is large enough both the permanence of mean $\mu_v = \mu_0$, the variance reduction criterion of Equation (4) as well as the normalisation of the cdf of Z_v due to the Central Limit Theorem are satisfied by this method. From Equations (4) and (5) it is evident that n_e is generally not an integer, and a solution for how to draw a non-integer number of samples from a population is given in the appendix. Due to the similarities of this approach with the bootstrap method (Efron and Tibshirani 1998) it is hereafter referred to as 'bootstrap'.

4.2. Edgeworth expansion

The second and third non-parametric approaches developed here are based on series expansions of cdfs about normal and gamma distributions respectively, where only a certain number of lower-order moments or cumulants of a cdf are retained. This will result in relatively simple results and is appropriate for most practical situations where limited data do not allow for reliable inference of higher-order moments. The term 'non-parametric' is justified by the fact that no distribution type is assumed for Z_0. If we denote the *i*th centralised moment and the *i*th cumulant of a random variable *Z* of mean μ and variance σ^2 by μ_i and κ_i, respectively, the following relationships apply (Hall 1992): $\kappa_1 = \mu_1 + \mu = \mu$, $\kappa_2 = \mu_2 = \sigma^2$, $\kappa_3 = \mu_3$ and $\kappa_4 = \mu_4 - 3\mu_2^2$, where $\mu_i = E[(Z-\mu)^i]$ with $E[]$ being the expectation operator. Standardised cumulants are

frequently used as κ_i/σ^i and are known as coefficient of skewness sk if $i = 3$ and as excess kurtosis ek if $i = 4$. Important properties of cumulants for the present work are that (1) if Z is scaled by a factor c, then respective cumulants are scaled by factors c^i, i.e. $\kappa_i(cZ) = c^i\kappa_i(Z)$ and (2) cumulants of sums of independent random variables are equal to the respective sums of cumulants, i.e. $\kappa_i(Z_1 + Z_2) = \kappa_i(Z_1) + \kappa_i(Z_2)$. From this, the cumulants of a mean

$$Z_v = \frac{1}{n}\sum_{j=1}^{n} Z_j$$

with Z_j independent and identically distributed are obtained as $\kappa_i(Z_v) = \kappa_i(Z_j)/n^{i-1}$ giving further $sk(Z_v) = sk(Z_j)/n^{1/2}$ and $ek(Z_v) = ek(Z_j)/n$.

For an expansion about the normal distribution, Edgeworth series are known to provide asymptotic approximations to a general class of cdfs and, in the case of averaging n independent variables Z, a general form limited to effects of skewness and excess kurtosis is (Hall 1992)

$$F(t) = F_N(t) - \left\{\frac{sk}{6\sqrt{n}}(t^2 - 1) + \frac{1}{24n}\left[ek(t^3 - 3t) + \frac{sk^2}{3}(t^5 - 10t^3 + 15t)\right]\right\}f_N(t). \tag{6}$$

Here $t = (Z_v - \mu)\sqrt{n}/\sigma$ is the standardised mean Z_v with $F(t)$ being the approximate cdf of t and $F_N()$ and $f_N()$ being the standard normal cdf and pdf, respectively, as defined in the online supplemental material. sk and ek are used for $sk(Z)$ and $ek(Z)$, respectively. While for $n = 1$ no averaging takes place and Equation (6) reduces to approximating the cdf of Z, for large n the corrective terms in the curly brackets vanish and $F(t)$ approaches $F_N(t)$ as required by the Central Limit Theorem. Similarly, for $sk = ek = 0$ skewness and excess kurtosis of Z agree with those of the normal distribution and the second-order Edgeworth expansion reduces to $F(t) = F_N(t)$. In analogy to the bootstrap approach, Equation (6) is applied to the up-scaling problem of the spatially correlated variable Z_0 in an approximate way by using $Z = Z_0$ and $n = n_e$ from Equation (5).

4.3. Gamma expansion

Since low-order expansions about the symmetric normal distribution can be expected to become inaccurate for averages of strongly non-normal variables and insufficient normalisation due to averaging, expansion about the gamma distribution is proposed for positively skewed non-negative variables. Bowers (1966) gives a solution for the approx-

imation $F(w)$ of a general cdf (without averaging) by a non-asymptotic series of gamma functions in the form of

$$\begin{aligned}F(w) = &\ F_{GA}(w, p_2) - A[f_{GA}(w, p_2 + 1) \\ &- 2f_{GA}(w, p_2 + 2) + f_{GA}(w, p_2 + 3)] \\ &+ B[f_{GA}(w, p_2 + 1) - 3f_{GA}(w, p_2 + 2) \\ &+ 3f_{GA}(w, p_2 + 3) - f_{GA}(w, p_2 + 4)]\end{aligned} \tag{7}$$

where terms containing higher-order moments than kurtosis were truncated. The expressions for $F_{GA}(w,p)$ and $f_{GA}(w,p)$ are given in the online supplemental material and are the gamma cdf and pdf, respectively, of shape parameter p for the standardised variable $w = Z\mu/\sigma^2$. This transformation assures that the mean and variance of w are both equal to $\mu^2/\sigma^2 = 1/CV^2$, which are then matched by $F_{GA}(w,p_2)$ with $p_2 = 1/CV^2$ (Table 1). The coefficients A and B are functions of the third and fourth centralised moments of w as well as of p_2. From the relationships between centralised moments and cumulants given above and knowing that $\kappa_3(GA) = 2p_2$ and $\kappa_4(GA) = 6p_2$ [with $\kappa_3(GA)$ and $\kappa_4(GA)$ being the third and fourth cumulants of $F_{GA}(w,p_2)$, respectively] one can rewrite the expressions of Bowers (1966) for A and B as

$$A = \frac{1}{6}(\kappa_3(w) - \kappa_3(GA)) \tag{8}$$

and

$$B = \frac{1}{24}[(\kappa_4(w) - \kappa_4(GA)) - 12(\kappa_3(w) - \kappa_3(GA))]. \tag{9}$$

This shows that corrective terms after $F_{GA}(w,p_2)$ in Equation (7) are weighted by simple functions of the differences between the third and fourth cumulants of the standardised variable w and $F_{GA}(w,p_2)$, the gamma distribution about which the expansion is built. From the relationship between Z and w, one obtains $\kappa_3(w) = sk(Z)/CV^3$ and $\kappa_4(w) = ek(Z)/CV^4$. In addition, with $\kappa_3(GA) = 2/CV^2$ and $\kappa_4(GA) = 6/CV^2$ A and B can be expressed in terms of parameters of Z only.

For the present purpose, Equations (7–9) are generalised to allow for approximating the cdf of some mean Z_v over n independent and identically distributed variables Z by using $w = Z_v\mu/\sigma_v^2 = Z_v\mu n/\sigma^2$, such that $p_2 = \mu^2 n/\sigma^2$ is equal to the common value of mean and variance of w. Taking advantage of the properties of cumulants under scaling and averaging as already discussed, $\kappa_3(w) = sk(Z)n/CV^3$ and $\kappa_4(w) = ek(Z)n/CV^4$ are used in Equations (8) and (7), to account for the effects of skewness and kurtosis reduction due to averaging; thus,

$$A = \frac{n}{6CV^2}\left(\frac{sk}{CV} - 2\right) \qquad (10)$$

$$B = \frac{n}{24CV^2}\left[\left(\frac{ek}{CV^2} - 6\right) - 12\left(\frac{sk}{CV} - 2\right)\right], \qquad (11)$$

where sk and ek equate to $sk(Z)$ and $ek(Z)$, respectively. For $n = 1$ these expressions reduce to Equations (8) and (9) for no averaging and $F(w)$ in Equation (7) becomes an approximation of the cdf of Z. For large n the coefficients A and B increase; however, proportionally large values of p_2 lead to a cancelling out of terms within the brackets of Equation (7), and the basic expansion term $F_{GA}(w,p_2)$ approaches a normal distribution in agreement with the Central Limit Theorem. Independent of n, for $k_3(w) = k_3(GA)$ and $k_4(w) = k_4(GA)$, the first four cumulants of the cdf of w and $F_{GA}(w,p_2)$ are identical leading to $A = B = 0$ and $F(w) = F_{GA}(w,p_2)$. This reduces the approach to the preceding parametric one of directly fitting a gamma distribution to a distribution of Z_v with known mean and variance. In this sense, the non-parametric gamma expansion extends the parametric gamma method by accounting for effects of skewness and kurtosis in addition to simply mean and variance. The parametric (direct) gamma method implicitly assumes that skewness and kurtosis are defined by the gamma distribution and not the properties of Z. Equations (7), (10) and (11) are applied to the up-scaling problem of the spatially correlated variable Z_0 in an approximate way by using $Z = Z_0$ and $n = n_e$ from Equation (5). Note, finally, that in contrast to the bootstrap method both the Edgeworth and gamma expansion methods can directly handle non-integer values of n_e.

5. Simulation study and results

The principal approximation involved in the approaches presented is that averaging of correlated variables is substituted by averaging of an effective number of independent variables. Moreover, the classic direct log-normal method assumes approximate log-normality of means of independent log-normals; also, the non-parametric Edgeworth and gamma expansion methods are limited to a finite number of terms and convergence is not always guaranteed (Hall 1992). To validate these approximations a comprehensive simulation study is performed, in which outcomes of the present approaches are compared to up-scaling by stochastic simulation of 10,000 random field realisations. Gaussian random fields are generated by the method of LU-decomposition with subsequent inverse normal score transformation (Goovaerts 1997) to achieve a target

distribution. A total of 16 test distributions including bimodal, truncated, negatively skewed and discrete distributions of $CV \leq 2$ and $-0.5 < sk \leq 14$ are used in the simulation study, which is described in detail in the online supplemental material.

To investigate the influence of different correlation patters inside the spatial averaging domains, the simulation study considers two-dimensional averaging in combination with an isotropic and an anisotropic spatial correlation structure. Hereby, averaging domain sizes are assumed to be squared and range from much smaller to much larger than the spatial correlation range. In addition, spatial averaging over a disjoint domain of two points separated by half the correlation range is considered as a type of worst-case scenario, where correlation is neither zero (i.i.d. case) nor perfect (no spatial averaging), but approximately 0.5.

It is uniformly observed that direct (parametric) GA, IG and LN approximations perform well if the underlying population distribution is of the same type or sufficiently similar (e.g. IG and LN for $CV \leq 0.5$). This confirms that, to the level of accuracy applied in this study (10,000 realisations), spatial averaging over a spatially correlated variable may be accurately approximated by simple averaging of n_e independent variables, for which an exact solution is known in the case of GA and IG distributions. For the LN the additional assumption of log-normality of means of independent variables is also seen to have a negligible effect on the results presented. For large numbers of n_e, results become acceptable independent of the combination of test/approximation distribution, thus confirming the expected convergence to normality from the Central Limit Theorem. From this and additional results using discrete test distributions (being bimodal, negatively skewed and/or truncated) it is further seen that the choice and appropriateness of direct GA, IG or LN up-scaling may be well evaluated by the proposed ratio sk/CV according to Table 1.

Among all methods studied, the bootstrap appears to be almost uniformly the best method. However, if the population distribution is given in a discrete form and n_e is close to 1, then artifacts of the discrete population cdf may remain after bootstrapping. This effect may be reduced by drawing bootstrap samples from a smoothed distribution. In the present study the discrete population cdfs of the non-parametric test distributions are linearly interpolated for both bootstrapping and random field simulation (without tail extrapolation). As to be expected, the performance of the Gaussian-based Edgeworth expansion method deteriorates rapidly as CV and sk increase and n_e decreases. Moreover, the improvement between first-order [Equation (6) neglecting the

term of order $1/n$; correcting for primary effects of skewness] and second-order [full Equation (6); correcting for primary effects of kurtosis and secondary effects of skewness; Hall 1992] expansions is quite limited or non-existent. However, simulation results and Equation (6) suggest the definition of a parameter $\Delta sk_N = |sk|/\sqrt{n_e} = |sk(Z_v)|$ as a measure of convergence to normality and applicability of the Edgeworth approximation. The expression $(t^2 - 1) f_N(t)/6$ in Equation (6) possesses a maximum absolute value of approximately $0.4/6$, from which it is inferred that for $\Delta sk_N \leq 0.15$ the first-order correction term is smaller than 1% for all t and the cdf of t can be assumed to be accurately approximated by the normal distribution $F_N(t)$. On the other hand, simulation results indicate that the Edgeworth method delivers acceptable results only for the approximate range of $\Delta sk_N \leq 1$. Failures of the Edgeworth method for $\Delta sk_N \leq 1$ are possible as demonstrated by test distributions, for example, whose bimodal nature is too complex to be captured by a single parameter based on skewness.

The gamma expansion method, as expected, improves on the Edgeworth method for positively skewed test distributions, with little or no improvement from a one-term [Equation (7) with $B = 0$] to two-term [full Equation (7)] expansion. For absolute values of skewness close to 0, the gamma expansion performs worse than the Edgeworth expansion; however, it still outperforms the parametric approximations. In general, the gamma expansion method is seen to consistently improve upon the parametric gamma approximation, except for cases where the parametric gamma approximation itself is in large error and the respective expansion becomes unstable. In analogy to Δsk_N Equations (7) and (8) may be used to define a parameter $\Delta sk_{GA} = |sk(Z_v) - sk(GA)| = |sk - 2CV|/\sqrt{n_e}$ expressing the difference in skewness between Z_v (or equivalently w) and the gamma fit $F_{GA}(w, p_2)$. The simulation study indicates that the gamma expansion method delivers acceptable results in the approximate range of $\Delta sk_{GA} \leq 0.5$ and that the improvement of the gamma expansion over the simple parametric gamma fit becomes negligible for $\Delta sk_{GA} \leq 0.15$.

6. Practical example

Based on FDOT (2009), Klammler et al. (2010) present a data analysis and case study of a site in Florida, where drilled shafts are considered for bridge foundation and 136 core sample rock strength data are available from six borings (see online supplemental material). The summary statistics of the data are $\mu = 2.04$ MPa, $CV = 0.50$ and $sk = 0.50$ with a spatial covariance function consisting of two components: 80% of the total variance has vertical and horizontal correlation ranges of 1.5 and 4.5 m, respectively (geometric anisotropy), and the remaining 20% of the total variance is only contained in the horizontal direction with a range of 4.5 m (zonal anisotropy; vertical range very large). These are parameters obtained from variogram analysis (e.g. Isaaks and Srivastava 1989) of the core sample data as performed by Klammler et al. (2010). Assuming shaft diameter and length of 1.2 and 9 m, respectively, Klammler et al. (2010) apply their charts to graphically find a variance reduction factor $\alpha = 0.23$ (see their Table 1, row for γ_A), which is directly converted into an effective number of independent variables by $n_e = 1/\alpha = 4.33$. With this, the methods presented here are applied to estimate the distribution of a shaft's side friction resistance and compared to results of full stochastic simulations [10,000 realisations; shaft discretised into 20 (circumference) $\times$ 50 (length) elements].

Results in terms of maximum absolute differences in per cent cdf values between approximations and stochastic simulation are as follows: direct GA: 1.4; direct IG: 2.9; direct LN: 2.9; bootstrap: 0.9; Edgeworth first order: 0.9; gamma one term: 1.0. Edgeworth second order and gamma expansion with two terms performed similar to or slightly worse than their simpler counterparts. These numbers may be compared to a benchmark of 2.3, which is the maximum absolute difference in cdf values between two samples of 10,000 realisations that is not exceeded with a probability of 99% according to the Kolmogorov–Smirnov test. From this it is seen that direct GA, bootstrap, Edgeworth and gamma expansions produce results within the margins of error of the stochastic simulation. Using the proposed ratio $sk/CV = 1$ and the last column of Table 1 predicts the evidently better performance of the direct GA method over direct IG or LN (as used in Klammler et al. 2010). Moreover, the proposed parameters $\Delta sk_N = \Delta sk_{GA} = 0.24$ (coincidentally the same) are below their limits found of 1 and 0.5, respectively, which is reflected by the good performance of the expansion methods. Furthermore, Figure 2 shows the lower tails of cdf(R) from selected methods. For a given probability (risk) p_f of failure a maximum permissible load Q (for simplicity of illustration assumed to be deterministic, i.e. without uncertainty) is obtained as $Q = R$ when entering the chart with cdf(R) $= p_f$. For example, for $p_f = 0.01$, Q from direct GA, bootstrap and gamma one term are within approximately 1 MN (3%) of $Q \approx 36$ MN from the full simulation result; for $p_f = 0.001$
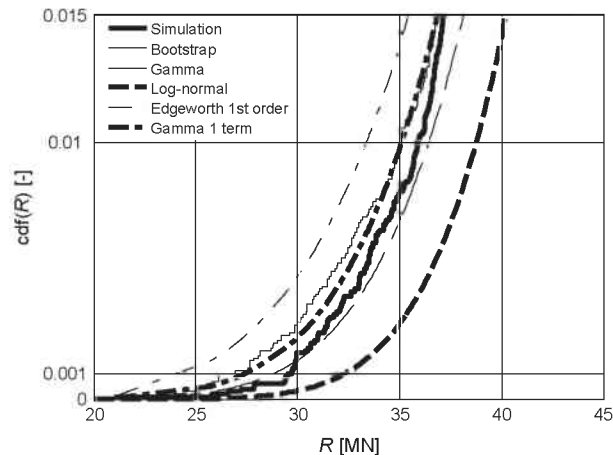
Figure 2. Lower tails of up-scaled resistance distributions for field example. For deterministic loads Q the probability of failure is equal to cdf(R) at $R = Q$.

deviations somewhat increase (illustrating the increasing difficulty when working in extreme portions of distribution tails); however, deviations are seen to occur consistently towards the conservative side in the present case. While Edgeworth first order results in more conservative Q, direct LN (as well as IG; not shown) up-scaling is consistently unconservative. However, as already stated, the ratio criterion sk/CV may be applied in practice to identify the latter two methods as potentially worse for the present data than the direct GA method (or its expansion).

7. Summary and conclusion

Risk- (or reliability-) based design of deep foundations aims at not exceeding a prescribed maximum probability of failure. For mathematical treatment of the problem according to Equation (1) and a given deterministic (zero uncertainty) or random load it is required to know the probability distribution of random resistance. The properties of the resistance distribution are affected by different sources of uncertainty. One of these sources is spatial variability, which is investigated in the present work in the context of ultimate (deformation independent) axial resistance of drilled shafts due to side friction, where local strength data is available at a quasi-point support (e.g. core samples). For this purpose, we present a series of simple approximate methods for up-scaling of linearly averaging variables based on a combination of classical and geostatistical principles that are linked by the use of an effective number n_e of independent variables. The number n_e is equivalent to a factor of variance reduction and is obtained from the geostatistical operation of regularisation. It is

used to approximate spatial averaging of a correlated variable over some domain by simple averaging of n_e independent variables. Two novel 'parametric' approaches are developed, which honor the frequent requirement of non-negativity and positive skewness and which explore the fact that means of independent gamma and inverse Gaussian variables possess the same distribution type (distribution permanence). The existing method of 'parametric' log-normal up-scaling is included in the study for comparative evaluation against the other methods developed and to define a new parameter for its potential range of applicability. Furthermore, three novel approaches termed 'non-parametric' are presented, which relate to bootstrap sampling and expansions of distributions about the normal (Edgeworth) and gamma distributions. A comprehensive simulation study is performed to validate each method's performance against up-scaling by full random field simulation, and a practical example for up-scaling of core sample rock strength data to drilled shaft side friction resistance with its associated risk of failure is presented.

As expected, results of the simulation study show that the parametric approaches produce acceptable results only when the distribution chosen for approximation is close enough to the actual test distribution. To decide which one (or if any) of the gamma, inverse Gaussian or log-normal is able to give an acceptable result, a simple criterion based on the ratio of the coefficient of skewness to the coefficient of variation of the test distribution is developed and successfully validated. The bootstrap approach is seen to be almost uniformly superior to the others; however, for values of n_e close to 1, previous smoothing of a possibly discontinuous distribution used for the point variable may be necessary to avoid discontinuity artifacts in the up-scaled distribution. Edgeworth and gamma expansions involving skewness and kurtosis are able to correct for a certain degree of deviations in the up-scaled distributions with respect to the normal and gamma distribution, respectively. The parameters Δsk_N and Δsk_{GA} based on skewness and coefficient of variation of the point support variable as well as n_e are developed to find $\Delta sk_N \leq 1$ and $\Delta sk_{GA} \leq 0.5$ as respective ranges of applicability of the Edgeworth and gamma expansion methods. For $\Delta sk_N \leq 0.15$ (and in the absence of extreme situations such as bimodality) the Central Limit Theorem is seen to effectively normalise the up-scaled distributions. Once n_e is determined (typically from numerical integration of the spatial correlation function or graphically as in Klammler *et al.* 2010) all of the approaches presented are simple to apply and honor the Central Limit Theorem for large n_e.

Acknowledgements

References

AASHTO, 2004. *LRFD bridge design specifications*. 3rd ed. Washington, DC: American Association of State Highway and Transportation Officials.

Babu, G.L.S., Srivastava, A., and Murthy, D.S.N., 2006. Reliability analysis of the bearing capacity of a shallow foundation resting on cohesive soil. *Canadian Geotechnical Journal*, 43 (2), 217–223.

Bayley, G.V. and Hammersley, J.M., 1946. The 'effective' number of independent observations in an autocorrelated time series. *Journal of Royal Statistical Society*, 8 (1B), 184–197.

Bowers, N.L., 1966. Expansion of probability density functions as a sum of gamma densities with applications in risk theory. *Transactions of Society of Actuaries*, 18, 1, 52, 125–137.

Chilés, J.P. and Delfiner, P., 1999. *Geostatistics: modeling spatial uncertainty*. New York: Wiley.

Cressie, N., 1993. *Statistics for spatial data*. New York: Wiley.

Deutsch, C.V., 2002. *Geostatistical reservoir modeling*. New York: Oxford University Press.

Deutsch, C.V., 2004. *A statistical resampling program for correlated data: spatial_bootstrap*. Center for Computational Geostatistics Annual Report 6. Edmonton, AB: University of Alberta, 9.

Efron, B. and Tibshirani, R.J., 1998. *An introduction to the bootstrap*. New York: CRC Press.

FDOT, 2006. *Appendix A. Soils and foundation handbook*. Gainesville, FL: Florida Department of Transportation, 146–155.

FDOT, 2009. *Modification of LRFD resistance factors based on site variability*. Tallahassee, FL, Florida Depart ment of Transportation, Final. Project Report BD545-76. Available from: http://www.dot.state.fl.us/research-center/Completed_StateMaterials.shtm [accessed 8 January 2011].

Fenton, G.A. and Griffiths, D.V., 2002. Probabilistic foundation settlement on spatially random soil. *Journal of Geotechnical and Geoenvironmental Engineering*, 128 (5), 381–390.

Fenton, G.A. and Griffiths, D.V., 2003. Bearing-capacity prediction of spatially random c – φ soils. *Canadian Geotechnical Journal*, 40 (1), 54–65.

Fenton, G.A. and Griffiths, D.V., 2005. Three-dimensional probabilistic foundation settlement. *Journal of Geotechnical and Geoenvironmental Engineering*, 131 (2), 232–239.

Fenton, G.A. and Griffiths, D.V., 2007. *Reliability-based deep foundation design*. Probabilistic Applications in Geotechnical Engineering, Geotechnical Specialty Publication No. 170, Denver, CO: ASCE.

Fenton, G.A., Griffiths, D.V., and Cavers, W., 2005. Resistance factors for settlement design. *Canadian Geotechnical Journal*, 42 (5), 1422–1436.

Fenton, G.A., Griffiths, D.V., and Zhang, X.Y., 2008. Load and resistance factor design of shallow foundations against bearing failure. *Canadian Geotechnical Journal*, 45 (11), 1556–1571.

Foye, K.C., Salgado, R., and Scott, B., 2006. Assessment of variable uncertainties for reliability-based design of foundations. *Journal of Geotechnical and Geoenvironmental Engineering*, 132 (9), 1197–1207.

Goovaerts, P., 1997. *Geostatistics for natural resources evaluation*. New York: Oxford University Press.

Gotway, C.A. and Young, L.G., 2002. Combining incompatible spatial data. *Journal of the American Statistical Association*, 97 (458), 632–648.

Haldar, S. and Babu, G.L.S., 2008. Load resistance factor design of axially loaded pile based on load test results. *Journal of Geotechnical and Geoenvironmental Engineering*, 134 (8), 1106–1117.

Hall, P., 1992. *The bootstrap and Edgeworth expansion*. New York: Springer.

Isaaks, E.H. and Srivastava, R.M., 1989. *An introduction to applied geostatistics*. New York: Oxford University Press.

Journel, A.G. and Huijbregts, C.J., 1978. *Mining geostatistics*. New York: Academic Press.

Kitanidis, P.K., 1997. *Introduction to geostatistics: applications to hydrogeology*. Cambridge: Cambridge University Press.

Klammler, H., *et al.*, Influence of spatially variable skin friction on single drilled shaft capacity and LRFD resistance factors. *Journal of Geotechnical and Geoenvironmental Engineering*, 136 (8), 1114–1123.

Krishnamoorthy, K., 2006. *Handbook of statistical distributions with applications*. New York: Chapman & Hall.

Paice, G.M., Griffiths, D.V., and Fenton, G.A., 1996. Finite element modeling of settlements on spatially random soil. *Journal of Geotechnical Engineering*, 122 (9), 777–779.

Pardo-Iguzquiza, E. and Dowd, P.A., 2004. Normality tests for spatially correlated data. *Mathematical Geology*, 36 (6), 659–681.

Petrov, V.V., 1975. *Sums of independent random variables*. New York: Springer.

Phoon, K.K. and Kulhawy, F.H., 1999a. Characterization of geotechnical variability. *Canadian Geotechnical Journal*, 36 (4), 612–624.

Phoon, K.K. and Kulhawy, F.H., 1999b. Evaluation of geotechnical variability. *Canadian Geotechnical Journal*, 36 (4), 625–639.

Phoon, K.K., Kulhawy, F.H., and Grigoriu, M.D., 2003. Development of a reliability-based design framework for transmission line structure foundations. *Journal of Geotechnical and Geoenvironmental Engineering*, 129 (9), 798–806.

Popescu, R., Deodatis, G., and Nobahar, A., 2005. Effects of random heterogeneity of soil properties on bearing capacity. *Probabilistic Engineering Mechanics*, 20 (4), 324–341.

Santos Filho, J.C.S., Cardieri, P., and Yacoub, M.D., 2005. Simple accurate lognormal approximation to lognormal sums. *Electronic Letters*, 21 (18), 1016–1017.

Vargaz-Guzmán, J.A., 2005. Change of support of transformations: conservation of lognormality revisited. *Mathematical Geology*, 37 (6), 551–567.

Zhang, L.M., Tang, W.H., and Ng, C.W.W., 2001. Reliability of axially loaded driven pile groups. *Journal of Geotechnical and Geoenvironmental Engineering*, 127 (12), 1051–1060.

Zhang, L.M., Xu, Y., and Tang, W.H., 2008. Calibration of models for pile settlement analysis using 64 load tests. *Canadian Geotechnical Journal*, 45 (1), 59–73.

Appendix 1. Bootstrap sampling for non-integer n_e

Given n_e is an integer it is straightforward to draw n_e independent random numbers from a known discrete or continuous distribution (Efron and Tibshirani 1998). If a large number of N samples of size n_e are drawn, then the respective N arithmetic averages approach a variance of $\sigma_v^2 = \sigma_0^2 / n_e$ [Equations (4) and (5)]. Furthermore, if N_1 samples of size n_{e1} and N_2 samples of size n_{e2} are drawn, where $N_1 + N_2 = N$, then the respective N arithmetic averages approach a variance of $\sigma_v^2 = (N_1 \sigma_0^2 / n_{e1} + N_2 \sigma_0^2 / n_{e2}) / N$. By choosing $n_{e1} = \text{int}(n_e)$, designating the integer part of n_e (e.g. int(3.78) = 3), and $n_{e2} = \text{int}(n_e) + 1$, with $d =$

$n_e - \text{int}(n_e)$ being the non-integer part of n_e, the preceding equations can be combined and written as

$$\frac{1}{n_{e1} + d} = \frac{b_1}{n_{e1}} + \frac{1 - b_1}{n_{e1} + 1} \quad \text{(A1)}$$

$b_1 = N_1 / N$ and $1 - b_1 = N_2 / N$ are used for the portions of samples drawn of size n_{e1} and n_{e2}, respectively. Solving for b_1 gives

$$b_1 = \frac{n_{e1}(1 - d)}{n_{e1} + d} \quad \text{(A2)}$$

Hence, the distribution of N sample means of non-integer size n_e is approximated by the requirement of equal variance reduction through the composite distribution of $N_1 = \text{round}(b_1 N)$ samples of integer size n_{e1} and $N_2 = N - N_1$ samples of size $n_{e1} + 1$. The expression 'round()' designates the nearest integer to the argument. Using $n_{e1} = \text{round}(n_e)$ and $N_1 = N$ is an accurate approximation for large n_e (> 100), since $n_{e1} / n_e \approx 1$. For an intermediate range of n_e (≈ 10) Equation (A2) can be simplified to $b_1 = 1 - d$, since $0 \leq d < 1$ and $d / n_e \approx 0$. Equation (A2) is most general and remains accurate even for small values of n_e close to 1.

Supplemental material

Online supplemental material is available with expressions for pdfs and cdfs of distributions used (normal, gamma, inverse Gaussian, log-normal), a detailed description of the simulation study and core sample rock strength data for the practical example.
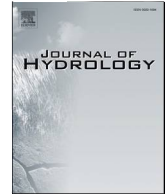
Effect of injection screen slot geometry on hydraulic conductivity tests

CrossMark

Harald Klammler [a,b,*], Bassel Nemer [a,b,c], Kirk Hatfield [a,b]

[a] Department of Civil and Coastal Engineering, University of Florida, Gainesville, FL, USA
[b] Inter-Disciplinary Program in Hydrologic Sciences, University of Florida, Gainesville, FL, USA
[c] Department of Engineering, University of Guelph, Guelph, Ontario, Canada

ARTICLE INFO

SUMMARY

Hydraulic conductivity and its spatial variability are important hydrogeological parameters and are typically determined through injection tests at different scales. For injection test interpretation, shape factors are required to account for injection screen geometry. Shape factors act as proportionality constants between hydraulic conductivity and observed ratios of injection flow rate and injection head at steady-state. Existing results for such shape factors assume either an ideal screen (i.e., ignoring effects of screen slot geometry) or infinite screen length (i.e., ignoring effects of screen extremes). In the present work, we investigate the combined effects of circumferential screen slot geometry and finite screen length on injection shape factors. This is done in terms of a screen entrance resistance by solving a steady-state potential flow mixed type boundary value problem in a homogeneous axi-symmetric flow domain using a semi-analytical solution approach. Results are compared to existing analytical solutions for circumferential and longitudinal slots on infinite screens, which are found to be identical. Based on an existing approximation, an expression is developed for a dimensionless screen entrance resistance of infinite screens, which is a function of the relative slot area only. For anisotropic conditions, e.g., when conductivity is smaller in the vertical direction than in the horizontal, screen entrance losses for circumferential slots increase, while they remain unaffected for longitudinal slots. This work is not concerned with investigating the effects of (possibly turbulent) head losses inside the injection device including the passage through the injection slots prior to entering the porous aquifer.

© 2014 Elsevier B.V. All rights reserved.

1. Introduction

The hydraulic conductivity K [L/T] is a fundamental hydrogeological parameter. For example, its effective value over large (e.g., >100 m) scales, directly influences the magnitude of natural or pumped groundwater flows in aquifers. Moreover, its spatial heterogeneity over smaller scales (e.g., <1 m) is of interest, as it determines the local properties of groundwater flow and solute transport (e.g., contaminant release from source zones and contaminant plume dispersion). Those are important pieces of information for a variety of hydrogeological problems (e.g., Sudicky, 1986; Sedighi et al., 2006). Under saturated conditions, i.e., below the water table of an aquifer, pump or slug tests are typically performed for investigations of K at different scales (Weight and Sonderegger, 2001). Accordingly, these tests may be performed on an entire well or on various portions of a well screen by use of single or double packer systems (Price and Williams, 1993; Butler et al., 2009). Different types of small diameter (i.e., <0.1 m) drive-point (also called push-in or direct-push) probes have also been proposed for quick and flexible investigation of K in unconsolidated media at small scales (Hinsby et al., 1992; Cho et al., 2000; Butler et al., 2007; Dietrich et al., 2008). A general relationship between injection head φ_0 [L] and injection flow rate Q [L^3/T] at steady-state is (Clark and Turner, 1983; Weight and Sonderegger, 2001)

$$\varphi_0 = \frac{Q}{KF} + CQ^2 \tag{1}$$

where the term Q/KF [L] represents linear head losses due to laminar flow in the porous aquifer medium (potentially influenced by non-ideal screen geometry) and CQ^2 [L] represents quadratic head losses due to turbulent flow along the well or injection device as well as across the screen openings prior to entering the aquifer. Coefficient C [T^2/L^5] is hereby a proportionality constant and F [L] is a shape factor accounting for the geometry of the imposed flow field in the aquifer. While well losses may be significant for production wells, small scale injection tests use relatively low values of Q,

* Corresponding author at: Department of Civil and Coastal Engineering, University of Florida, Gainesville, FL, USA. Tel.: +1 (352) 392 9537x1441; fax: +1 (352) 392 3394.

E-mail address: haki@gmx.at (H. Klammler).

such that the quadratic term in Eq. (1) is small and sensitivity to aquifer properties (i.e., K) is maximized. Liu et al. (2012) propose a step drawdown procedure to estimate C, such that K may be estimated from a single steady-state injection test as

$$K = \frac{Q}{(\varphi_0 - CQ^2)F} \approx \frac{Q}{\varphi_0 F} \qquad (2)$$

Here, φ_0 and Q are observed quantities at steady-state during an injection test and F needs to be determined for a given injection screen geometry (Hvorslev, 1951). The final expression in Eq. (2) applies when turbulent losses are negligible.

Numerous studies investigate the problem of quantifying F (or respective generalizations for transient conditions, such as type curves, for example) through different methods. A common feature of the most sophisticated approaches is to assume axi-symmetric potential flow imposed by a mixed type boundary condition along the injection well or probe (constant head along injection screen interval and impermeable casing above/below screen). Most recent results include the numerical work of Ratnam et al. (2001); Liu et al. (2008); Kobayashi et al. (2013) as well as the semi-analytical work based on integral transforms of Chang and Chen (2002); Perina and Lee (2006); Mathias and Butler (2007); Barua and Bora (2010). Furthermore, Chang and Yeh (2010) approach the mixed type boundary problem by solving a system of triple series equations, while Klammler et al. (2011) apply an approach related to trigonometric interpolation. Silvestri et al. (2011) quantify injection flow by conformal mapping in combination with a subsequent numerical integration to account for axi-symmetry of the problem (rather than plane two-dimensional). However, all of these and related studies treat the injection screen as a perfect (ideal) constant head boundary without accounting for the exact widths and separation distances of individual injection screen slots or perforations (Fig. 1). The goal of the present work is to investigate the effects of such non-ideal screens on injection test interpretation (i.e., on the value of F in Eq. (2)) for the purpose of (1) improving estimates of K and (2) assisting in injection screen slot design, such that existing results for the shape factor F for ideal screens remain applicable. The present work is not concerned with investigating the magnitude of the head losses inside the injection device including the passage through the injection slots prior to entering the porous aquifer (e.g., constant C in Eqs. (1) and (2)).

Work related to intake efficiency of non-ideal screens may be found in literature related to drainage pipes or tiles. Kirkham (1950) provides analytical solutions for upper and lower bounds based on geometric approximations of the boundary conditions near circumferential slots. Intake efficiency of circumferential slots was further investigated using the Gram-Schmidt method (Selim and Kirkham, 1974; including application to well pumping), by numerical solution of a Fredholm integral equation (Sneyd and Hosking, 1976) and by solution of dual trigonometric series (Prasad et al., 1981; Hazenberg and Panu, 1991). Nieuwenhuis and Wesseling (1979); Youngs (1980) study effects of filter materials around drains by exploring a conformal mapping solution of Widmoser (1966) for longitudinally slotted screens. Furthermore, Panu and Filice (1992) consider circular perforations in a dual trigonometric series approach and Dierickx and van der Molen (1981) refines a distributed line source and sink model for different slot and perforation geometries, which is validated by electrolytic experiments. However, consistent with the typically large extent of drainage pipes, results are not applicable to finite (short) screen lengths as customary for small scale injection tests using push-in probes, for example. In summary, hence, a need remains for investigating the combined effects of screen perforation/slotting and finite screen length on the hydraulic performance of an injection screen in terms of F. Since ideal screens of finite length possess flow singularities at their extremes (e.g., Sneyd and Hosking, 1976; Prasad et al., 1981; Mathias and Butler, 2007; Klammler et al., 2011), deviations from ideal screen geometry may have a significantly different impact on the performance of short screens than for screens of infinite length (or fully penetrating between confining layers, which do not possess flow singularities). For the purpose of measuring K by means of small scale injection tests, screen lengths may be at the order of the device radius and narrow screen slots are preferred over other types of perforation. Circular perforations, for example, may allow partial collapse of surrounding aquifer material into the screen. This may alter the geometry of the injection boundary condition with significant effects on the hydraulic behavior (Sneyd and Hosking, 1976).

In what follows we limit attention to injection screens possessing circumferential slots and apply the method of Klammler et al. (2011) to investigate the effect of screen slot geometry (slot width and separation distance) on screens of arbitrary lengths and in the absence of any nearby boundaries (as relevant for small scale injection tests, for example). The semi-analytical approach solves an axi-symmetric steady-state potential flow problem and honors the mixed type boundary condition along the injection probe at a finite but increasing number of control points, such that extrapolation to an exact solution (i.e., infinite number of control points) is possible. Thus, it is easily adapted for the present problem, where screen slotting represents a sequence of many constant head and impermeable boundary segments (Fig. 1b). The subsequent section briefly reviews the method applied and constructs a general solution. Results are then expressed in terms of a hydraulic screen
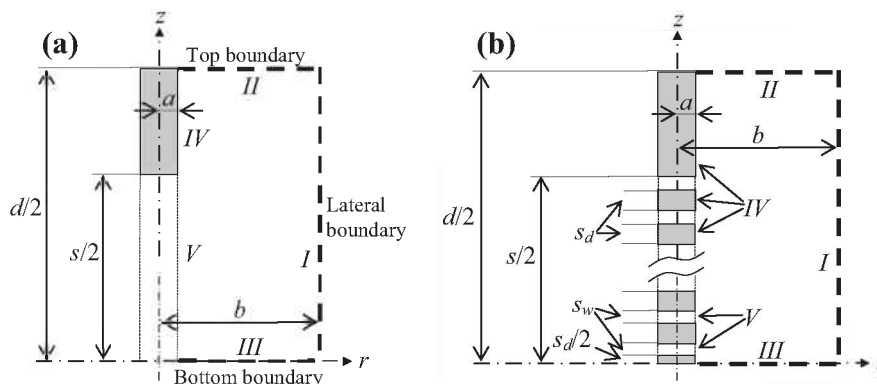

Fig. 1. Schematic of boundary conditions for upper half of (a) ideal and (b) non-ideal (circumferentially slotted) injection screen of uniform slot width s_w and uniform distance between slots s_d. Total screen length of n_s slots is $s = n_s(s_w + s_d) - s_d$, (b) is shown for even n_s, and modification to odd n_s is straight-forward.

resistance R_s [1/L], which represents the additional aquifer resistance to injection flow due to non-ideal slot geometry. Use of R_s is convenient, as it will be shown that it rapidly stabilizes as the top boundary is moved away from the screen (d growing in Fig. 1). This significantly alleviates the computational burden of dealing with excessively large numbers of control points due to high control point resolution required by narrow screen slots in combination with large flow domains. For long screens results are validated against an approximate analytical solution due to Prasad et al. (1981); Hazenberg and Panu (1991) and practical examples are given. Furthermore, also for long screens, the results for circumferential slots are compared to those of Widmoser (1966) for longitudinal slots and effects of anisotropy in aquifer K are discussed with respect to slot direction.

2. Mathematical solution approach

2.1. Problem statement and general solution

The upper half of the relevant homogeneous and axi-symmetric flow domain is depicted in Fig. 1, where r [L] and z [L] are the radial and vertical coordinates, respectively, being delimited by $a < r < b$ [L] and $0 < z < d/2$ [L]. The lower half of the flow domain is omitted due to symmetry about the $z = 0$ plane. This symmetry can be introduced without loss of generality, since final results below are presented for theoretically infinite flow domains, i.e., when the distances to upper and lower boundaries are sufficiently large, such that the actual boundary types (excluding trivial cases where $F = 0$, i.e., zero flow at steady-state) and distances from the screen become irrelevant. a is used to represent the radius of the probe/well, while b is the radial distance to a lateral boundary and $d/2$ the distance to a top boundary. Fig. 1a corresponds to an ideal screen of length s [L], while Fig. 1b shows a non-ideal screen consisting of n_s [−] circumferential slots of width s_w [L] and separation distance s_d [L], such that $s = n_s(s_w + s_d) - s_d$. The governing Laplace equation for steady-state flow and isotropic hydraulic conductivity in axi-symmetric cylindrical coordinates is

$$\frac{\partial^2 \varphi}{\partial r^2} + \frac{1}{r}\frac{\partial \varphi}{\partial r} + \frac{\partial^2 \varphi}{\partial z^2} = 0 \tag{3}$$

where $\varphi = \varphi(r,z)$ [L] is the hydraulic head. In the sequel, solutions of Eq. (3) will be sought for different boundary conditions. The external boundaries I and II (i.e., in the aquifer; Fig. 1) are chosen at constant head zero, while boundary III is an impermeable boundary due to symmetry. Mathematically, this may be expressed as

$$I : \varphi = 0 \quad \text{at } r = b \quad \text{for } 0 \leqslant z \leqslant d/2 \tag{4}$$

$$II : \varphi = 0 \quad \text{at } z = d/2 \quad \text{for } a \leqslant r \leqslant b \tag{5}$$

$$III : \frac{\partial \varphi}{\partial z} = 0 \quad \text{at } z = 0 \quad \text{for } a \leqslant r \leqslant b \tag{6}$$

Using Eq. (9) of Klammler et al. (2011) with $d/2$ instead of d and $d/2-z$ instead of z, a solution to Eq. (3) honoring boundary conditions I, II and III for $b \to \infty$ (i.e., for laterally infinite flow domains) is

$$\varphi = \sum_{n=1}^{N} B_n \frac{K_0(mr)}{K_0(ma)} \sin\left[m\left(\frac{d}{2}-z\right)\right] \quad \text{with } m = \frac{(2n-1)\pi}{d} \tag{7}$$

where n and N [−] can take positive integer values, B_n [L] are yet unknown coefficients and where K_j is used for modified Bessel functions of the second kind and order j (Dwight, 1947). The radial derivative of Eq. (7) is proportional to the radial flux component and can be written as

$$\frac{\partial \varphi}{\partial r} = -\sum_{n=1}^{N} B_n m \frac{K_1(mr)}{K_0(ma)} \sin\left[m\left(\frac{d}{2}-z\right)\right] \tag{8}$$

knowing that $dK_0(r)/dr = -K_1(r)$. The coefficients B_n in Eqs. (7) and (8) are to be determined to meet the remaining mixed type boundary conditions IV and V along the injection device corresponding to impermeable and constant injection head segments, respectively. The function $G(z)$ is hereby defined by

$$IV : \frac{\partial \varphi}{\partial r} = 0 \quad \text{at } r = a \quad \text{for } G(z) = 0 \tag{9}$$

$$V : \varphi = \varphi_0 \quad \text{at } r = a \quad \text{for } G(z) = 1 \tag{10}$$

$$G(z) = \begin{cases} 1 & \text{for } 0 < z < s/2 \quad \text{and } R\left[\frac{s/2-z}{s_w+s_d}\right] < \frac{s_w}{s_w+s_d} \\ 0 & \text{otherwise} \end{cases} \tag{11}$$

and is used to distinguish open slot areas ($G = 1$) from impermeable casing between slots ($G = 0$; Fig. 1b), where the function $R[\,]$ denotes the non-integer remainder of the fraction in the argument. Note that for $s_d = 0$ Eqs. (9)–(11) collapse to the boundary conditions of Fig. 1a for an ideal screen.

2.2. Particular solution for mixed type boundary

Further following the method of Klammler et al. (2011), Eqs. (7) and (8) are substituted into Eqs. (9) and (10). At the same time, the vertical coordinate z is discretized into a finite number of equidistant points z_k, where $k = 1, 2, \ldots, N$, $z_1 = d/(4N)$ and $z_{k+1}-z_k = d/(2N)$. This leads to

$$\sum_{n=1}^{N} B_n \sin\left[m\left(\frac{d}{2}-z_k\right)\right] = \varphi_0 \quad \text{for } G(z_k) = 1 \tag{12}$$

$$\sum_{n=1}^{N} B_n m \frac{K_1(ma)}{K_0(ma)} \sin\left[m\left(\frac{d}{2}-z_k\right)\right] = 0 \quad \text{for } G(z_k) = 0 \tag{13}$$

which constitute a linear system of N equations in N unknown coefficients B_n. After solving for B_n, the hydraulic head distribution is known by Eq. (7) and associated with an injection flow rate $Q = -4\pi a K \varphi_0 \int_0^{d/2} \frac{\partial \varphi_u}{\partial r}\Big|_{r=a} dz$ for the entire screen, where $\varphi_u = \varphi/\varphi_0$ [−] is the hydraulic head normalized to unit injection head. Using Eqs. (2) and (8), this further translates into a shape factor F_c [L] for non-ideal circumferentially slotted screens as (Klammler et al., 2011; Eq. (31) multiplied by 2 because of symmetry and with $d/2$ instead of d, i.e., using m as given in Eq. (7) of the present work)

$$F_c = 4\pi a \sum_{n=1}^{N} B_{n,u} \frac{K_1(ma)}{K_0(ma)} \tag{14}$$

where $B_{nu} = B_n/\varphi_0$ [−] are the normalized solution coefficients for unit injection head. For a given screen geometry, the coefficients $B_{nu}(N)$ and $F_c(N)$ may be evaluated for systematically increasing values of N (here by doubling) and hyperbolically extrapolated to an exact solution for $N \to \infty$. This can be done graphically by plotting F_c over $1/N$ and fitting a straight line to $1/N = 0$. When using only two values of F_c corresponding to $N/2$ and N control points, this linear extrapolation is equivalent to computing $F_c(N \to \infty) = 2F_c(N) - F_c(N/2)$. Convergence to a stable value of $F_c(N \to \infty)$ is usually fast and computation can be stopped at a desired level of accuracy (here, less than approximately 0.1% change in consecutive values of $F_c(N \to \infty)$). Initial values of N should be large enough to locate at least one control point z_k in each boundary segment and small enough to avoid unnecessary computational cost. In what follows, F_c is used as a short notation for the extrapolated $F_c(N \to \infty)$.

2.3. Hydraulic screen entrance/exit resistance R_s

We define a hydraulic screen entrance/exit resistance R_s as (Nieuwenhuis and Wesseling, 1979; Dierickx and van der Molen, 1981)

$$R_s = \frac{1}{F_c} - \frac{1}{F_i} \qquad (15)$$

where $F_i = F_c(s_d = 0)$ [L] is the shape factor for an ideal screen (Fig. 1a). Based on Eqs. (1) and (2), $1/F_c$ represents the hydraulic resistance of an aquifer to flow from a slotted screen, while $1/F_i$ represents the respective resistance for an ideal screen. The difference between both is due to non-ideal screen geometries caused by the impermeable boundary segments between injection slots and the related difference in aquifer flow fields near the injection screen. Fig. 2a graphically illustrates this difference in terms of the hydraulic head along an injection device. This head is constant along an ideal injection screen (dashed), while it is smaller on average over a non-ideal injection screen (continuous), even though the applied injection head is the same. Fig. 2b shows the respective injection flux (radial flux along the device), which is zero above and below the screen as well as over the impermeable screen intervals between slots. Thus, for an equal injection flow rate, the local fluxes immediately outside non-ideal screen slots are larger than for an ideal screen and cause an additional head loss proportional to entrance/exit resistance R_s. Knowing F_i from existing studies (here using Klammler et al., 2011) in combination with R_s allows for substituting

$$\frac{1}{F} = \frac{1}{F_c} = \frac{1}{F_i} + R_s \qquad (16)$$

in Eqs. (1) or (2).

For a most general investigation, it is of interest to determine R_s for a variety of non-ideal screen geometries and in the absence of effects of nearby external boundaries (i.e., $d \rightarrow \infty$). However, to the authors' knowledge, all existing solution approaches are limited to finite values of d and $d \rightarrow \infty$ is approximated by $d \gg s$ (e.g., $d/s = 100$). With the present approach, this may become impractical when considering many narrow screen slots (s_w or $s_d \ll s \ll d$), since the required number N of control points becomes large. To overcome this difficulty, Eq. (15) is evaluated for increasing values of d, where it is found that R_s quickly converges to its asymptotic result $R_s(d \rightarrow \infty)$ for $d/s > 2$. This is illustrated in Fig. 3 after normalization to screen radius a. It may be explained by the fact that R_s is due to differences in the flow fields between ideal and non-ideal screens, which occur over a very limited extent near the injection screen. Further illustration is given by the
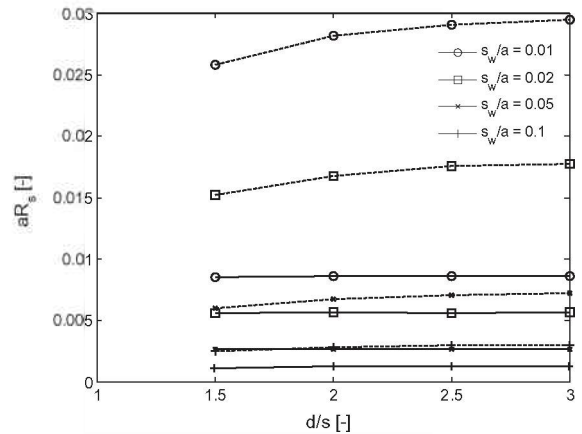

Fig. 3. Examples of convergence of aR_s to a stable value for increasing d/s. Dashed and continuous lines are for $n_s = 2$ and 10, respectively ($s_d/a = 0.1$).

example of Fig. 2a showing large agreement between the hydraulic head distributions along the impermeable casing above an ideal and a slotted injection screen. In what follows, reported values of R_s are for $d/s = 3$ as it was observed that the relative change in R_s between $d/s = 2$ and $d/s = 3$ is less than approximately 1% with respect to $1/F_i(d \rightarrow \infty)$. Hereby, we determine $F_i(d \rightarrow \infty)$ by computing F_i for successively increasing values of d and hyperbolic extrapolation to $d \rightarrow \infty$ (which is exact for spherical flow fields of diameter d). Maximum differences between successive values of $F_i(d \rightarrow \infty)$ occur for $s/a \ll 1$ and are approximately 1%. In what follows F_i is used as a short notation for $F_i(N \rightarrow \infty; d \rightarrow \infty)$.

For the case of a uniform and infinite sequence of slots or a uniform and finite sequence of slots between top and bottom confining layers, a screen resistance R_s' [$1/L$] for a single slot (as indicated by the prime notation hereafter) may be defined. It may be determined by considering the boundary value problem of Fig. 1a with both top and bottom boundaries II and III impermeable due to symmetry and the method of images. Consequently, s in Fig. 1a becomes the width s_w of a single slot and d becomes $d' = s_w + s_d$. Different solutions exist for this boundary value problem (e.g., Selim and Kirkham, 1974; Hazenberg and Panu, 1991) and the solution of Klammler et al. (2011) is summarized in the appendix for convenience. Once R_s' is found, the screen resistance for n_s slots acting in a parallel flow system between confining layers is known to be R_s'/n_s, where $n_s = (s + s_d)/d' = s/d'$ for $s \gg s_d$. With this, the equality $sR_s(s \rightarrow \infty) = sR_s'/n_s = d'R_s'$ may be applied to express
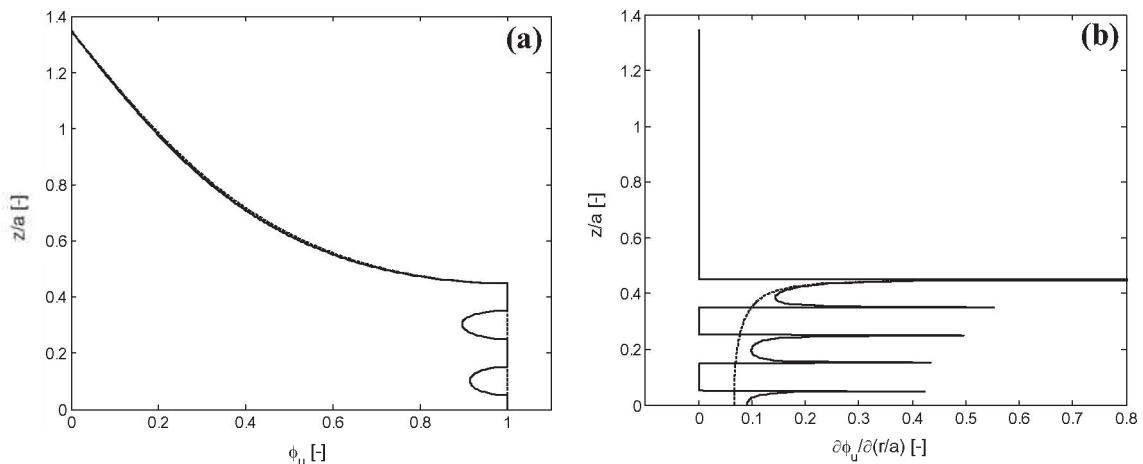

Fig. 2. Examples of (a) head and (b) radial head gradient distributions along top half of injection device. Dashed is for ideal screen and continuous for slotted screen with $n_s = 5$ and $s_w/a = s_d/a = 0.1$ ($d/s = 3$).

$$sR_s(s \to \infty) = \frac{\ln\frac{b}{a}}{2\pi}\left(\frac{1}{B_{0u}} - 1\right) \tag{17}$$

where $B_{0u} \to 1$ as $b \to \infty$, such that $sR_s(s \to \infty)$ is finite. In the present work, Eq. (17) is evaluated for $b/a = 10^3$ and 10^6 with identical results to working precision.

3. Results, validation and discussion

3.1. Circumferential slots

Results from above for circumferential slots are depicted as thin continuous lines in Fig. 4 for different slot widths and distances and in terms of a dimensionless screen resistance sR_s as a function of a/s. This is a convenient representation, as it includes the limiting case of $s \to \infty$ on the ordinate, for which sR_s approaches a finite and non-zero limit according to Eq. (17). Convergence of results for finite but increasing s to that of Eq. (17) provides a first partial validation of outcomes for finite s. The bold continuous and dashed graphs correspond to s/F_i and 10% of s/F_i, respectively, and serve to assess the relative impact of R_s on F (Eq. (16)) and, hence, the estimate of K (Eq. (2)). Thus, for a maximum error of 10% due to applying F_i to non-ideal screen slot geometry, the dashed line should not be exceeded. The same information of Fig. 4 is represented in a different form by the continuous lines in Fig. 5 in terms of the relative difference $F_c/F_i = 1/(1 + F_iR_s)$ derived from Eq. (15). The dashed lines correspond to $F_c/F_i = 1/(1 + F_iR'_s/n_s)$ and illustrate the impact of using a screen resistance R'_s/n_s for a finite number n_s of slots contained in an infinite sequence of slots (or between two confining layers separated by distance $s + s_d$), rather than R_s for finite screens of n_s slots and distant boundaries. As to be expected,

the difference is larger for shorter screens, while continuous and dashed lines approach each other as screen length s increases. In the limit of $s \to \infty$ ($a/s \to 0$) all graphs reach $F_c/F_i = 1$, because R_sF_i and $R'_sF_i \to 0$. This is reflected by the finite values of sR_s on the ordinates of Fig. 4, while $s/F_i \to \infty$. Intuitively speaking, this means that for fully penetrating screens between confining layers, the aquifer resistance dominates (theoretically infinite for $b \to \infty$ and at steady-state, as considered here) and R_s, although larger than zero, becomes insignificant. In the case of a very long screen in the absence of confining layers, this further means that R_s decreases faster with growing s than F_i increases. Overall, Fig. 5 clearly illustrates how effects of non-ideal screen geometry increase for shorter screens. Since R_s is not strongly affected by the distance to top and bottom boundaries (Fig. 2), the present results for R_s (at least for $d/s > 3$) may be directly combined with results for F_i in the presence of nearby boundaries (e.g., from Klammler et al., 2011; Figs. 4, 5, 7 or 8). That is, previously published shape factors for ideal screens and moderately close aquifer boundaries may be used as F_i in the present work (i.e., Eq. (16) and Figs. 4–6).

The charts in Figs. 4 and 5 also share a large degree of similarity considering the difference in scaling. In fact, for $s \to \infty$ an analytical result of Prasad et al. (1981); Hazenberg and Panu (1991; Eq. (22)) exists, which can be used for additional validation of the present results and for gaining further insight into their properties. The solution is an approximation valid for large values of both a/d' and b/a and can be translated into a shape factor F'_c for a single circumferential slot contained in a uniform and infinite sequence of slots. In the present notation this results in

$$F'_c \approx \frac{2\pi d'}{\ln\frac{b}{a} - \frac{d'}{\pi a}\ln\left(\sin\frac{\pi\varepsilon}{2}\right)} \tag{18}$$
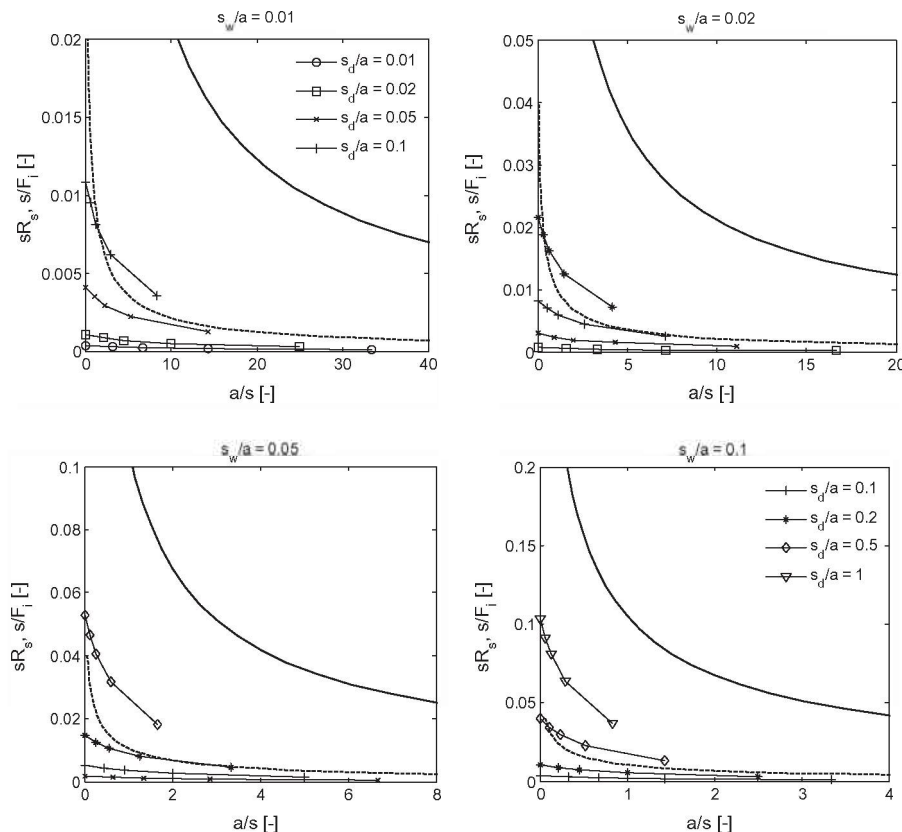

Fig. 4. Dimensionless screen resistance sR_s (thin continuous) as a function of a/s for different screen slot geometries (s_w/a and s_d/a). Symbols correspond to $n_s = \{2, 4, 8, 16, \infty\}$ from right to left. Graphs for s/F_i (bold continuous) and $s/(10F_i)$ (bold dashed) are shown for reference.
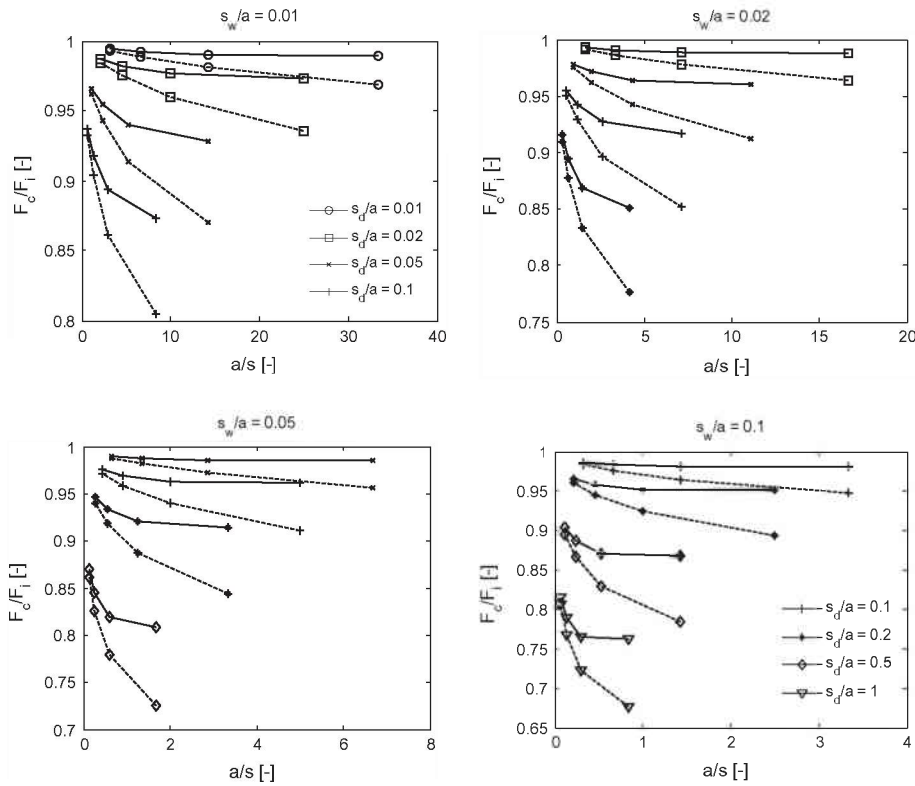
Fig. 5. F_c/F_i as a function of a/s for different screen slot geometries (s_w/a and s_d/a). Symbols correspond to $n_s = \{2, 4, 8, 16\}$ from right to left. Continuous lines correspond to $F_c/F_i = 1/(1 + F_iR_s)$, while dashed lines represent $F_c/F_i = 1/(1 + F_iR_s'/n_s)$ based on the semi-analytical solution given in the appendix (i.e., considering well screen entrance resistance of n_s slots contained between confining layers rather than for distant boundaries). $F_c/F_i = 1$ for $a/s = 0$ in all cases.

where $\varepsilon = s_w/d'$ [−] represents the portion of the screen surface occupied by slots. Eq. (18) collapses to F_i^* of Eq. (A13) in the appendix for $\varepsilon = 1$ and applying Eq. (15) gives

$$aR_s' \approx -\frac{1}{2\pi^2} \ln\left(\sin\frac{\pi\varepsilon}{2}\right) \tag{19}$$

This is an interesting and convenient expression, since it shows that the dimensionless screen resistance aR_s' can be expressed as a function of ε only (as opposed to both s_w and s_d separately). With this, an analytical approximation of Eq. (17) can be written as

$$sR_s(s \to \infty) \approx -\frac{d'}{2\pi^2 a} \ln\left(\sin\frac{\pi\varepsilon}{2}\right) \tag{20}$$

which is found to be consistently equal to or larger than Eq. (17), but within approximately 10% for $d'/a < 2$ (over the full range $0 < \varepsilon < 1$).

3.2. Effects of anisotropic conductivity and practical examples

In all of the above it is assumed that hydraulic conductivity K is the same in all directions. However, in practice it is common to encounter situations where hydraulic conductivity in the horizontal direction K_r [L/T] is significantly different (e.g., several orders of magnitude larger) than its vertical counterpart K_z [L/T]. Given the respective anisotropy ratio $\rho^2 = K_z/K_r$ [−] a scaling of the horizontal coordinate to $r\rho$ while maintaining z allows for treating the resulting flow domain as isotropic with conductivity K_r (such that continuity of flows after scaling is assured; Hvorslev, 1951). This means that all results from above remain directly applicable if $a\rho$ is used instead of a and if the effective and, hence, estimated conductivity by Eq. (2) is regarded as K_r. Thus, Eqs. (19) and (20) illustrate how R_s' for one slot segment of an infinite screen increases proportionally with $1/a\rho \sim (K_r/K_z)^{1/2}$. Strictly speaking, this is true within the range of validity of the approximation involved in those

equations (i.e., small d'/a). The dashed lines in Fig. 6 graphically illustrate this behavior in terms of $F_c/F_i = 1/(1 + F_iR_s'/n_s)$ based on R_s' from Eq. (19). In contrast, the continuous lines correspond to the exact semi-analytical solution for finite length screens and are consistent with results depicted in Fig. 4 (thin continuous) and Fig. 5 (bold continuous). By using the parameters n_s and s_w/s, which are not affected by the scaling of the radial coordinate, Fig. 6 is convenient for illustrating the behavior under anisotropy. That is, a translation on the abscissa immediately indicates the impact of anisotropy on F_c/F_i by following the graph for a given non-ideal screen geometry. In general, it is evident that screen entrance resistance increases as K_z and ρ decrease, which is a fact that may be attributed to the additional resistance to the vertical flow components between screen slots.

As a practical example we consider the case of $a = s = 2.5$ cm, which is roughly representative of the short injection screens applied by Butler et al. (2007; $a = 2.25$ cm, $s = 2.5$) and Dietrich et al. (2008; $a = 3.5$ cm, $s = 2.5$ cm). Assuming a slot width of $s_w = 0.05$ cm gives $s_w/s = 0.02$ and the squares in Fig. 6 indicate that, in order to limit non-ideal screen effects to approximately 10% (i.e., $F_c/F_i \approx 0.9$), a number of $n_s = 8$ slots is necessary under isotropic conditions of $K_r = K_z$, while for $\rho^2 = K_z/K_r = 0.01$ a number of $n_s = 16$ slots is required. Similarly, the circular dots indicate that halving the number of slots reduces F_c/F_i to approximately 0.8 and, thus, doubles the relative error to approximately 20%. In practical situations, however, the existence and magnitude of anisotropy in hydraulic conductivity is rarely known and may represent a significant source of uncertainty. Fig. 6 may still be useful in such cases by selecting screen slot geometries, such that uncertainty in F_c/F_i is minimized for a range of plausible (but unknown) anisotropy values. For example, if slot width is chosen as $s_w = 0.25$ cm, i.e., $s_w/s = 0.1$, the triangle in Fig. 6 shows that screen design with $n_s = 4$ slots result in $F_c/F_i > 0.8$ for arbitrary values of $K_z/K_r > 0.01$. However, as stated above, the estimated conductivity
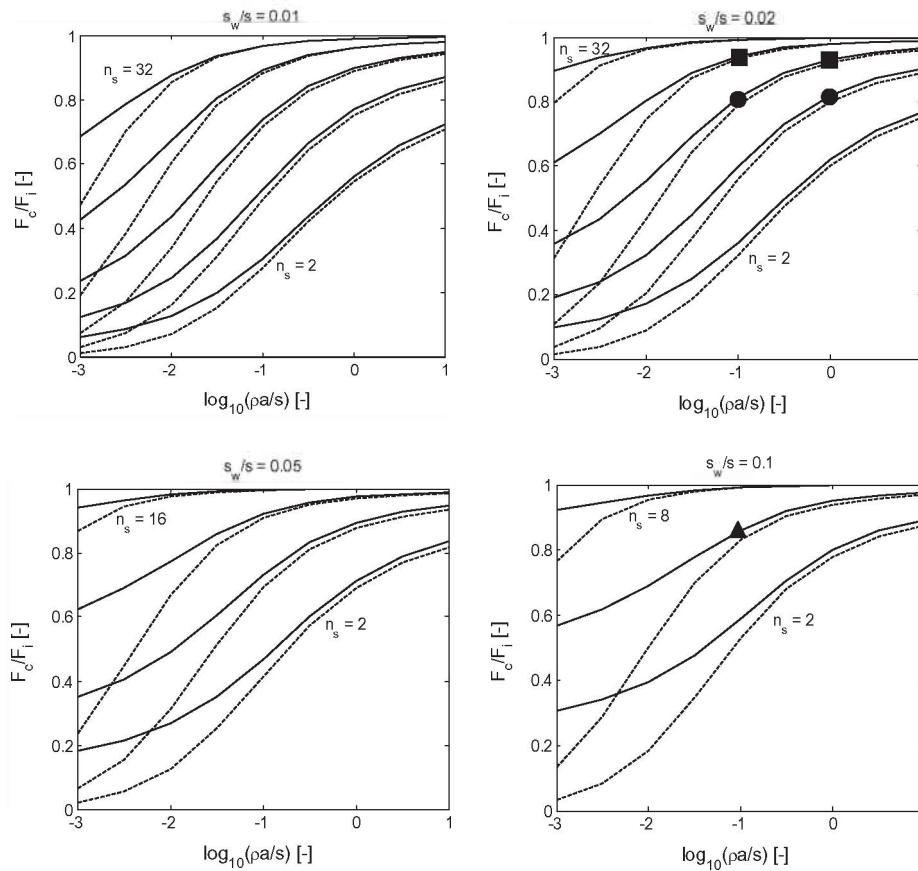
Fig. 6. F_c/F_i as a function of $\log_{10}(\rho a/s)$ for different screen slot geometries (s_w/s and n_s). Graphs correspond to $n_s = \{2, 4, 8, 16, 32\}$ from bottom up as indicated. Continuous lines correspond to $F_c/F_i = 1/(1 + F_i R_s)$, while dashed lines represent $F_c/F_i = 1/(1 + F_i R_s'/n_s)$ based on the analytical approximation of Eq. (19). Dots, squares and triangles are used in example.

under anisotropic conditions corresponds to K_r and K_z may only be determined if ρ is known independently.

Besides these rather short screens, the deployment of longer screens on small scale injection probes has also been reported in literature (Hinsby et al., 1992, $a = 2.5$ cm, $s = 25$ cm; Cho et al., 2000, $a = 1.25$ cm, $s = 45$ cm). For the geometry of Hinsby et al. (1992) $a/s = 0.1$ and for the initial assumption of $s_w = 0.05$ one finds $s_w/s = 0.002$. This is beyond the range depicted in Fig. 6 as the semi-analytical solution approach becomes computationally intensive in such cases (large number of control points required). However, Figs. 4 and 5 illustrate that R_s may be increasingly well approximated by R_s'/n_s as screen length and the number of slots increase. In combination with Eq. (19) this may be used to provide conservative (lower bound) estimates of F_c/F_i. This is reflected by the dashed and continuous graphs in Fig. 6 and may be generalized knowing that R_s'/n_s consistently overestimates R_s (compare thin continuous lines in Fig. 4), while Eq. (19) also overestimates R_s'. Thus, assuming $\rho = 1$ and $n_s = \{10, 20, 50\}$ slots one finds $F_i = 75$ cm (Klammler et al., 2011) and $F_c/F_i > 1/(1 + F_i R_s'/n_s) = \{0.65, 0.82, 0.95\}$. For $\rho = 0.1$ respective results are $F_i = 37$ cm and $F_c/F_i > \{0.27, 0.48, 0.78\}$.

3.3. Comparison to longitudinal slots

In the case of long screens consisting of longitudinal slots flow is purely horizontal ($\partial\varphi/\partial z = 0$ everywhere) and an exact analytical solution was obtained by conformal mapping (Widmoser, 1966; Nieuwenhuis and Wesseling, 1979; Youngs, 1980). Youngs (1980; Eq. (11)) express the effects of screen entrance resistance by an

effective radius a_e [L] of an ideal screen with equal shape factor as a non-ideal screen of radius a.

$$\frac{a_e}{a} = \left[\sin\left(\frac{\alpha n}{4}\right)\right]^{\frac{2}{n}} \tag{21}$$

Here, α [rad] is the angular width of a single slot and n [–] is the number of slots around the circumference. With the hydraulic resistance to purely radial flow emerging from an ideal screen of radius a being equal to $\ln(b/a)/(2\pi d')$, the ratio a_e/a may be converted into a screen resistance $R_s' = \ln(b/a_e)/(2\pi d') - \ln(b/a)/(2\pi d') = -\ln(a_e/a)/(2\pi d')$. Substituting the right-hand-side of Eq. (21) for a_e/a and knowing that $\alpha = 2\pi\varepsilon/n$ and $n = 2\pi a/d'$ in the present notation, one obtains Eq. (19) (after multiplication by a to non-dimensionalize). This means that the screen entrance resistances of circumferentially and longitudinally slotted screens of equal radius and ε are identical, which is in agreement with a conclusion of Diericks and van der Molen (1981) based on a line source/sink approximation. Furthermore, the dimensionless screen entrance resistance does not depend on any other screen or aquifer parameter, but ε. However, it is recalled that, while Eq. (19) is exact for longitudinal slots, it is based on an approximation for circumferential slots when d'/a is small. If this similarity also holds for screens of finite length is unknown, but it is surmised that it should persist to some significant extent, such that the present results also become tentatively applicable to longitudinally slotted screens. Full validation of this hypothesis is not performed here and may require a three dimensional solution to the flow problem of screens with longitudinal slots of finite length and distant boundaries. For screens with longitudinal slots under anisotropic conditions, Eqs. (19) and (20) also

remain valid, however, a is not substituted by $a\rho$, since the occurrence of a is a result of the substitution $n = 2\pi a/d$ and the number of slots n does not change with rescaling of r. This means that R'_s in this case is not affected by anisotropy in K, which makes intuitive sense, as vertical flow components do not exist.

4. Summary

The magnitude and spatial variability of hydraulic conductivity are important hydrogeological parameters affecting groundwater flow (or drainage), contaminant source zone and plume behavior. This has further impacts on environmental risk assessment and optimization of remedial actions. In the recent years, push-in probes have been developed as convenient tools for performing small scale injection tests in unconsolidated aquifers at flexible locations and depths. Interpretation of these injection tests at steady-state requires shape factors F, which act as proportionality constants between hydraulic conductivity and observed ratios of injection flow rate and injection head. While literature provides shape factors F_i for ideal injection screens of arbitrary lengths, and for non-ideal (e.g., slotted) screens of infinite length, the present work investigates shape factors F_c accounting for the combined effects of circumferential screen slot geometry and finite screen length s. This is done in terms of a screen entrance/exit resistance R_s using the approach of Klammler et al. (2011) for solving the steady-state potential flow problem in a homogeneous axi-symmetric domain with mixed boundary types corresponding to the sequence of constant injection head (slots) and impermeable (casing) elements along the injection probe. The approach is convenient as it is easily applied to sequences of different boundary types (multiple slots), but it is limited to flow domains of finite vertical extent d. The latter is overcome by computing R_s for increasing values of d and observing that R_s approaches its asymptotic value at $d \to \infty$ very quickly (i.e., for small values of d/s). This reflects the intuitive fact that the influence of screen slot geometry is limited to a small zone near the injection screen.

Results are represented in terms of a dimensionless screen entrance resistance sR_s (Fig. 4) and the relative impact F_c/F_i (Figs. 5 and 6). As to be expected, it is found that R_s grows with increasing distance between screen slots. It is also found that F_c/F_i decreases as the number of slots or the anisotropy ratio K_z/K_r decrease, which illustrates the importance of including screen length and slot arrangement in the study of non-ideal screens. Results are compared to an approximate analytical solution for an infinite sequence of circumferential slots, which is presented here in a novel form, such that a dimensionless screen entrance resistance becomes a function of relative slot area only (i.e., no other screen or aquifer parameters involved). Practical examples are given and it is shown that the approximate analytical solution for an infinite sequence of circumferential slots is identical to an exact analytical solution for infinite screens consisting of longitudinal slots. It is found that for a given conductivity in the horizontal direction, R'_s for longitudinal slots is not affected by changing vertical conductivity (because flow between slots is horizontal), while R'_s for circumferential slots increases with a decreasing vertical conductivity (because flow between slots is vertical). The present work is not concerned with investigating the effects of (possibly turbulent) head losses inside the injection device including the passage through the injection slots prior to entering the porous aquifer. In practice, circumferential screen slots have to be interrupted to provide the injection device with sufficient mechanical stability, which may violate the assumption of axi-symmetric flow taken here.

Acknowledgements

Appendix A. – determination of R'_s

The problem is described by Fig. 1a, where $s = s_w$, $d = d' = s_w + s_d$ and where both top and bottom boundaries are impermeable yielding the boundary conditions

$$I : \varphi = 0 \quad \text{at } r = b \text{ for } 0 \leqslant z \leqslant \frac{d'}{2} \tag{A1}$$

$$II : \frac{\partial \varphi}{\partial z} = 0 \quad \text{at } z = \frac{d'}{2} \text{ for } a \leqslant r \leqslant b \tag{A2}$$

$$III : \frac{\partial \varphi}{\partial z} = 0 \quad \text{at } z = 0 \text{ for } a \leqslant r \leqslant b \tag{A3}$$

$$IV : \frac{\partial \varphi}{\partial r} = 0 \quad \text{at } r = a \text{ for } \frac{s_w}{2} < z \leqslant \frac{d'}{2} \tag{A4}$$

$$V : \varphi = \varphi_0 \quad \text{at } r = a \text{ for } 0 \leqslant z \leqslant \frac{s_w}{2} \tag{A5}$$

Adopting Eqs. 8, 10, and 11 of Klammler et al. (2011) gives a general solution of the form

$$\varphi = B_0 \frac{\ln(b/r)}{\ln(b/a)} + \sum_{n=1}^{N-1} B_n f_0(m'r) \cos(m'z) \quad \text{with } m' = \frac{2n\pi}{d'} \tag{A6}$$

$$f_0(m'r) = \frac{\dfrac{K_0(m'r)}{K_0(m'b)} - \dfrac{I_0(m'r)}{I_0(m'b)}}{\dfrac{K_0(m'a)}{K_0(m'b)} - \dfrac{I_0(m'a)}{I_0(m'b)}} \tag{A7}$$

where I_j is used for modified Bessel functions of the first kind and order j (Dwight, 1947). This gives a radial derivative of

$$-\frac{\partial \varphi}{\partial r} = \frac{B_0}{r \ln(b/a)} + \sum_{n=1}^{N-1} B_n m' f_1(m'r) \cos(m'z) \tag{A8}$$

$$f_1(m'r) = -\frac{1}{m'} \frac{df_0}{dr} = \frac{\dfrac{K_1(m'r)}{K_0(m'b)} + \dfrac{I_1(m'r)}{I_0(m'b)}}{\dfrac{K_0(m'a)}{K_0(m'b)} - \dfrac{I_0(m'a)}{I_0(m'b)}} \tag{A9}$$

knowing that $dI_0(r)/dr = I_1(r)$. Substituting Eqs. (A6) into (A5) and (A8) into (A4) and using N discrete control points z_k, similar to Eqs. (12) and (13), where $k = 1, 2, \ldots, N$, $z_1 = d'/(4N)$ and $z_{k+1} - z_k = -d'/(2N)$ gives the following linear system of N equations in N unknown coefficients B_0 and B_n.

$$B_0 + \sum_{n=1}^{N-1} B_n \cos(m'z_k) = \varphi_0 \quad \text{for } 0 \leqslant z_k \leqslant \frac{s_w}{2} \tag{A10}$$

$$\frac{B_0}{a \ln(b/a)} + \sum_{n=1}^{N-1} B_n m' f_1(m'a) \cos(m'z_k) = 0 \quad \text{for } \frac{s_w}{2} < z_k \leqslant \frac{d'}{2} \tag{A11}$$

After solving for the coefficients, the shape factor F'_c [L] for a single slot on an infinitely long screen is (Klammler et al., 2011)

$$F'_c = \frac{2\pi d'}{\ln \frac{b}{a}} B_{0u} \tag{A12}$$

where $B_{0u} = B_0/\varphi_0$ [−]. For an ideal screen $s_w = d'$ and Eq. (A11) becomes irrelevant resulting in $B_{0u} = 1$ and a respective shape factor F'_i [L] of

$$F_i' = \frac{2\pi d'}{\ln\frac{b}{a}} \tag{A13}$$

which corresponds to the common solution for purely radial flow. Eq. (15) then leads to R_s' and to Eq. (17) after multiplication by d'.

References

Barua, G., Bora, S.N., 2010. Hydraulics of a partially penetrating well with skin zone in a confined aquifer. Adv. Water Res. 33, 1575–1587.

Butler, J.J., Dietrich, P., Wittig, V., Christy, T., 2007. Characterizing hydraulic conductivity with the direct-push permeameter. Ground Water 45 (4), 409–419.

Butler, A.P., Mathias, S.A., Gallagher, A.J., Peach, D.W., Williams, A.T., 2009. Analysis of flow processes in fractured chalk under pumped and ambient conditions. Hydrogeol. J. 17 (8), 1849–1858.

Chang, C.C., Chen, C.S., 2002. An integral transform approach for a mixed boundary problem involving a flowing partially penetrating well with infinitesimal well skin. Water Resour. Res. 38 (6), 1071–1077.

Chang, Y.C., Yeh, H.D., 2010. A new analytical solution solved by triple series equations method for constant-head tests in confined aquifers. Adv. Water Resour. 33, 640–651.

Cho, J.S., Wilson, J.T., Beck Jr., F.P., 2000. Measuring vertical profiles of hydraulic conductivity with in situ direct-push methods. J. Environ. Eng. 126 (8), 775–777.

Clark, L., Turner, P.A., 1983. Experiments to assess the hydraulic efficiency of well screens. Ground Water 21 (3), 270–281.

Dierickx, W., van der Molen, W.H., 1981. Effect of perforation shape and pattern on the performance of drain pipes. Agric. Water Manag. 4, 429–443.

Dietrich, P., Butler, J.J., Faiß, K., 2008. A rapid method for hydraulic profiling in unconsolidated formations. Ground Water 46 (2), 323–328.

Dwight, H.B., 1947. Tables of Integrals and Other Mathematical Data. MacMillan Company.

Hazenberg, G., Panu, U.S., 1991. Analysis of flow into draintile in three-dimensional flow field. J. Hydrol. 122, 321–333.

Hinsby, K., Bjerg, P.L., Andersen, L.J., Skov, B., Clausen, E.V., 1992. A mini slug test method for determination of a local hydraulic conductivity of an unconfined sandy aquifer. J. Hydrol. 136 (1–4), 87–106.

Hvorslev, M.J., 1951. Time lag and soil permeability in groundwater observations. U.S. Army Corps of Engineers Waterway Experimentation Station, Bulletin 36.

Kirkham, D., 1950. Potential flow into circumferential openings in drain tubes. J. Appl. Phys. 21, 655–660.

Klammler, H., Hatfield, K., Nemer, B., Mathias, S.A., 2011. A trigonometric interpolation approach to mixed-type boundary problems associated with permeameter shape factors. Water Resour. Res. 47, W03510.

Kobayashi, T., Onoue, N., Oba, S., Yasufuku, N., Omine, K., 2013. A constant-head pumping test method using direct-push equipment for in situ hydraulic conductivity measurements – discussion. Geotechnique 63 (6), 525–527.

Liu, G., Bohling, G.C., Butler, J.J., 2008. Simulation assessment of the direct-push permeameter for characterizing vertical variations in hydraulic conductivity. Water Resour. Res. 44, W02432.

Liu, G., Butler, J.J., Reboulet, E., Knobbe, S., 2012. Hydraulic conductivity profiling with direct push methods. Grundwasser 17, 19–29.

Mathias, S.A., Butler, A.P., 2007. Shape factors for constant-head double-packer permeameters. Water Resour. Res. 43, W06430.

Nieuwenhuis, G.J.A., Wesseling, J., 1979. Effect of perforation and filter material on entrance resistance and effective diameter of plastic drain pipes. Agric. Water Manag. 2, 1–9.

Panu, U.S., Filice, A., 1992. Techniques of flow rates into draintubes with circular perforations. J. Hydrol. 137, 57–72.

Perina, T., Lee, T.C., 2006. General well function for pumping from a confined, leaky or unconfined aquifer. J. Hydrol. 317, 239–260.

Prasad, S.N., Alonso, C.V., DeCoursey, D.G., 1981. Analysis of three-dimensional flow into draintile. J. Hydrol. 51, 295–303.

Price, M., Williams, A.T., 1993. A pumped double-packer system for use in aquifer evaluation and groundwater sampling. Proc. Inst. Civ. Eng. 2 (101), 85–92.

Ratnam, S., Soga, K., Whittle, R.W., 2001. Revisiting Hvorslev's intake factors using the finite element method. Geotechnique 51 (7), 641–645.

Sedighi, A., Klammler, H., Brown, C., Hatfield, K., 2006. A semi-analytical model for predicting water quality from aquifer storage and recovery system. J. Hydrol. 329 (3–4), 403–412.

Selim, M.S., Kirkham, D., 1974. Screen theory for wells and soil drainpipes. Water Resour. Res. 10 (5), 1019–1030.

Silvestri, V., Abou-Samra, G., Bravo-Jonard, C., 2011. Shape factors of cylindrical piezometers in uniform soil. Ground Water 50 (2), 279–284.

Sneyd, A.D., Hosking, R.J., 1976. Seepage flow through homogeneous soil into a row of drain pipes. J. Hydrol. 30, 127–146.

Sudicky, E.A., 1986. A natural gradient experiment on solute transport in a sand aquifer – spatial variability of hydraulic conductivity and its role in the dispersion process. Water Resour. Res. 22 (13), 2069–2092.

Weight, W.D., Sonderegger, J.L., 2001. Manual of applied field hydrogeology. McGraw-Hill.

Widmoser, P., 1966. Potentialströmung zu geschlitzten Rohren. Schweizer Bauzeitung 84H (52), 913–919.

Youngs, E.G., 1980. The hydraulic effect of filter materials around gappy non-ideal field drains. Agric. Water Manag. 3, 17–34.

Dimensionless parameters to summarize the influence of microbial growth and inhibition on the bioremediation of groundwater contaminants

M. Mohamed · K. Hatfield

Abstract Monod expressions are preferred over zero- and first-order decay expressions in modeling contaminants biotransformation in groundwater because they better represent complex conditions. However, the wide-range of values reported for Monod parameters suggests each case-study is unique. Such uniqueness restricts the usefulness of modeling, complicates an interpretation of natural attenuation and limits the utility of a bioattenuation assessment to a small number of similar cases. In this paper, four Monod-based dimensionless parameters are developed that summarize the effects of microbial growth and inhibition on groundwater contaminants. The four parameters represent the normalized effective microbial growth rate (η), the normalized critical contaminant/substrate concentration (S*), the critical contaminant/substrate inhibition factor (N), and the bioremediation efficacy (η*). These parameters enable contaminated site managers to assess natural attenuation or augmented bioremediation at multiple sites and then draw comparisons between disparate remediation activities, sites and target contaminants. Simulations results are presented that reveal the sensitivity of these dimensionless parameters to Monod parameters and varying electron donor/acceptor loads. These simulations also show the efficacy of attenuation (η*) varying over space and time. Results suggest electron donor/acceptor amendments maintained at relative concentrations S* between 0.5 and 1.5 produce the highest remediation efficiencies. Implementation of the developed parameters in a case study proves their usefulness.

Keywords Modeling · Bioremediation · Monod kinetics · Inhibition · Dimensionless · Groundwater

M. Mohamed (✉)
Civil and Environmental Engineering Department, United Arab Emirates University, P.O. Box 17555, Al-Ain, UAE
e-mail: m.mohamed@uaeu.ac.ae

M. Mohamed
Irrigation and Hydraulics Department,
Faculty of Engineering, Cairo University,
P.O. Box 12211, Giza, Egypt

K. Hatfield
Civil and Coastal Engineering Department,
University of Florida, P.O. Box 116580, Gainesville,
FL 32611, USA

Introduction

Modeling contaminant biodegradation is an essential element of subsurface bioremediation design and risk assessment. Several models that simulate subsurface contaminant attenuation have been developed varying from those with first-order decay coefficients to others using Monod expressions (e.g. Tomson and Jackson 2000; Murphy and Ginn 2000; Murphy et al. 1997; Brun and Engesgaard 2002; Prommer et al. 2002). Alvarez-Cohen and Speitel (2001) reviewed the cometabolism kinetics for chlorinated solvents.

Murphy and Ginn (2000) presented an overview of approaches used to represent physicochemical and biological processes in porous media. They categorized the processes that control subsurface contaminants biodegradation into physicochemical and biological processes. The physicochemical processes include advection, diffusion, dispersion, exclusion, straining, and physical filtration. The physicochemical processes are primarily based on the structure and properties of the groundwater flow system and porous media. Consequently, most reactive transport models incorporate some of the major physical processes, and these processes have been the focus of numerous experimental and numerical modeling studies on colloid and bio-colloid research.

Molz et al. (1986) separate biological process modeling into three distinct conceptual approaches. The first assumes unconsolidated solid aquifer materials are uniformly covered by a thin biofilm (e.g. Rittmann et al. 1980; Bouwer and McCarty 1984; Bouwer and Cobb 1987; Champagne et al. 1999; Långmark et al. 2004; Kim et al. 2004; Iliuta and Larachi 2005; Liang and Chiang 2007; Liang et al. 2007; Simpson 2008; Buchanan et al. 2008). In a second approach, bacteria are assumed to grow and attenuate contaminants within small discrete colonies (or 'micro-colonies') attached to surfaces of aquifer materials (e.g. Watson and Gardner 1986; Yoshida et al. 2006). Both biofilm and micro-colony assume substrate (i.e. contaminant) reaction kinetics are either first-order, instantaneous reaction, or multi-term Monod (Monod 1949). Other investigators (e.g. Bazin et al. 1976; Corapcioglu and Haridas 1984, 1985; Borden and Bedient 1986; Celia and Kindred 1987; Champagne et al. 1999; Långmark et al. 2004; Kim et al. 2004; Iliuta and Larachi 2005; Mohamed et al. 2006; Bauer et al. 2008) adopted a third approach which assumes partitioning between free flowing and adsorbed microorganisms (Corapcioglu and Haridas 1984, 1985) but their distribution and interaction play no role in depicting the growth dynamics (Baveye and Valocchi 1989). Monod expressions are typically assumed for most applications of this approach, because knowledge of the microorganism population distribution within the pore space is not required (Odencrantz et al. 1990). Regardless of the modeling approach taken, one of the challenges is obtaining reliable kinetic parameters to simulate in situ biotransformations.

Few studies (e.g. Clement et al. 2000; Schirmer et al. 2000) have used reactive transport models to evaluate how biodegradation processes and rates change from the laboratory to the field, which is critical information for field-scale remediation design. Clement et al. (2000) used multispecies reactive transport modeling to understand processes and rates that control natural attenuation at the Dover Air Force Base site in Delaware. Their calibrated two-dimensional model predicted the observed distributions of TCE, PCE, DCE, vinyl chloride (VC), and chloride plumes. The field-scale decay rates were within the range of values that were estimated based on laboratory-scale microcosm and field-scale transect analyses. Phanikumar et al. (2005) developed a three-dimensional reactive transport model of carbon tetrachloride (CT) bioremediation at the Schoolcraft site in western Michigan. The model simulates the transport and reactions of aqueous and sorbed phase CT, acetate, and electron acceptor (nitrate). The model was used to predict solute concentrations across the site using laboratory-based reaction parameters. A reasonable agreement was found between predicted and observed acetate and nitrate concentrations. Schirmer et al. (1999) used the numerical model BIOBATCH to determine Monod kinetic parameters for laboratory batch experiments. They indicated that measurements of several initial substrate concentrations were crucial to overcome the problem of non-uniqueness of the fitted Monod parameters. Their calculated Monod parameters for the batch degradation experiments were reasonable and comparable to other literature values. Schirmer et al. (2000) used the numerical model BIO3D and applied laboratory-derived Monod kinetic degradation parameters to simulate dissolved gasoline transport and degradation at the Canadian Forces Base site, Borden. Tebes-Stevens and Valocchi (2000) developed approaches to compute reaction parameter sensitivity coefficients to gain insight into the relative significance of parameters and to rank them in terms of their importance. Schafer (2001) applied the 3-D numerical reactive transport model TBC to understand contaminant spread and pump and treat remediation of xylene at an abandoned refinery site in Germany. Mayer et al. (2001) used multicomponent reactive transport modeling to evaluate the potential for natural attenuation of a plume containing phenolic compounds at a site in West Midlands, UK. Phanikumar et al. (2002) developed a seven-component reactive transport model to

describe microbially mediated CT degradation. It was found that the CT degradation rate in the columns was lower than values obtained from batch studies, and processes in addition to the growth and decay of strain KC cells (due to native flora) are necessary to describe the observed nitrate consumption. Phanikumar and Hyndman (2003) showed that considerations of bio-availability have a profound effect on degradation. Bioattenuation involving organic substrates and redox-sensitive species has also been the focus of several studies (e.g. Prommer et al. 1998; Brooks et al. 1999; Saiers et al. 2000; Vainshtein et al. 2003; Curtis 2003; Khan and Husain 2003; Guha 2004; Yu et al. 2007; Bauer et al. 2008). To model these systems, it is critical to capture the biogeochemistry.

Many of the early models simulated contaminant decay assuming zero order, first order, and instantaneous reaction kinetics. For zero-order reactions, the rate of substrate transformation is assumed independent of concentration (Sims et al. 1989). Zero-order decay is simple and easy to use; however, the fact that it does not consider changes in the substrate concentration limits its applicability in subsurface modeling. First-order reactions are linearly dependent on substrate concentrations. However, it is difficult to estimate field-scale first-order parameters from laboratory and field data, and it is a poor assumption that first-order parameters estimated for one field site are transferable to another (Chapelle and Lovely 1990; Schirmer et al. 1999; Goudar and Strevett 2000). Furthermore, first-order reaction models cannot distinguish between aerobic and anaerobic conditions, nor can they include coupled reaction constraints imposed by ancillary electron donor/acceptors reactions and microbial growth. Instantaneous reactions between electron acceptor/donor and contaminant are employed when microbial growth rates are relatively high compared to the groundwater velocities (Borden et al. 1984; Koussis et al. 2003; Atteia and Guillot 2007). This is not always the case in subsurface environments as some contaminants may be easily degraded while others are recalcitrant. Instantaneous reaction kinetics cannot account for cases of varying degradation rates which limits their utility to highly degradable contaminants. Thus, model simulations of natural attenuation predicated on instantaneous reaction kinetics can under predict concentration distributions.

A multiple-term Monod expression is commonly used when it is unknown which species is rate-limiting

(Mohamed and Hatfield 2005; Bauer et al. 2008). An important advantage of Monod reaction terms is their ability to simulate zero-, first-, and mixed-order reaction rates. Models based on the Monod terms are favorable over first-order growth and decay terms primarily because the later predict unbounded growth (or decay) and these are not found in nature. In general, Monod reaction terms describe nonlinear contaminant attenuation processes which are coupled to microbial growth and in turn spatial and temporal variations in microbial biomass (MacQuarrie et al. 1990). Bedient et al. (1994) showed Monod model simulations were more accurate than those derived from instantaneous reactions and first-order kinetics. Bekins et al. (1997) compared results from zero- and first-order models to a Monod model and found that the first-order model invalid for substrate concentrations above the half-saturation constant. Dette et al. (2003) demonstrated theoretically that the application of optimal design theory in Monod model is an efficient method for both parameter value identification and economic use of experimental resources. More recently, Strigula et al. (2009) presented the optimal design method as a computational tool for the efficient design of experiments in the Monod model.

Monod expressions uniquely take into consideration both microbial population and substrate levels, as interactions between these levels greatly affect the pattern of contaminant degradation (Simkins and Alexander 1984). However, the dependency of degradation rates on numerous parameters that take on a broad range of values complicates efforts to use Monod expressions to characterize biodegradation at any given site much less compare results between sites. Previous investigators developed simplified and modified Monod expressions (e.g. Bell and Binning 2002; Ribes et al. 2004; Strigula et al. 2009; McCuen and Surbeck 2008) in order to describe laboratory and field results. Others developed dimensionless parameters to facilitate interpretations and applications of Monod reactions in batch reactors (e.g. Lai and Shieh 1997; Tanyola and Tuncel 1993; Muslu 2000). In this paper, four dimensionless parameters are derived from Monod expressions to facilitate the application, description, and interpretation of Monod-based contaminant biodegradation in groundwater as influenced by microbial growth and inhibition. The dimensionless nature of these parameters enables one to compare contaminant attenuation conditions between sites.

Governing equations

In this paper, the term substrate is used interchangeably with contaminant; although, it is possible an inhibiting substrate is not a contaminant, but an amendment (i.e. a critical electron donor/acceptor) required to bring about contaminant degradation or transformation (e.g. reduction or oxidation). For a heterogeneous porous medium, the time-dependent reaction–advection–dispersion equation of a contaminant (k) (and/or electron donor/acceptor) whose spatial concentration distribution is denoted by $C(x_i, t)$ is given by:

$$R_k \frac{\partial C_k}{\partial t} = \frac{\partial}{\partial x_i}\left(D\frac{\partial C_k}{\partial x_i}\right) - V\frac{\partial C_k}{\partial x_i} + Q_k^{bio} \tag{1}$$

where x_i is the distance in i direction (i = 1,2,3 or x_i = x, y, z) [L], the local pore water velocity is V [L T^{-1}]; $\mathbf{D}$ [L^2 T^{-1}] is the tensor of the hydrodynamic dispersion coefficient, and R is the retardation factor [dimensionless]. These equations are coupled through contaminant source/sink terms Q [ML^{-3} T^{-1}] as follows:

$$Q_k^{bio} = \frac{-M\chi_k}{\theta} \tag{2}$$

where M is the microbial biomass concentration [ML^{-3}], θ is the aquifer porosity [dimensionless], and χ_k is the utilization rate of substrate k by the bacterial species (or effective consortium) [T^{-1}]. Utilization of each substrate k by a bacterial species can be written as:

$$\chi_k = \frac{\mu}{Y_k} \tag{3}$$

where Y_k is the yield coefficient [dimensionless] representing the mass of bacterial species produced per unit mass of substrate k utilized. The specific growth rate of the microbial species utilizing substrate k is described by the Haldane model as follows (Andrews 1968):

$$\mu = \mu_{max} \prod_{k=1}^{k=NS}\left(\frac{S_k}{K_c^k + S_k + \frac{s_k^2}{K_i^k}}\right) \tag{4}$$

where μ_{max} is the microbial maximum specific growth rate constant [T^{-1}], K_c^k is the half saturation coefficient for substrate k [ML^{-3}], and K_i^k is the inhibition

coefficient representing the concentration of substrate k that exerts toxic effect on the microbial species [ML^{-3}]. From Eq. 4, it evident μ is always less than μ_{max} as long as substrate inhibition exists.

Different schemes of including inhibition in the growth kinetics model exist in the literature (e.g. Edwards 1970; Luong 1987; Ohtake et al. 1990; Yamamoto et al. 1993; Christ and Abriola 2007; Jia et al. 2007). Andrews' (1968) equation (4) is the most commonly used form of growth kinetic model that includes inhibition (e.g. Jackson and Edwards 1972; Shen and Wang 1994; Sheintuch et al. 1995; Chen and Hao 1996; Surmacz-Gorska et al. 1996; López-Fiuza et al. 2002; Carrera et al. 2004; Papagianni et al. 2007). The mass balance equation for growth and decay of the microbial population can be written as:

$$\frac{dM}{dt} = M(\mu - B) \tag{5}$$

where B is the first order decay rate constant which accounts for cell decay.

Dimensionless parameters

Equations 1–5 show that the biodegradation/transformation of a contaminant or of a substrate k depends on many parameters including μ_{max}, K_c^k, K_i^k, B as well as its concentration S_k. A comparison of natural attenuation or augmented bioremediation from different sites and for different contaminants requires dimensionless Monod-based parameters. The first dimensionless parameter presented represents the ratio of net microbial growth rate at any time and location to a hypothetical maximum microbial growth rate assuming substrate inhibition and cell death are absent.

$$\eta = \prod_{k=1}^{k=NS}\left(\frac{S_k}{K_c^k + S_k + \frac{s_k^2}{K_i^k}}\right) - \frac{B}{\mu_{max}} = \frac{\mu - B}{\mu_{max}}$$
$$= \frac{1}{M\mu_{max}}\frac{dM}{dt} \tag{6}$$

η is the normalized effective microbial growth rate ($\eta = \omega_{act}/\omega_{max}$); where $\omega_{max} = \mu_{max}\ell/Y_cV$ represents, for a unit flow distance (ℓ), the ratio of the convective transport timescale ℓ/V to the timescale required to degrade/transform a unit mass of

contaminant per unit mass of microbes (Y_C/μ_{max}) in the absence of substrate inhibition and microbial cell death (Mohamed et al. 2006); $\omega_{act} = (\mu - B)\ell/Y_cV$ is the ratio of the convective transport timescale to the timescale required to degrade/transform a unit mass of contaminant per net unit mass of microbes ($Y_C/\eta\mu_{max}$) in presence of substrate inhibition and microbial cell death. Both ω_{act} and ω_{max} are equivalent to a DamKohler number of first kind (Rifai and Bedient 1990; Rashid and Kaluarachchi 1999). For $\omega_{act} \leq 1$, contaminant attenuation may be sensitive to local variations in groundwater velocity. This sensitivity may arises because the characteristic maximum specific growth rate for the microbial population, μ_{max} is small; the normalized effective microbial growth rate, η is small due to low substrate concentrations or small because of substrate inhibition; the yield coefficient, Y_C is large, or groundwater velocities are sufficiently high that time require for attenuation is significantly greater than the average groundwater hydraulic residence time. Because η incorporates multiple Monod kinetic parameters including K_c and K_i as well as solutes' concentrations, it can be used to characterize net effect of contaminant attenuation, microbial growth and inhibition over spatial and temporal scales.

The second dimensionless parameter of interest is S_{cr} or the critical substrate concentration. This variable was defined previously in the wastewater treatment literature for bacterial inhibition in batch reactors as the concentration at which μ peaks (e.g. Grady et al. 1999). As indicate above, the maximum feasible value of μ under substrate inhibition is always less than μ_{max} (Eq. 4) in the presence of substrate inhibition. As μ approaches a maximum in the presences of substrate inhibition, it is also the case that $\eta \to \eta_{max}$. Again, in the presence of substrate inhibition and cell death η_{max} is always <1; however, it represents the maximum feasible normalized microbial growth rate. The critical contaminant/substrate concentration or the critical concentration S_{cr} for any substrate m (one of the k substrates defined earlier), can be obtained by taking the derivative of η (Eq. 6) with respect to this concentration S_m:

$$S_{cr}^m = \sqrt{K_c^m K_i^m} \tag{7}$$

After substituting the definition of critical concentration back into Eq. 6, one obtains the function for η_{max}:

$$\eta_{max} = \frac{S_{cr}^m}{S_{cr}^m + 2K_c^m} \prod_{k=1}^{k=NS-1} \left(\frac{S_k}{K_c^k + S_k + \frac{S_k^2}{K_i^k}} \right) - \frac{B}{\mu_{max}} \tag{8}$$

where S_{cr}^m and K_c^m are the respective critical concentration and half-saturation coefficient for substrate m. Linking S_{cr}^m to contaminant transport, means comparing spatial and temporal variations in S_m (contaminant concentration here substrate m) to S_{cr}^m. To facilitate this comparison, a second dimensionless parameter can be defined to express normalized critical contaminant or substrate concentrations:

$$S^* = \frac{S_m}{S_{cr}^m} \tag{9}$$

Substituting this definition back in Eq. 6 gives:

$$\eta(S^*, N) = \frac{S^*}{S^* + \frac{1}{N}(1 + S^{*2})} \prod_{k=1}^{k=NS-1} \frac{S_k}{K_c^k + S_k + \frac{S_k^2}{K_i^k}} - \frac{B}{\mu_{max}} \tag{10}$$

where

$$N = \sqrt{\frac{K_i^m}{K_c^m}} \tag{11}$$

N is yet another dimensionless parameter representing the inhibition factor for contaminant/substrate m. Grady et al. (1999) used the inverse of N to indicate that inhibition in batch reactors is not solely explained by K_i. The appearance of N in Eq. 10 assures inhibition is considered through the relative value of K_i/K_c. Clearly, as N increases or K_i^m increases with respect to K_r^m, and inhibition becomes less important. N will vary between sites and between contaminants; however, the interpretation and the utility of N remain fixed. Thus, S* varies over space and time as contaminant concentrations vary due to advection, dispersion, and microbial biodegradation/transformation; the latter which can be characterized in terms of dimensionless parameters η, N and S_{cr}.

It is generally assumed microbial growth (and in turn contaminant attenuation) is limited by one substrate at any point in time (Grady et al. 1999). Assuming contaminant attenuation and microbial growth are coupled to multiple auxiliary electron donors/acceptors

and nutrients, then inhibition will vary in space and time. These variations are not just due to single substrate concentration variations, it also possible the cause of inhibition transitions between different controlling substrates. However, if inhibition from a single substrate is considered, a family of η curves can be derived for given values of N and B/μ_{max}. Values of B are typically much smaller than μ_{max} (e.g. Schafer 2001; Brusseau et al. 1999) such that B is ignored or assumed zero (e.g. Salvage and Yeh 1997; Wang and Shen 1997; Schirmer et al. 1999, 2000). The same assumption is made here, and the term B/μ_{max} is dropped in Eq. 10. This simplification produces Fig. 1a, a contour plot (on a Log-scale) of η with respect to S^* and N. This figure depicts the symmetric behavior of bioremediation potential with respect to Log S^*. Similar figures can be generated for values of $B/\mu_{max} > 0$. These figures would look similar to Fig. 1a except with different values reflecting the effect of higher decay rate. Figure 1a suggests the maximum normalized effective microbial growth rate, η_{max} occurs when Log S^* is zero (i.e. $S_m = S_{cr}^m$); however, closer examination of Eq. 10 also indicates $\eta \to 1$ if Log S^* approaches zero and Log N approaches ∞ (the case where inhibition is negligible or nonexistent). Thus, η_{max} is generally <1, unless the inhibition coefficient K_i is much larger than the half saturation coefficient K_c. For a large range of S^* and N values, Fig. 1a can be used to estimate values of η within a plume regardless of location or contaminant type. However, for small changes in S^*, Fig. 1b may be more suitable, as it presents a family of η–S^* curves for different values of N. In contrast with Fig. 1a, Fig. 1b depicts a non-symmetric behavior of η with respect to S^*. That is, η increases with S^* and arrives at the maximum feasible value (η_{max}) for S^* equal to 1.0 ($S_m = S_{cr}^m$), and then it decreases at a rate dependent on the value of N. Together the contaminant, auxiliary electron acceptors/donors, and the microbial consortium define the value of N and in turn the upper limit on the remediation potential η_{max}.

Using the definition of N in Eq. 8, the following expression can be derived for the maximum feasible normalized microbial growth rate:

$$\eta_{max} = \frac{N}{N+2} \prod_{k=1}^{k=NS-1} \left(\frac{S_k}{K_c^k + S_k + \frac{S_k^2}{K_i^k}} \right) \qquad (12)$$

The asymmetric curve in Fig. 2 represents the behavior of η_{max} with a change in Log N. This curve is asymmetric around Log N = 0.301 which is equivalent to N = 2 and where $\eta_{max} = 0.5$. At this point, the slope of this curve has a maximum value of 0.576. The asymmetry indicates, for any constant increment of ΔLog N = P about the axis of asymmetry, the following equation is pertinent

$$\frac{10^{\log 2+P}}{10^{\log 2+P} + 2} + \frac{10^{\log 2-P}}{10^{\log 2-P} + 2} = 1 \qquad (13)$$

Because Figs. 1a, b, and 2 are dimensionless, they can be used with a variety of microorganisms or consortia and for different electron acceptors/donors. They can be used in remediation system design or remediation system evaluation. In the case of system design, η_{max} is determined first. Conditions maximizing N will yield the largest feasible η but also guarantee the highest degradation rate over a widest distribution of S^* (essentially over the greatest spatial extent of plume). Different combinations of available electron acceptors/donors and microorganisms (endemic or introduced) will yield different estimates of η_{max}. Using identified values of K_i and K_c, values of N and S_{cr}^m can be calculated from which desired levels of applied auxiliary substrate concentrations S_o (electron donor/acceptors added to achieve contaminant remediation) can be determined. It would be impractical to design a system that would maintain the maximum remediation potential η_{max} everywhere in the plume at all times. A more practical target, however, is to design a remediation system with S^* in the range of (1.0–1.5) (see Fig. 1b). This would guarantee a spatial distribution of microbial growth near the maximum feasible rate η_{max} at most locations in the plume.

For the purpose of remediation system evaluation, K_i and K_c must be known or determined first. From these parameters, N, S_{cr}^m and η_{max} are respectively determined from Eqs. 7, 11, and 12. Field measured values of S_m and S_k can be used to calculate S^* and η (using Eqs. 9 and 10 or Fig. 1a) at all monitoring locations within the plume to compare against the calculated value of η_{max}. When local values of η are close to η_{max} remediation rates are close to optimal. However, at this juncture, it may be more effective to introduce a fourth dimensionless parameter, the "bioremediation efficacy" (η^*) or the ratio of the normalized effective microbial growth rate to the maximum

Fig. 1 **a** Contours of normalized effective microbial growth rate (η) in the (N–S*) log domain. **b** Normalized effective microbial growth rate versus critical contaminant/substrate concentration for different values of contaminant/substrate inhibition factor (N)
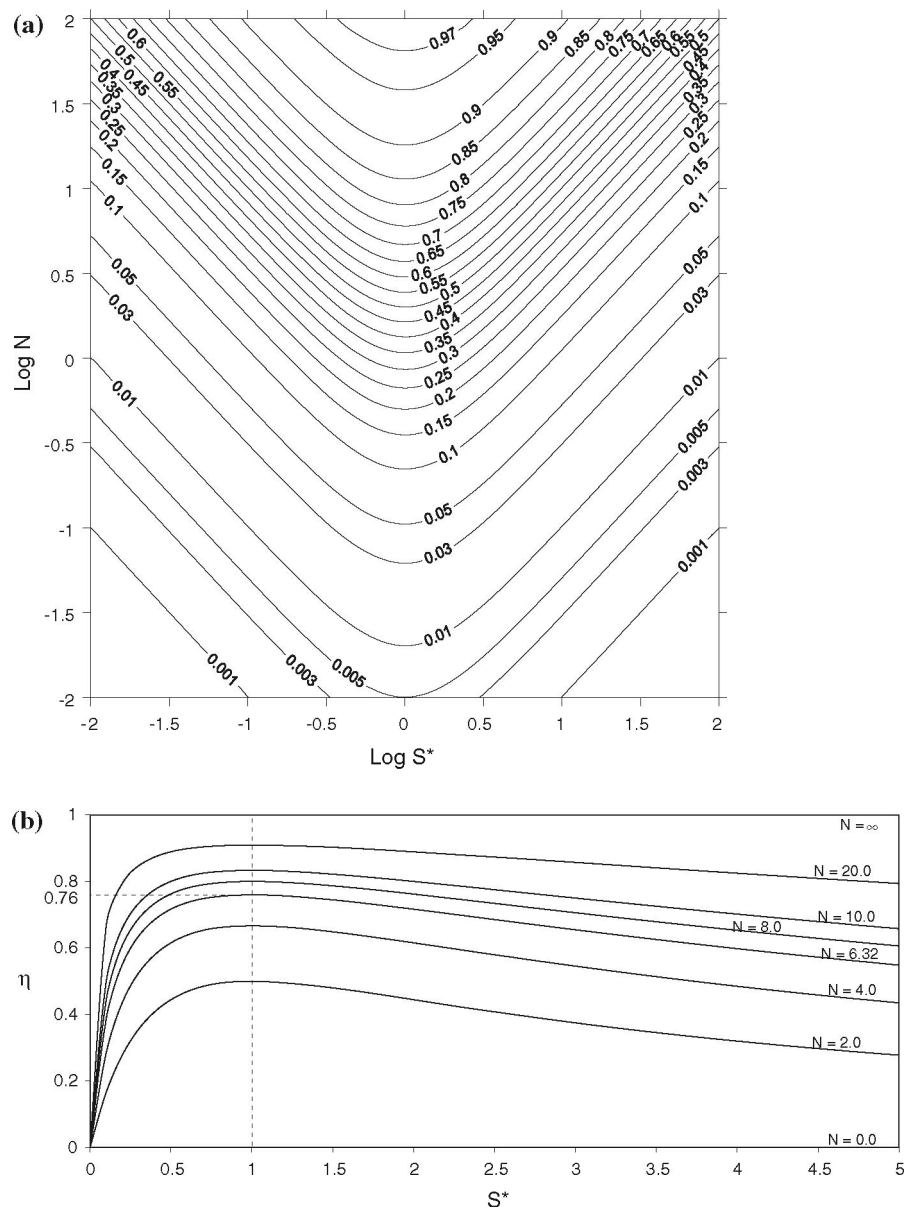

feasible microbial growth rate. From Eqs. 10 and 12, η^* is defined as follows.

$$\eta^* = \frac{\eta}{\eta_{max}} = \frac{N + 2}{N + S^* + 1/S^*} \qquad (14)$$

The bioremediation efficacy is metric for characterizing bioremediation efficiency. Unlike other previously dimensionless parameters used for bioremediation assessment, η^* is linked to microbial growth, decay and inhibition coefficients (such as μ_{max}, B, K_c, and K_i) as well as availability of both electron donors and acceptors as reflected in S* and S_{cr}. Therefore, this parameter provides a unique description of the actual bioremediation status of an aquifer. Other parameters use traditional mass loss ratios to indicate bioremediation efficiency (such as Phanikumar and Hyndman 2003; Mohamed et al. 2006, 2010a, b, c). This method uses the ratio of biodegraded contaminant mass to the total contaminate mass; whereas η^* (in the same sense) reflects the biodegraded contaminant mass to the total biodegradable contaminant mass. This, in our opinion, presents more accurate estimation of the

Fig. 2 Change of
maximum normalized
effective microbial growth
rate with Log N
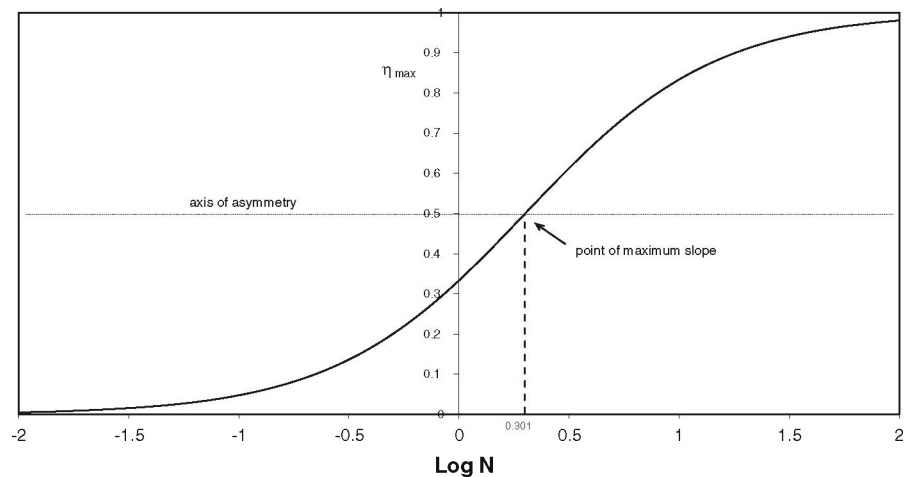
bioremediation potential of the aquifer. For example, $\eta^* = 0.4$ simply states microbial growth and in turn contaminant remediation is occurring at 40% of the feasible maximum and not 40% of μ_{max}. Additionally, the use of bioremediation efficacy is not only useful in the evaluation of natural attenuation or historical remediation activities of contaminated sites, but also helps in the design of feasible bioremediation systems including proper selection of added electron acceptors types and rates. Bioremediation efficacy is particularly valuable, because its determination enables one to assess natural attenuation or augmented bioremediation at any sites and then draw comparisons between disparate remediation activities, sites and target contaminants. Furthermore, the linkage of η^* to the microbial parameters enables one to view η^* in the context of up-scale formulas useful for linking laboratory investigations to field studies.

Figure 3a shows contours of η^* with respect to S* and N on a Log scale. This figure clearly indicates that estimations of η^* is not only site specific, but substrate specific as well. In other words, for the same site, contours of η^* could be developed for each substrate present in the site. This is of particular importance in the cases of cometabolism and competitive inhibition. For example, in the case of cometabolism (Eq. 9 in Table 2, Murphy and Ginn 2000), which involves the transformation of a compound by a microorganism that is incapable of using the compound as a source of energy for growth (e.g. Chang et al. 1993; Criddle 1993; Smith and McCarty 1997), changes in η^* will be solely due to changes in concentrations and not microbial growth. In the case

of competitive inhibition (Eq. 8 in Table 2, Murphy and Ginn 2000), when two or microbial species compete for the same nutrients (e.g. Bailey and Ollis 1986; Semprini et al. 1991), estimation of the inhibition constant (K_i), the inhibitor maximum concentration (C_i) and the inhibitor half saturation coefficient (K_c) would be of great importance. These constants are incorporated in the dimensionless parameters N and S* defined in this paper.

Another case that shows the uniqueness of the developed parameters is the case when the biomass M in Eq. 2 is partitioned into attached (M_{im}) and free-swimming (M_m) compartments. In this case Eq. 5 describes the growth of both compartments and can be separated into two equations for M_{im} and M_m (similar to Eqs. 3 and 4 in Table 2, Murphy and Ginn 2000); however, another equation will be needed to describe the transport of the free-swimming microorganisms (M_m) that includes mechanisms of microbial attachment and detachments. Consequently, the concentration of each compartment can be estimated at any time. The values of η (Eq. 6), and thus η^*, can be calculated for each compartment separately or for the total biomass M. This indicates that calculations of η^* could be flexible enough to reflect overall biodegradation or that mediated by each microbial compartment. Thus, the above discussion suggests that contours of η^* are not only substrate specific as indicated above, but also species specific. Even for the same microbial species, η^* is compartment (attached or free-swimming) specific.

Figure 3a shows the relation η^*–Log S* is symmetric (similar to Fig. 1a); and that the axis of

Fig. 3 **a** Contours of bioremediation efficacy (η^*) in the (N–S*) log domain. **b** Bioremediation efficacy (η^*) for different values of the inhibition factor N
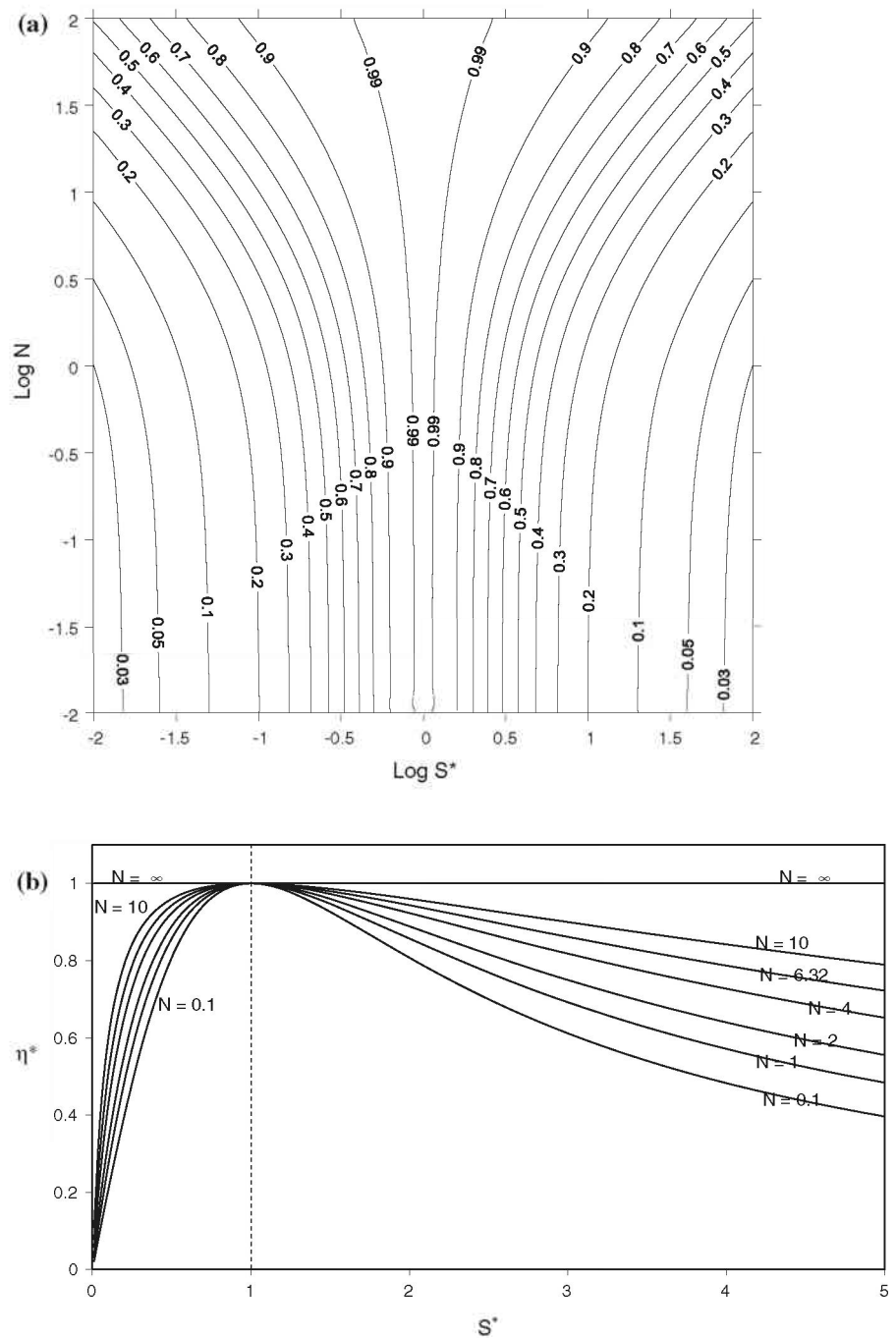
symmetry is at Log S* = 0 (i.e. S* = 1). The importance of designing a remediation system or inducing remediation conditions that maximize N is evident in Fig. 3a. η^* contours are shown extending away from the axis of symmetry as the value of N increases, which suggests the highest remediation efficacy can be maintained with less dependence on substrate variations for S* near 1.0. Thus, higher remediation efficacies can be achieved over more of the contaminant plume. For example, if it is assumed that $-2 <$ Log S* < 2 and Log N = 2, the minimum value of η^* obtained is 0.5; this is considerably larger than a value of 0.03 obtained when Log N approaches zero (i.e. $K_c = K_i$).

Figure 3b shows a family of η^*–S^* curves for different values of N assuming a range of potential contaminants. While this figure is similar to Fig. 1b, it must be the case that $\eta^* = 1$ (i.e. $\eta = \eta_{max}$) when $S^* = 1$ (i.e. $S_m = S_{cr}$) meaning remediation has achieved maximum efficacy. Figure 3a also demonstrates that in order to obtain the highest efficacy (for the same range of S^*), larger values of N are required. For example, increasing N by an order of magnitude (from 1 to 10) increases η^* from 0.8 to 0.95 for S^* equals 2.3. Again a well design remediation system would maximize N and in turn generate the greatest spatial distribution of elevated values of η^* within the plume.

Numerical simulations and testing

Problem description

To demonstrate the utility of the above dimensionless parameters, a numerical model METABIOTRANS (Mohamed et al. 2006; Mohamed and Hatfield 2007) was used to conduct simulations of a two-dimensional homogeneous horizontal aquifer with dimensions 50 m × 25 m (Fig. 4) using a mesh of 31,250 rectangular elements (250 × 125) and 31,626 nodes. The uniform pore water velocity in the x-direction (V_x) was 0.5 m/d and the respective longitudinal and transverse dispersivities were 0.1 and 0.05 m. The aquifer porosity was assumed to be 0.3. It was assumed that the aquifer was fully contaminated with a hydrocarbon which serves as an electron donor for microorganisms requiring an electron acceptor for the redox reaction to occur. Normally, contaminant biodegradation would occur at the highest rates at the fringes of the contaminant or electron donor (ED) plume where a sufficient supply of an electron acceptor (EA) exists, whereas the lowest rates of bioattenuation occur within
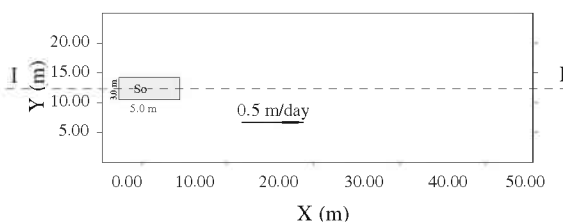
Table 1 Input parameters for the different scenarios

Scenario	S_o	K_i	S_{cr}	S_o^*	N	η_{max}
1	25	200	31.62	0.79	6.32	0.76
2	50	200	31.62	1.58	6.32	0.76
3	100	200	31.62	3.16	6.32	0.76
4	200	200	31.62	6.32	6.32	0.76
5	100	100	22.36	4.47	4.47	0.69
6	100	50	15.81	6.32	3.16	0.61
7	100	25	11.18	8.94	2.24	0.53

the plume interior or where the supply of requisite EA has been exhausted. The addition of an EA, therefore, is essential to enhance hydrocarbon (ED) bioattenuation within the interior regions of the plume. An electron acceptor such as dissolved nitrate with initial concentration of S_o is supplied to enhance bioremediation as shown in Fig. 4. Table 1 lists assumed values for Monod parameters K_i, and K_c. μ_{max} and Y_c are assumed 0.2 day^{-1} and 0.01, respectively. They kept unchanged in all simulations of this study; and consequently, the value of ω is maintained constant. Therefore, simulated changes in η are due to changes in ω_{act} only. Mohamed et al. (2006) studied the influence of changing ω on contaminants biodegradation in a stochastic framework.

Results and discussion

Several scenarios are simulated to study the spatial and temporal sensitivity of η, η^* and S^* to Monod parameters and the concentration of electron acceptor S_o^* introduced into the contaminant plume (see Table 1). Results generated using different Monod parameters can be view as results from different contaminants or the same contaminant attenuated under different microbial or site conditions. Simulations and calculated dimensionless parameters are based on representative values for Monod parameter reported in the literature (see Table 2). The first four scenarios examine the sensitivity of η, η^* and S^* to S_o^*. Constant values are assumed for K_c and K_i which produce fixed values for N and S_{cr} (see Table 1). Scenarios 3, 5, 6, and 7 are used to study the effects of substrate inhibition on spatial and temporal distributions of S^* and η^* within the plume.

Figure 5a and b respectively show model simulated remediation potentials η and efficacies η^* along

Fig. 4 Problem layout and boundary conditions

Table 2 Literature values for some of the biological parameters

| Reference	Parameter	Value/range	Calculated dimensionless variables[a]
Papagianni et al. (2007)	μ_{max}	0.23–0.65 h^{-1}	N = 1–7.32
	K_s	0.021–28 mg/l	S_{cr} = 5.6–200
	K_i	0–1500 mg/l	η_{max} = 0.33–0.79
Vavilin and Lokshina (1996)	μ_{max}	0.1–0.585 day^{-1}	N = 1–3.87
	K_s	20–200 mg/l	S_{cr} = 20–245
	K_i	20–300 mg/l	η_{max} = 0.33–0.66
Carrera et al. (2004)	μ_{max}	0.132–0.46 min^{-1}	N = 7.56–26
	K_s	1.7–37 mg/l	S_{cr} = 30.8–107.7
	K_i	559–2908 mg/l	η_{max} = 0.8–0.93
Schafer (2001)	μ_{max}	0.1 day^{-1}	N = 3.8–70.7
	K_s	0.2–70 mg/l	S_{cr} = 14.1–264.6
			η_{max} = 0.66–0.97
Brusseau et al. (1999)	μ_{max}	0.1 day^{-1}	N = 18.3–44.7
	K_s	0.5–3 mg/l	S_{cr} = 22.3–54.8
			η_{max} = 0.9–0.96
Salvage and Yeh (1997)	μ_{max}	0.9288–32.4 day^{-1}	N = 11.5
	K_s	7.5 mg/l	S_{cr} = 86.6
			η_{max} = 0.85
Wang and Shen (1997)	μ_{max}	0.6588–1.5443 day^{-1}	N = 0–13.57
	K_s	5.43–8.64 mg/l	S_{cr} = 0–93
			η_{max} = 0–0.89
Schirmer et al. (1999)	μ_{max}	4.128–4.5 day^{-1}	N = 0–14.6
	K_s	0.79–4.7 mg/l	S_{cr} = 28–68.6
			η_{max} = 0.33–0.79

[a] Calculated based on K_i = 0–1000 mg/l if not given in the corresponding literature

section I–I (see Fig. 4) assuming different initial normalized substrate concentrations (scenarios 1–4). From these figures both η and η^* increase with S_o^* which suggests greater augmented microbial growth and contaminant attenuation occurring over greater portions of the aquifer. S_{cr} is 31.62 mg/l in scenarios 1 through 4; which means maximum microbial growth and bioremediation is achieved when EA concentrations are maintained near 31.62 mg/l. In scenario 3, initial EA concentrations were sufficiently high after 20 days that microbial growth achieved the maximum feasible normalized rate of η_{max} = 0.76 over much the interior regions of the introduced EA plume. However, when S_o^* is further increased to 6.4, as in scenario 4, it is evident that after 20 days microbial growth is less than η_{max} near the centroid of the EA plume, because elevated EA concentrations are inducing significant inhibition. In fact, because dispersion decreases electron acceptor concentrations

between the interior and the fringe regions of the EA plume, remediation potential is seen to rebound and transition through η_{max} on both the leading and trailing sections of the EA plume.

An effective remediation strategy minimizes off-site risks. To achieve this, strategic use of auxiliary substrates (i.e. electron donors/acceptors) is desirable, and the above dimensionless parameters can be used with an available bioremediation simulation model to achieve this goal. Consider again, scenarios 1–4 where at t = 20 days a value of S_o^* = 3.2 (scenario 3) creates the largest zone of favorable remediation conditions (i.e. maximum remediation potential). Under this scenario, much of the remediation occurs near the source area which reduces risks to receptors close to source area. Using greater concentrations of auxiliary substrates, as in scenario 4, produces residual remediation that is greater than all the other scenarios at 60 days. This strategy may be appropriate

Fig. 5 Effect of changing
S_o* on the profile of
a normalized effective
microbial growth rate;
b bioremediation efficacy,
at section I–I for scenarios 1
through 4
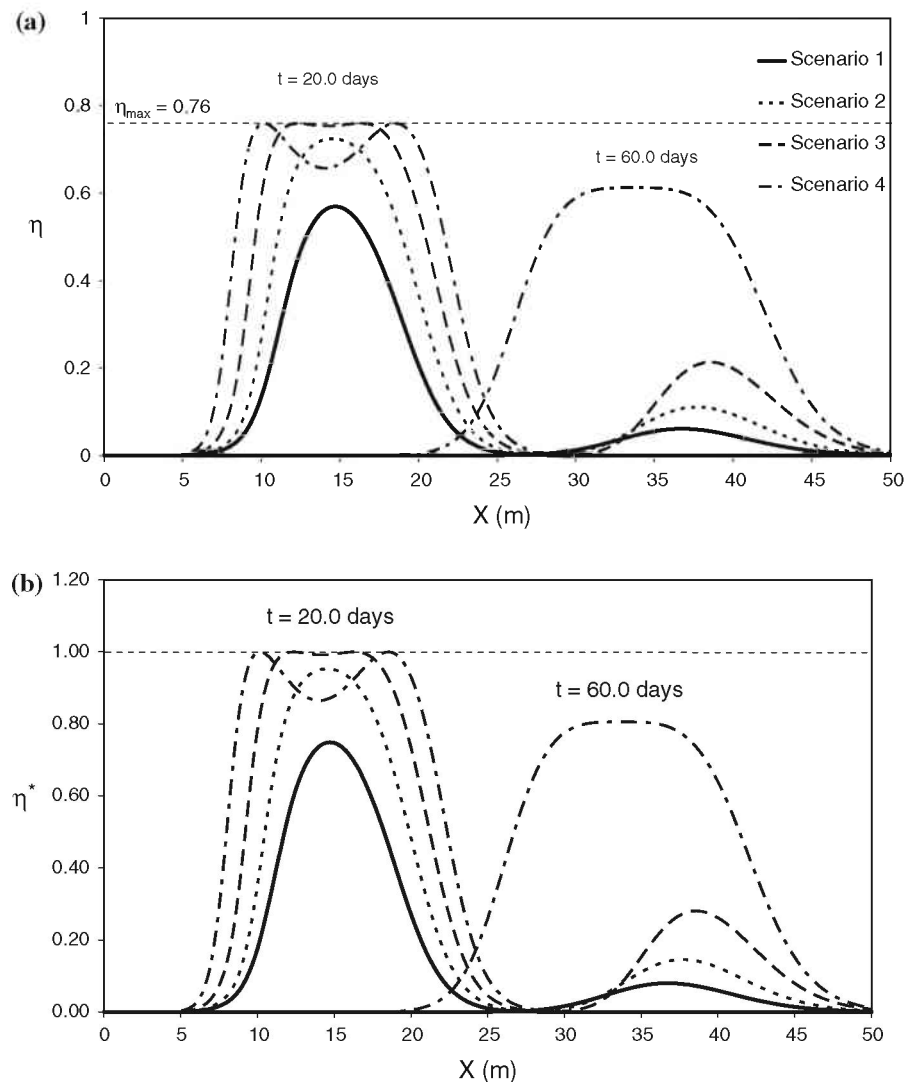
where significant residual remediation is needed over greater spatial scales, but off-site risks are low because potential receptors are far from the contaminant source.

Figure 6a illustrates how η varies with respect to N from scenarios 3, 5, 6, and 7. The inhibition factor (N), along with the critical concentration S_{cr}, define the level at which a toxic effects are manifested on microorganisms. As N decreases microorganisms are more vulnerable to inhibition. For example, manifestations of growth inhibition and contaminant attenuation appear less under Scenario 3, because the assumed N is largest. The inhibition factor can portent the likelihood of inhibition; however, the normalized concentration S* provides confirmation.

Consider again the third scenario, S* is everywhere less than one after 20 days, and η remains near η_{max}. For smaller values for N, as in scenarios 5, 6 and 7, inhibition is more prevalent; consequently, substrate inhibition constrains microbial growth which in turn produces a trough in the longitudinal spatial profile of η. It follows that smaller values of N produce smaller values of η_{max} (Fig. 2). This leads to larger zones of constrained microbial growth and contaminant degradation/transformation within the electron acceptor plume as shown in Fig. 6a. In addition, decreasing the inhibition factor gives the appearance that EA transport is retarded. Indeed, the EA plume is migrating at a velocity equal to that of groundwater. A reasonable explanation for this 'apparent

Fig. 6 Effect of changing N on the profile of **a** normalized effective microbial growth rate; **b** bioremediation efficacy, at section I–I for scenarios 3 and 5 through 7
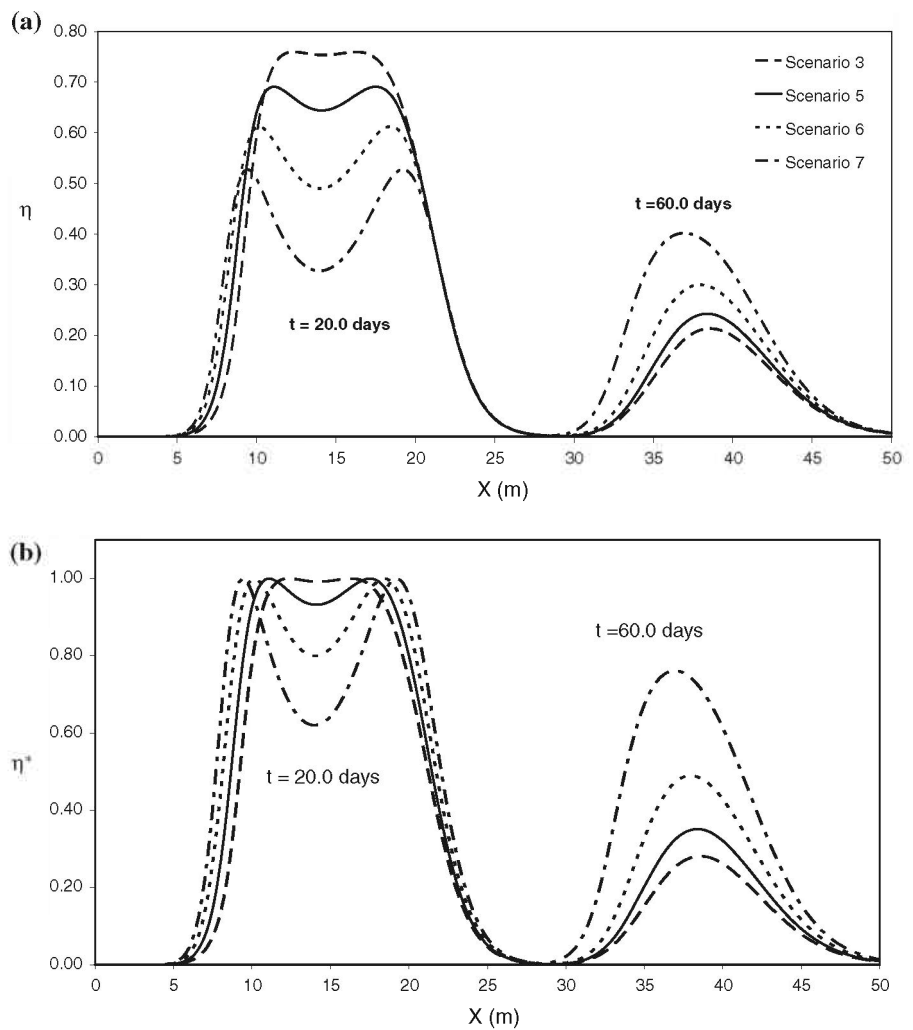

retardation' is that inhibition is limiting EA consumption to the leading edge of the EA plume, which in turn produces an up-gradient shift in the plume centroid (see results for day 60 in Fig. 6a or b). This is happening because inhibition increases rapidly from the leading edge (where EA concentrations are less-than-or-equal to critical, $S^* \leq 1$) to the interior regions of the EA plume (where EA concentrations are much greater than critical, $S^* \gg 1$). The developed dimensionless parameters indicate microbial growth and in turn contaminant attenuation are occurring at a maximum rate in regions where the normalized concentration (S^*) is equal to one.

Figure 6b presents longitudinal profiles of the bioremediation efficacy for scenarios 3, 5, 6, and 7. Efficacy is seen to achieve a maximum value of 1 somewhere within the longitudinal η^* profile of each scenario at t = 20 days. However, because introduced EA concentrations were too high in scenarios 5, 6, and 7, contaminant attenuation is depressed within the interior regions of the EA plume as evidenced by efficacies well below 1 and $S^* > 1$. This 'doughnut effect' is clearly illustrated in Fig. 7 for η and η^* and is not evident from contours of S. Areas of significant inhibition are identifiable wherever $S^* > 1$. Predicted contours of bioremediation efficacy (η^*) like those shown in Fig. 7d, can be used to assess the strengths and weaknesses of a proposed remediation designs. The discussion of the following case study shows the implementation of these dimensionless parameters to assess bioremediation in a contaminated site.

Fig. 7 Contours of **a** EA concentration, **b** relative concentration, **c** normalized effective microbial growth rate, and **d** bioremediation efficacy for scenario 6
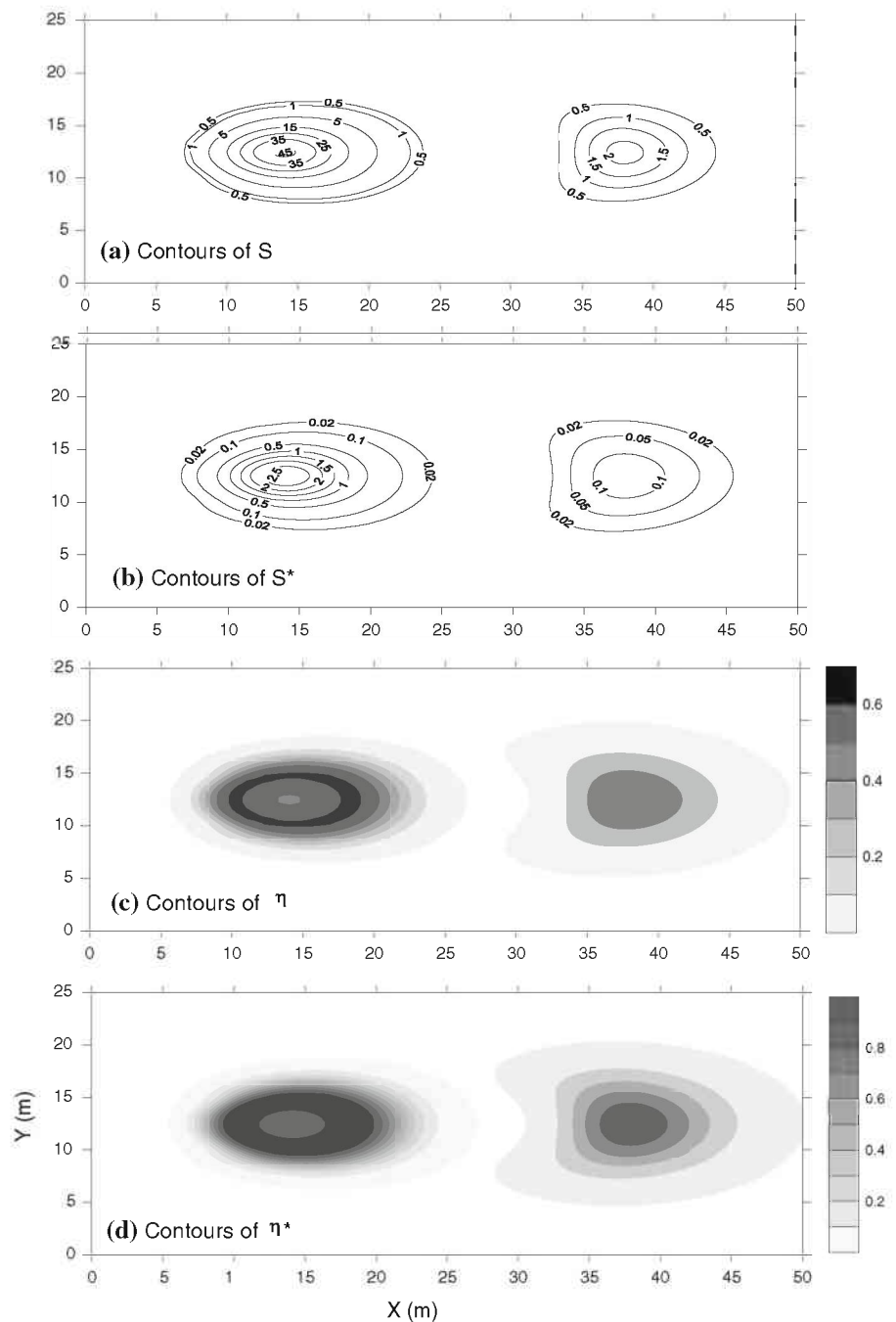
Case study: bioremediation of benzene in the contaminated Liwa aquifer, UAE

Dissolved benzene was detected in the shallow unconfined Liwa aquifer, located 150 km southwest of UAE capital Abu Dhabi (Fig. 8). The unconfined Liwa aquifer is the main water supply for irrigation, recreation, and washing for the nearby camp area (Fig. 8) and bottled water is used for drinking. After benzene contamination was discovered in 2000, soil investigations at the site were performed through 142 organic vapor analysis (OVA) readings from 27 test pits field measurements and hydrocarbons were detected in the soil. It was found that contaminated
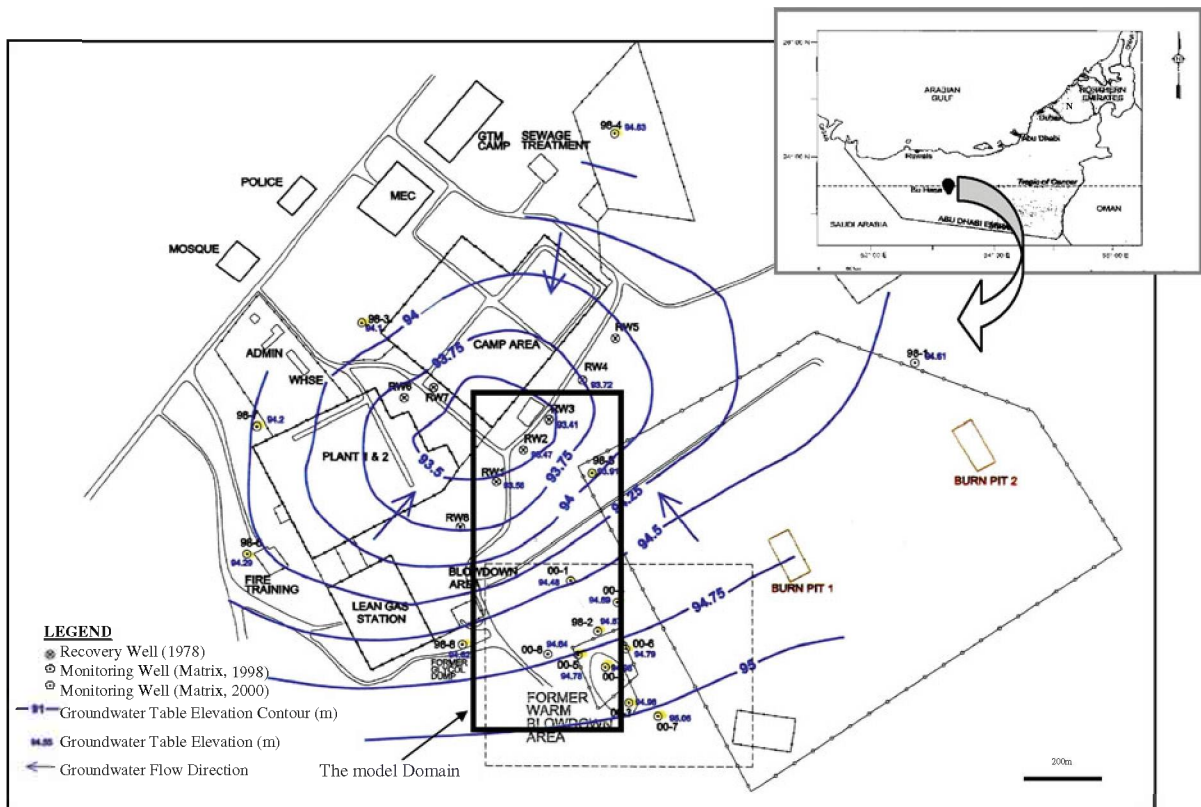
Fig. 8 Site location of Bu Hasa Liquid Recovery Plant, including site plan, water table elevations, and model domain

soil had higher concentrations than background OVA measurements. A monitoring wells network was installed to investigate the extent of hydrocarbon plume from the source zone (Fig. 8). The presence of free phase hydrocarbons floating on the water table was confirmed. The location of the non-aqueous phase liquid (NAPL) measured in the soil is consistent with observations of the dissolved hydrocarbons (Forrest and Arnell 2001). This suggests that the pure NAPL in the soil migrated downward in the unsaturated zone and, being lighter than water, formed a body floating near the water table. For an ideal NAPL mixture in contact with water, the aqueous phase concentration of a component in NAPL can be calculated using the aqueous analog of Raoult's law as the product of its pure aqueous solubility and its mole fraction. Benzene constitutes the highest dissolved concentration of NAPL constituents at the site. Partial dissolution of benzene in the surrounding groundwater results in the formation of a dissolved plume. This dissolved benzene plume migrates by advection and dispersion processes. McNab et al.

(1997) assumed that the mole fraction of benzene is equal to 0.5% of its weight fraction, the pure benzene solubility is equal to 1770 mg/l; therefore the aqueous phase concentration of the benzene in NAPL mixture is 8.85 mg/l. However, Johnson et al. (2000) reported that the equilibrium concentration of BETX resulted from typical gasoline mixture in contact with water has a benzene concentration of 18 mg/l. Assuming ideal NAPL mixture, the aqueous phase benzene concentration for this site is estimated to be 8.5 mg/l.

Groundwater elevation data (Woodward 1996) indicate that the regional groundwater flow direction in Liwa aquifer is to the northwest. The hydraulic gradient of the groundwater in the site is variable. The gradient increases towards the pumping wells; therefore, the groundwater velocity also increases in the same area. The hydraulic gradient between the contamination source zone and the supply water wells is 0.25%. Water depths were recorded in November 2000 using the monitoring network and used to calculate groundwater table elevations. Contour map

of groundwater elevation is produced in Fig. 8, based on the records of groundwater levels, and used to estimate groundwater flow direction and horizontal hydraulic gradient. The groundwater flow direction is found to be in agreement with the direction of the regional groundwater flow in Liwa aquifer. Field estimated values for effective porosity of 0.3 and hydraulic conductivity of 1×10^{-4} m/s were used to estimate the average linear groundwater velocity of 25 m/year. It was found that the contamination source is located directly up-gradient of the supply wells; which puts these wells at potential risk of being contaminated.

Simulation of benzene transport in Liwa aquifer is conducted using METABIOTRANS. The simulated model domain covers an area of approximately 292,250 m^2. It was oriented so that it includes the contamination source zone in the southeast corner and the nearest supply wells RW1–RW3 (Fig. 8) representing potential receptors in the northwest corner, directly downstream of the contamination. The domain extends 350 m in x-direction and 850 m in y-direction. A two dimensional finite element grid of 11,900 elements was used for spatial discretization of the study area. Limited measurements were available to determine input parameters for the transport of the dissolved benzene. Values of longitudinal and transverse dispersivities were estimated through model calibration. Model calibration was performed using the observed benzene concentrations at the location of the monitoring well 00-8. Benzene concentration of 0.03 mg/l was observed in this well in July 2000 (Forrest and Arnell 2001). Values of longitudinal and transverse dispersivities were estimated to be 2.3 and 0.23 m, respectively. These values are average for this type of aquifers (e.g. Weaver and Charbeneau 2000).

The calibrated model is used to simulate the transport and fate of the dissolved benzene plume in Liwa aquifer. The slow-release oxygen source (SOS) in situ remediation technique is used in these simulations. This techniques is developed by researchers from the United States Environmental Protection
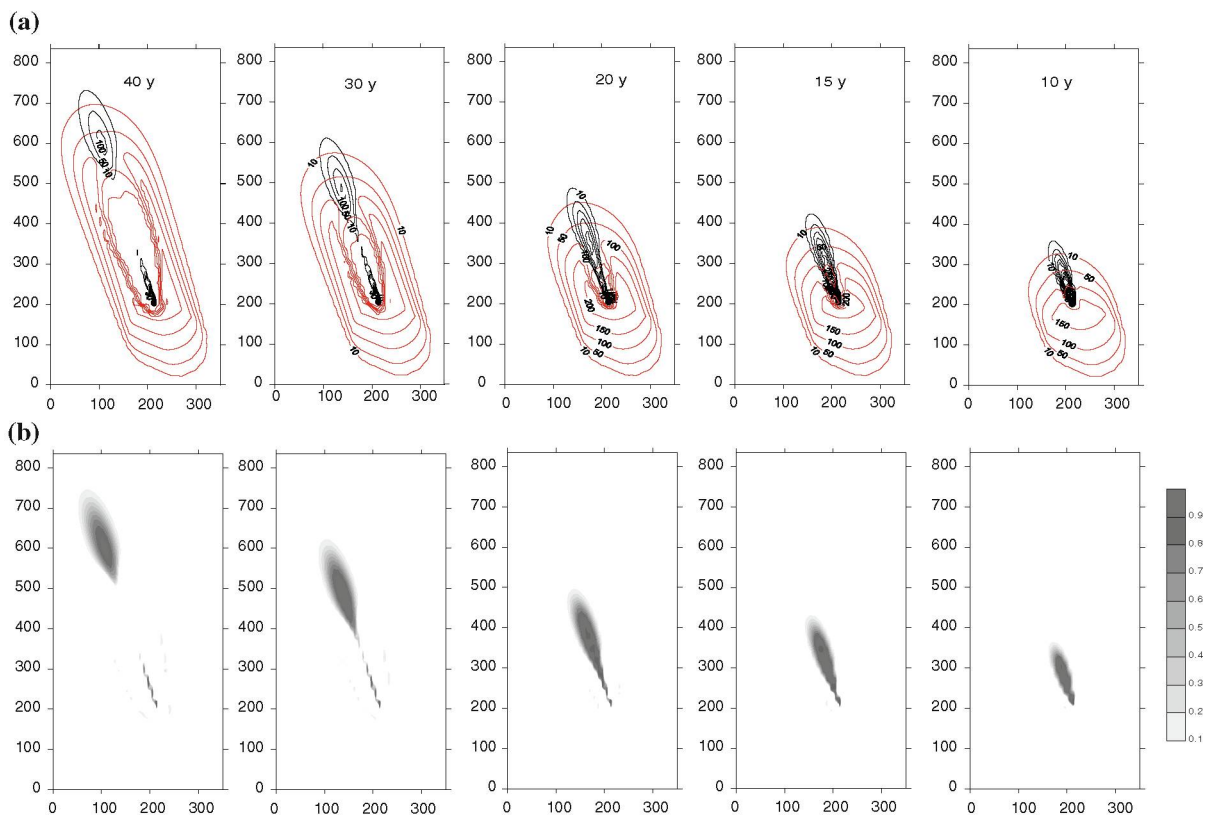

Fig. 9 Evolution of the **a** benzene and oxygen plumes and **b** biodegradation efficacy contours in the aquifer of Bu Hasa field

Agency (US-EPA) in which a constant and controlled release of oxygen through the treatment zone is introduced (Hoover 2007). The technique is based on earlier work of using solid oxygen sources to introduce oxygen in contaminated sites (Vesper et al. 1994). An SOS, located at X = 210 m and Y = 200 m of the domain, is used to enhance bioremediation of the benzene plume. Values of the biological parameters are selected based on values reported in similar studies (e.g. Vavilin and Lokshina 1996; Table 2). The K_s and K_i values are selected to be 125 and 300 mg/l, respectively. Based on these values S_{cr} is calculated to be 194 mg/l and N equals 1.55. Figure 9a shows the two simulated plumes of benzene and oxygen at different times. Using an SOS enhanced remediation in the core of the benzene plume. However, some of the dissolved benzene escaped remediation as depicted by the leading edge of the benzene plume downstream of the injection point. This occurred probably because oxygen concentrations needed time to increase and stimulate bacterial growth and also because microorganisms grow only when the benzene plume encounter the remediation zone. That is why the leading edge of the plume will always encounter lower microbial concentration than the trailing edge, and therefore will continuously experience less bioremediation. Figure 9b shows the evolution of simulated η^* contours. This figure facilitates the assessment of biodegradation efficacy and clearly shows regions of enhanced bioremediation in the aquifer at different times. Simulated concentrations of the oxygen were higher at earlier times (10 and 15 years) than later times which depicts higher values of η^* (near maximum) at earlier times. At later times, because oxygen concentration as well as benzene concentrations decrease due to dispersion and biodegradation, values of η^* decrease as well. However, maximum bioremediation still occurs near the center of the oxygen plume.

Summary and conclusions

This paper presented four dimensionless parameters that enable the evaluation of natural attenuation and augmented bioremediation across different contaminants and sites. These parameters were the normalized effective microbial growth rate (η), the bioremediation efficacy (η^*), the contaminant/substrate inhibition factor (N) and the normalized critical contaminant/substrate concentration (S*). Simulations revealed the sensitivity of these dimensionless parameters to Monod parameters and to varying electron donor/acceptor loads. These simulations also showed the efficacy of attenuation (η^*) varied over space and time. The contaminant/substrate inhibition factor (N) could be used to alert site managers that substrate inhibition could interfere with microbial growth and contaminant attenuation. Whereas the normalized critical contaminant/substrate concentration (S*) would be the most appropriate for confirming the existence and potential whereabouts of inhibition with respect to microbial growth and contaminant attenuations in contaminated aquifers. Results suggested electron donor/acceptor amendments maintained at relative concentrations S* between 0.5 and 1.5 produce the highest remediation efficiencies.

Microorganisms and electron acceptors/donors added to augment remediation should be selected whenever possible to generate a highest substrate inhibition factor (N). This would not only result in higher remediation efficiencies, but would also guarantee higher rates sustained over a wider range of normalized substrate concentrations. Finally, contour maps of bioremediation efficacy (η^*) could be used to provide site-wide characterization of remediation efficiency. The implementation of such contour maps is proven to be useful through the design of a remediation system for a contaminated site using a slow-release oxygen source.

References

Alvarez-Cohen L, Speitel GE (2001) Kinetics of aerobic cometabolism of chlorinated solvents. Biodegradation 12(2):105–126

Andrews JF (1968) A mathematical model for the continuous culture of microorganisms utilizing inhibitory substance. Biotechnol Bioeng 10:707–723

Atteia O, Guillot C (2007) Factors controlling BTEX and chlorinated solvents plume length under natural attenuation conditions. J Contam Hydrol 90(1–2):81–104

Bailey JE, Ollis DF (1986) Biochemical engineering fundamentals, 2nd edn. McGraw-Hill, New York

Bauer RD, Maloszewski P, Zhang Y, Meckenstock RU, Griebler C (2008) Mixing-controlled biodegradation in a toluene plume—results from two-dimensional laboratory experiments. J Contam Hydrol 96(1–4):150–168

Baveye P, Valocchi A (1989) An evaluation of mathematical models of the transport of biologically reacting solutes in saturated soils and aquifers. Water Resour Res 25(6): 1413–1421

Bazin MJ, Saunders PT, Prosser JI (1976) Models of microbial interactions in the soil. CRC Crit Rev Microbiol 4: 463–498

Bedient PB, Rifai HS, Newell CJ (1994) Ground water contamination—transport and remediation. Prentice-Hall, Englewood Cliffs, NJ

Bekins BA, Warren E, Godsy ME (1997) Comparing zero- and first-order approximations to the Monod model. In: Proceedings of the fourth international in situ and on-site bioremediation symposium, Battelle Press, New Orleans, LA, vol 5, pp 547–552

Bell LSJ, Binning P (2002) A forward particle tracking Eulerian Lagrangian Localized Adjoint Method for multicomponent reactive transport modelling of biodegradation. Dev Water Sci 47:703–710

Borden RC, Bedient PB (1986) Transport of dissolved hydrocarbons influenced by oxygen-limited biodegradation: 1. Theoretical development. Water Resour Res 22(13): 1973–1982

Borden RC, Lee MD, Wilson JT, Ward CH, Bedient PB (1984) Modeling the migration and biodegradation of hydrocarbons derived from a wood-creosoting process waste. In: Proceedings of the National Water Well Association, American Petroleum Institute conference on petroleum hydrocarbons and organic chemicals in groundwater: prevention, detection and restoration, Houston, TX, pp 130–143

Bouwer EJ, Cobb GD (1987) Modeling of biological processes in the subsurface. Water Sci Technol 19:769–779

Bouwer EJ, McCarty PL (1984) Modeling of trace organics biotransformation in the subsurface. Ground Water 22:433–440

Brooks SC, Carroll SL, Jardine PM (1999) Sustained bacterial reduction of Co(III) EDTA in the presence of competing geochemical oxidation during dynamic flow. Environ Sci Technol 33:3938

Brun A, Engesgaard P (2002) Modelling of transport and biogeochemical processes in pollution plumes: literature review and model development. J Hydrol 256(3–4):211–227

Brusseau M, Xie L, Li L (1999) Biodegradation during contaminant transport in porous media: 1. Mathematical analysis of controlling factors. J Contam Hydrol 37: 269–293

Buchanan W, Roddicka F, Porter N (2008) Removal of VUV pre-treated natural organic matter by biologically activated carbon columns. Water Res 42(13):3335–3342

Carrera J, Jubany I, Carvallo L, Chamy R, Lafuente J (2004) Kinetic models for nitrification inhibition by ammonium and nitrite in a suspended and an immobilised biomass systems. Process Biochem 39(9):1159–1165

Celia MA, Kindred JS (1987) Numerical simulation of subsurface contaminant transport with multiple nutrient biodegradation. In: Proceedings of the international conference on the impact of physiochemistry on the study, design, and optimization of processes in natural porous media, Presses University de Nancy, Nancy, France

Champagne P, Parker WJ, Van-Geel P (1999) Modeling cometabolic biodegradation of organic compounds in biofilms. Water Sci Technol 39(7):147–152

Chang M-K, Voice TC, Criddle CS (1993) Kinetics of competitive inhibition and cometabolism in the biodegradation of benzene, toluene, and p-xylene by two Pseudomonas isolates. Biotechnol Bioeng 41:1057–1065

Chapelle FH, Lovely DR (1990) Rates of bacterial metabolish in deep coastal plain aquifers. Appl Environ Microbiol 56:1865–1874

Chen JM, Hao OJ (1996) Environmental factors and modeling in microbial chromium(VI) reduction. Water Environ Res 68(7):1156

Christ JA, Abriola LM (2007) Modeling metabolic reductive dechlorination in dense non-aqueous phase liquid sourcezones. Adv Water Resour 30(6–7):1547–1561

Clement TP, Johnson CD, Sun YW, Klecka GM, Bartlett C (2000) Natural attenuation of chlorinated ethene compounds: model development and field-scale application at the Dover site. J Contam Hydrol 42(2–4):113–140

Corapcioglu MY, Haridas A (1984) Transport and fate of microorganisms in porous media: a theoretical investigation. J Hydrol 72:149–169

Corapcioglu MY, Haridas A (1985) Microbial transport in soils and groundwater: a numerical model. Adv Water Resour 8:188–200

Criddle CS (1993) The kinetics of cometabolism. Biotechnol Bioeng 41:1048–1056

Curtis GP (2003) Comparison of approaches for simulating reactive solute transport involving organic degradation reactions by multiple terminal electron acceptors. Comput Geosci 29:319–329

Dette H, Melas VB, Pepelyshev A, Strigul N (2003) Efficient design of experiments in the Monod model. J R Stat Soc B 65(3):725–742

Edwards VH (1970) The influence of high substrate concentration on microbial kinetics. Biotechnol Bioeng 12: 679–712

Forrest B, Arnell P (2001) Hydrocarbon delineation and pilot testing program at the Bu Hasa Liquids Recovery Plant Abu Dhabi report, United Arab Emirates. Matrix Solutions Inc. Report 01-47

Goudar CT, Strevett KA (2000) Estimating in situ Monod biodegradation parameters using a novel explicit solution of a one-dimensional contaminant transport equation. Ground Water 38:894–898

Grady CPLJ, Daigger GT, Lim HC (1999) Biological wastewater treatment. Marcel Dekker, New York

Guha H (2004) Biogeochemical influence on transport of chromium in manganese sediments: experimental and modeling approaches. J Contam Hydrol 70:1–36

Hoover D (2007) Process for the biodegradation of hydrocarbons and ethers in subsurface soil by introduction of a solid oxygen source by hydraulic fracturing. United States Patent 7,252,986

Iliuta I, Larachi F (2005) Modeling simultaneous biological clogging and physical plugging in trickle-bed bioreactors for wastewater treatment. Chem Eng Sci 60(5):1477–1489

Jackson JV, Edwards VH (1972) Kinetics of substrate inhibition of exponential yeast growth. Biotechnol Bioeng 17:943–964

Jia Y, Aagaard P, Breedveld GD (2007) Sorption of triazoles to soil and iron minerals. Chemosphere 67:250–258

Johnson R, Pankow J, Bender D, Price C, Zogorski J (2000) Environ Sci Eng 2–9

Khan FI, Husain T (2003) Evaluation of a petroleum hydrocarbon contaminated site for natural attenuation using 'RBMNA' methodology. Environ Model Softw 18(2):179–194

Kim H, Peter RJ, Young LY (2004) Simulating biodegradation of toluene in sand column experiments at the macroscopic and pore-level scale for aerobic and denitrifying conditions. Adv Water Resour 27(4):335–348

Koussis AD, Pesmajogloua S, Syriopoulou D (2003) Modelling biodegradation of hydrocarbons in aquifers: when is the use of the instantaneous reaction approximation justified? J Contam Hydrol 60(3–4):287–305

Lai B, Shieh K (1997) Substrate inhibition kinetics in a fluidized bioparticle. Chem Eng J 65:117–121

Långmark J, Storeya MV, Ashboltb NJ, Stenström TA (2004) Artificial groundwater treatment: biofilm activity and organic carbon removal performance. Water Res 38(3):740–748

Liang C, Chiang P (2007) Mathematical model of the non-steady-state adsorption and biodegradation capacities of BAC filters. J Hazard Mater 139(2):316–322

Liang C, Chiang P, Chang E (2007) Modeling the behaviors of adsorption and biodegradation in biological activated carbon filters. Water Res 41(15):3241–3250

López-Fiuza J, Buys B, Mosquera-Corral A, Omil F, Méndez R (2002) Toxic effects exerted on methanogenic, nitrifying and denitrifying bacteria by chemicals used in a milk analysis laboratory. Enzyme Microb Technol 31:976–985

Luong JHJ (1987) Generalization of Monod kinetics for analysis of growth data with substrate inhibition. Biotechnol Bioeng 29:242–248

MacQuarrie KTB, Sudicky EA, Frind EO (1990) Simulation of biodegradable organic contaminants in groundwater: 1. Numerical formulation in principal directions. Water Resour Res 26(2):207–222

Mayer KU, Benner SG, Frind EO, Thornton SF, Lerner DN (2001) Reactive transport modeling of processes controlling the distribution and natural attenuation of phenolic compounds in a deep sandstone aquifer. J Contam Hydrol 52(3–4):341–368

McCuen RH, Surbeck CQ (2008) An alternative to specious linearization of environmental models. Water Res 42(15):4033–4040

McNab WW, Dooher BP, Rice DW, Kavanaugh MC, Johnson PC, Cullen SJ, Everett LG, Kastenberg WE (1997) Assessment of appropriate fuel hydrocarbon risk management strategies for George Air Force Base, Victorville, California using a risk based approach. Lawrence Livermore National Laboratory, University of California. UCRL-AR-125619

Mohamed M, Hatfield K (2005) Modeling microbial-mediated reduction using the quasi-steady-state approximation. Chemosphere 59:1207–1217

Mohamed M, Hatfield K, Hassan AE (2006) Monte Carlo evaluation of microbial-mediated contaminant reactions in heterogeneous aquifers. Adv Water Resour 29:1123–1139

Mohamed M, Hatfield K, Perminova IV (2007) Evaluation of Monod kinetic parameters in the subsurface using moment analysis: theory and numerical testing. Adv Water Resour 30:2034–2050

Mohamed M, Saleh N, Sherif M (2010a) Modeling in-situ benzene bioremediation in the contaminated Liwa Aquifer (UAE) using the slow-release oxygen source technique. Environ Earth Sci 61(7):1385–1399

Mohamed M, Hatfield K, Hassan AE, Klammler H (2010b) Stochastic evaluation of subsurface contaminant discharges under physical, chemical, and biological heterogeneities. Adv Water Resour 33(7):801–812

Mohamed M, Saleh N, Sherif M (2010c) Sensitivity of natural attenuation to variations in kinetic and transport parameters. Bull Environ Contam Toxicol 84(4):443–449

Molz FJ, Widdowson MA, Benefield LD (1986) Simulation of microbial growth dynamics coupled to nutrient and oxygen transport in porous media. Water Resour Res 22(8):1207–1216

Monod J (1949) The growth of bacterial cultures. Annu Rev Microbiol 3:371–394

Murphy EM, Ginn TR (2000) Modeling microbial processes in porous media. Hydrogeol J 8:142–158

Murphy EM, Ginn TR, Chilakapati A, Resch CT, Phillips JL, Wietsma TW, Spadoni CM (1997) The influence of physical heterogeneity on microbial degradation and distribution in porous media. Water Resour Res 33(5):1087–1103

Muslu Y (2000) A study on performance characterization of suspended growth systems. Water Air Soil Pollut 124:285–300

Odencrantz JE, Valocchi AJ, Rittmann BE (1990) Modeling two-dimensional solute transport with different biodegradation kinetics. In: Proceedings of the petroleum hydrocarbons and organic chemicals in groundwater: prevention, detection and restoration, National Water Well Association, Houston, TX, pp 355–368

Ohtake H, Fuji E, Toda K (1990) Bacterial reduction of hexavalent chromium: kinetic aspects of chromate reduction by *Enterobacter cloacae* HO1. Biocatalysis 4(2):227

Papagianni M, Boonpooh Y, Matty M, Kristiansen B (2007) Substrate inhibition kinetics of *Saccharomyces cerevisiae* in fed-batch cultures operated at constant glucose and maltose concentrations levels. J Ind Microbiol Biotechnol 34:301–309

Phanikumar MS, Hyndman DW (2003) Interactions between sorption and biodegradation: exploring bioavailability and pulsed nutrient injection efficiency. Water Resour Res 39(5):1122. doi:10.1029/2002WR001761

Phanikumar MS, Hyndman DW, Wiggert DC, Dybas MJ, Witt ME, Criddle CS (2002) Simulation of microbial transport and carbon tetrachloride biodegradation in intermittently fed aquifer columns. Water Resour Res 38(4):1033. doi:10.1029/2001WR000289

Phanikumar MS, Hyndman DW, Zhao X, Dybas MJ (2005) A three-dimensional model of microbial transport and

biodegradation at the Schoolcraft, Michigan, site. Water Resour Res 41:5011. doi:10.1029/2004WR003376

Prommer H, Barry DA, Davis GB (1998) A one-dimensional reactive multi-component transport model for biodegradation of petroleum hydrocarbons in groundwater. Environ Model Softw 14(2–3):213–223

Prommer H, Barry DA, Davis GB (2002) Modelling of physical and reactive processes during biodegradation of a hydrocarbon plume under transient groundwater flow conditions. J Contam Hydrol 59(1–2):113–131

Rashid M, Kaluarachchi J (1999) A simplified numerical algorithm for oxygen- and nitrate-based biodegradation of hydrocarbons using Monod expressions. J Contam Hydrol 40(1):53–77

Ribes J, Keesman K, Spanjers H (2004) Modeling anaerobic biomass growth kinetics with a substrate threshold concentration. Water Res 38(20):4502–4510

Rifai HS, Bedient PB (1990) Comparison of biodegradation kinetics with an instantaneous reaction model for groundwater. Water Resour Res 26:637–645

Rittmann BE, McCarty PL, Roberts PV (1980) Trace-organics biodegradation in aquifer recharge. Ground Water 18:236–243

Saiers JE, Guha H, Jardine PM, Brooks S (2000) Development and evaluation of a mathematical model for the transport and oxidation–reduction of CoEDTA. Water Resour Res 36:3151–3165

Salvage KM, Yeh GT (1997) Development and application of a numerical model of kinetics and equilibrium microbiological and geochemical reactions (BIOKEMOD). J Hydrol 209:27–52

Schafer W (2001) Predicting natural attenuation of xylene in groundwater using a numerical model. J Contam Hydrol 52:57–83

Schirmer M, Butler BJ, Roy JW, Frind EO, Barker (1999) A relative-least-squares technique to determine unique Monod kinetic parameters of BTEX compounds using batch experiments. J Contam Hydrol 37:69–86

Schirmer M, Molson JW, Frind EO, Barker JF (2000) Biodegradation modeling of a dissolved gasoline plume applying independent laboratory and field parameters. J Contam Hydrol 46(3–4):339–374

Semprini L, Hopkins GD, Roberts PV, Grbic-Galic D, McCarty PL (1991) A field evaluation of in-situ biodegradation of chlorinated ethenes: Part 3. Studies of competitive inhibition. Gr Water 29:239–250

Sheintuch M, Tartakovsky B, Narkis N, Rebhun M (1995) Substrate inhibition and multiple states in a continuous nitrification process. Water Res 29:953–963

Shen H, Wang YT (1994) Modeling hexavalent chromium reduction in E. coli 33456. Biotechnol Bioeng 43(4):293

Simkins S, Alexander M (1984) Models for mineralization kinetics with the variables of substrate concentration and population density. Appl Environ Microbiol 47:1299–1306

Simpson DR (2008) Biofilm processes in biologically active carbon water purification. Water Res 42(13):2839–2848

Sims JL, Sims RC, Matthews JE (1989) Bioremediation of contaminated surface soils. R.S. Kerr Environmental Research Laboratory, U.S. Environmental Protection Agency, Ada, UK

Smith LH, McCarty PL (1997) Laboratory evaluation of a twostage treatment system for TCE cometabolism by a methaneoxidizing mixed culture. Biotechnol Bioeng 55:650–659

Strigula N, Detteb H, Melasc VB (2009) A practical guide for optimal designs of experiments in the Monod model. Environ Model Softw 24(9):1019–1026

Surmacz-Gorska J, Gernaey K, Demuynck C, Vanrollehem P, Verstraete W (1996) Nitrification monitoring in activated sludge by oxygen uptake rate (OUR) measurements. Water Res 30:1228–1236

Tanyola A, Tuncel SA (1993) Effectiveness factor for spherically growing mixed culture in substrate inhibition media. Enzyme Microb Technol 15:144–149

Tebes-Stevens CL, Valocchi AJ (2000) Calculation of reaction parameter sensitivity coefficients in multicomponent subsurface transport models. Adv Water Resour 23(6):591–611

Tomson AFB, Jackson KJ (2000) Reactive transport in heterogeneous systems: an overview. In: Lichtner P et al (eds) Reactive transport in porous media, vol 36. Mineralogical Society of America, Washington, DC, pp 269–310

Vainshtein M, Kuschk P, Mattusch J, Vatsourina A, Wiessner A (2003) Model experiments on the microbial removal of chromium from contaminated groundwater. Water Res 37(6):1401–1405

Vavilin VA, Lokshina LY (1996) Modeling of volatile fatty acids degradation kinetics and evaluation of microorganism activity. Bioresour Technol 57:69–80

Vesper SJ, Murdoch LC, Hayes S, Davis-Hooverb WJ (1994) Solid oxygen source for bioremediation in subsurface soils. J Hazard Mater 36:265–274

Wang Y, Shen H (1997) Modeling Cr(VI) reduction by pure bacterial cultures. Water Resour Res 31(4):727–732

Watson JE, Gardner WR (1986) A mechanistic model of bacterial colony growth response to substrate supply. A paper presented at the Chapman conference on microbial processes in the transport, fate, and in situ treatment of subsurface contaminants, Snowbird, UT

Weaver JW, Charbeneau RJ (2000) A screening approach to simulation of aquifer contamination by fuel hydrocarbons (BTEX and MTBE). National Exposure Research Laboratory, United States Environmental Protection Agency, Athens, Georgia, pp 1–47

Woodward D (1996) Potential for contamination of the Liwa aquifer by disposal of Brine in the Bu Hassa and Asab Fields, Abu Dhabi

Yamamoto K, Kato J, Yano T, Ohtake H (1993) Kinetics and modeling of hexavalent chromium reduction in Enterobacter cloacae. Biotechnol Bioeng 41(1):129

Yoshida H, Yamamoto K, Yogo S, Murakami Y (2006) An analogue of matrix diffusion enhanced by biogenic redox reaction in fractured sedimentary rock. J Geochem Explor 90(1–2):134–142

Yu J, Molstad L, Frostegård Å, Aagaard P, Breedveld GD, Bakken LR (2007) Kinetics of microbial growth and degradation of organic substrates in subsoil as affected by an inhibitor, benzotriazole: model based analyses of experimental results. Soil Biol Biochem 39(7):1597–1608
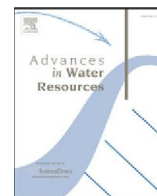
Stochastic evaluation of subsurface contaminant discharges under physical, chemical, and biological heterogeneities

M. Mohamed [a,b,*], K. Hatfield [c], A. Hassan [b], H. Klammler [c,d]

[a] Civil and Environmental Engineering Department, United Arab Emirates University, P.O. Box 17555, Alain, United Arab Emirates
[b] Irrigation and Hydraulics Department, Faculty of Engineering, Cairo University, P.O. Box 12211, Giza 12613, Egypt
[c] Civil and Coastal Engineering Department, University of Florida, P.O. Box 116580, Gainesville, FL 32611, USA
[d] Department of Environmental Science and Sustainable Development, Federal University of Bahia, Barreiras, Bahia, Brazil

ARTICLE INFO

ABSTRACT

A finite element 2D Monte Carlo approach is used to evaluate the sensitivity of groundwater contaminant discharges to a Damkohler number ω and spatial variability in aquifer hydraulic conductivity, initial microbial biomass concentrations, and electron acceptor/donor concentrations. Bioattenuation is most sensitive to spatial variations in incipient biomass and critical electron donors/acceptors for $\omega \gtrsim 1$ (i.e., when pore-water residence times are high compared to the time needed for microbial growth or contaminant attenuation). Under these conditions, critical reaction processes can become substrate-limited at multiple locations throughout the aquifer; which in turn increases expected contaminant discharges and their uncertainties at monitored transects. For $\omega \lesssim 0.2$, contaminant discharge is not sensitive to incipient biomass variations. Physical heterogeneities expedite plume arrival and delay departure at transects and in turn attenuate peak discharges but do not affect cumulative contaminant discharges. Physical heterogeneities do, however, induce transect mass discharge variances that are bimodal functions of time; the first peak beings consistently higher. A simple stream tube model is invoked to explain the occurrence of peaks in contaminant discharge variance.

© 2010 Elsevier Ltd. All rights reserved.

1. Introduction

Estimation of subsurface contaminant mass discharge (i.e., contaminant mass per unit time) at specified control planes (CPs) is an effective approach of defining groundwater source terms and boundary conditions; assessing natural attenuation viability; designing time-effective enhanced remediation systems; and evaluating source zone remediation success [1–4]. Traditional estimations of contaminant mass discharges using collected groundwater samples are inaccurate because they ignore spatial variations in both concentrations and groundwater flows [5]. Direct measurements of groundwater and contaminant discharges, which accounts for spatial variations of contaminant concentrations and discharges, are possible through the deployment of Passive Flux Meters (PFM) [1,6–9]; and improved analyses of the Integral Pumping Test (IPT) approach [10–15]. As a partial consequence of improved flux monitoring, several investigators have used or proposed to use measured reductions in contaminant discharge as an indicator of contaminant source mass depletion [1,16–28].

Various types of heterogeneities have been reported to affect contaminant fate and transport, and therefore discharge in the subsurface including physical, chemical, and biological heterogeneities [e.g. 29–37]. The relationship between source mass and CP discharge is a function of these heterogeneities and the correlation between them [1,16,19,22,23]. Physical aquifer heterogeneity, represented by spatial variability in hydraulic conductivity, has been studied extensively to characterize field-scale dispersion [e.g. 29–34]. A typical manifestation of this heterogeneity is the apparent presence of anisotropy at the aquifer scale, despite point scale observations of isotropic hydraulic conductivities [30,38]. Another intensively investigated manifestation of physical heterogeneity is macro-dispersion [33,34,39–42]. Chemical heterogeneity in the subsurface is represented as spatial variability in abiotic contaminant reaction parameters including abiotic degradation rates; sorption coefficients and redox conditions and spatial variability in electron donor/acceptor concentrations that are critical for biotic reactions [35–37,43–47]. Chemical heterogeneity in the aquifer matrix has been recognized at laboratory scale [48–52], and at field scale [44,53]. Finally, biological heterogeneity is manifested as spatial variability in microbial species, biomass, and microbial activity. Several stochastic modeling techniques have been used to examine organic subsurface biodegradation at the field scale [54,55]. Monte Carlo simulations were used to study the effects of spatially distributed rates of biodegradation and hydraulic

* Corresponding author. Civil and Environmental Engineering Department, United Arab Emirates University, P.O. Box 17555, Alain, United Arab Emirates. Tel.: +971 3 7133509.
  E-mail address: m.mohamed@uaeu.ac.ae (M. Mohamed).

conductivity on plume-scale rates of biodegradation [56–58]. They were also used for assessing the effects of waste sites on groundwater quality [59–62].

Accounting for spatial variability is particularly essential for accurate estimation of subsurface contaminant mass discharges and thus successful remedial design [15]. The effect of spatially variable hydraulic conductivity on the variances of both the contaminant concentrations and discharges has been studied analytically for solutes undergoing first-order sorption kinetics under pulse or continuous injections of concentrations from source zones [63–65]. However, the effect of biological variability, correlation between spatial hydraulic conductivity and biological variability, and electron donor/acceptor availability on contaminant mass discharges has not been examined to the best of the authors' knowledge. Zones with high contaminant discharge may have different microbial activity than low-discharge zones, which would impact plume remedial design that is based on enhancement of biological processes [1].

The objective of this paper is to examine the sensitivity of microbial mediated contaminant mass discharges to physical, chemical, and biological heterogeneities in a 2-dimensional aquifer. Monte Carlo simulations are used to simulate contaminant plumes in a two-dimensional aquifer, and at two sections transverse to the mean groundwater flow direction, and generate temporal distributions of the mean subsurface contaminant discharge and variance. One can legitimately argue than two-dimensional simulations are poor approximations to natural three-dimensional systems. However, two-dimensional models are of value when studying problems at the regional scale [7]. The regional scale is defined for aquifers whose planar dimension is much larger than the aquifer thickness. In this case formation properties are averaged over depth and are regarded as functions of the horizontal dimension only [66]. Steady, uniform, and two-dimensional flow prevails at the natural gradient tracer experiment in the sand aquifer that was carried out at the Borden site [67–69]. Freyberg [69] found that the motion of the plume and its center of mass is essentially horizontal. Barry et al. [70] also found the assumption of two-dimensional flow to yield good results. In the other commonly cited natural tracer test, performed at the Cape Cod site, LeBlanc et al. [71] found that the plume centroid moved vertically downward for a small distance which enabled Deng et al. [72] to reproduce the field spatial moments using a two-dimensional stochastic model. Chaudhuri and Sekhar [61] performed 1D Monte Carlo Simulations (MCS) to evaluate a perturbation technique. Then, they used this technique on 3D simulations. They concluded that 100 realizations were not enough to obtain good MCS results in 3D simulations. This is an added difficulty of simulating 3D with MCS. The induced variations in plume discharge are the result of spatial heterogeneities in aquifer hydraulic conductivity, microbial biomass concentrations, and electron donor/acceptor concentrations. Microbial growth is simulated using modified Monod kinetics [73] under conditions where microbial growth will be substrate-limited depending on the local concentrations of contaminant and an auxiliary electron acceptor/donor.

2. Governing equations

One of the challenges in modeling biotransformation is obtaining reliable conceptual description. Molz et al. [74], separated biodegradation models into three distinct conceptual approaches. In the first approach, it is assumed that solid particles are uniformly covered by a thin biofilm [57,75–85]. Consumption of contaminants occurs in this biofilm in the presence of electron acceptors and nutrients. This approach will be employed in this paper. In the second approach, bacteria are assumed to grow, in small discrete colonies (or 'micro-colonies') attached to a particle surface, as the result of substrate and electron acceptor utilization [86,87]. Both biofilm and micro-colony approaches employ one of the following three reaction kinetics: first-

order decay, instantaneous reaction kinetics, and multi-term Monod (or Michaelis–Menten) expressions. The third approach has been adopted by many researchers [88–93]. In this approach, partitioning between free flowing and adsorbed microorganisms is assumed [89,90] but their distribution and interaction play no role in depicting the growth dynamics [94].

For a heterogeneous porous medium, the time-dependent reaction–advection–dispersion equation of a contaminant (and/or electron donor/acceptor) (i) whose spatial concentration distribution is denoted by $C_i(x, t)$ is given by:

$$R_i \frac{\partial C_i}{\partial t} = \frac{\partial}{\partial x}\left(D \frac{\partial C_i}{\partial x}\right) - V \frac{\partial C_i}{\partial x} + Q_i^{\text{bio}} \tag{1}$$

where the local pore-water velocity vector is V [L T^{-1}]; D [L^2 T^{-1}] is the tensor of the hydrodynamic dispersion coefficient, and R is the retardation factor [dimensionless]. For multi-solute transport (electron acceptors/donors, and/or nutrients), these equations are coupled through contaminant source/sink terms Q as follows:

$$Q_i^{\text{bio}} = \frac{-M \mu}{Y_i \theta} \tag{2}$$

where M is the microbial biomass concentration [M L^{-3}], θ is the aquifer porosity [dimensionless], Y_i are the yield coefficients [dimensionless] representing the mass of bacterial species produced per unit mass of electron donor/acceptor. Modified Monod kinetics [73] is used to describe specific growth rate of the microbial species utilizing electron donor and electron acceptor:

$$\mu = \mu_{\max} \prod \left(\frac{C_i}{K_{C_i} + C_i} \right) \tag{3}$$

where $\mu_{\max}$ is the maximum specific growth rate for the microbial species [T^{-1}], K_{C_i} is the half saturation coefficient for the electron donor/acceptor [M L^{-3}]. Assuming B as the first-order microbial decay rate, the microbial mass balance equation can be written as follows [95,96]:

$$\frac{dM}{dt} = M(\mu - B). \tag{4}$$

3. Methodology and problem description

Monte Carlo (MC) simulations are used in this study to investigate spatial–temporal variations in subsurface microbial mediated contaminant discharge affected by a Damkohler number ω and physical, chemical, and biologically heterogeneities in a 2-D aquifer. Physical heterogeneity is represented as spatial variations in hydraulic conductivity. Biological heterogeneity is manifested as spatial variations in initial and transient distributions of microbial biomass, and finally chemical heterogeneity is represented as spatial variations in the concentration of a requisite electron donor/acceptor. Monte Carlo simulations provide predictions for ensemble mean discharges at transects as well as the uncertainty in these predictions represented as discharge variances. Comparisons between Monte Carlo simulations and corresponding homogeneous scenarios of assumed uniform physical, chemical, and biological properties is used to elucidate the effects of physical, chemical, and biological heterogeneities and their possible correlation on contaminant mass discharges. Quantifying the uncertainty of the prediction has been recognized as crucial information for remediation design and risk assessment studies [97,98].

The methodology used here is as follows: (1) a random field generator (RFG) [99,100] is used to create multiple realizations of spatially varying fields of aquifer hydraulic conductivity and initial concentrations of a requisite electron donor/acceptor and biomass assuming a known spatial correlation structure of second-order stationarity. The method used in this RFG is based on Fast Fourier Transform (FFT) and is chosen in this study because of its computational efficiency. The basic concept of this method is to generate a set of uniformly distributed random numbers by using a random number generator. By taking the FFT of these numbers, the resulting spectrum will have a uniform density of unity. By multiplying the transformed numbers by the square root of the spectral density function of the conductivity field (the Fourier transform of ln K covariance), the resulting numbers will have the same spectrum as that of the hydraulic conductivity field. Finally taking the inverse FFT of those numbers gives a set of numbers in real space having the same correlation structure as that of the conductivity field; (2) the groundwater flow is established for all conductivity realizations under the specified boundary conditions (Fig. 1); (3) the finite element model METABIOTRANS [57,101,102] is used to solve the coupled transport equations and microbial growth equation (Eqs. (1)–(4)); (4) contaminant discharges at sections 1 and 2 (Fig. 1) are obtained from each realization; and finally (5) the ensemble mean discharge and discharge variance are calculated for all realizations.

The hydraulic conductivity, initial concentrations for the requisite electron donor/acceptor, and biomass are assumed to have a log-normal distribution with an exponential covariance structure ($\mathrm{Cov}(r) = \sigma^2 e^{-r/\lambda}$) in which σ^2 is the process variance, r is the spatial lag, and λ is the correlation length which is proportional to the distance over which hydraulic conductivity (K), the requisite initial electron donor/acceptor (A) concentration, or initial biomass (M) concentration are spatially correlated. The value of λ is kept as 1.0 m for all simulations. Depending on the simulation, it is assumed that Log K and Log A variances are both 1.0, Log M variance is 1.0 or 3.0, and the arithmetic mean for M equals 1% of C_o (initial concentration). The element size in the finite element mesh is a constant 0.2λ. Longitudinal and transverse dispersivities are assumed to be 0.1λ and 0.05λ, respectively. Summary of all input parameters used in this paper is presented in Table 1.

The log-normal distribution with exponential covariance structure is a common assumption in stochastic groundwater studies. In the same way as the Central Limit Theorem dictates that the sums of a large number of independent variables approaches a normal distribution it dictates (after exponentiation) that the product of a large number of independent (non-negative) variables approaches a log-normal distribution. This is known to be true even if partial correlation between variables is present; however, in this case convergence to (log-) normality is slowed down [106]. As illustrated by the governing equations, the processes studied here are purely multiplicative and limited to non-negative variables. Regarding the

Table 1
Summary of input parameters.

Problem domain	$36\lambda \times 18\lambda$
Element size in X-direction ($\Delta x/\lambda$)	0.2
Element size in Y-direction ($\Delta y/\lambda$)	0.2
Dispersivity in X-direction (α_x/λ)	0.1
Dispersivity in Y-direction (α_y/λ)	0.05
Porosity (n)	0.3
Retardation factor (R)	1.0
Half saturation coefficient for ED (K_s/C_o)	0.4 [103,104]
Half saturation coefficient for EA (K_a/C_o)	0.4 [103,104]
B/μ_{max}	0.1 [104,105]
Size of the contamination initial source	$4\lambda \times 2\lambda$

state of a variable as the outcome of a large number of such multiplicative but not necessarily uncorrelated processes (e.g., along a stream line in space or at a location over time) lends support to the assumption of log-normality for the respective variables. Moreover, we hypothesize that deviations from the log-normal distribution (e.g., towards other non-negative distributions such as gamma, chi-squared, etc.) may have some quantitative but no significant qualitative impact on simulation results and conclusions as long as mean and variance remain unaffected.

In the case of the spatial covariance model chosen, we argue that deviations from the exponential model (e.g., towards other stationary models such as spherical, Gaussian, etc.) do not have a significant impact on results as long as the correlation length remains unaffected and the spatial scale of the study (i.e., transect size over which local fluxes are added up to determine discharges) exceeds the correlation length by some factor. Under these conditions it is assured that some "average" level of correlation between different locations within the model domain is maintained, which determines the overall behavior of the (spatially-averaged or integrated) outcome. From this we hypothesize that results presented retain approximate quantitative and general qualitative validity for the set of fundamental parameters mean, variance and correlation length and independent of particular distributional or spatial covariance properties. This is consistent with the level of information that may typically be expected in field situations (limited data may not even allow for making strong inferences about distributions or spatial correlation structures).

Field measurements revealed that the spatially varying hydraulic conductivity could be described by a log-normal distribution. Furthermore, conductivity values were found to be spatially correlated with a correlation structure that varies from site to site. The exponential, Gaussian, hole-type, and fractal covariance structures are among the commonly used covariances. Examples of studies that employed the exponential model include Mohamed et al. [57] and Hassan et al. [92,93]. The latter is assumed to also apply to biomass and electron donors in the present work due to their correlation with
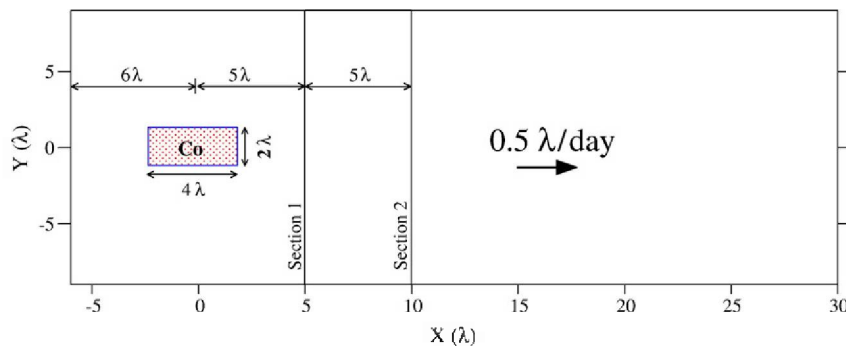

Fig. 1. Problem layout.

conductivity. For the case of no correlation we maintain the exponential variogram for better comparison.

Five different scenarios are used to study plume contaminant discharges under various conditions of spatial heterogeneity (Table 2). The first scenario includes three homogeneous simulations from which reference conditions are defined. The computational time of any of these deterministic simulations was 20.5 min on a 2 GHz machine. The next two scenarios examine separate influences of physical heterogeneity (hydraulic conductivity variations) and biological heterogeneity (spatial variations in initial microbial biomass concentrations). The fourth scenario focuses on the composite influence of correlated physical and microbial heterogeneities. In the final scenario, chemical heterogeneity is examined through a single MC simulation conducted with uncorrelated spatial variations in initial electron donor/acceptor concentrations, and spatially correlated variations in hydraulic conductivity and microbial biomass. Simulations include sensitivity studies on the assumed dimensionless microbial effective growth rate ($\omega = \lambda \mu_{max}/V$), and the assumed the initial biomass concentration variance. ω is equivalent to a Damkohler number [107,108], and it expresses the ratio of pore fluid hydraulic residence time to the time required for microbial growth and contaminant attenuation. Thus, $\omega \leq 1$ suggests contaminant attenuation may be sensitive to local variations in groundwater velocity. This sensitivity may arises because the characteristic maximum specific growth rate for the microbial population is sufficiently low, or groundwater velocities are sufficiently high that the time require for attenuation and microbial growth is significantly greater than the average groundwater hydraulic residence time. For a given μ_{max}, as the groundwater velocity decreases the hydraulic residence time increases; thus, ω increases indicating there is sufficient pore-water residence time to support microbial growth and contaminant attenuation. Based on available literature values for μ_{max}, the parameter ω can range from 0.001 to 64 [57].

In the three homogeneous simulations (1–3 from Table 2) ω varied from 0 to 1. Simulations results serve as references in subsequent comparisons with MC simulations. Background biomass concentrations in the first three simulations were equated to 1% of the initial contaminant concentrations (Co), which is within the range of 0.5–10% assumed in previous studies [e.g. 40,52,54]. To ensure meaningful comparisons between the homogenous simulations and those involving biological heterogeneities, this value of background biomass

Table 2
Summary of simulation parameters.

Scenario	Simulation	Number of realizations	Random variable	ω	Variance of K, M, and A
1	1	Homogenous	–	0	–
	2	Homogenous	–	0.2	–
	3	Homogenous	–	1.0	–
2	4	500	K	0	1.0
	5	500	K	0.2	1.0
	6	500	K	1.0	1.0
3	7	250	M	0.2	1.0
	8	250	M	1.0	1.0
	9	250	M	1.0	3.0
4	10	500	K and M (uncorrelated)	0.2	1.0 and 1.0
	11	500	K and M (negative correlation)	0.2	1.0 and 1.0
	12	500	K and M (uncorrelated)	1.0	1.0 and 1.0
	13	500	K and M (negative correlation)	1.0	1.0 and 1.0
	14	500	K and M (positive correlation)	1.0	1.0 and 1.0
	15	500	K and M (positive correlation)	1.0	1.0 and 3.0
5	16	500	K and M (negative correlation) and uncorrelated to A	1.0	1.0 and 1.0 and 1.0

concentration is used to represent the mean biomass concentration in the Monte Carlo simulations presented in scenarios 2, 4, and 5. For the same reason and to ensure meaningful comparisons between the homogenous simulations and those involving physical heterogeneities, the geometric mean of the log-normal K equals the uniform hydraulic conductivity field in the simulations presented in scenarios 3–5. In addition, the same hydraulic gradient is used in all simulations to achieve the same integrated groundwater discharge at any transect in the flow domain (i.e. the same spatially-averaged specific discharge over any arbitrary transect draw perpendicular to the predominant flow direction).

Results of all simulations are shown as dimensionless graphs expressed in terms of the normalized time ($\tau = tV/\lambda$) and normalized ensemble mean contaminant mass discharge (ND $= Q/Q_{max}$); where Q is the actual mass discharge [M T^{-1}] and Q_{max} is the maximum mass discharge representing mass recharge when dispersion and biodegradation are ignored. The maximum mass discharge (Q_{max}) is equivalent to ($VM_r/4\lambda$); where M_r is the total initially released mass of the contaminant [M]. Discharges are evaluated at two sections located at distances 5λ and 10λ, respectively, downstream from the center of the initial contaminant release as presented in Fig. 1.

4. Numerical simulations and discussion

4.1. Physical heterogeneity

The effects of physical heterogeneity on plume contaminant discharge are examined through three MC simulations (4–6, Table 2). In all three, 500 realizations of the hydraulic conductivity field of unit log-variance are used to generate 500 heterogeneous velocity fields, which are then used in the transport model. Biodegradation is not simulated in 4 ($\omega = 0$); whereas in MC simulations 5 and 6, biological activity is simulated using values of ω comparable to homogeneous simulations 2 and 3 (i.e. 0.2 and 1.0), respectively (Table 2).

Physical heterogeneity increases dispersion in both longitudinal and transverse directions, which explains the early increase and the delayed decrease in ensemble mean contaminant discharges at each transect and in turn the attenuated peak discharges compared to homogeneous simulations (see Fig. 2a). Theses peaks occur at approximately the time when the centroid of the ensemble contaminant plume traverses the transect plane. However, this is not the case with mass discharge variance (DV). At any given transect, the DV produces two peaks over time corresponding to two periods of high uncertainty in mass discharge (Fig. 2b). The first peak is observed to be associated with the arrival of the leading edge of the ensemble plume (i.e., when the steepest increase in ND occurs), while the second occurs as the plume's trailing edge traverses the transect plane (i.e., when the steepest decrease in ND occurs).

A simple stream tube model with longitudinal and transverse dispersion between stream tubes can be invoked to explain the two peaks is discharge variance. First, it is assumed n [dimensionless] stream tubes of equal water flux crossing a control section and each stream tube either makes a contribution to mass discharge or not. At short times all contaminated stream tubes may be assumed to convey a mass flux q_{max} corresponding to some maximum (saturated) contaminant concentration. Next, it is assumed that the probability that a stream tube is contaminated is p [dimensionless] and to be clean $1 - p$. The resulting distribution is known as Bernoulli distribution, which, after summation over n stream tubes, becomes a Binomial distribution of mean npq_{max} and variance $np(1-p)q_{max}^2$. By equating ND $= npq_{max}$ (expected mass discharge) Fig. 2a indicates that p rises from zero to some maximum value $p_{max} \lesssim 1$ and decreases towards zero afterwards. This reflects the effect of longitudinal dispersion and the lower probability of encountering contaminated stream tubes before and after the plume core. By further equating
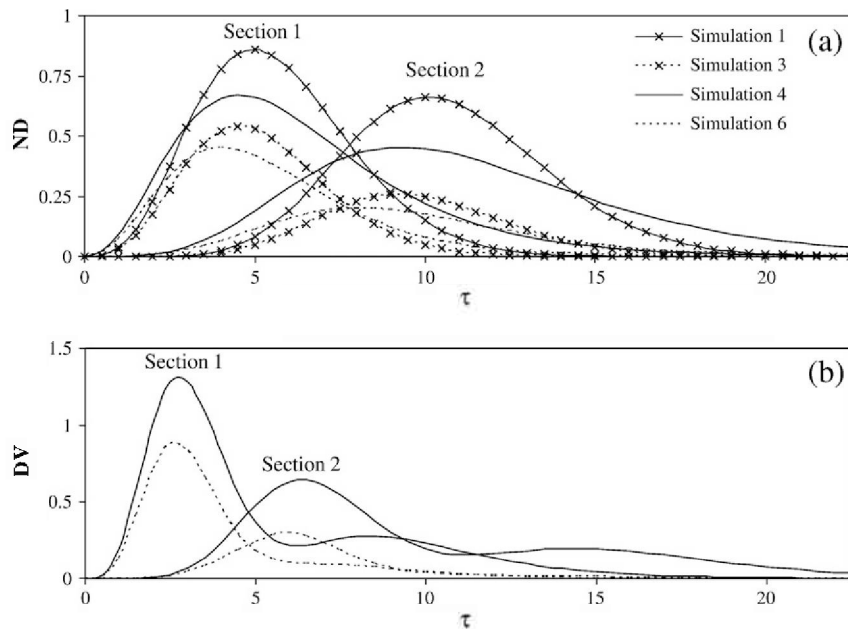
Fig. 2. Comparison between homogenous simulations [1($\omega = 0.0$) and 2($\omega = 0.2$)] and physical heterogeneity simulations [4 ($\omega = 0.0$) and 5 ($\omega = 0.2$)] (a) normalized mean discharge, and (b) discharge variance.

$DV = np(1-p)q_{max}^2$ and noting that $p(1-p)$ is a concave function equal to zero for $p = 0$ and 1 while reaching a maximum at $p = 0.5$, it is shown that DV possesses two maxima corresponding to p reaching 0.5 at the leading and trailing edges of the plume. From a different perspective these peaks can be related to the uncertainty in plume arrival/departure times and the magnitudes of the arriving and departing discharge gradients in flow direction. At very short and very large times p and, hence, DV are zero, while in between peaks $0.5 < p \leq p_{max}$ and DV reaches a local minimum. Now considering also transverse dispersion between stream tubes, which grows with the length of the flow path and time, stream tubes can convey arbitrary discharges q between zero and q_{max}. This does not directly affect ND, since transverse dispersion does not discriminate between faster and slower stream tubes (i.e., its effects on ND cancel out on average), but it does decrease DV, since individual stream tube discharges are moved closer to the mean value. This may explain the smaller amplitude of the second peak (trailing plume "fingers" are fuzzier than leading plume fingers) as well as of the peaks at the down-gradient section 2. Cases may exist where this effect (possibly in combination with degradation) is strong enough to eliminate a second peak or where $p_{max} \leq 0.5$.

In the absence of biodegradation, time-integrated contaminant discharges must equate to the initial source mass. Results shown in Table 3 for simulations 1 and 4 verify this claim, and they also validate the numerical scheme used to integrate discharges at each section. Biodegradation decreases the time-integrated discharge between sequential transect planes; the magnitude of decrease is sensitive to ω but insensitive to spatial variations in hydraulic conductivity. For example, from a comparison of simulations 2 and 3 with 5 and 6 (see Table 3), essentially the same contaminant mass is observed to traverse respective transects at the levels of physically heterogeneity simulated in this study. It is important to keep in mind for these simulations; Monod parameters (Table 1) are spatially uniform. However, if these conditions were otherwise, biodegradation rates would vary spatially in accordance with spatial variation in Monod parameters.

Contaminant concentration reductions due to biodegradation decrease DV as a plume migrates through a transverse section. A closer look at the differences between simulations 4 and 5 in Fig. 2b suggests a greater relative decrease in DV occurs at the trailing edge of a simulated

plume (second peak) than at the leading edge (first peak). This occurs most likely because the trailing edge encounter a higher density of active biomass produced as microbial growth increased to consume the leading edge of the plume, and also because the travel time and in turn the exposure to active microbial colonies is longer for contaminants in the trailing edge of plume. Increasing ω in simulation 6 increases significantly the contaminant mass degraded; however, it does not affect the arrival time of the leading edge of plumes in either homogenous or physically heterogeneous cases (compare Figs. 2a and 3a). Thus, q_{max} and contaminant DV decrease at both sections in simulation 6 (Fig. 3b), so much so that the second variance peak is almost negligible.

4.2. Biological heterogeneity

In this third scenario, variability in initial biomass concentrations is considered. Biological heterogeneity is represented in this paper by a spatial variability in the distribution of microbial species, biomass, and microbial activity. Though this is the least understood of the other factors of heterogeneity, spatial variations in biological processes are believed to have a significant effect on contaminant transport in the

Table 3
Ratios of cumulative contaminant mass discharges and total contaminant source mass for sections 1 and 2 at end of simulations ($\tau = 35$).

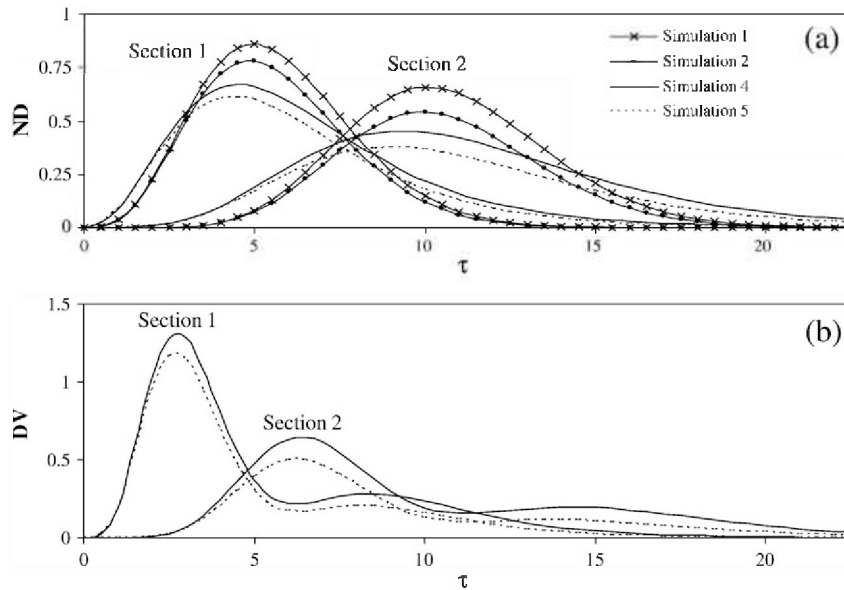| Simulation	Section 1	Section 2
1	1.00	1.00
2	0.90	0.81
3	0.63	0.39
4	1.00	1.00
5	0.88	0.81
6	0.62	0.40
7	0.90	0.82
8	0.66	0.42
9	0.70	0.46
10	0.88	0.81
11	0.89	0.81
12	0.65	0.44
13	0.65	0.44
14	0.65	0.43
15	0.71	0.51
16	0.87	0.77

Fig. 3. Comparison between homogenous simulations [1($\omega=0.0$) and 3($\omega=1.0$)] and physical heterogeneity simulations [4($\omega=0.0$) and 6($\omega=1.0$)] (a) normalized mean discharge, and (b) discharge variance.

subsurface. Both Miralles-Wilhelm et al. [54,55] and Scholl [56] have used stochastic modeling techniques to examine organic subsurface biodegradation at the field scale. Miralles-Wilhelm et al. [54] presents an analytical model to quantify subsurface oxygen-limiting biodegradation at the field scale. Their model incorporates effects of chemical and microbiological heterogeneities. The purpose of the modeling exercise was to investigate field-scale effective coefficients of retardation, dispersion, and decay of a soluble contaminant undergoing advection, sorption, and biodegradation in the subsurface. To simplify the analytical model, they assumed a steady-state microbial population; ignoring, thereby, the transient affects of microbial growth and perhaps more importantly the transient evolution of a contaminant plume that is in reality inextricably coupled to a dynamic microbial biomass plume. Miralles-Wilhelm et al. [54] concluded that the effective contaminant decay rate was less than the spatial mean.

Scholl [56] performed Monte Carlo simulations using the USGS model (BIOMOC) to study the effects of spatially distributed rates of biodegradation and hydraulic conductivity on plume-scale rates of biodegradation derived from field data. Three sets of simulations were performed, each involving 10 realizations, with different degrees of physical aquifer heterogeneity. Others used Monte Carlo analysis and Bayesian decision theory for assessing the effects of waste sites on groundwater quality [e.g. 20,41,42]. James and Freeze [62] developed a Bayesian decision framework for addressing questions of hydrogeological data worth associated with engineering design at sites in heterogeneous geological environments. They studied the specific case when one of remedial contaminant containment in an aquifer underlain by an aquitard of uncertain continuity. The framework is used to evaluate the worth of hard and soft data in investigating the aquitard's continuity. Similar to Miralles-Wilhelm et al. [54] study, Scholl [56] ignored biomass growth, death, and growth inhibition. Scholl calculated biodegradation rates from steady-state contaminant plumes using decrease in concentration down-gradient and a single flow velocity estimate; hence, the simulations performed did not reflect Monod kinetics or the transient changes of a contaminant plume that is coupled to a dynamic microbial biomass plume. Scholl [56] concluded for a steady-state contaminant plume that using an effective hydraulic conductivity/flow velocity and biomass distribution underestimates the time required to remediate a contaminated aquifer. Scholl did not investigate the affects of biological heterogeneity nor its correlations with spatial variations in aquifer permeability.

Three simulations (7–9) are performed; in which 250 different realizations of initial biomass concentration were enough to achieve stable mean discharges. For rational comparisons, the same initial total volumetric biomass is maintained in all simulations. In simulation 7, an ω of 0.2 is used to represent microbial characteristics or hydraulic conditions that limit microbial growth, while a higher value of 1.0 is used in simulations 8 and 9. The spatial log-variance (σ^2) of the initial biomass distribution is 1.0 in simulations 7 and 8 and 3 in simulation 9. For this reason, the biomass distribution in simulation 9 reflects the greatest range in bacterial concentrations (as depicted in Fig. 4 in [57]).

By comparing contaminant discharge curves for simulations 2 and 7 in Fig. 4 and or the time-integrated discharges in Table 2, it is evident that for low effective growth rates ($\omega \leq 0.2$), incipient biological heterogeneity does not significantly alter mass discharges at sections 1
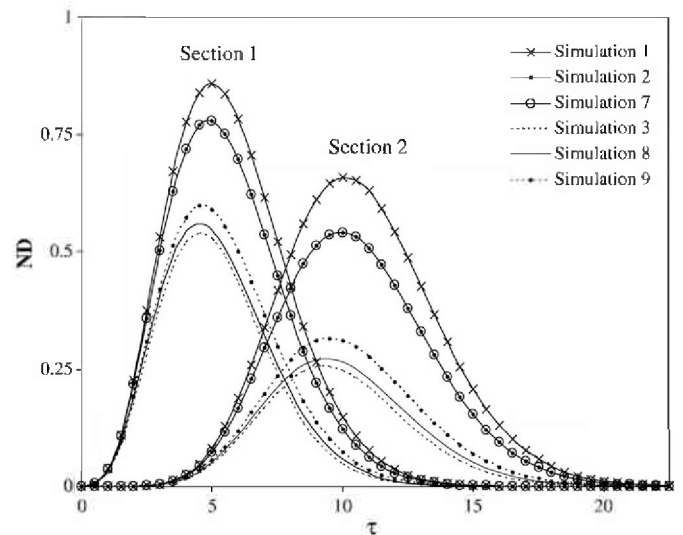

Fig. 4. Comparison between normalized mass discharge of homogenous simulations [1($\omega=0.0$), 2($\omega=0.2$) and 3($\omega=1.0$)] and biological heterogeneity simulations [7($\omega=0.2$, $\sigma_M^2=1.0$), 8($\omega=1.0$, $\sigma_M^2=1.0$) and 9($\omega=1.0$, $\sigma_M^2=3.0$)].

and 2 relative to the homogenous case. This suggests that a homogeneous aquifer assumption may in fact be sufficiently accurate for small ω values. In other words, for high flow velocities or low microbial activities, aquifers may be simulated as biologically homogeneous systems for the purpose of determining the contaminant mass discharge if critical electron donor/acceptors are not limiting. However, the uncertainty in the discharge prediction is not given from a deterministic homogeneous simulation. Fig. 4 also shows that when ω is increased to 1, as in simulation 8, contaminant attenuation is less efficient when the initial biomass distribution is non-uniform as oppose to being homogenous (simulation 3); which is consistent with finding of others [e.g. 55–57]. This means that the expected total mass passing sections 1 and 2 is higher in the heterogeneous case as shown in Table 3. Furthermore, attenuation decreases even more when the variance of the initial biomass distribution (σ^2) is increased as in simulation 9 (Fig. 4, Table 3). This is an outcome of the fact that increasing the incipient biomass distribution variance produces large regions where the initial biomass concentration is low and only small "islands" of large biomass concentrations. As a result, the contaminant plume escapes attenuation in large regions of low biomass, and because contaminant degradation and microbial growth are coupled, the absence of attenuation in these regions is not compensated by higher attenuation in other regions of greater biomass. For the highest value of ω considered in this work, simple calculations based on simulation output can show that maximum volume changes in biomass are several orders of magnitude smaller than initial pore space. As a consequence, effect of biomass clogging on porosity (and conductivity according to a model by Thullner et al. [109]) is found to be negligible. By comparing simulations 8 and 9 in Fig. 4 and Table 3 to the homogenous simulation 3, it is obvious that for high ω values, the assumption of a homogenous biomass distribution underestimates contaminant mass discharge. Because changes in mass discharges between the homogenous and biological heterogeneous systems are more apparent as the microbial effective growth rate (ω) increases, the estimation of ω is critical for predicting natural or induced bioattenuation.

4.3. Physical and biological heterogeneities

In this fourth scenario, correlated and uncorrelated biological and physical variability are considered. Brockman et al. [110] reported that it was indicated by different researchers that subsurface microbiological properties have similar spatial correlation length scales to those well established for subsurface physical and chemical parameters, and the microbiological properties appear to be spatially correlated to geologic, hydrologic and/or geochemical properties. This

indicates that the possibility exists that the biological parameters (biomass distribution and electron done/acceptor) can have a spatial distribution and correlation structure similar to that of the hydraulic conductivity, K. It was also shown [111,112] that denitrification is highly variable and exhibits a distribution that is typically positively skewed and approximates the log-normal distribution. Brockman et al. [110] also indicate that if geologic or other physical properties in the subsurface control nutrient availability, spatial correlations between subsurface environmental and microbiological properties might be expected. Such correlation means that it is possible that the subsurface biological properties have similar variability structure to that of hydraulic conductivity.

Scheibe et al. [113] demonstrated that the widely observed decrease of the apparent rate of bacterial attachment (particularly as parameterized by the collision efficiency in filtration-based models) with transport distance could be interpreted as a field-scale manifestation of local-scale correlation between hydraulic conductivity variability and attachment rate coefficient variability. Because collision efficiency depends on properties of microbial cell surfaces [113], such dependency and the correlation to K imply that the biomass distribution in a heterogeneous aquifer may be related to hydraulic conductivity. Therefore, the spatial correlation structure of the hydraulic conductivity may have an imprint on the spatial structure of the biomass variability.

The above discussion indicates the possibility that biomass concentration and electron donors/acceptors may have similar spatial variability structure to that of hydraulic conductivity. However, there is no conclusive evidence in the literature substantiated by field data at the scale of interest in our study (focusing on engineering bioremediation applications) that supports or precludes this possibility. Thus, it is worth to examine the effects of the possible case that the biological parameters have spatial variation structure similar to that of K.

Additional six simulations (10–15) of 500 realizations each are considered in this scenario. In simulations 10 and 12 the two heterogeneities are assumed uncorrelated; while in simulations 11 and 13 they are assumed negatively correlated (Table 2). Negative correlations have been justified by others assuming that the high pore-water velocities, present in zones of high hydraulic conductivity regions, tend to wash out attached bacteria or precluded bacterial adhesion [114]. A positive correlation, on the other hand, has been justified assuming zones of high hydraulic conductivity facilitate the transport of nutrients necessary for microbial growth. The effect of a positive correlation between biological and physical heterogeneities is studied through simulations 14 and 15 (Table 2).

For simulations 10 and 11, a low effective growth rate ($\omega = 0.2$) is used. Looking at time-integrated contaminant discharges alone
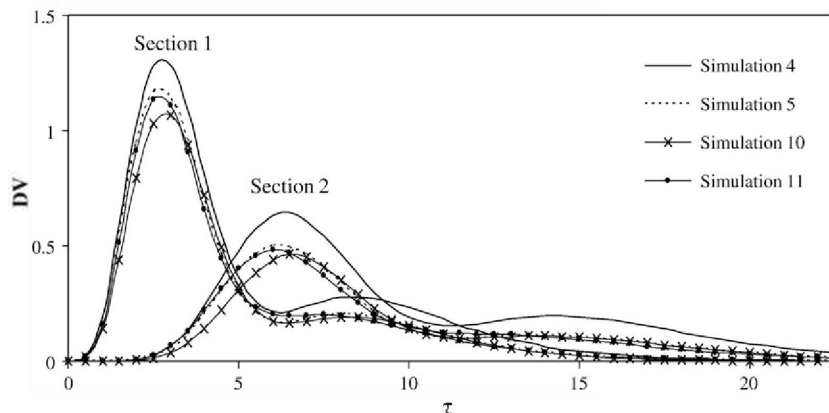

Fig. 5. Effect of −ve correlation between K and M for low ω (0.2) on discharge variance.

(Table 3), one surmises contaminant discharges are essentially the same as those generated under previous heterogeneous simulations 6 and 8 and homogeneous simulation 3. It appears again, low ω values determined by relatively high pore-water velocities or low maximum growth rates, define conditions for which non-uniform aquifer and biomass characteristics and their correlations can be effectively ignored if critical electron donors/acceptors are not limiting and the objective is to predict contaminant discharge but not its variance. With respect to discharge variance, a negative correlation between aquifer conducting and the incipient microbial biomass appears to increase discharge variance (or uncertainty) at the leading edge [see Fig. 5]. A negative correlation between K and microbial biomass produces flux variations at the leading edge that persist under low ω values. This occurs because initial microbial concentrations are lowest in the most permeable zones of the aquifer (which are also zones of high contaminant flux), and under low ω conditions, microbes are not growing fast enough to dampen spatial variations in contaminant flux.

In simulations 12, 13, and 14 ω is increased to 1. Results are comparable to those of heterogeneous simulations 6 and 8 and homogeneous simulation 3. In fact, results from Table 3 suggest contaminant discharge is insensitive to spatial correlations between aquifer conductivity and microbial biomass. The homogeneous simulation 3 over predicts attenuation by 10%; however, this error is well within the uncertainty of most contaminant transport models. Discharge variance appears to decrease at the first transect for MC simulation 13 where the correlation between aquifer conductivity and incipient microbial biomass concentrations is negative (see Fig. 6a). Conditions are more favorable for microbial growth/bioattenuation in this simulation than in 11, and in turn this growth has dampened spatial variations in contaminant flux. In fact, a closer examination of Fig. 6b suggests microbial growth may be obscuring much of the impact that initial biomass heterogeneities have on discharge variance; compare DV results of MC simulations 13 to 6 are almost identical at the first transect and in simulation 6 the initial biomass is spatially uniform. When the correlation is positive, higher concentrations of initial microbial biomass are located in higher contaminant flux zones and lower concentrations in lower flux zones. Discharge variances from positive and uncorrelated simulations 12 and 14 are almost indistinguishable which suggest DV is not dependent or less so

when the correlation is positive. In MC simulation 15, the incipient biomass concentration variance is increased to 3.0. A comparison of this simulation and that of 9 shows the same level of contaminant attenuation irrespective of spatial correlations between varying parameters. The apparent loss of attenuation efficiency is due the high variance in the incipient biomass. In general, results suggest it may be difficult at best to discern the presence of positive or negative correlations between aquifer conductivity and microbial biomass from contaminant discharge alone. However, others have shown the effects of such correlations can be seen in plume concentration distributions [57].

4.4. Physical, chemical and biological heterogeneity

Chemical heterogeneity is examined in this last scenario. Several researchers studied this type of heterogeneity [115–119]. Li et al. [115,116] simulated reactive transport processes at the pore scale, accounting for heterogeneities of both physical and mineral properties. Mass balance principles were then used to calculate reaction rates at the continuum scale. In this final scenario the availability of the electron donor (ED)/acceptor (EA) which is crucial for the biodegradation is assumed to vary spatially. This assumption, which is justified by several researchers [e.g. 120–123], places additional constraints on where and at what rate contaminant attenuation occurs. With 500 realizations, only one MC simulation (16) is performed in which physical and biological heterogeneities are also considered. Similar to simulation 13, physical and biological heterogeneities are assumed to be negatively correlated; however, both are independent of the initial concentration distribution for the electron donor/acceptor. Also assumed is a unit microbial effective maximum growth rate and unit variances in the logarithms of hydraulic conductivity, incipient biomass concentration and incipient electron donor/acceptor concentrations.

Fig. 7a shows higher contaminant discharges in simulation 16, than in simulation 13; indicating that increasing system heterogeneity with respect to ED/EA variability reduces the efficiency of subsurface bioattenuation. This is because critical reaction processes became substrate-limited at multiple locations throughout the aquifer (as depicted in Fig. 9c in [57]). Table 3 suggests that cumulative attenuation
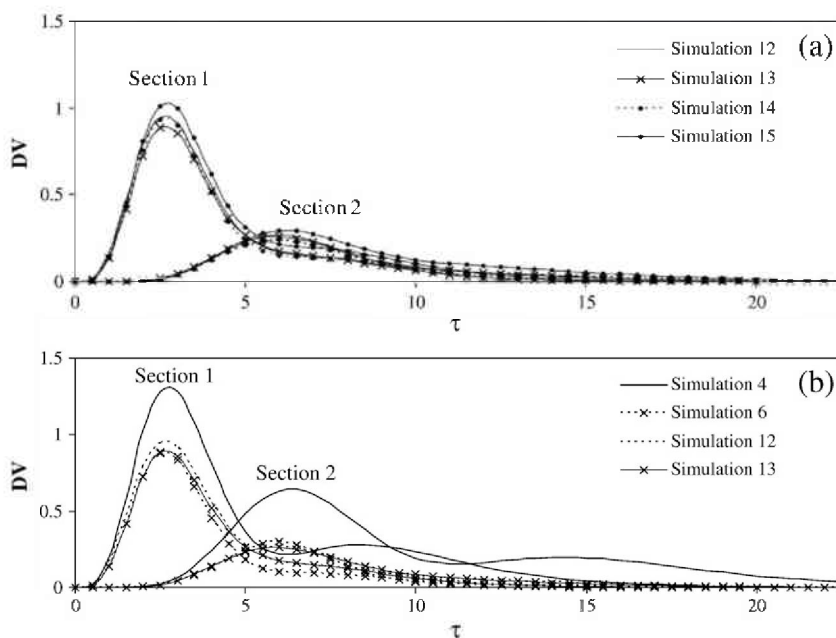

Fig. 6. Effect of correlation between K and M for high ω (1.0) in simulations 12 (no correlation, $\sigma_M^2 = 1.0$), 13 (negative correlation, $\sigma_M^2 = 1.0$), 14 (positive correlation, $\sigma_M^2 = 1.0$), and 15 (positive correlation, $\sigma_M^2 = 3.0$) on discharge variance.
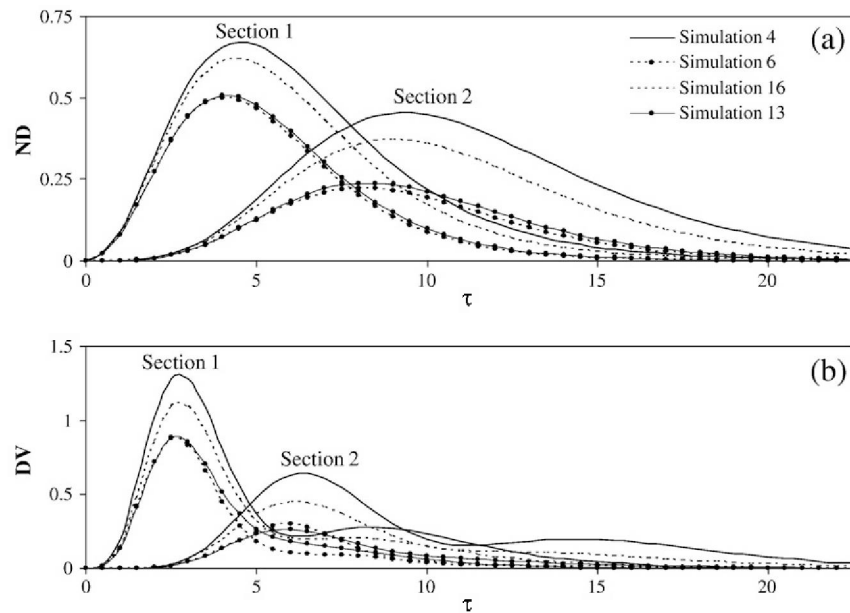
Fig. 7. Effect of electron donor/acceptor availability (a) normalized mean discharge, and (b) discharge variance.

efficiencies are most sensitive to ED/EA variability and the assumed concentration distribution for incipient biomass when groundwater velocity conditions favored microbial growth ($\omega \geq 1$) [see simulations 8, 9, 12, 13, 14, 15, and 16]. Only when ED/EA variability is considered, are noticeable changes to the cumulative discharge observed at both sections (compare simulations 3, 6, 13 and 16 in Table 3). This is consistent with the conclusions of Li et al. [115,116]. The spatial variability of ED/EA concentrations increases DV as well (Fig. 7b). That is the increase in ND for simulation 16 compared to simulation 13 is accompanied by an increase in DV. Hence, ignoring ED/EA variability can lead to an underestimation of the mass discharge and an underestimation of the uncertainty associated with that discharge.

5. Summary and conclusions

In this paper, Monte Carlo simulations were conducted to investigate spatial–temporal variations in subsurface microbial mediated contaminant discharge affected by a Damkohler number ω and physical, chemical, and biologically heterogeneities in a 2-D aquifer. Physical heterogeneity was represented as spatial variations in hydraulic conductivity. Biological heterogeneity was manifested as spatial variations in initial and transient distributions of microbial biomass, and finally chemical heterogeneity was included as spatial variations in the concentration of a requisite electron donor/acceptor. Monte Carlo simulations provided predictions for ensemble mean discharges at transects as well as the uncertainty in these predictions represented as discharge variances. Comparisons between Monte Carlo simulations and corresponding homogeneous scenarios of assumed uniform physical, chemical, and biological properties were used to elucidate the effects of physical, chemical, and biological heterogeneities and their possible correlation on contaminant mass discharges.

Physical heterogeneity increases dispersion in both longitudinal and transverse directions compared to homogenous simulations, which explained the early increase and the delayed decrease in ensemble mean contaminant discharges at model transects. The physical heterogeneities induced discharge variances at transects that varied over time; producing two peaks over time corresponding to two periods of high uncertainty in mass discharge. The first peak was observed to be associated with the arrival of the leading edge of the ensemble plume (i.e., when the steepest increase in mass discharge

occurred), while the second occurred as the plume's trailing edge traverses the transect plane (i.e., when the steepest decrease in mass discharge occurred). A simple stream tube model was invoked to explain the occurrence of peaks in contaminant discharge variance.

Microbial mediated degradation decreased the expected contaminant mass discharge at a section transect and the discharge variance. The increasing microbial activity did not affect the arrival time of plumes in either homogenous or physically heterogeneous cases. A greater relative decrease in discharge variance occurred at the trailing edge of a simulated plume (second peak) than at the leading edge (first peak). This occurred most likely because the trailing edge encounters a higher density of active biomass produced as microbial growth increased to consume the leading edge of the plume, and also because the travel time and in turn the exposure to active microbial colonies was longer for contaminants in the trailing edge of plume.

When conditions were less favorable for microbial growth/attenuation ($\omega \leq 0.2$), the presence of physical heterogeneities and/or incipient biological heterogeneities did not significantly alter the contaminant mass discharge at a transect plane compared to predictions from deterministic homogenous simulations. This suggests that a homogeneous aquifer assumption may in fact be sufficiently accurate for small ω values. However, as growth conditions improved (ω increased) contaminant attenuation efficiency decreased significantly as the variations increased in the incipient biomass distribution. This was an outcome of the fact that increasing the biomass distribution variance produced large regions where initial biomass concentrations were low and only small "islands" of large biomass concentrations. As a result, the contaminant plume escaped attenuation in large regions of low biomass, and because contaminant degradation and microbial growth are coupled, the absence of attenuation in these regions was not compensated by higher attenuation in other regions of greater biomass.

The final MC simulation examined the sensitivity of contaminant discharge to spatial variations in the incipient concentrations of a critical electron donor/acceptor. The expected mass discharge and variance was quite sensitive to this particular chemical heterogeneity. More specifically, electron donor/acceptor variability produced significant reduction in subsurface bioattenuation efficiencies because critical reaction processes had become substrate-limited at locations throughout the aquifer. Expect contaminant discharges increased at

each transect as did discharge uncertainties. In general cumulative attenuation efficiencies were most sensitive to spatial variations in ED/EA and incipient biomass concentrations when conditions favored microbial growth ($\omega \geq 1.0$).

Acknowledgements

References

[1] Basu NB, Rao PSC, Falta RW, Annable MD, Jawitz JW, Hatfield K. Temporal evolution of DNAPL source and contaminant discharge distribution: impacts of source mass depletion. J Contam Hydrol 2008;95(1–2):93–109.

[2] Einarson MD, Mackay DM. Predicting impacts of groundwater contamination. Environ Sci Technol 2001;35:66A–73A.

[3] Schwarz R, Ptak T, Holder T, Teutsch G. Groundwater risk assessment at contaminated sites: a new investigation approach. Groundwater quality: remediation and protection. Proceedings of the GQ'98 Conference Tübingen, Germany: IAHS Publication; 1998. p. 49–55.

[4] Feenstra S, Cherry JA. Diagnosis and assessment of DNAPL sites. In: Pankow JF, Cherry JA, editors. Dense chlorinated solvents and other DNAPLs in groundwater. Portland, OR: Waterloo Press; 1996. p. 395–473.

[5] Hatfield K, Annable MD, Cho J, Rao PSC, Klammler H. A direct passive method for measuring water and contaminant fluxes in porous media. J Contam Hydrol 2004;75(3–4):155–81.

[6] Hatfield, K., Rao, P.S.C., Annable, M.D., Campbell T., 2002. Device and method for measuring fluid and solute fluxes in flow systems, Patent US 6, 402, 547 B1.

[7] Annable MD, Hatfield K, Cho J, Klammler H, Parker BL, Cherry JA, et al. Field-scale evaluation of the passive discharge meter for simultaneous measurement of groundwater and contaminant fluxes. Environ Sci Technol 2005;39(18): 7194–201.

[8] Basu NB, Rao PSC, Poyer IC, Annable MD, Hatfield K. Flux-based assessment at a manufacturing site contaminated with trichloroethylene. J Contam Hydrol 2006;86(1–2):105–27.

[9] Lee J, Rao PSC, Poyer IC, Toole RM, Annable MD, Hatfield K. Oxyanion discharge characterization using passive discharge meters: development and field testing of surfactant-modified granular activated carbon. J Contam Hydrol 2007;9, doi:10.1016/j.

[10] Bockelmann A, Ptak T, Teutsch G. An analytical quantification of mass fluxes and natural attenuation rate constants at a former gasworks site. J Contam Hydrol 2001;53(3–4):429–53.

[11] Bockelmann A, Zamfirescu D, Ptak T, Grathwohl P, Teutsch G. Quantification of mass fluxes and natural attenuation rates at an industrial site with limited monitoring network: a case study. J Contam Hydrol 2003;60(1–2):97–121.

[12] Bauer S, Bayer-Raich M, Holder T, Kolesar C, Muller D, Ptak T. Quantification of groundwater contamination in an urban area using integral pump tests. J Contam Hydrol 2004;75(3–4):183–213.

[13] Bayer-Raich M, Jarsjö J, Liedl R, Ptak T, Teutsch G. Average contaminant concentration and mass flow in aquifers from time dependent pumping well data: analytical framework. Water Resour Res 2004;40:W08303, doi: 10.1029/2004WR003095.

[14] Bayer-Raich M, Jarsjö J, Liedl R, Ptak T, Teutsch G. Integral pumping test analysis of linearly sorbed groundwater contaminants using multiple wells: inferring mass flows and natural attenuation rates. Water Resour Res 2006;42:W08411, doi:10.1029/2005WR004244.

[15] Brooks MC, Wood L, Annable MD, Hatfield K, Cho J, Holbert C, et al. Changes in contaminant mass discharge from DNAPL source mass depletion: evaluation at two field sites. J Contam Hydrol 2008;102:140–53.

[16] Rao PSC, Jawitz JW, Enfield CG, Falta RW, Annable MD, Wood AL. Technology integration for contaminated site remediation: cleanup goals and performance criteria. In: Thornton SF, Oswald SE, editors. Groundwater quality: natural and enhanced restoration of groundwater pollution. Sheffield, UK: IAHS Press; 2002. p. 571–8.

[17] Enfield CG, Wood AL, Brooks MC, Annable MD. Interpreting tracer data to forecast remedial performance. In: Thornton SF, Oswald SE, editors. Groundwater quality: natural and enhanced restoration of groundwater pollution. Sheffield, UK: IAHS Press; 2002. p. 11–6.

[18] Enfield CG, Wood AL, Espinoza FP, Brooks MC, Annable M, Rao PSC. Design of aquifer remediation systems: (1) describing hydraulic structure and NAPL architecture using tracers. J Contam Hydrol 2005;81(1–4):125–47.

[19] Rao PSC, Jawitz JW. Comment on "Steady state mass transfer from single-component dense nonaqueous phase liquids in uniform flow fields" by T.C. Sale and D.B. McWhorter. Water Resour Res 2003;39(3):1068.

[20] Parker JC, Park E. Modeling field-scale dense nonaqueous phase liquid dissolution kinetics in heterogeneous aquifers. Water Resour Res 2004;40:W05109, doi:10.1029/2003WR002807.

[21] Zhu J, Sykes JF. Simple screening models of NAPL dissolution in the subsurface. J Contam Hydrol 2004;72(1–4):245–58.

[22] Falta RW, Rao PSC, Basu N. Assessing the impacts of partial mass depletion in DNAPL source zones: I. Analytical modeling of source strength functions and plume response. J Contam Hydrol 2005;78(4):259–80.

[23] Falta RW, Rao PSC, Basu N. Assessing impacts of partial mass depletion in DNAPL source zones: II. Coupling source strength functions to plume evolution. J Contam Hydrol 2005;79(1–2):45–66.

[24] Jawitz JW, Fure AD, Demy GG, Berglund S, Rao PSC. Groundwater contaminant discharge reduction resulting from nonaqueous phase liquid mass reduction. Water Resour Res 2005;41, doi:10.1029/2004WR003825.

[25] Park E, Parker JC. Evaluation of an upscaled model for DNAPL dissolution kinetics in heterogeneous aquifers. Adv Water Resour 2005;28(12):1280–91.

[26] Fure AD, Jawitz JW, Annable MD. DNAPL source depletion: linking architecture and discharge response. J Contam Hydrol 2006;85(3–4):118–40.

[27] Christ JA, Ramsburg CA, Pennell KD, Abriola LM. Estimating mass discharge from dense nonaqueous phase liquid source zones using upscaled mass transfer coefficients: an evaluation using multiphase numerical simulations. Water Resour Res 2006;42:W11420, doi:10.1029/2006WR004886.

[28] McGuire TM, McDade JM, Newell CJ. Performance of DNAPL source depletion technologies at 59 chlorinated solvent-impacted sites. Ground Water Monit Remediat 2006;26(1):73–84.

[29] Gelhar LW, Gutjahr AL, Naff RL. Stochastic analysis of macrodispersion in a stratified aquifer. Water Resour Res 1979;15(6):1387–97.

[30] Gelhar LW, Axness CL. Three-dimensional stochastic analysis of macrodispersion in aquifers. Water Resour Res 1983;19(1):161–80.

[31] Dagan G. Solute transport in heterogeneous porous formations. J Fluid Mech 1984;145:151–77.

[32] Dagan G. Time-dependent macrodispersion for solute transport in anisotropic heterogeneous aquifers. Water Resour Res 1988;24(90):1491–500.

[33] Kabala ZJ, Sposito G. A stochastic model of reactive solute transport with time-varying velocity in a heterogeneous aquifer. Water Resour Res 1991;27(3):341–50.

[34] Kabala ZJ, Sposito G. Statistical moments of reactive solute concentration in a heterogeneous aquifer. Water Resour Res 1994;30(3):759–68.

[35] Cvetkovic VD, Shapiro AM. Mass arrival of sorptive solute in heterogeneous porous media. Water Resour Res 1990;26(9):2057–67.

[36] Cvetkovic VD, Dagan G, Cheng H. Contaminant transport in aquifers with spatially variable hydraulic and sorption properties. Proc R Soc London Ser A 1998;454:2173–207.

[37] Dagan G, Cvetkovic VD. Spatial moments of a kinetically sorbing solute plume in a heterogeneous aquifer. Water Resour Res 1993;29(12):4053–61.

[38] Vert M, Ptak T, Biver P, Vittori J. Geostatistical generation of three-dimensional aquifer realizations using the conditional SIS approach with direction trends imposed on variogram models. In: Gomez-Hernandez JJ, et al, editor. geoENV II—geostatistics for environmental applications. Dordrecht: Kluwer Academic; 1999. p. 343–54.

[39] Dagan G. Flow and transport in porous formations. Berlin: Springer; 1989.

[40] Ptak T, Teutsch G. Macrodispersivity in highly heterogeneous porous aquifers. In: Hötzl H, Werner A, editors. Tracer hydrology. Rotterdam: Balkema; 1992. p. 149–55.

[41] Gelhar LW. Stochastic subsurface hydrology from theory to applications. Water Resour Res 1986;22(9):135–45.

[42] Gelhar LW. Stochastic subsurface hydrology. Prentice Hall: Englewood Cliffs; 1993.

[43] Bellin A, Rinaldo A, Bosma WJP, van der Zee SM, Rubin Y. Linear equilibrium adsorbing solute transport in physically and chemically heterogeneous porous formations, 1: analytical solutions. Water Resour Res 1993;29(12):4019–30.

[44] Burr DT, Sudicky EA, Naff RL. Non-reactive and reactive solute transport in three-dimensional heterogeneous porous media: mean displacement, plume spreading, and uncertainty. Water Resour Res 1994;30(3):791–815.

[45] Hu BX, Cushman JH, Deng FW. Nonlocal reactive transport with physical, chemical, and biological heterogeneity. Adv Water Resour 1997;20(5–6): 293–308.

[46] Hu BX, Deng FW, Cushman JH. Nonlocal reactive transport with physical and chemical heterogeneity: linear nonequilibrium sorption with random Kd. Water Resour Res 1995;31(9):2239–52.

[47] Valocchi AJ. Spatial moment analysis of the transport of kinetically adsorbing solutes through stratified aquifers. Water Resour Res 1989;25(2):273–9.

[48] Grathwohl P, Kleineidam S. Impact of heterogeneous aquifer materials on sorption capacities and sorption dynamics of organic contaminants. Groundwater quality: remediation and protection. IAHS Publ 1995;225:79–86.

[49] Ptak T, Strobel H. Sorption of fluorescent tracers in a physically and chemically heterogeneous aquifer material. In: Arehart GB, Hulston JR, editors. Water–rock interaction. Rotterdam: Balkema; 1998. p. 177–80.

[50] Karapanagioti HK, Sabatini DA, Kleineidam S, Grathwohl P, Ligouis B. Phenanthrene sorption with heterogeneous organic matter in a landfill aquifer material. Phys Chem Earth Bio 1999;24(6):535–41.

[51] Kleineidam S, Rügner H, Grathwohl P. Impact of grain scale heterogeneity on slow sorption kinetics. Environ Toxic Chem 1999;18(8):1673–8.

[52] Rügner H, Kleineidam S, Grathwohl P. Long term sorption kinetics of phenanthrene in aquifer materials. Environ Sci Technol 1999;33(10):1645–51.

[53] Ptak T, Schmid G. Dual-tracer transport experiments in a physically and chemically heterogeneous porous aquifer: effective transport parameters and spatial variability. J Hydrol 1996;183(1–2):117–38.

[54] Miralles-Wilhelm F, Gelhar LW, Kapoor V. Stochastic analysis of oxygen-limited biodegradation in three-dimensionally heterogeneous aquifers. Water Resour Res 1997;33(6):1251–63.

[55] Miralles-Wilhelm F, Gelhar LW. Stochastic analysis of oxygen-limited biodegradation in heterogeneous aquifers with transient microbial dynamics. J Contam Hydrol 2000;42:69–97.

[56] Scholl MA. Effects of heterogeneity in aquifer permeability and biomass on biodegradation rate calculations—results from numerical simulations. Ground Water 2000;38(5):702–12.

[57] Mohamed MAM, Hatfield K, Hassan AE. Monte Carlo evaluation of microbial-mediated contaminant reactions in heterogeneous aquifers. Adv Water Resour 2006;29:1123–39.

[58] Chaudhuri A, Sekhar M. Stochastic finite element method for analysis of transport of nonlinearly sorbing solutes in three-dimensional heterogeneous porous media. Water Resour Res 2007;43:W07442, doi:10.1029/2006WR004892.

[59] Marin CM, Medina Jr MA, Butcher JB. Monte Carlo analysis and Bayesian decision theory for assessing the effects of waste sites on groundwater: I. Theory. J Contam Hydrol 1989;5:1–13.

[60] Medina Jr MA, Butcher JB, Marin CM. Monte Carlo analysis and Bayesian decision theory for assessing the effects of waste sites on groundwater: II. Applications. J Contam Hydrol 1989;5:15–31.

[61] Chaudhuri A, Sekhar M. Analysis of biodegradation in a 3-D heterogeneous porous medium using nonlinear stochastic finite element method. Adv Water Resour 2007;30(3):589–605.

[62] James BR, Freeze RA. The worth of data in predicting aquitard continuity in hydrogeological design. Water Resour Res 1993;29(7):2049–65.

[63] Dagan G. Transport in heterogeneous porous formations – spatial moments, ergodicity, and effective dispersion. Water Resour Res 1990;26(6):1281–90.

[64] Dagan G, Fiori A. The influence of pore-scale dispersion on concentration statistical moments in transport through heterogeneous aquifers. Water Resour Res 1997;33(7):1595–605.

[65] Fiori A, Berglund S, Cvetkovic V, Dagan G. A first-order analysis of solute discharge statistics in aquifers: the combined effect of pore-scale dispersion, sampling, and linear sorption kinetics. Water Resour Res 2002;38(8):1137 [Art].

[66] Rubin Y. Prediction of tracer plume migration in disordered porous media by the method of conditional probabilities. Water Resour Res 1991;27(6): 1291–308.

[67] Curtis GP, Roberts PV, Reinhard M. A natural gradient experiment on solute transport in a sand aquifer, 4, sorption of organic solutes and its influence on mobility. Water Resour Res 1986;22(13):2059–68.

[68] Mackay DM, Freyberg DL, Roberts PV, Cherry JA. A natural gradient experiment on solute transport in a sand aquifer, 1, approach and overview of plume movement. Water Resour Res 1986;22(13):2017–29.

[69] Freyberg DL. A natural gradient experiment on solute transport in a sand aquifer, 2, spatial moments and the advection and dispersion of nonreactive tracers. Water Resour Res 1986;22(13):2031–46.

[70] Deng F-W, Cushman JH, Delleur JW. A Fast Fourier transform stochastic analysis of the contaminant transport problem. Water Resour Res 1993;29 (9):3241–7.

[71] LeBlanc DR, Garabedian SP, Hess KH, Gelhar LW, Quadri RD, Stollenwerk KG, et al. Large-scale natural gradient tracer test in sand and gravel, Cape Cod, Massachusetts, 1, experimental design and observed tracer movement. Water Resour Res 1991;27(5):895–910.

[72] Barry DA, Coves J, Sposito G. On the Dagan model of solute transport in groundwater: application to the Borden site. Water Resour Res 1988;24(10):1805–17.

[73] Bailey JE, Ollis DF. Biochemical engineering fundamentals. New York: McGraw Hill; 1977.

[74] Molz FJ, Widdowson MA, Benefield LD. Simulation of microbial growth dynamics coupled to nutrient and oxygen transport in porous media. Water Resour Res 1986;22(8):1207–16.

[75] Rittmann BE, McCarty PL, Roberts PV. Trace-organics biodegradation in aquifer recharge. Ground Water 1980;18:236–43.

[76] Bouwer EJ, McCarty PL. Modeling of trace organics biotransformation in the subsurface. Ground Water 1984;22:433–40.

[77] Bouwer EJ, Cobb GD. Modeling of biological processes in the subsurface. Water Sci Technol 1987;19:769–79.

[78] Champagne P, Parker WJ, Van-Geel P. Modeling cometabolic biodegradation of organic compounds in biofilms. Water Sci Technol 1999;39(7):147–52.

[79] Långmark J, Storeya MV, Ashboltb NJ, Stenström TA. Artificial groundwater treatment: biofilm activity and organic carbon removal performance. Water Res 2004;38(3):740–8.

[80] Kim H, Jaffé Peter R, Young Lily Y. Simulating biodegradation of toluene in sand column experiments at the macroscopic and pore-level scale for aerobic and denitrifying conditions. Adv Water Resour 2004;27(4):335–48.

[81] Iliuta I, Larachi F. Modeling simultaneous biological clogging and physical plugging in trickle-bed bioreactors for wastewater treatment. Chem Eng Sci 2005;60(5):1477–89.

[82] Liang C, Chiang P, Chang E. Modeling the behaviors of adsorption and biodegradation in biological activated carbon filters. Water Res 2007;41(15):3241–50.

[83] Liang C, Chiang P. Mathematical model of the non-steady-state adsorption and biodegradation capacities of BAC filters. J Hazar Mater 2007;139(2):316–22.

[84] Simpson DR. Biofilm processes in biologically active carbon water purification. Water Res 2008;42(13):2839–48.

[85] Buchanan W, Roddicka F, Porter N. Removal of VUV pre-treated natural organic matter by biologically activated carbon columns. Water Res 2008;42(13): 3335–42.

[86] Watson JE, Gardner WR. A mechanistic model of bacterial colony growth response to substrate supply. A paper presented at the Chapman Conference on Microbial Processes in the Transport, Fate, and In Situ Treatment of Subsurface Contaminants. Snowbird, UT; 1986.

[87] Yoshida H, Yamamoto K, Yogo S, Murakami Y. An analogue of matrix diffusion enhanced by biogenic redox reaction in fractured sedimentary rock. J Geochem Explor 2006;90(1–2):134–42.

[88] Bazin MJ, Saunders PT, Prosser JI. Models of microbial interactions in the soil. CRC Crit Rev Microbiol 1976;4:463–98.

[89] Corapcioglu MY, Haridas A. Transport and fate of microorganisms in porous media: a theoretical investigation. J Hydrol 1984;72:149–69.

[90] Corapcioglu MY, Haridas A. Microbial transport in soils and groundwater: a numerical model. Adv Water Resour 1985;8:188–200.

[91] Borden RC, Bedient PB. Transport of dissolved hydrocarbons influenced by oxygen-limited biodegradation: 1. Theoretical Development. Water Resour Res 1986;22(13):1973–82.

[92] Celia MA, Kindred JS. Numerical simulation of subsurface contaminant transport with multiple nutrient biodegradation. Proceedings of the International Conference on the Impact of Physiochemistry on the Study, Design, and Optimization of Processes in Natural Porous Media. Nancy, France: Presses University de Nancy; 1987.

[93] Bauer RD, Maloszewski P, Zhang Y, Meckenstock RU, Griebler C. Mixing-controlled biodegradation in a toluene plume—results from two-dimensional laboratory experiments. J Contam Hydrol 2008;96(1–4):150–68.

[94] Baveye P, Valocchi A. An evaluation of mathematical models of the transport of biologically reacting solutes in saturated soils and aquifers. Water Resour Res 1989;25(6):1413–21.

[95] MacQuarrie KTB, Sudicky EA, Frind EO. Simulation of biodegradable organic contaminants in groundwater 1. Numerical formulation in principal directions. Water Res Res 1990;26(2):207–17.

[96] Chiang CY, Dawson CN, Wheeler MF. Modeling of in-situ biorestoration of organic compounds in groundwater, technical report. Trans porous media 1991;6:667–702.

[97] Andricevic R, Cvetkovic V. Evaluation from contaminants migrating by groundwater. Water Resour Res 1996;32(3):611–21.

[98] Maxwell RM, Kastenberg WE. Stochastic environmental risk analysis: an integrated methodology for predicting risk from contaminated groundwater. Stoch Env Res Risk Assess 1999;13:27–47.

[99] Hassan AE, Cushman JH, Delleur JW. Monte Carlo studies of flow and transport in fractal conductivity fields: comparison with stochastic perturbation theory. Water Resour Res 1997;33(11):2519–34.

[100] Hassan AE, Cushman JH, Delleur JW. A Monte Carlo assessment of Eulerian flow and transport perturbation models. Water Resour Res 1998;34(5): 1143–63.

[101] Mohamed MAM. METABIOTRANS: A finite element model for metals transport and biotransformation in saturated groundwater, Ph.D. Dissertation, University of Florida, USA, 2001.

[102] Mohamed MM, Hatfield K, Perminova IV. Evaluation of Monod kinetic parameters in the subsurface using moment analysis: theory and numerical testing. Adv Water Resour 2007;30:2034–50.

[103] Kindred JS, Celia MA. Contaminant transport and biodegradation 2: conceptual model and test simulation. Water Resour Res 1989;25:1149–59.

[104] Schafer D, Schafer W, Kinzelbach W. Simulation of reactive processes related to biodegradation in aquifers: 1. Structure of the three-dimensional reactive transport model. J Contamin Hydrol 1998;31(1–2):167–86.

[105] Brusseau M, Xie L, Li L. Biodegradation during contaminant transport in porous media: 1. Mathematical analysis of controlling factors. J Contamin Hydrol 1999;37:269–93.

[106] Isaaks, Srivastava. An introduction to applied geostatistics. Oxford University Press; 1989. p. 486.

[107] Rifai HS, Bedient PB. Comparison of biodegradation kinetics with an instantaneous reaction model for groundwater. Water Resour Res 1990;26:637–45.

[108] Rashid M, Kaluarachchi J. A simplified numerical algorithm for oxygen- and nitrate-based biodegradation of hydrocarbons using Monod expressions. J Contam Hydrol 1999;40(1):53–77.

[109] Thullner M, Schroth MH, Zeyer J, Kinzelbach W. Modeling of a microbial growth experiment with bioclogging in a two-dimensional saturated porous media flow field. J Contam Hydrol 2004;70:37–62.

[110] Brockman FJ, Christopher JM. Subsurface microbiological heterogeneity: current knowledge, descriptive approaches and applications. FEMS Microbiol Rev 1997;20:231–47.

[111] Parkin TB. Soil microsites as a source of denitrification variability. Soil Sci Soc Am 1987;51:1194–9.

[112] Parkin RB, Robinson JA. Stochastic models of soil denitrification. Appl Environ Microbiol 1989;55:72–7.

[113] Scheibe TD, Dong H, Xie Y. Correlation between bacterial attachment rate coefficients and hydraulic conductivity and its effect on field-scale bacterial transport. Adv Water Resour 2007;30:1571–92.

[114] Murphy EM, Ginn TR, Chilakapti A, Reseh CT, Phillips JL, Wietsma TW, et al. The influence of physical heterogeneity on microbial degradation and distribution in porous media. Water Resour Res 1997;33(5):1087–103.

[115] Li L, Peters CA, Celia MA. Upscaling geochemical reaction rates using pore-scale network modeling. Adv Water Resour 2006;29(9):1351–70.

[116] Li L, Peters CA, Celia MA. Applicability of averaged concentrations in determining geochemical reaction rates in heterogeneous porous media. Am J Sci 2007;307: 1146–66.

[117] Glassley WE, Simmons AM, Kercher JR. Mineralogical heterogeneity in fractured, porous media and its representation in reactive transport models. Appl Geochem 2002;17(6):699–708.

[118] Scheibe TD, Fang Y, Murray CJ, Roden EE, Chen J, Chien Y. Transport and biogeochemical reaction of metals in a physically and chemically heterogeneous aquifer. Geosphere 2006;2(4), doi:10.1130/GES00029.1.

[119] Tompson AFB, Schafer AL, Smith RW. Impacts of physical and chemical heterogeneity on cocontaminant transport in a sandy porous medium. Water Resour Res 1996;32(4):801–18.

[120] Lovley DR, Coates JD, Blunt-Harris EL, Phillips EJP, Woodward JC. Humic substances as electron acceptors for microbial respiration. Nature 1996;382: 445–8.

[121] Lovley DR, Fraga JL, Coates JD, Blunt-Harris EL. Humics as an electron donor for anaerobic respiration. Environ Microbiol 1999;1:89–98.

[122] Gu BH, Chen J. Enhanced microbial reduction of contaminant and U(VI) by different natural organic matter fractions. Geochim Cosmochim Acta 2003;67:3575–82.

[123] Perminova IV, Hatfield K. Remediation chemistry of humic substances: theory and implications for technology. In: Use of humic substances to remediate polluted environments: from theory to practice. In: Perminova IV, Hatfield K, Hertkorn N, editors. NATO Science Series: IV: Earth and Environmental Sciences, Vol. 52. Springer; 2005. p. 3–36.